Magnetically-driven phase transitions in multiferroics

A Dissertation Presented for the

Doctor of Philosophy

Degree

The University of Tennessee, Knoxville

Michael Odell Yokosuk

August 2019

Acknowledgments

First and foremost I wish to thank my advisor, Professor Janice L. Musfeldt, for guiding me to become a stronger scientist by teaching me spectroscopy, discussing problems, and pushing me to do my best. You have been a big influence on both my personal and professional development.

I am grateful to Professors Charles Feigerle, Xiling Xue,David Mandrus,and Bruce Bursten for serving on my committee, as well as for all of their interest, help, and advice.

I wish to acknowledge all the members of our research group: Dipanjan Mazumdar, Judy Cherian, Amal al-Wahish, Peng Chen, Brian Holinsworth, Ken O'Neal, Amanda Clune, Kendall Hughey, Shiyu Fan, Nathan Harms, Kevin Smith, Sabine Neal, Avery Blockmon, Kiman Park, Lakenzie Crawford, Joshua Bleu Wright, and Brandon Chapman for their help, encouragement, and collaboration. I am grateful to all the faculty and staff of the Chemistry Department who shared their knowledge with me and helped in a variety of ways during my graduate program.

A special thank you goes to my labmate and fiancé, Kendall Hughey, as her encouragement and support was unrelenting.

Lastly, I wish to acknowledge the DMREF team I worked with at Rutgers University, including Drs. David Vanderbilt, Sang-Wook Cheong, Kristjan Haule, etc. for pushing me to leave my comfort zone of chemistry and learn more physics and materials science.

Finally, I wish to thank my parents, family, and friends for always believing in and supporting me. I could not have finished my degree without your help, patience, and understanding.

Abstract

Multifunctional materials provide a platform to showcase the interplay between charge, structure, and magnetism. Complex oxides, with their delicate balance of energy scales, present a unique opportunity to unravel the cross-coupling between these interactions. Moreover, spin-orbit coupling and broken symmetries give rise to new exotic physical properties in these systems. In this dissertation, I present a spectroscopic investigation of two model complex oxides under external stimuli of temperature, magnetic field, and chemical substitution. Studying these different phase transitions from a microscopic viewpoint enhances fundamental understanding of how phase transitions occur.

Multiferroic magnetoelectrics are interesting materials in that the application of electric (magnetic) fields can change their magnetic (electric) state. We combine high field optical spectroscopy and first principles calculations to analyze the electronic structure of nickel tellurium oxide across the 53 K, 9 T, and 52 T magnetic transitions to reveal that the color properties are sensitive to magnetic order due to field-induced changes in the crystal field environment. We also reveal broadband nonreciprocal effects in nickel tellurium oxide in two different and underexplored symmetry orientations at much higher energies than typically observed.

Infrared spectroscopy is a powerful tool to investigate a wide range of physics problems such as spin-phonon coupling, broken symmetries, the onset of metallicity, and the role of spin-orbit coupling on the lattice. When a magnetic field is

applied along the easy axis of antiferromagnets, second-order spin-flop transitions are revealed via broken symmetry and large spin-orbit coupling, different than the conventional first-order mechanism. We measure the infrared vibrational properties of nickel tellurium oxide and demonstrate that the phonon anomalies are consistent with a second-order mechanism. Chemical substitution can also induce quantum phase transitions. As an example, we measure the infrared response of several different niobium-substituted europium titanium oxide systems to reveal a semiconducting to metallic state crossover. Together, these findings provide insight on how spin, charge, and the lattice couple. They also explore the fundamental mechanisms of how quantum phase transitions occur in systems with low symmetry and large spin-orbit coupling.

Table of Contents

1 Introduction: Optical properties of functional oxides **1**

2 Literature survey **16**

2.1 Material properties 16

2.1.1 Electronic transitions and crystal field splitting 16

2.1.2 The harmonic oscillator and infrared spectrosopy 23

2.1.3 Spin-orbit coupling 28

2.1.4 Magnetism and magnetic phase transitions 31

2.1.4.1 Spectroscopy in high magnetic fields 42

2.2 Multifunctional and multiferroic materials 44

2.2.1 Multifunctional materials and charge-spin-lattice coupling . . 44

2.2.2 Multiferroic materials 44

2.2.3 Magnetoelectric coupling 50

2.2.4 Nonreciprocal Directional Dichroism 52

2.2.5 Magnetoelastic coupling 60

2.3 Materials of interest 62

2.3.1 Ni_3TeO_6 62

2.3.2 $EuTiO_3$ and Nb-substitution 71

3 Experimental and theoretical techniques **74**

3.1 Optical theory 74
3.1.1 Maxwell's equations 75
3.1.2 Beer's law 80
3.1.3 Kramers-Kronig analysis and sum rules 81
3.1.4 Drude and Lorentz models 83
3.1.5 Computational methods 86
3.2 Spectroscopic instrumentation 86
3.2.1 Fourier transform spectroscopy 87
3.2.2 Bruker IFS 113v Fourier transform infrared spectrometer . . . 89
3.2.3 Bruker Equinox 55 FTIR spectrometer with Bruker IR Scope II 91
3.2.4 Perkin Elmer λ-900 grating spectrometer 91
3.3 Spectroscopy under extreme conditions 93
3.3.1 Variable temperature spectroscopy 95
3.3.2 Applied high magnetic field spectroscopy 97
3.4 Materials of interest: sample preparation, measurements, and complementary calculations 99
3.4.1 Ni_3TeO_6 99
3.4.2 $EuTiO_3$ and Nb-substituted analogs 102

4 Magnetoelectric coupling through the magnetic transitions in Ni_3TeO_6 104
4.1 Electronic structure of Ni_3TeO_6 104
4.2 Magneto-optics on Ni_3TeO_6 through the spin-flop transition 111
4.3 Driving through the metamagnetic transition in Ni_3TeO_6 119

5 Nonreciprocal directional dichroism in Ni_3TeO_6 122
5.1 Additional information 131
5.1.1 Evidence for a single chiral domain in our polished crystals . . 131

5.1.2 Nonreciprocal effects in raw data 132
5.1.3 Comparing all of the different orientations by absorption differences 134
5.1.4 Comparing the nonreciprocal response for each experimental orientation 137
5.1.5 Observation of fine structure 138
5.1.6 Size of the broadband nonreciprocal directional dichroism effect 140

6 Tracking the continuous spin-flop transition in Ni_3TeO_6 by infrared spectroscopy 144

6.1 Vibrational spectra of Ni_3TeO_6 144
6.2 Spin-lattice coupling across the Néel transition 148
6.3 Spin-lattice coupling through the field-driven spin flop transition . . . 152

7 $EuTiO_3$ and Nb-substituted 157

7.0.1 Variable temperature studies on $EuTiO_3$ 159
7.0.2 Development of metallicity at room temperature 161
7.0.3 Comparing the cubic and tetragonal phases 165

8 Summary and outlook 168

Bibliography 172

Vita 189

List of Tables

1.1 Energies moving down the periodic table 7

1.2 Scientific problems and important findings in this dissertation 9

2.1 Energies moving down the periodic table 30

2.2 Critical exponents for various models of magnetic phase transitions . 38

2.3 Spatial-inversion and time-reversal symmetry in ferroics 46

3.1 Relationships between the various response function $\epsilon(\omega)$, $\sigma(\omega)$, and $N(\omega)$ 79

3.2 Bruker IFS 113v operating parameters 89

3.3 Operating parameters of Bruker IRscope II 91

3.4 λ-900 operating parameters 93

6.1 Phonon frequencies obtained from DFT calculations ($U = 8$ eV), experimental mode frequencies, mode symmetries, spin-lattice coupling constants (the λ's in the text), and displacement patterns. The mode description in the final column encodes shifts of the three Ni ions and the Te center in the sequence Ni1-Ni2-Ni3-Te. u/d = shifts up/down along the c axis; l/r = motion to the left/right in the ab-plane; "-" indicates almost no displacement; octahedral distortions (compression/extension along certain axis/in plane) and rotations are also indicated. 147

7.1 Phonon lifetime τ_{ph} of the Ti-O stretching mode in $EuTiO_3$ at several characteristic temperatures. 161

7.2 Parameters extracted from Drude fits for $Eu(Ti_{1-x}Nb_x)O_3$ at 300 K . 163

List of Figures

1.1 (a) The $H - T$ phase diagrams for $(Fe_{1-y}Zn_y)_2Mo_3O_8$ with various values of y under $H \| c$. [5, 6] (b) Thermodynamic temperature vs. pressure phase diagram for $CsOs_2O_6$, $RbOs_2O_6$, and KOs_2O_6. [7] (c) A schematic phase diagram of yttrium barium copper oxide (YBCO) superconductors as a function of the hole density ρ and the temperature T. [8,9] (d) Magnetic field-temperature phase diagram of $LuFe_2O_4$. [10] (e) Magnetic and electric phase diagrams of $MnWO_4$ with magnetic fields applied along the x, y, and z axes. [11] (f) Phase diagram of $Mn_{1-x}Co_xWO_4$ as a function of temperature and Co concentration x. [12] 2

1.2 Methods for controlling quantum phases: Elementary excitations in quantum materials and select control techniques arranged (clockwise) in order of ascending frequency. [14] 5

1.3 Typical energy ranges of various optically accessible excitations of complex oxides. 6

1.4 Optical properties characteristic to pure electric-dipole, mixed magetoelectric, and pure magnetic-dipole excitations. (a) Counter-propagating beams are absorbed with the same strength in case of pure electric (red region) and magnetic (blue region) dipole transitions illustrated by the two absorption peaks at ω_0. When approaching the limit of ideal magnetoelectric resonance (white region), the material tends to show one-way transparency. (b) Electric- and magnetic-dipole transitions emerge with opposite line shapes in the normal-incidence reflectivity spectrum, while an ideal magnetoelectric resonance remains hidden. (c) Presents a list of materials having the possibility of showing this nonreciprocal directional dichroism effect. [30] 11

1.5 Summary of structural and magnetic phase transitions for $EuTi_{1-x}Nb_xO_3$. [42] 15

2.1 Energy diagram of an electronic transition from one energy level to another higher energy level. 17

2.2 Energy diagram of the band gap defined by the energy difference between the top of the valence band to the bottom of the conduction band. 19

2.3 (a) Depicts a tetrahedral environment. (b) Depicts an octahedral environment. (c) Depicts the orbital overlap between a d_{xy} orbital with the neighboring p atomic orbitals. (d) Depicts the orbital overlap between the $d_{x^2-y^2}$ orbital with the neighboring p atomic orbitals. (e) Shows the crystal field splitting for both a tetrahedral and octahedral environment. 20

2.4 Depicts how the crystal field strength for a d^6 electron configuration in an octahedral environment can alter the total spin moment. . . . 21

2.5 Tanabe-Sugano diagram for a d^6 system. 22
2.6 The potential wells of both the harmonic oscillator (green) and the anharmonic (Morse) potential (blue). 25
2.7 Phonon dispersion curves for the simple linear diatomic chain (-A-B-A-B- type), with optical and acoustic branches. 27
2.8 Diagram of how the orbital angular momentum (L) and the spin angular momentum (S) add to form J - spin-orbit coupling. 29
2.9 Schematic energy diagrams of Sr_2IrO_4 and the $5d^5$ (t_{2g}^5) configurations (a) without SOC and U, (b) with an unrealistically large U but no SOC, (c) with SOC but no U, and (d) with SOC and U. Optical transitions are labeled in (d) with arrows. (e) $5d$ level splittings by the crystal field and SOC. (f) Optical conductivity of Sr_2IrO_4. Peaks A and B correspond to transitions denoted in (d). [51] 31
2.10 Depicts the superexchange in a magnetic oxide. The arrows show how the spins of the four electrons would arrange and be distributed over the transition metal (M) and oxygen (O) atoms. (a-f) Show different arrangements of spins, with (e,f) violating the Pauli exclusion principle. 34
2.11 Lists and depicts many different magnetic states. 36
2.12 (a) Spin spiral diagram of $BiFeO_3$. [56] (b) Spin structure of $Cr_{1/3}NbS_2$. The spin magnetic moments of localized electrons rotate in the ab-plane along the helical c-axis. 37
2.13 A plot of $1/\chi$ vs. T 39

2.14 (a) Depicts how an external magnetic field applied perpendicular to the easy spin axis affects the magnetic spins in an antiferromagnet. (b,c) Depicts how external magnetic field parallel to the easy spin axis affects the antiferromagnetic spins. (d) Energy diagram of energy of the magnetic state vs. external magnetic field, showing different phases. 40

2.15 (a-c) Magneto-optical data on $Ni_3V_2O_8$. (a) Absorption coefficient, $\alpha(E)$, in the visible range at selected fields and temperatures. The inset shows a direct optical gap analysis. (b) Optical gap analysis as a function of magnetic field at selected temperatures. (c) Absorption difference spectra $\alpha(B) - \alpha(0T)$ at selected fields in the visible region. The inset shows photograph images of $Ni_3V_3O_8$ at different temperatures and magnetic fields. [59] (d-f) Magneto-infrared data on $[(CH_3)_2NH_2]Mn(HCOO)_3$. (d) Infrared response of the absolute absorption spectrum of the formate bending mode at 0 and 35 T at 4.2 K along with the 35 T absorption difference spectrum. (e) Waterfall plot of the formate bending mode at incremental fields, showing that the magneto-infrared response grows as a function of magnetic field. (f) Normalized magnetization, square of magnetization, and integrated absorption difference as a function of applied field. [17] 43

2.16 Diagram of the correlations and interplay between multiple degrees of freedom, including charge, magnetic spins, orbital, and lattice degrees of freedom. [3] 45

2.17 The electric field E, magnetic field H, and stress σ control the electric polarization P, magnetization M, and strain ϵ, respectively. In a ferroic material, P, M, or σ are spontaneously formed to produce ferromagnetism, ferroelectricity, or ferroelasticity, respectively. In a multiferroic, the coexistence of at least two ferroic forms of ordering leads to additional interactions. In a magnetoelectric multiferroic, a magnetic field may control P or an electric field may control M (green arrows). [60] 47

2.18 (a) Ferromagnets - The local magnetic moment **m** may be represented classically by a charge that dynamically traces an orbit, as indicated by the arrowheads. A spatial inversion produces no change, but time reversal switches the orbit and thus **m**. (b) Ferroelectrics - The local dipole moment **p** may be represented by a positive point charge that lies asymmetrically within a crystallographic unit cell that has no net charge. There is no net time dependence, but spatial inversion reverses **p**. (c) Multiferroics that are both ferromagnetic and ferroelectric possess neither symmetry. [63] 48

2.19 Ferromagnets (ferroelectrics) form a subset of magnetically (electrically) polarizable materials such as paramagnets and antiferromagnets (paraelectrics and antiferroelectrics). The intersection (red hatching) represents materials that are multiferroic. Magnetoelectric coupling (blue hatching) is an independent phenomenon that can, but need not, arise in any of the materials taht are both magnetically and electrically polarizable. In practive, it is likely to arise in all such materials, either directly or via strain. [63] 51

2.20 (a) Four magnetization levels controlled by applying electric field in a repeated sequence of -1 MV/m $\rightarrow$ 0 $\rightarrow$ 1 MV/m $\rightarrow$ 0 in a Y-type hexaferrite. [73] (b) Magnetic field dependence of magnetization $M(H)$ and polarization $P(H)$ at $T = 55$ K in $Fe_2Mo_3O_8$. Numbers and arrows indicate the measurement sequence. [5] 53

2.21 (a) List of materials exhibiting this nondirectional dichroism effect. [30] (b) Visualization of how opposite light propagations can give different responses. [32] (c) An object moving along the ferro-toroidal vector direction (**P**x**M** direction) is non-reciprocal, since two relevant reciprocal situations cannot be linked by symmetry operations. [31] (d) An object moving along the chiral axis is non-reciprocal if the chiral system is ferromagnetic with magnetization (**M**) along the chiral axis or when a magnetic field is applied along the chiral axis, since two relevant reciprocal situations cannot be related by any one or combination of symmetry opterations. [31] 54

2.22 Nonreciprocal effect of different materials in the terahertz infrared region. The materials shown are $BiFeO_3$ (a) [33], $CaBaCo_4O_7$ (b) [34], $FeZnMo_3O_8$ (c) [35], and $Ba_2CoGe_2O_7$ (d) [37] 58

2.23 Nonreciprocal effect of different materials in the optical region. The materials shown are $GaFeO_3$ (a) [76] and CuB_2O_4 (b) [77] 59

2.24 Far infared absorption and magneto-infrared results on $Mn[N(CN)_2]_2$. [16] 63

2.25 (a) Crystal structure of Ni_3TeO_6. (b) Magnetic structure of Ni_3TeO_6 from neutron powder diffraction. Arrows denote magnetic moments in particular nickel sites: Ni1-black, Ni2-red, Ni3-blue. [92] 64

2.26 (a,b) Temperature dependence of pyroelectric current $J(T)$, and electric polarization $P(T)$ of Ni_3TeO_6 at 1, 8.5, and 9 T, respectively. (c,d) Magnetic field dependence of magnetization $M(H)$ and dielectric constant $\epsilon(H)$ of Ni_3TeO_6 at various temperatures for both increasing and decreasing magnetic fields. A black dashed line in (c) depicts linear fit to $M(H)$ curve for $H > H_c$ and at T=47 K. (e,f) Experimental results and theoretical calculations for the magnetic field dependence of the electric polarization $\Delta P(H)$ at various temperatures, respectively. A black dashed line in (e) indicates linear fit to $\Delta P(H)$ curve for $H > H_c$ and at T=47 K. (g-i) The dependence of $f(\theta)$ of the free-energy density on the direction of the antiferromagnetic order parameter for different values of fourth-order anisotropy constant K_4 in various magnetic fields. Free-energy minima are indicated by red dots. [28] 66

2.27 (a,b) Magnetization and change of electric polarization (ΔP) of Ni_3TeO_6 for magnetic fields applied along the c-direction. (c) c-axis magnetostriction as a function of magnetic field applied along the c-axis. Solid lines are experimental data taken under isothermal conditions and open squares are from model calculations. [29] (d) Phase diagram of Ni_3TeO_6 from an assortment of measurements including dielectric constant, magnetoelectric current, polarization, magnetization, specific heat measurements, and optics. [28, 29, 93] 68

2.28 (a) displays the basic building block of Ni_3TeO_6, which corresponds to one third of one unit cell. The red triangle is associated with unequal bond lengths: 2.78, 2.88, and 3.20 Å, which can be considered as a part of the first $Ni_{(iii)}O_6$-TeO_6 honeycomb layer. Then, the neighboring $Ni_{(i)}O_6$-$Ni_{(ii)}O_6$ layer is associated with the blue triangle with unequal bond lengths: 2.61, 3.11, and 3.15 Å. We denoted the shortest bonds in red and blue triangles as bold lines. (b) shows two different ferri-chiral states: left panel with net left-handed chirality and right panel with net right-handed chirality. Red and Blue helixes, shown by following the rotation of the bold red and blue bonds, respectively, rotate in an opposite fashion, and a net chirality exists due to the asymmetry of red and blue triangles (helices). (c) is an optical microscope image of a 100 μm-thick single crystal of Ni_3TeO_6: the scale bar equals to 1 mm. The chiral domains of a Ni_3TeO_6 crystal are visible in transmission polarized optical microscope images shown in (d-j). Blue and red bars represent the angles of a polarizer and an analyzer, respectively. (d,e) show the contrast inversion of the chiral domains with rotating the analyzer from θ=90°-φ to 90°+φ. (f), compared with (d) shows no contrast change with flipping the crystal with a fixed polarizer/analyzer angle. (g-j) demonstrate no contrast change with in-plane rotation of the crystal with a fixed polarizer/analyzer angle (a red arrow labels one landmark which is an embedded different chiral domain, with which the crystal orientation can be identified). [27] 70

2.29 (a) Temperature dependence of the shear modulus C_{44} for selected values of substitution concentration of $Eu(Ti_{1-x}Nb_x)O_3$. Data is shifted for clarity. [42] (c) The temperature vs substitution phase diagram indicating structural and magnetic phase transitions in $Eu(Ti_{1-x}Nb_x)O_3$. [42] 73

2.30 (a) Crystal structure of $EuTiO_3$ at room temperature with space group $Pm\bar{3}m$. (b) Summary of the *dc* resistivity for several different substitution concentrations. [42] (c) Schematic view of the properties of $EuTiO_3$ as a function of temperature and Nb substitution. [42] 73

3.1 The instruments used in the lab: (a) Bruker IFS 113v FTIR spectrometer (b) Bruker Equinox 55 FTIR Spectrometer with Bruker IR Scope II (c) Perkin Elmer λ-900 Grating Spectrometer 87

3.2 Schematic view of a Michelson interferometer 88

3.3 Schematic view of the Bruker IFS 113v FTIR spectrometer. 90

3.4 Optical path diagram of Bruker IRscope II. 92

3.5 Optical layout of Perkin-Elmer λ-900 94

3.6 Set-up of LT-3-110 Heli-Tran liquid transfer line and cryostat. 96

3.7 (a) A schematic energy scale of various magnets (superconducting, resistive, hybrid, and pulsed magnets) at NHMFL. (b) Magnetic field profile of the short pulsed magnet at NHMFL-LANL. 97

3.8 (a) Schematic of the magneto-optical set-up at the NHMFL. (b) Schematic of the magneto-infrared set-up at the NHMFL 99

3.9 The image displays the polishing process of the crystal. (a) Displays the mounted crystal on the polishing puck. (b) Displays the ab-plane equilateral triangle exposed and ready to be polished and thinned. (c,d) Shows the same crystal at different times during the polishing process. (e) Shows the resulting crystal thinned and polished down to 28 μm. 100

3.10 (a,d) Depicts how the measurements were performed with respect to the chiral axis in Ni_3TeO_6. (b,e) Shows crossed polarizer images of the crystals, where lighter and darker green regions indicate different chiral domains. The red circles in these images indicate the area of measurement. (c) Intensity signal of the light throughput of the crystal in (b) under crossed polarizer and analyzer images. 101

4.1 (Color online) (a) Absorption coefficient of Ni_3TeO_6, $\alpha(E)$, in the ab-plane and the c-direction at 300 and 4.2 K. Vertical lines near the bottom mark the computed d-to-d excitations for the d^8 Ni ions, with red, green, and blue indicating excitations on Ni1, Ni2, and Ni3 sites, respectively. The insets show photographs of the crystal along c. (b) Ion-projected density of states per magnetic unit cell obtained from DFT and (c) components of linear optical dielectric response tensor calculated within the random phase approximation in the $q \to 0$ limit with no microscopic contributions (solid lines: with spin-orbit coupling included; dashed: without). The splitting of free Ni ion d^8 multiplets in the presence of an octahedral crystal field and the crystal field excitations between these levels is shown in the inset. 105

4.2 (a) Tanabe-Sugano diagram for a Ni^{2+} center in the d^8 configuration. The crystal field strength of Ni_3TeO_6 is shown in red. (b) Here, the Tanabe-Sugano diagram is turned on its side and paired with the absorption spectrum along the *ab*-plane and *c*-axis. The calculated Ni *d*-to-*d* excitations for each of the three distinct Ni centers are displayed as red, green, and blue hash marks. Expectations from the Tanabe-Sugano diagram and the theoretically predicted excitations align very well with our experimental observations. 107

4.3 (Color online) Results of DFT calculations on Ni_3TeO_6: (a) ion-projected density of states per magnetic unit cell, (b) splitting of free Ni ion d^8 multiplets in the presence of an octahedral crystal field and the crystal field excitations between these levels, and (c) components of linear optical dielectric response tensor calculated within the random phase approximation in the $q \rightarrow 0$ limit with no microscopic contributions (solid lines: with spin-orbit coupling included; dashed: without). . . . 110

4.4 Variable temperature absorption difference, $\Delta\alpha = [\alpha(E, T) - \alpha(E, T = 7\ K)]$, at (a) 0 T and (b) 12 T. 112

4.5 (Color online) Absorption difference spectra, $\Delta\alpha = [\alpha(E, B) - \alpha(E, B = 0\ \mathrm{T})]$, of Ni_3TeO_6 in the (a) *ab*-plane for $B \parallel c$ at selected fields up to 35 T: (pink 4 T, purple 10 T, green 20 T, red 35 T). The 4.2 K absolute absorption spectrum is included for comparison (on the bottom, in blue). (b) Full field (35 T) absorption difference spectra taken in the *ab*-plane and along the *c*-direction. Red, green, and blue vertical lines indicate the predicted *d*-to-*d* excitations. (c,d) Absorption difference spectra in the *ab*-plane ($B \parallel c$) and *c*-direction ($B \perp c$) at selected fields around the spin-flop transition. (e) Integrated absorption difference of the data in panels (c) and (d). 113

4.6 (a) Absolute absorption spectrum of Ni_3TeO_6 at 0 and 35 T in the *ab*-plane along with the full field absorption difference at 4.2 K. (b) Absorption spectrum at 0 and 35 T in the *c*-direction along with the absorption difference given by $\Delta\alpha = \alpha(E, B = 35\ T) - \alpha(E, B = 0\ T)$ at 4.2 K. The vertical tick marks at the bottom of each graph indicate the predicted *d*-to-*d* excitation energies of each of the Ni centers (Ni1 in red, Ni2 in green, Ni3 in blue). 116

4.7 Close-up views of the Ni *d*-to-*d* excitations in the vicinity of the (a) 1.0, (b) 1.7, and (c) 2.5 eV bands in the *ab*-plane. The set of vertical tick marks show the calculated excitations for each type of Ni center (Ni1 in red, Ni2 in green, Ni3 in blue). As discussed here and in the main text, the relative position of these excitations reveals the relative size of the crystal field splitting. 117

4.8 Close-up views of the Ni d-to-d excitations in the vicinity of the (a) 1.0, (b) 1.7, and (c) 2.5 eV bands in the c-direction. The set of vertical tick marks at the bottom of each panel indicate the calculated excitations for each type of Ni center (Ni1 in red, Ni2 in green, Ni3 in blue). [139] 117

4.9 (a) Integrated absorption difference vs. magnetic field in several different energy windows in the ab-plane. The red points correspond to analysis of the spectral data in panel (b), the green points with (c), and the blue with data in (d). The 9 T spin-flop transition is indicated by a vertical gray line. 118

4.10 Summary of the optical and magneto-optical properties of Ni_3TeO_6 in the antiferromagnetic, spin flop, and metamagnetic phases. (a, b, c) Optical absorption spectrum obtained from first principles calculations with and without spin orbit coupling as compared with the experimental absorption spectrum (α) at 4.2 K. The three different Ni centers are projected out (Ni1 in red, Ni2 green, Ni3 blue, and the total in teal). The gray band highlights a region where spin-orbit coupling is needed to capture features in the experimental data. (d, e, f) Field-induced absorption difference of Ni_3TeO_6 from first principles calculations and experiment. Here, the absorption difference is defined as $\Delta\alpha = \alpha(H) - \alpha(H = 0\ \text{T})$. The absolute absorption spectrum is reproduced at the bottom of the experimental panel. (g) Oscillator strength change in the 1.3 - 1.4 eV energy region as a function of applied field. The 9 T spin-flop and 52 T metamagnetic transition are indicated. The inset shows a close-up view of the absorption difference data in the relevant energy window. 120

5.1 Phase diagram, optical properties, and measurement geometries of Ni_3TeO_6. (a) Comprehensive phase diagram. [28, 29, 93] (b) Optical absorption of Ni_3TeO_6. (c) Field vs. time profile from the short pulse magnet. (d,e) Our two samples expose the chiral c-axis differently. In (d), the chiral axis is out of the plane of the polished crystal. In (e), the chiral axis is in-plane. (f) Schematic representation of magnetochiral dichroism. It requires a chiral axis in the material as well as light ($\pm k$) and field $\pm H$ aligned along that same chiral direction in the Faraday geometry. The nonreciprocal effect will depend upon light propagation and field direction. (g) Image of the ab-plane sample under crossed polarizer and analyzer in transmittance. The red circle indicates the location of our measurement. (h) Optical rotation measurement using crossed polarizer and analyzer. The angle Θ corresponds to the angle between the analyzer and normal from the polarizer. The red data points correspond to the lighter green portion of the crystal, and the blue data points correspond to the darker green triangles in the corners. (i) The nonreciprocal effect can also take place in the transverse magnetochiral orientation. Here, we maintain the Faraday geometry (with $\pm k$ and $\pm H$) but the chiral (c) axis is in the plane of the polished crystal. (j) Image of the polished crystal in which the c-axis is exposed under crossed polarizer and analyzer. 125

5.2 Directional dichroism for different measurement symmetries. (a, d) Schematic view of H and k relative to the chiral axis of Ni_3TeO_6 in the magnetochiral orientation. (b) Magneto-optical response as measured by the absorption difference at full field, $\Delta\alpha = \alpha(H = \pm 62\text{ T}) - \alpha(H = 0\text{ T})$. Data in the $+H$ direction are different than those in the $-H$ direction. (c) Nonreciprocal directional dichroism of Ni_3TeO_6 in the metamagnetic phase in the magnetochiral orientation, obtained by reversing the field direction with fixed k. Thus, $\Delta\alpha_{NDD} = \alpha(H_{up} = 62\text{ T}) - \alpha(H_{down} = 62\text{ T})$ which is the same as $\Delta\alpha(H_{up} = 62\text{ T}) - \Delta\alpha(H_{down} = 62\text{ T})$. For reference in (c, f), we include the linear absorption spectrum, α. (e, f) Similar $\Delta\alpha$ and $\Delta\alpha_{NDD}$ spectra are obtained by reversing the light propagation direction under constant field. Here, $\Delta\alpha$ is $\alpha(H = +62\text{ T}) - \alpha(H = 0\text{ T})$ for $\pm k$, and $\Delta\alpha_{NDD}$ is $\alpha(k_{up}) - \alpha(k_{down})$ which is the same as $\Delta\alpha(k_{up}) - \Delta\alpha(k_{down})$ with $H_{up} = 62$ T. (g, j) Schematic view of H and k relative to the chiral axis of Ni_3TeO_6 in the transverse magnetochiral orientation. (h, i) Magneto-optical and nonreciprocal directional dichroism of Ni_3TeO_6 at 62 T in the transverse magnetochiral orientation obtained by reversing the field direction under constant k. For reference in (i, l) we include the linear absorption spectrum. (k, l) Similar $\Delta\alpha$ and $\Delta\alpha_{NDD}$ spectra are obtained by varying the light propagation direction under constant field. 127

5.3 Reciprocal non-reciprocal optical effect. (a) $\Delta\alpha_{NDD}$ under different field and light propagation directions in the magnetochiral orientation for Ni_3TeO_6. (b) $\Delta\alpha_{NDD}$ under different field and light propagation directions in the transverse magnetochiral orientation. (c) Linear absorption spectrum at 4.2 K for reference. (d,e) Changes in the nonreciprocal response of Ni_3TeO_6, as measured by the change in oscillator strength Δf, as a of function magnetic field for the magnetochiral and transverse magnetochiral orientations, respectively. Zero field data, both before and after the field pulse, is shown. Insets display close-up views of $\Delta\alpha_{NDD}$ spectra as a function of magnetic field. (f-i) Comparison of $\Delta\alpha$ and $\Delta\alpha_{NDD}$ spectra when both H and k are switched in the magnetochiral (f,g) and transverse magnetochiral (h,i) orientations. 130

5.4 Raw power spectra data of Ni_3TeO_6 in both the magnetochiral and transverse magnetochiral orientations. The first plot in each is the 0 T power spectra before the magnet pulse. The second plot is the full field power spectra for the respective orientations. The final plot is the 0 T power spectra after the magnet pulse compared to 0 T spectra before the magnet pulse. This eliminates hysteretic concerns. 133

5.5 Absorption difference spectra for each comparison are plotted, with the ($+H$, up k) in green, (-H, up k) in violet, ($+H$, down k) in red, and (-H, down k) in blue. The left most panel (a-f) is the magnetochiral orientation while the right most panel (h-m) is the transverse magnetochiral orientation. The bottom-most curve is the linear absorption of the *ab*-plane for the magnetochiral orientation on the left in (g) and both *ab*-plane and *c*-direction absorption for the right transverse magnetochiral orientation in (n). 136

5.6 Comparison of all six different subtractions for both the magnetochiral and transverse magnetochiral orientations. 139

5.7 Close-up view of the $\Delta\alpha$ spectra for the $+H$, up k (red) and -H, up k (blue) for the magnetochiral (a) and transverse magnetochiral (c) orientations. The nonreciprocal effects are plotted in green underneath in (b) magnetochiral and (d) transverse magnetochiral orientations. The *ab*-plane and *c*-axis absorption spectra are underneath for reference. 139

5.8 Close-up view of the absorption data data as a function of temperature around the vicinity of the fine structure in both the *ab*-plane (a) and *c*-direction (b). 140

5.9 Close-up view of the absorption data around the vicinity of the fine structure in both the *ab*-plane and *c*-direction. Here, the phonon spectra of the *ab*-plane and *c*-direction is plotted underneath for reference. 141

5.10 Nonreciprocal effects for both the magnetochiral (top) and transverse magnetochiral (bottom) orientations. The middle plot in green represents the percent change of the entire observed nonreciprocal response. The rightmost two panels are zoomed in on the fine structure of Ni_3TeO_6. 142

6.1 (a) Polarized infrared absorption spectrum of Ni_3TeO_6 at 300 K for both the *ab*-plane and *c*-direction phonons. 145

6.2 (a) Polarized infrared absorption spectrum of Ni_3TeO_6 at 300 K. (b-f) Peak position vs. temperature for several characteristic phonons. A Boltzmann sigmoid fit was used to model traditional anharmonic effects, and the difference between the low temperature limit of this model (which gives the unperturbed frequency) and the phonon position at base temperature was used to extract the frequency shifts ($\delta\omega$'s). The Néel temperature is indicated by a vertical line at 53 K. (g) Spin-lattice coupling-induced frequency shifts, $\delta\omega$'s, for the three *ab*-plane phonon modes from panels (d-f), now plotted on a linear temperature scale, together with linear fits. 149

6.3 Displacement patterns for the three characteristic phonons that display large spin-lattice coupling across the Néel transition. Ni and Te ions are shown in green and blue respectively; oxygens (not drawn) are at octahedral vertices. Ionic displacements are are indicated by pink arrows whose length is proportional to the displacement. The rhombohedral unit cell, indicated by the orange lines, contains one Ni_3TeO_6 formula unit. 150

6.4 (a) Polarized infrared absorption spectrum, the polycrystal response, and the absorption difference spectrum at 20 T. The latter highlights the changes in the local lattice distortions between the AFM I and AFM II phases and is defined as $\Delta\alpha = \alpha(\omega, H) - \alpha(\omega, H = 0)$. (b, c, d) Close-up view of the field-induced absorption difference spectrum in the vicinity of the 310 cm^{-1} mode through the 9 T spin flop transition along with the field-induced frequency shift and line width changes. The curves in (b) are offset by 80 cm^{-1} for clarity, and the dotted arrow is a 20 cm^{-1} scale bar. The vertical line in (c, d) indicates the 9 T critical field. (e, f) Close-up view of the field-induced absorption difference spectra in the vicinity of the most collective vibrational modes along with a contour plot revealing the subtle frequency shifts through the spin flop transition. The curves in (e) are offset by 80 cm^{-1}, and a 20 cm^{-1} scale bar is included. (g) Waterfall plot in the vicinity of the 451 and 456 cm^{-1} modes providing evidence for an unexplored transition between 30 and 35 T. Each curve in the waterfall plot is offset by 85 cm^{-1}, and the scale bar is 20 cm^{-1}. All data was taken at 4.2 K. 154

7.1 Summary of temperature and substitution effects in $Eu(Ti_{1-x}Nb_x)O_3$. The cubic to tetragonal phase transition increases in temperature as substitution increases. A crossover between an AFM and FM state occurs between $x = 0.05$ and 0.10. PE = paraelectric, PM = paramagnetic, AFM = antiferromagnetic, FM = ferromagnetic. [42, 111] . . 158

7.2 (a) Optical conductivity of $EuTiO_3$ at several different temperatures. (b,c) Close-up view of the Ti-O stretching and Ti-O-Ti bending modes, respectively. (d) Frequency vs. temperature plot of the Ti-O-Ti bending mode showing doublet splitting in the low temperature phase. The structural phase transition at 288 K is indicated, and the dotted lines guide the eye. (e) Splitting of the Ti-O-Ti bending mode vs. temperature along with a power law fit. We find $\beta = 0.39$. 160

7.3 (a) Reflectance of the $Eu(Ti_{1-x}Nb_x)O_3$ series of materials at room temperature. (b) Optical conductivity of $Eu(Ti_{1-x}Nb_x)O_3$ at 300 K obtained from a Kramers-Kronig analysis of the reflectance. The spectra are offset for clarity. 162

7.4 (a) Optical conductivity of the $Eu(Ti_{1-x}Nb_x)O_3$ series of materials viewing a larger frequency range. The inset shows only the $x = 0.03$, 0.05, 0.1, and 0.2 data for simplicity. (b) Fits to the $Eu(Ti_{0.8}Nb_{0.2})O_3$ data using two Drude models as well as a Lorentz model. 164

7.5 (a) Reflectance of the $Eu(Ti_{1-x}Nb_x)O_3$ series of materials well below the structural transition in the tetragonal phase (a) and well above the transition into the cubic phase (b). The spectra are offset for clarity. 167

Chapter 1

Introduction: Optical properties of functional oxides

Some of the most complex materials in existence are transition metal oxides. They span a wide range of crystalline structures (often based on a perovskite structure) and host an incredible variety of physical phenomena. Behaviors such as insulating to metallic character, ferroelectricity, and magnetism can occur in even the most simple oxides. Many ferroelectric oxides have been exploited in various application purposes. For example, $Pb(Zr,Ti)O_3$ has been used for various sensing devices due to its excellent piezoelectric properties. [1,2] Other examples include using $(Ba,Sr)TiO_3$ for capacitors for its high dielectric permittivity, $LiNbO_3$ in optoelectronic components, and $BaTiO_3$ in thermistors. [3] Other complex oxides can exhibit even more interesting phenomena, such as multiferroicity, colossal magnetoresistance, and high temperature superconductivity. [4]

Many of these materials display some type of quantum phase transition when probed by external stimuli such as applied magnetic field, pressure, and chemical substitution (Fig. 1.1). Unlike traditional phase transitions, these transitions are not driven by thermal effects; temperature is not a factor to drive through the tran-

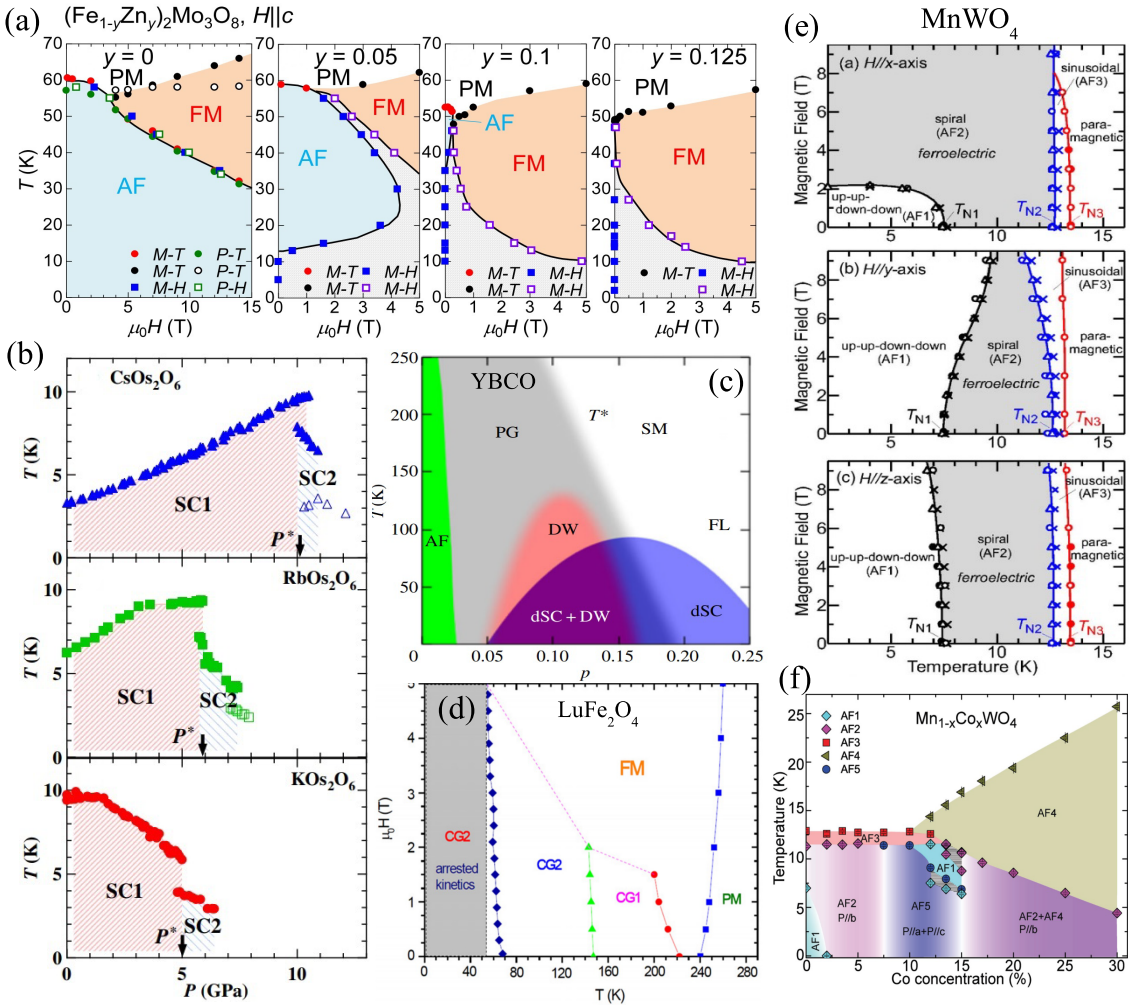


Figure 1.1: (a) The $H-T$ phase diagrams for $(Fe_{1-y}Zn_y)_2Mo_3O_8$ with various values of y under $H\|c$. [5,6] (b) Thermodynamic temperature vs. pressure phase diagram for $CsOs_2O_6$, $RbOs_2O_6$, and KOs_2O_6. [7] (c) A schematic phase diagram of yttrium barium copper oxide (YBCO) superconductors as a function of the hole density ρ and the temperature T. [8,9] (d) Magnetic field-temperature phase diagram of $LuFe_2O_4$. [10] (e) Magnetic and electric phase diagrams of $MnWO_4$ with magnetic fields applied along the x, y, and z axes. [11] (f) Phase diagram of $Mn_{1-x}Co_xWO_4$ as a function of temperature and Co concentration x. [12]

sition. They result from competing ground states in complex oxides. Different phases emerge from a variety of probing techniques. $Fe_2Mo_3O_8$, a multiferroic material, becomes antiferromagnetic below 60 K. By controlling both temperature and an applied magnetic field, the spins can flip and a ferrimagnetic phase develops. By replacing a certain amount of iron with zinc, the ferrimagnetic phase starts to dominate while eliminating the antiferromagnetic one (Fig. 1.1(a)). [5,6] High temperature superconductivity has been explored due to its fascinating physics and potential technological applications. Finding a material with this phenomena has been approached a variety of ways. $A Os_2O_6$ (A=Cs, Rb, K) show different superconducting phases when probed with temperature and pressure, as shown in Fig. 1.1(b). [7] A different approach using hole density (ρ) as a tuning parameter shows superconducting phases in yttrium barium copper oxide (Fig. 1.1(c)). [8,9] Non-collinear magnetic structures can surface in these complex oxides as well. $LuFe_2O_4$ exhibits many different magnetic and spin-glass transitions when probed by magnetic field and temperature, as shown in Fig. 1.1(d). [10] Figure 1.1(e,f) shows different phase digrams for $MnWO_4$ and Co-substituted analogs. Depending on crystal orientation and measurement axis, $MnWO_4$ displays a complex array of electric and magnetic phases. Similarly, as a function of cobalt substitution, different spin structures can occur as well as changes in polarization. [11, 12] Thus, we see that these and other oxide materials sport a variety of competing ground states and phase transitions.

An interdisciplinary background in physics, chemistry, and materials science is needed to fully understand these complex materials. Sorting out the interplay between charge, structure, and magnetism is at the heart of this type of research. Many different techniques can be used to study these complex oxides. Static measurements, such as magnetization, *dc* resistivity, and polarization are used to study bulk properties. Spectroscopy is different in that it is a microscopic technique. Moreover,

measurements in different energy regions can probe many different types of elementary excitations, as shown in Fig. 1.2. Two fundamental excitations of interest to my work include phonons, d-to-d excitations, and band gaps. Interestingly, many of these fundamental excitations can couple to different aspects of a material, resulting in interactions such as spin-charge coupling and spin-orbit coupling. Spin-orbit coupling, which increases in systems as a function of atomic number, can manifest so strongly that electronic structure is altered. In my work, spin-orbit coupling is important due to the tellurium and europium ions in the materials of interest. Another interesting interaction that is prominent in oxides is spin-lattice coupling. [13] Here, magnetostriction measurements can be used to probe how the lattice is sensitive to different magnetic transitions. However, magneto-infrared spectroscopy, being a microscope probe of the lattice, unveils which specific phonons are sensitive to different magnetic reorientations. Thus, the combination of bulk techniques with spectroscopy reveals a complete picture of a material and its properties.

Electromagnetic radiation covers a wide range of energy, from radio and microwaves to the high energy of X-rays. For our spectroscopic investigations, we use infrared through ultraviolet light. Each energy region can give rise to any number of unique types of elementary excitations, from vibrational responses in the infrared to charge transfer gaps in the ultraviolet. Figure 1.3 gives an overview of the typical excitations that are probed in each respective energy region.

In the low frequency range, infrared spectroscopy can be employed to detect magnetic excitations, low lying electronic excitations, and vibrational modes (phonons), which play a major role in many material properties including thermal and electrical conductivities. [15] Raman spectroscopy is also used to compliment infrared techniques. Combined with lattice dynamics calculations and a group theory analysis, phonon behavior can be used to understand local structure environment and

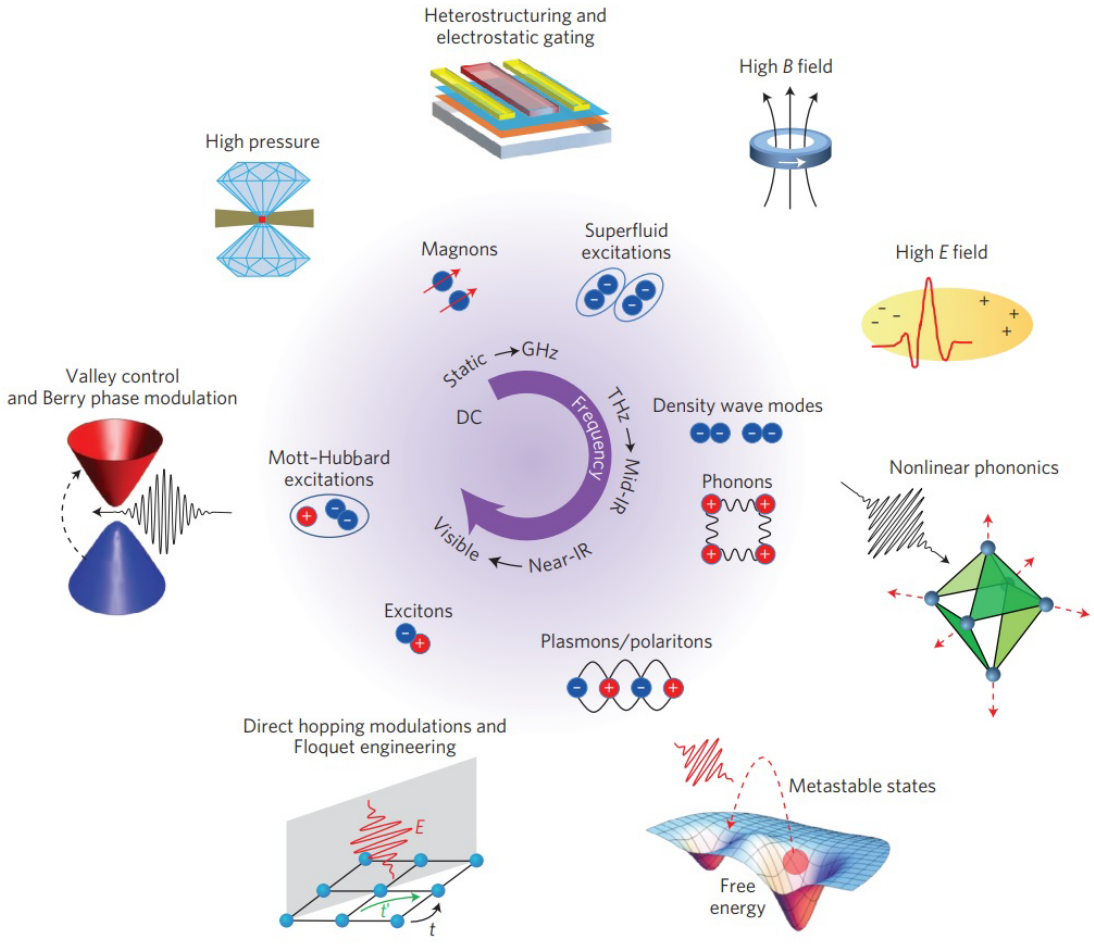


Figure 1.2: Methods for controlling quantum phases: Elementary excitations in quantum materials and select control techniques arranged (clockwise) in order of ascending frequency. [14]

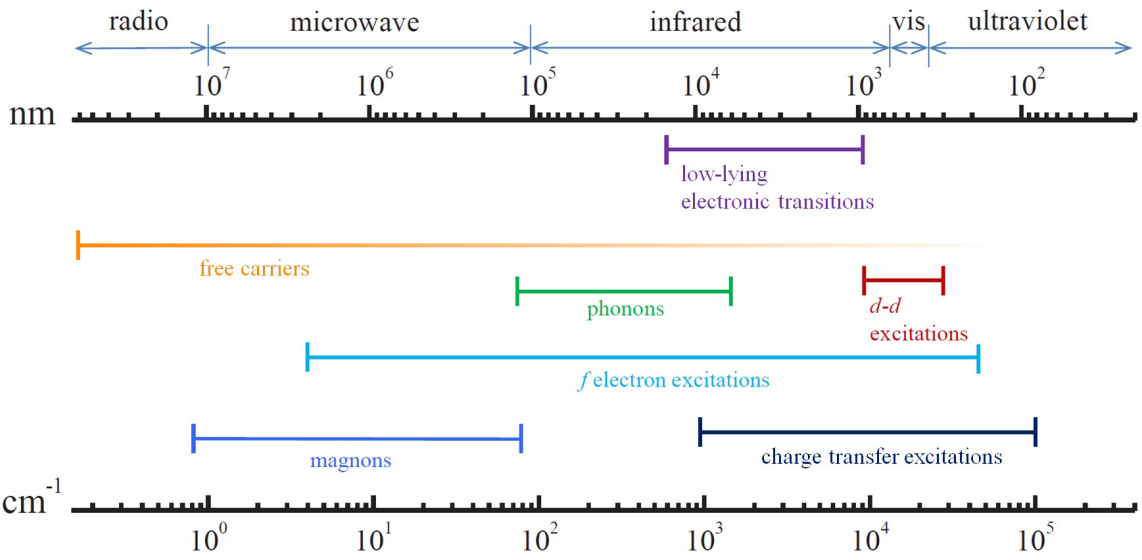


Figure 1.3: Typical energy ranges of various optically accessible excitations of complex oxides.

symmetry. [16] Phonons are the most fundamental excitations of the lattice and can couple with magnetism. For example, the lattice can be sensitive to any number of spin transitions, such as a spin-flop transition, a Néel transition, or spins aligning towards the fully polarized magnetic state. [17, 18] Phonons can also be sensitive to the onset of ferroelectricity by tracking the soft mode (or modes), revealing the displacive nature of a ferroelectric phase transition. [19]

In the higher frequency range, metal d-to-d on-site and charge transfer excitations appear in the absorption spectrum. For transition metal oxides, oxygen is a strong-field ligand, and a Tanabe-Sugano diagram predicts where on-site d-to-d excitations should manifest, depending on the crystal field symmetry around the metal ion. Charge transfer excitations determine the band gap of oxides, typically resulting from transitions between a fully occupied oxygen $2p$ orbital to a vacant metal $3d$ orbital. First-principles calculations, such as density of states, band symmetry, and band hybridization, provide insight into the electronic structure of a material. These calculations can be used to compare with experimental optical results. [20,21] Collec-

tive excitations, such as excitons and magnon sidebands, can also be revealed by optical spectrosocpy. More often than not, they are on the leading edge of an electronic transition, induced by exchange coupling and very sensitive to variations in magnetic order, making them sensitive probes of magnetic ordering transitions. [21–24] The mixing between electronic- and magnetic-dipole matrix elements is largely due to spin-orbit coupling effects. Row $3d$ of the periodic table is largely dominated by electronic correlations. For $4d$ atoms and on, spin-orbit coupling begins to compete energetically, sometimes even dominating these electronic correlation effects. With large atomic spin-orbit coupling, interesting magnetic effects can arise in what are seen as purely electronic transitions. [25, 26] These trends can be seen in Table 1.1.

Complex oxides have competing phases due to constant competition between chemical bonding, charge, and magnetism. Contrary to bulk techniques, spectroscopy is well-suited to microscopically study how elementary excitations change as a function of an applied stimulus. By driving through different phase boundaries, we can unravel how local lattice distortions, electronic structure, and on-site excitations are altered, allowing access to new non-equilibrium states.

In this dissertation, I will be focusing on how temperature, high magnetic field, and chemical substitution alter the properties of low symmetry oxides. The two materials of interest are Ni_3TeO_6 and Nb-substituted $EuTiO_3$. With each having a

Table 1.1: Energies moving down the periodic table

Row	t (orbital overlap)	U (electron-electron correlations)	λ (spin-orbit coupling constant)
$3d$	0.5 eV	8 eV	0.1 eV
$4d$	$\downarrow$	$\downarrow$	$\downarrow$
$5d$	1 eV	1 eV	0.5 - 0.8 eV

different type of quantum phase transition as well as large spin-orbit coupling, these materials were chosen to explore how optical and infrared properties change when driving through different electronic, structural, and magnetic phase transitions. A list of the scientific problems and our findings are summarized in Table 1.2.

Ni_3TeO_6 is a multiferroic oxide containing one of the largest magnetoelectric coupling constants in a single phase material known to date. Crystallizing in a modified corundum structure with space group $R3$, Ni_3TeO_6 is both polar and chiral at ambient conditions. [27] The three Ni^{2+} centers are inequivalent to one another and align along the c-axis in a Ni1, Ni2, Ni3, Te fashion. This system is a collinear antiferromagnet (easy c-axis) below 53 K, and the polarization begins to change when magnetic order sets in. Applying a 9 T magnetic field, the spins flop, driving another change in polarization. [28] Higher field magnetization and polarization measurements reveal another magnetic reorientation at 52 T (metamagnetic transition), associated with a third change in polarization significantly larger than that at 9 T. [29] With the bulk polarization changes in Ni_3TeO_6 stemming from ionic displacements, we explore how the electronic structure changes as a function of temperature and magnetic fields (up to 65 T). Using visible and ultraviolet spectroscopy, we unveil a series of Ni on-site d-to-d excitations, giving the single crystal its beautiful green color. Fine structure appears on the leading edge of several of the excitations that we attribute to being an exciton with phonon sidebands. Combining optical absorption with complementary electronic structure calculations, we find the gap to be slightly above 2.7 eV. Magneto-optical measurements with $H \parallel c$ reveal sharp changes in the Ni on-site excitations at both the 9 and 52 T magnetic transitions, whereas measurements with $H \perp c$ unveils a gradual response with increasing field. With three different crystal field splittings associated with each inequivalent Ni ion, we can hint at which Ni sites are most affected by magnetic transitions, concluding

Table 1.2: Scientific problems and important findings in this dissertation

Model Compound	Scientific Problem	Our Findings
Ni_3TeO_6	• Charge-spin interactions at the onset of magnetic order at T_N • Magneto-optical effects at B_{SF} and B_{MM} • Nonreciprocal directional dichroism effects at electronic energies • Different symmetries in which the nonreciprocal effect can arise	• Modest changes in optical spectra with the onset of magnetic order at T_N • Large optical effects due to magnetoelectric coupling in Ni on-site excitations and crystal field splittings driving through B_{SF} and B_{MM} • Nonreciprocal effects found in typically purely electronic features due to magnetic- and electric-dipole mixing from large atomic spin-orbit coupling • Broad and higher energy effects than previously reported of nonreciprocity in the optical region using unpolarized light • Evidence for both a magnetochiral and transverse magnetochiral directional dichroism mechanism
	• Magnetoelastic coupling at the onset of magnetic order at T_N • Phonon sensitivity to B_{SF}	• Three E symmetry phonon modes are sensitive to the onset of magnetic ordering below 53 K • Selective phonons change frequency, line width, and oscillator strength at the spin-flop transition of 9 T • Hints of a higher field magnetic transition due to phonon sensitivity around 30 T
$EuTi_{1-x}Nb_xO_3$	• Analyze the effects of disorder in the system as a function of chemical substitution • Exploration of the cubic to tetragonal phase transition in the parent and substituted materials • Origin and robustness of metallicity in this system • Role of Nb substitution in the development of metallic character	• Separated out the effects that the development of metallicity and disorder play in the system • Modest effects of the cubic to tetragonal phase transition in the parent and substituted materials • Onset of metallic character as a function of substitution with the development of the Drude response between the x=0.03 and 0.05 compounds

that the Ni1 and Ni2 pair is most affected. We illustrate how and why the electronic properties of Ni_3TeO_6 can be controlled by magnetic field, as well as describe the color property tunability to field-induced changes in crystal field environments of the associated Ni d-to-d excitations.

Many effects arise when a material is magnetoelectric. One of the most rare and interesting phenomena is called nonreciprocal directional dichroism. When the motion of an object in one direction is different than that in the opposite direction, it is known as a nonreciprocal effect. [31] In spectroscopy, it is simply the difference in absorbed light between opposite propagation directions ($\pm k$) at some type of magnetoelectric excitation. Theoretically, a material could have a tunable one way transparency, as shown in Fig. 1.4(a). Previous reports of this effect are rare, but of the materials showing nonreciprocity, the effect manifests only at very low energies, where most magnetoelectric excitations occur. [32–37] With such low crystallographic and magnetic symmetry, Ni_3TeO_6 is a prime candidate to search for this unique phenomenon deemed nonreciprocal directional dichroism. The specific symmetry requirements are rare; however, with Ni_3TeO_6 having a chiral axis, a static polarization, different magnetic orientations, large magnetoelectric coupling, and intrinsic spin-orbit coupling stemming from the tellurium ion in the system, it has the correct symmetry for this effect to emerge. Ni_3TeO_6 is also presented in the candidate list of materials presented in Fig. 1.4(c). Interestingly, we find nonreciprocal directional dichroism in the vicinity of the Ni d-to-d excitations, as large as 11% in some regions. While crystal field excitations are typically purely electronic in nature, we reveal that the on-site excitations in Ni_3TeO_6 are not purely electronic in character but have a magnetic component to them as well, making them magnetoelectric excitations. This stems from the mixing of electric and magnetic components in these d-to-d excitations due to the large spin-orbit coupling in the system. Being

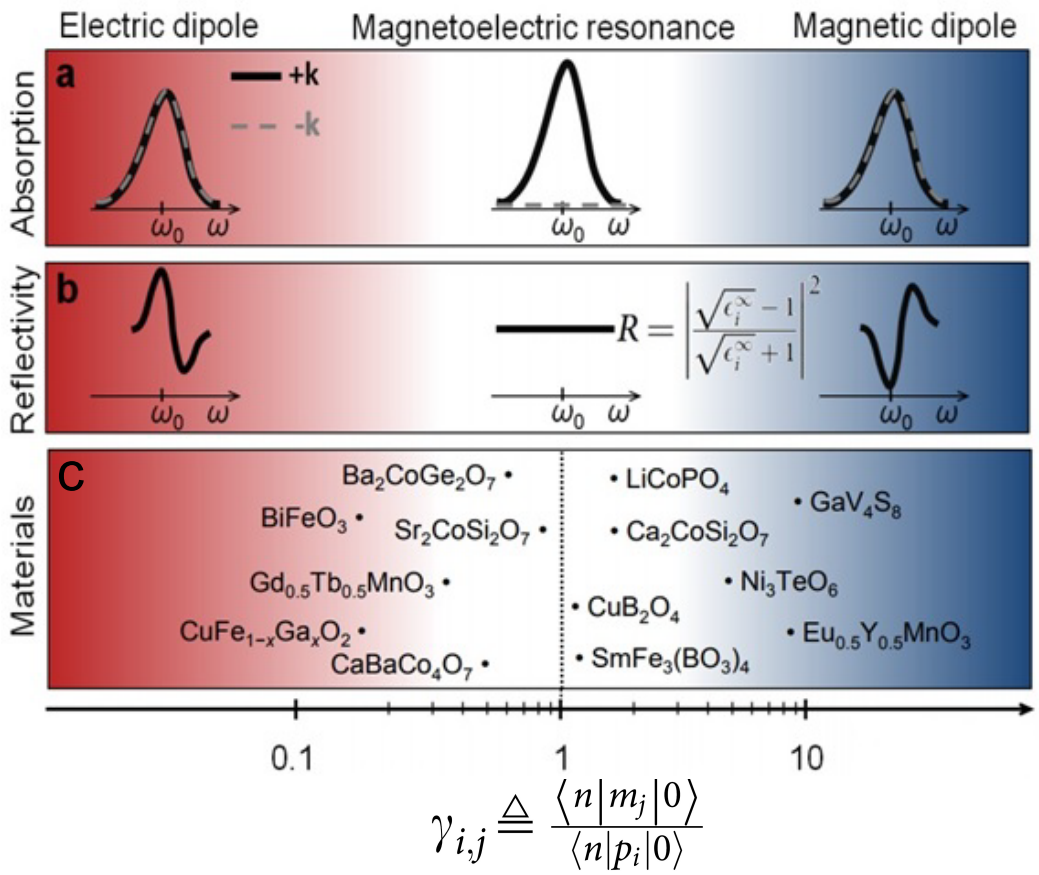


Figure 1.4: Optical properties characteristic to pure electric-dipole, mixed mageto-electric, and pure magnetic-dipole excitations. (a) Counter-propagating beams are absorbed with the same strength in case of pure electric (red region) and magnetic (blue region) dipole transitions illustrated by the two absorption peaks at ω_0. When approaching the limit of ideal magnetoelectric resonance (white region), the material tends to show one-way transparency. (b) Electric- and magnetic-dipole transitions emerge with opposite line shapes in the normal-incidence reflectivity spectrum, while an ideal magnetoelectric resonance remains hidden. (c) Presents a list of materials having the possibility of showing this nonreciprocal directional dichroism effect. [30]

able to tune a nonreciprocal response that is broad and at much higher energies than previously reported opens an entire field of study that is largely untapped.

Along with large changes in polarization at magnetic reorientations, Ni_3TeO_6 also sports a large magnetostriction effect, suggesting that the lattice is also sensitive to these magnetic transitions. [29] Therefore, we investigated the vibrational spectrum of Ni_3TeO_6 using infrared spectroscopy. With a symmetry analysis, we predict 18 phonons, $9A$ and $9E$ symmetry modes. Since Ni_3TeO_6 is already known to be anisotropic, the *ab*-plane modes reveal E symmetry, whereas the *c*-axis modes are A symmetry. All of the modes are present in the infrared response save one, and that mode is observed clearly in the Raman spectrum. Variable temperature infrared spectroscopy can reveal which, if any, phonons are sensitive to phase transitions. Driving through the 53 K Néel transition, we observe three *ab*-plane phonons sensitive to the onset of magnetic order, suggesting that these phonons are magnetoelastically coupled. Magneto-infrared measurements also reveal which phonons are responsive to magnetic reorientations. Ni_3TeO_6 again shows the same three phonons are also sensitive to the spin-flop transition at 9 T. Measurements up to 35 T show hints of a higher field spin transition (the 52 T metamagnetic transition). Analyzing phonon displacements from calculations, we reveal that each of the three phonons sensitive to magnetism all alter the exchange coupling between Ni1 and Ni2, again hinting that these sites are most affected by magnetic phase transitions.

Along with magnetic transitions, other types of phase transitions can be probed by measuring the infrared response of a material, such as structural transitions and metal-insulator transitions. Vanadium oxide (VO_2) is a classic example of a material showing a metal-insulator transition when probed with temperature. In VO_2, the onset of a Drude response with increasing temperature is revealed using infrared spectroscopy. [38,39] The ability to probe a metal-insulator phase transition with our

infrared techniques is what drew us to the next material of interest, $EuTi_{1-x}Nb_xO_3$. Not only does this set of materials develop metallicity, but it also provides the opportunity to explore the effects of inhomogeneity as a function of chemical substitution. The parent compound, $EuTiO_3$, has been extensively studied as sister compounds of multiferroic $SrTiO_3$ and EuO. [40, 41] The ground state is a quantum paraelectric antiferromagnet. [42] A symmetry analysis on the cubic perovskite structure of $EuTiO_3$ reveals three phonon modes, all with T_{1u} symmetry. A subtle $Pm\bar{3}m \leftrightarrow I4/mcm$ structural transition exists in $EuTiO_3$. When substituting Nb into the system, the structural transition increases in temperature, crossing room temperature when doped above 3%. Also, the spin structure changes as a function of Nb-substitution. $EuTi_{1-x}Nb_xO_3$ keeps an antiferromagnetic ground state when x=0.05. However, at amounts of x=0.1 and 0.2, the ground state becomes ferromagnetic. [42] A summary of the structural and magnetic transitions is presented in Fig. 1.5. Interestingly, as a function of chemical substitution, the system is in the vicinity of a quantum critical phase. When niobium is substituted into the system, the system is doped with electrons. Therefore, with an insulating parent $EuTiO_3$ and a metallic $EuTi_{0.8}Nb_{0.2}O_3$, infrared spectroscopy opens up an opportunity to investigate the onset of metallicity as a function of chemical substitution. We reveal that with Nb-substitution, the onset of the Drude arises between doping levels of x=0.03 and 0.05 and dramatically increases with higher substitutions. Since Nb is being substituted into the system in place of Ti, the phonons show hints of splitting, evidence of disorder. Along with accessing different phases using external stimuli, this analysis on $EuTi_{1-x}Nb_xO_3$ allows different phases to be reached starting from the growth process, either with electron doping, hope doping, or chemical substitution.

The remainder of the dissertation is organized as follows: Chapter 2 presents a literature survey of the model complex oxide systems with a focus on the systems of

interest here, as well as many different couplings and new phenomena that we aim to capture. Chapter 3 discusses the basics of infrared and optical spectroscopies, theories of how light interacts with matter, sample preparation, and other experimental and theoretical techniques. It also will include many fundamental ideas that are prominent in the materials of interest. Chapter 4 presents our optical investigations and results on Ni_3TeO_6 in the visible and ultraviolet regions of electromagnetic radiation through both the spin-flop and metamagnetic transitions. Chapter 5 reveals a brief understanding of the nonreciprocal directional dichroism response, along with our means of capturing the effect in our material. Chapter 6 gives details on the vibrational response of Ni_3TeO_6 under extreme conditions. Chapter 7 switches to the substituted $EuTiO_3$ with the aim to capture the metallic response as a function of chemical substitution. Chapter 8 summarizes my work.

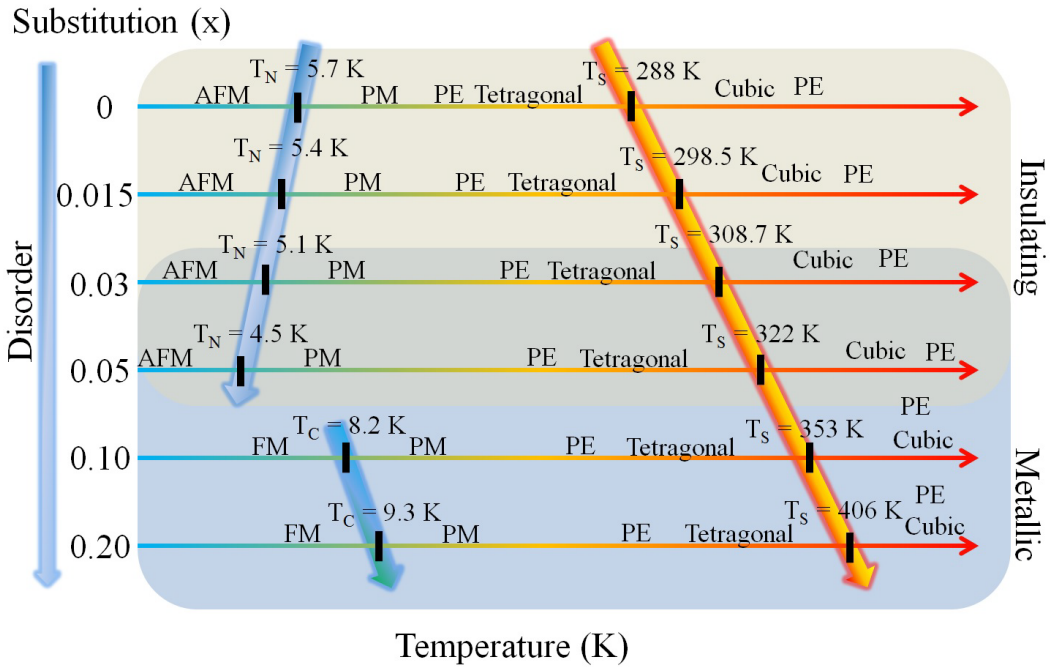


Figure 1.5: Summary of structural and magnetic phase transitions for $EuTi_{1-x}Nb_xO_3$. [42]

Chapter 2

Literature survey

2.1 Material properties

2.1.1 Electronic transitions and crystal field splitting

While infrared light probes the vibrational and low energy electronic response of a material, higher energy light (near infrared through ultraviolet regions) probes more electronic properties of a material. Most simply, an electronic transition can be the excitation of an electron from a lower energy level to a higher one, as shown in Fig. 2.1. The difference here is that these transitions excite an electron from one potential well to another, while the vibrational transitions take place within a single potential well. Several selection rules for this type of transition exist. They are listed below:

$$\Delta S = 0 \tag{2.1}$$

$$\Delta l = \pm 1 \tag{2.2}$$

These rules, known as the spin selection rule and the LaPorte selection rule respec-

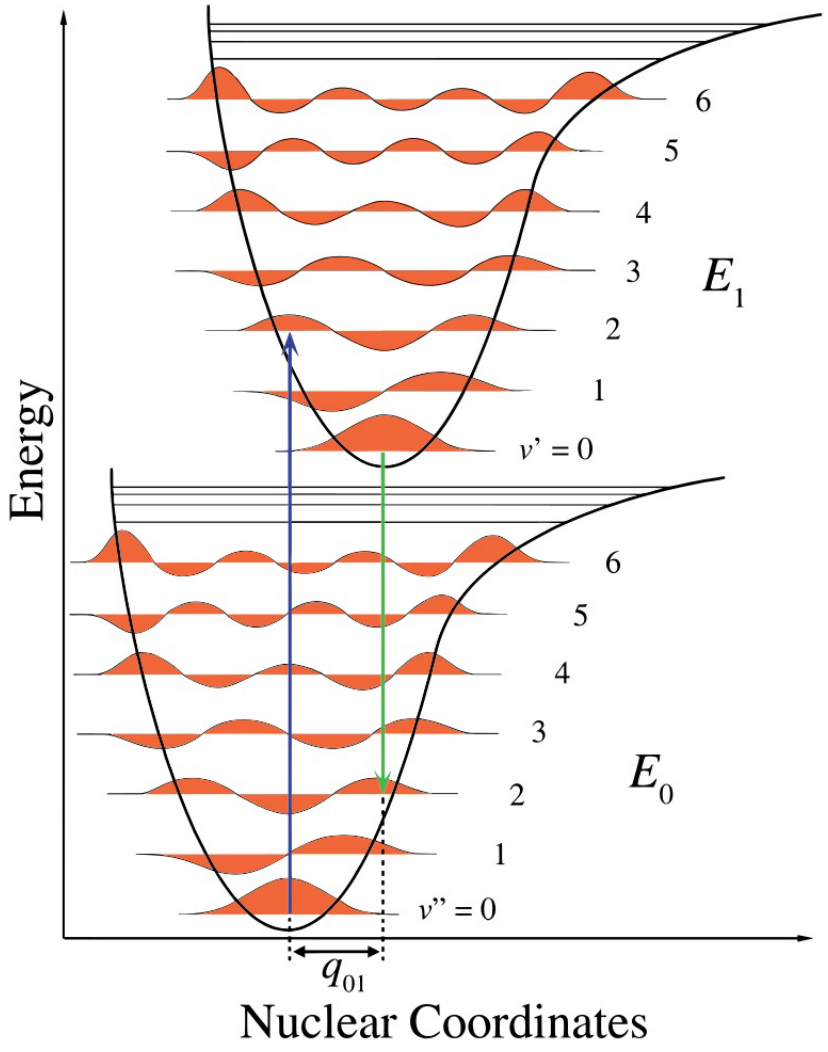


Figure 2.1: Energy diagram of an electronic transition from one energy level to another higher energy level.

tively, can be broken several ways. First, broken inversion symmetry and spin-orbit coupling can give rise to spin-forbidden transitions. Second, vibronic coupling (the vibrational and electronic energies influence one another) can break these selection rules. Last, hybridization of orbitals can also give rise to these forbidden transitions. It is important to note that all electronic energy transitions are quantized. Several of these characteristic electronic transitions such as the band gap and crystal field excitations will be discussed below.

Band gap transitions are defined by the energy difference between the top of the valence band and the bottom of the conduction band, as depicted by Fig. 2.2(a). With the hybridization of orbitals in a complex lattice, these bands can change across the zone. These different symmetry coordinates are designated by wave vector k here (Fig. 2.2(b,c)). A direct gap is one in which the electron travels without changing in k-space (Fig. 2.2(b)). An indirect gap is defined by the energy difference from valence band to conduction band, but it includes a change in k, as seen in Fig. 2.2(c). This change in k-space is associated with the momentum shift caused by a phonon. In optical analysis, a Tauc plot can be calculated, and a gap energy equation can be written to include both of these terms:

$$\alpha(E) = A(E - E_g^{direct})^{0.5} + B(E - E_g^{indirect} \pm E_{phonon})^2 \tag{2.3}$$

where A and B are parameters, E_g are the direct and indirect gaps, and the phonon energy is E_{phonon}. Plots of $(\alpha E)^2$ and $(\alpha E)^{0.5}$ can indicate a direct or indirect gap, respectively, with line segments that are linear in each graph. [43–47]

Another type of electronic transition can be due crystal field splitting, and often times they occur as on-site d-to-d transitions on transition metal ion, barring if the transition metal is d^{10}. A basic understanding of the orbital shapes and the ligand potential is necessary for this discussion. In general, the crystal field is an

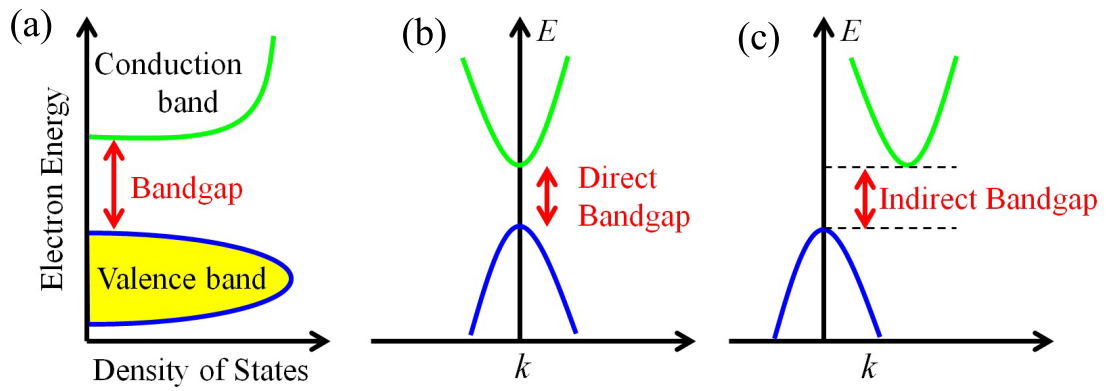


Figure 2.2: Energy diagram of the band gap defined by the energy difference between the top of the valence band to the bottom of the conduction band.

electric field derived from neighboring atoms in the crystal. Figure 2.3(a) and (b) show the tetrahedral and octahedral environments, respectively. These two different crystal fields will split the five degenerate d orbitals of the metal center into different arrangements based on orbital overlap. Pictured in Fig. 2.3(c) is the d_{xy} orbitals with the neighboring p orbitals from the ligands in an octahedral coordination. Here, looking at a cross section of the xy-plane, there is minimal orbital overlap. Figure 2.3(d) shows the $d_{x^2-y^2}$ orbital with the same p orbitals. This orbital overlap is much greater. It is clear that since the d_{xy} orbital has lower overlap than the $d_{x^2-y^2}$ does with the neighboring p orbitals, it will have a lower electrostatic energy. The five atomic d orbitals can be grouped into a set of 2 and a set of 3. The three triply degenerate orbitals include d_{xy}, d_{xz}, and d_{yz}, deemed the t_{2g} orbitals, while the doubly degenerate orbitals include $d_{x^2-y^2}$ and d_{z^2} and are called the e_g orbitals. With the crystal fields being different for the tetrahedral and octahedral configurations, it follows that there will be more or less orbital overlap with certain orbitals and therefore different crystal field splittings. The t_{2g} orbitals are always lower in energy for an octahedral environment with the e_g levels being higher, and vice versa for a tetrahedral environment. This splitting from the five degenerate d orbitals to the two different environments is pictured in Fig. 2.3(e). In general, the symmetry around

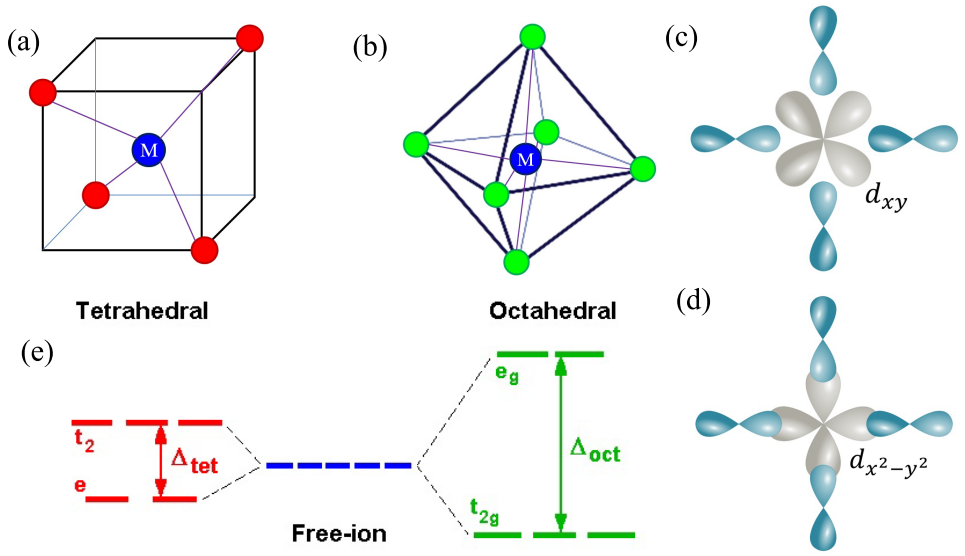


Figure 2.3: (a) Depicts a tetrahedral environment. (b) Depicts an octahedral environment. (c) Depicts the orbital overlap between a d_{xy} orbital with the neighboring p atomic orbitals. (d) Depicts the orbital overlap between the $d_{x^2-y^2}$ orbital with the neighboring p atomic orbitals. (e) Shows the crystal field splitting for both a tetrahedral and octahedral environment.

the metal center can determine the crystal field splittings. Different effects, such as the Jahn-Teller distortion (octahedral environment but elongation of the primary z axis, causing more splitting in the crystal field orbitals), can also come about. [48]

Along with these splittings, there can either be a strong-field or a weak-field case, as shown in Fig. 2.4. For example, in a d^6 electron configuration in an octahedral environment, there can be two different total spins on the metal atom. First, with a weak field case, the total spin moment will be 2, as the electrons have enough energy to bridge the crystal field splitting gap. In the case with strong crystal field splitting, the electrons will all stay in the t_{2g} orbitals, leaving a total spin of zero. In an octahedral environment, the transition of an electron from the t_{2g} orbital to an e_g orbital is formally forbidden according to the selection rules. However, there are several instances in which these rules are broken, as has been mentioned before. With large spin-orbit coupling, broken inversion symmetry, or vibronic coupling,

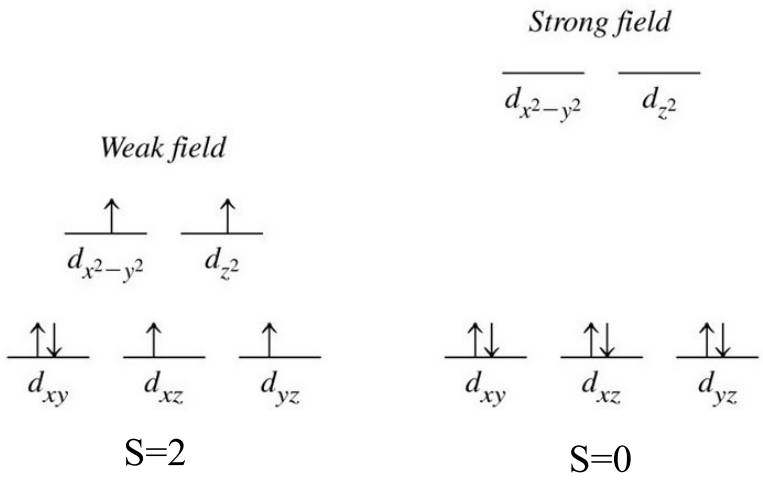


Figure 2.4: Depicts how the crystal field strength for a d^6 electron configuration in an octahedral environment can alter the total spin moment.

these transitions can be seen in optical spectra, often times in the visible region.

Bringing together the crystal field splitting strength along with the spin-state of certain systems, a Tanabe-Sugano diagram (Fig. 2.5) can be used. This diagram plots the excitation energy (E) versus the crystal field splitting strength, also known as the ligand field splitting parameter (Δ or D_q). Both terms are scaled by the Racah parameter (B), which is an estimate of the total electrostatic repulsion between electrons. The Racah parameter varies from atom to atom. For the transition metal ions, d^1, d^9, and d^{10} do not have Tanabe-Sugano diagrams, as they only have one electron, one hole, and fully filled orbitals, respectively. The other seven do have Tanabe-Sugano diagrams. Four of these systems (d^4, d^5, d^6, and d^7) are slightly more complicated than the other three (d^2, d^3, and d^8) because they can have a high-spin and low-spin ground state, with respect to the strength of the crystal field splitting. An example of a Tanabe-Sugano diagram for a d^6 system is given in Fig. 2.5. The high-spin state corresponds to lower crystal field splitting strengths, which is on the left side of the diagram. This leads to the low-spin state being on the right side of the diagram with larger crystal field splittings. The two different spin-states

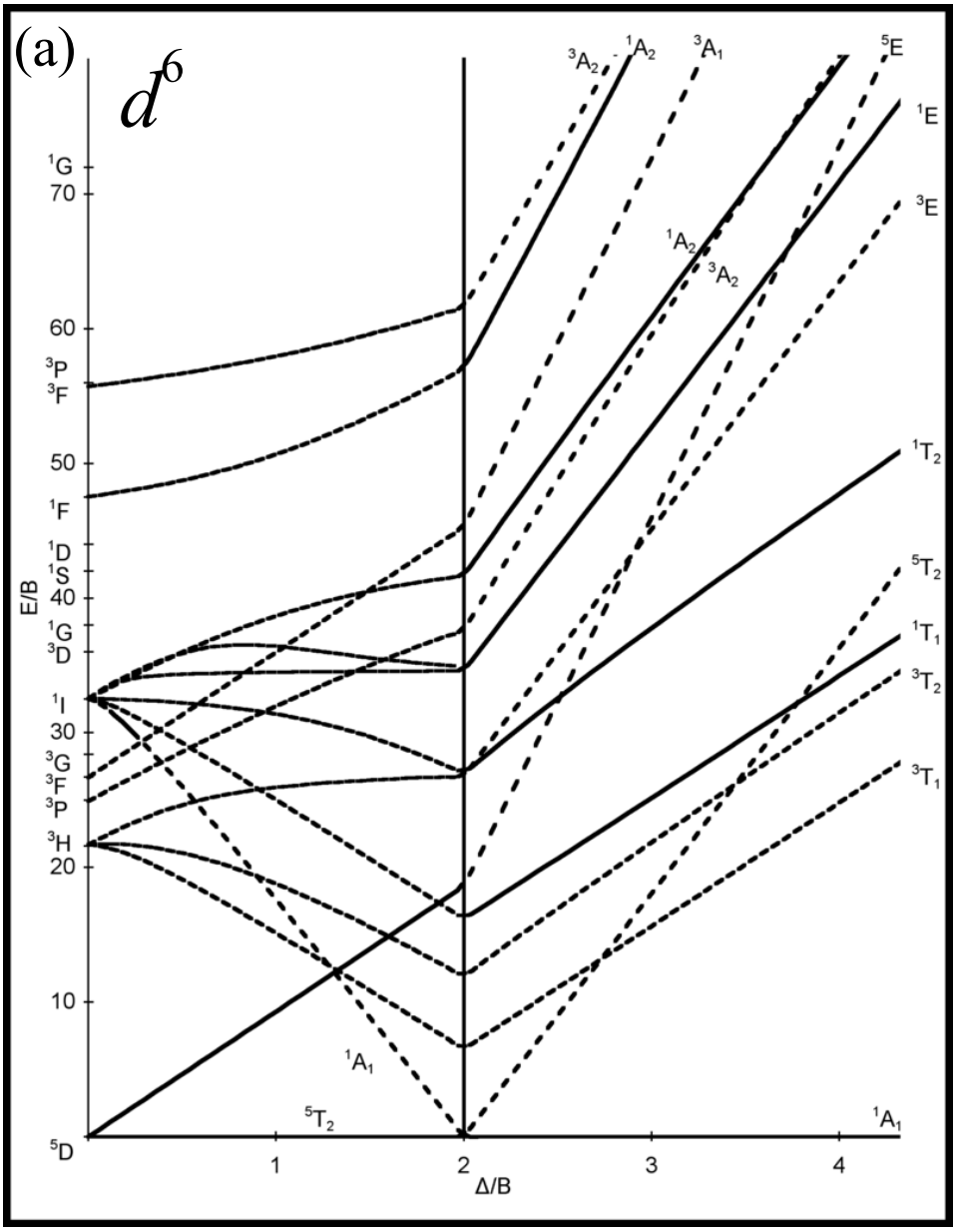


Figure 2.5: Tanabe-Sugano diagram for a d^6 system.

are separated by a point in the diagram, shown by the vertical line in the diagram. The line corresponds to when the ligand field splitting is equal to the spin pairing energy. [49]

From an analysis using a Tanabe-Sugano diagram, the relative energetics of on-site d-to-d excitations can be predicted along with the strength of the crystal field. My work focuses on a Ni^{2+} system with a d^8 electron configuration. Using the appropriate Tanabe-Sugano diagram, the crystal field splitting, energy of excitation, and term symbol of the excitation can be found.

2.1.2 The harmonic oscillator and infrared spectrosopy

In order to understand the vibrational spectra of a material, a simple model of a harmonic oscillator is commonly used. From a broader macroscopic standpoint, a simple Hooke's law model can be used, for both a single mass system and a diatomic system. Treating the diatomic harmonic oscillator problem quantum mechanically, the Schrödinger equation can be written as [50]:

$$-\frac{\hbar^2}{2\mu}\frac{\partial^2\psi}{\partial x^2} + V(x)\psi(x) = E\psi(x) \tag{2.4}$$

with μ being the reduced mass, $\hbar = h/2\pi$, and the potential energy of the vibration $V(x) = \frac{1}{2}kx^2$, k being the force constant and x the displacement from the equilibrium position $(r - r_e)$. Solving Eqn. 2.4 for quantized energy values yields:

$$E_\nu = h\nu(n + \frac{1}{2}), n = 0, 1, 2... \tag{2.5}$$

with

$$\nu = \frac{1}{2\pi}(\frac{k}{\mu})^{\frac{1}{2}}, \tag{2.6}$$

where ν is the frequency of the vibration and n is the vibrational quantum number. The energy levels are equally spaced by $h\nu$ in the harmonic potential well described in Fig. 2.6.

This harmonic oscillator description isn't physical, though. From experimentation, scientists saw that overtone modes were not equally spaced but actually decreased in energy. This is because, in real materials and molecules, the separation between adjacent levels is not perfectly $h\nu$ but becomes smaller with increasing n, as described by Fig. 2.6. The energy difference between the minimum of the potential well and the dissociation limit is D_e; the energy difference between the zero-point vibrational energy and the dissociation limit is D_0. D_0 is the value that is experimentally measured, and the two are related by

$$D_0 = D_e - \frac{1}{2}h\nu. \tag{2.7}$$

The Morse potential energy function can be used in the form

$$V(x) = D_e(1 - e^{-ax})^2 \tag{2.8}$$

where a controls the width of the potential well. Using this more realistic potential energy equation (2.8) and a Taylor series expansion, new energy values can be solved for from the more physical Schródinger equation:

$$E_\nu = hc\nu_e(n + \frac{1}{2}) - hc\nu_e x_e(n + \frac{1}{2})^2 + ..., n = 0, 1, 2... \tag{2.9}$$

where $hc\nu_e$ and $hc\nu_e x_e$ are directly related to parameters of the Morse potential. The harmonic oscillator model provides a good approximation when n is small, but it becomes much less reliable when n gets closer to D_e. According to quantum mechanics, the vibrational selection rules only allow transitions as $\Delta n = \pm 1$ (fun-

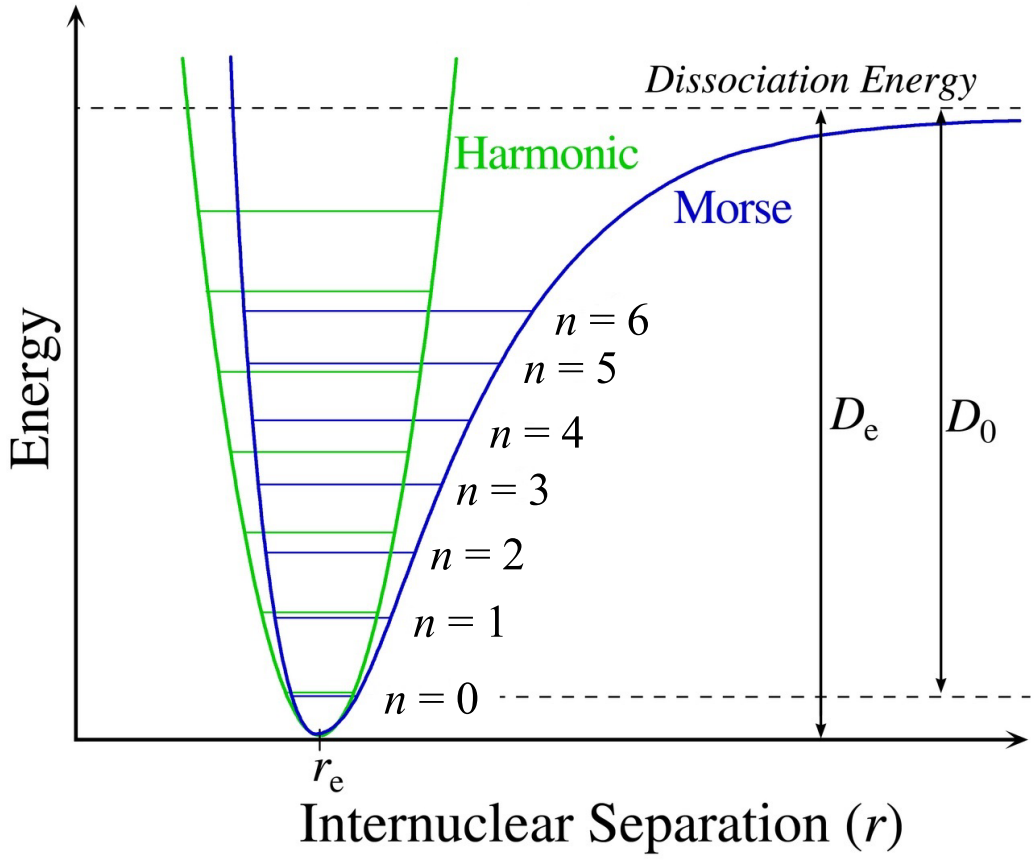


Figure 2.6: The potential wells of both the harmonic oscillator (green) and the anharmonic (Morse) potential (blue).

damental transitions). These transitions are much more prominent in intensity than overtone modes, which are allowed experimentally ($\Delta n = \pm 2, 3...$). [50]

In infrared spectroscopy (or any electric dipole spectrsocopy), the fundamental selection rule requires a change in the dipole moment of the molecule or lattice during a vibration. Quantum mechanically, the intensity of the vibrational transition depends on the magnitude of the transition moment integral M:

$$M = \int \psi^*_{vib} \mu(r) \psi^n_{vib} dr \tag{2.10}$$

where ψ^*_{vib} refers to the excited/upper state, ψ^n_{vib} refers to the ground/lower state, and $\mu(r)$ is the dipole moment operator. This dipole moment is a function of r and can be expanded as a Taylor series about the equilibrium position $r = r_e$. Expanded out and substituted back into Eqn. 2.10, each term can be evaluated. If the overlap is equal to zero, the vibrational response is not allowed. If the response is not equal to zero, then the vibrational transition is allowed. The magnitude of M gives the intensity of the vibrational response. More specifically, the intensity is actually proportional to the square of the change in the dipole moment:

$$I \propto |M|^2 \propto |\frac{d\mu}{dr}|^2_{r_e}. \tag{2.11}$$

Due to the periodic arrangement of atoms/ions/molecules in a solid state, optical spectroscopy of solids differs slightly from the spectroscopy of a molecule. In solids, the vibrations of an atom affect all of its neighboring atoms. This leads to collective excitations, called phonons. In a 3D crystalline material with N number of atoms per unit cell, lattice vibrations are described in terms of $3N$ branches for the phonon dispersion curves. These dispersion curves contain three acoustic branches and $3N$-3 optical branches (Fig. 2.7). Infrared spectroscopy probes excitations at k=0,

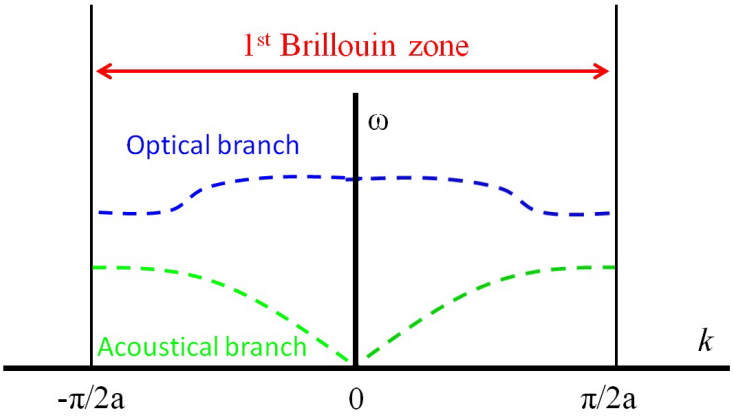


Figure 2.7: Phonon dispersion curves for the simple linear diatomic chain (-A-B-A-B- type), with optical and acoustic branches.

and the rest of k space can be explored by inelastic neutron scattering techniques. Acoustic phonons correspond to uniform translations of the entire crystal, analogous to translational modes of a molecule. Optical phonons are what would be called the vibrations of a molecule. Due to the periodicity of an infinite lattice, a solid may have much lower symmetry than a molecule, giving rise to a larger number of phonons, seen as mode splitting or the activation of silent vibrations. Correlation theory (analysis between molecular, site, and space group symmetries) can be used to predict the number of spectral bands and their symmetries. While other techniques are probes of bulk effects, spectroscopy is useful in that it gives a response to a local symmetry within the material.

The study of phonons is an essential part of condensed matter physics. They play a key role in the physical properties of solids, such as specific heat, thermal and electrical conductivity. Furthermore, phonons and other elementary/collective excitations provide fundamental information on elastic and optical properties of materials.

2.1.3 Spin-orbit coupling

Many different interactions can affect the way a material will behave spectroscopically, including electron-electron interactions. Another important aspect in the area of condensed matter physics is the coupling between the electronic spin and electronic orbital degrees of freedom. When these interactions are coupled, the term spin-orbit coupling is used. A diagram of this type of interaction can be seen in Fig. 2.8. The premise of this effect is from the electron's point of view. The electron spin itself creates an intrinsic magnetic field. The electron then "sees" a positively charged nucleus orbiting it. The interaction of these can lead to several different scenarios.

First, and for lighter atoms (lower atomic numbered elements), there is Russell-Saunders coupling (also known as L·S coupling). This is the sum of all orbital angular momentums and spin angular momentums to form J:

$$J = L + S \qquad \text{where} \qquad L = \sum_i l_i \qquad \text{and} \qquad S = \sum_i s_i. \tag{2.12}$$

This approximation is more valid for lighter elements. When atoms get heavier, the story becomes different. Each individual angular momentum can interact with the corresponding spin momentum. Therefore, each individual total angular momentum per particle (j_i) must be calculated as such:

$$J = \sum_i j_i = \sum_i (l_i + s_i). \tag{2.13}$$

Spectroscopically, spin-orbit interaction can further split spectral lines. This means that the crystal field splitting presented in Fig. 2.3(e) can further split and lift degeneracies in a system, if there is significant spin-orbit interaction in the system. For a hydrogen-like atom, the Hamiltonian can be written as a combination of different Hamiltonians, including one for spin-orbit coupling:

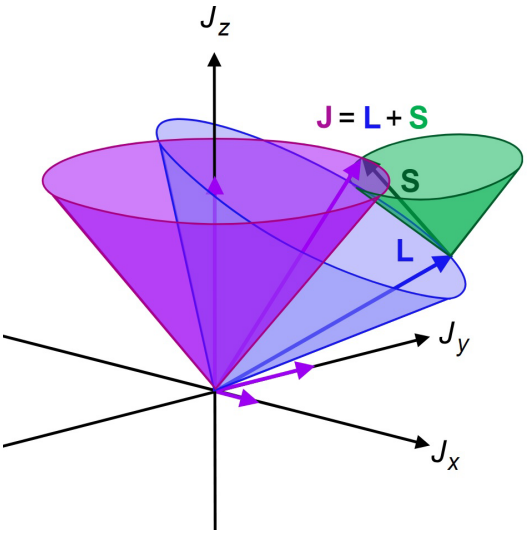


Figure 2.8: Diagram of how the orbital angular momentum (L) and the spin angular momentum (S) add to form J - spin-orbit coupling.

$$\hat{H} = \hat{H}^0 + \hat{H}^1_{SO} = \hat{H}^0 + \frac{g_e Z e^2}{4c^2 m^2 r^3} S \cdot L. \tag{2.14}$$

The energies associated can be written as

$$E = E_n + \frac{\lambda[J(J+1) - S(S+1) - L(L+1)]}{L(L+1)(L+0.5)} \tag{2.15}$$

where Δ_n is described by the expression

$$\lambda = \frac{g_e Z^4 e^2 \hbar^2}{8c^2 m^2 a^3 n^3}. \tag{2.16}$$

Here, λ is the spin-orbit coupling constant. The important variables here are the atomic number Z and the principle quantum number n. It follows that as atoms get heavier, spin-orbit coupling will increase. The relation is such that $E \sim Z^4$. However, more recent studies have shown that the dependence is more like Z^2. [25, 26] The trend still follows that as the atoms get heavier, spin-orbit coupling energies can start to compete with the typically more dominant energies, as shown in Table 2.1.

Table 2.1: Energies moving down the periodic table

Row	t (orbital overlap)	U (electron-electron correlations)	λ (spin-orbit coupling constant)
$3d$	0.5 eV	8 eV	0.1 eV
$4d$	↓	↓	↓
$5d$	1 eV	1 eV	0.5 - 0.8 eV

As elements go from $3d$ to $5d$ transition metals, spin-orbit coupling becomes larger, bringing about some new and interesting physics in materials. In fact, the spin-orbit coupling energy can be so large that it manifests itself in optical excitations. Sr_2IrO_4, for example, has large spin-orbit coupling from the $5d$ iridium ions. The iridium has 5 d electrons, giving it an almost full t_{2g}^5 shell. The electronic structure in this material changes with the large spin-orbit coupling, as shown by Fig. 2.9. Schematics from calculations, shown in Fig. 2.9(a-e), show a clear story. In summary, electron correlations will split the t_{2g}^5, revealing a gap. Spin-orbit coupling will split the bands (in particular, the lower valence band) even more, bringing about new J_{eff}=1/2 and 3/2 bands. Direct evidence for these bands is shown in Fig. 2.9(f). The peaks A and B are the excitations from J_{eff}=1/2 LHB (lower Hubbard band) and J_{eff}=3/2 to J_{eff}=1/2 UHB (upper Hubbard band), respectively, as shown by the arrows in Fig. 2.9(d). [51]

Spin-orbit coupling can not only effect electronic structure but also some properties of magnetism in materials. Many examples with heavier elements can introduce spin-orbit coupling effects, examples being $1T$-TaS_2 [52], Ba_2NaOsO_6 [53], $Cd_2Os_2O_7$, and $Cd_2Re_2O_7$. [54]

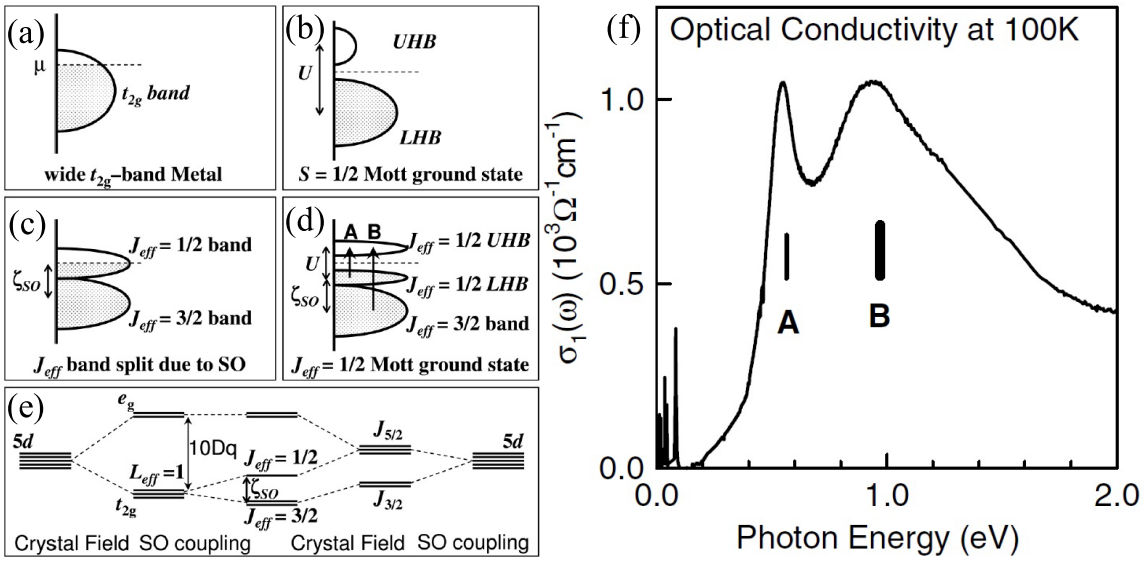


Figure 2.9: Schematic energy diagrams of Sr_2IrO_4 and the $5d^5$ (t_{2g}^5) configurations (a) without SOC and U, (b) with an unrealistically large U but no SOC, (c) with SOC but no U, and (d) with SOC and U. Optical transitions are labeled in (d) with arrows. (e) $5d$ level splittings by the crystal field and SOC. (f) Optical conductivity of Sr_2IrO_4. Peaks A and B correspond to transitions denoted in (d). [51]

2.1.4 Magnetism and magnetic phase transitions

In multifunctional materials, there are many different properties that can be observed. One such property is the magnetism in the material. This magnetism stems from a transition metal that has unpaired electrons in its d orbitals, giving each atom or ion a net magnetic moment of the electronic spins. When these magnetic ions begin to interact, an effect such as long range magnetic ordering can set in.

The origin of magnetism can be traced back to the origin of exchange. This is most easily described by understanding exchange in a simple atomic scenario. Following Hund's rules and the Pauli exclusion principle, the exchange between two electrons in a single atom is understood. Hund's first rule states that the electronic wave function must be arranged so as to maximize S (as $S = 2s + 1$). The Pauli exclusion principle, in reference to an electron, states that each electron in a poly-electron atom must have unique values of each of the four quantum numbers. More

simply, an electron cannot coexist in a single orbital with another electron with the same spin (two electrons can coexist in the same orbital, but they must have different spins). With respect to symmetry, the spatial and spin parts must also exchange. For electrons, the overall wave function must be antisymmetric. Therefore, the spin part of the wave function must either be an antisymmetric singlet state ($S = 0$) in the case of a symmetric spatial state or a symmetric triplet state ($S = 1$) in the case of an antisymmetric spatial state. The spin-dependent term in the effective Hamiltonian can be written as:

$$\hat{\mathcal{H}}^{spin} = -2JS_1 \cdot S_2 \tag{2.17}$$

with J being the exchange constant. This Hamiltonian only takes into account the interaction from $S_1 \rightarrow S_2$, so a factor of two is included to incorporate the reverse situation ($S_2 \rightarrow S_1$). This motivates the Hamiltonian of the Heisenberg model:

$$\hat{\mathcal{H}} = -\sum_{ij} J_{ij} S_i \cdot S_j \tag{2.18}$$

where J_{ij} is the exchange constant between the i^{th} and j^{th} spins. The factor of two is omitted because the summation includes each pair of spins twice. The calculation of the exchange constant can be complicated. Generally, if two electrons are on the same atom, the exchange integral is usually positive, as the value of S wants to be maximized from Hund's rules. This also forces the electrons to be in separate orbitals (obeying the symmetry of the spatial part), which minimizes the Coulomb repulsion between the two electrons. [48]

When two electrons are on neighboring atoms instead of on the same atom, the story is very different. The exchange will happen between electrons on different atoms, so some of the single site symmetry rules are broken. Several different types

of exchange can occur between atoms. If the electrons on neighboring magnetic atoms interact via an exchange interaction, this is known as a direct exchange, as there is an exchange interaction directly without the need for an intermediary. Problems arise in direct exchange when there is insufficient direct overlap between orbitals on neighboring atoms. Thus, in many magnetic materials, it is necessary to consider some kind of indirect exchange interaction. [48]

The exchange mechanism which uses an intermediate atom between magnetic atoms is known as superexchange, shown in Fig. 2.10. Formally, it is defined as an indirect exchange interaction between non-neighboring magnetic ions which is mediated by a non-magnetic ion placed between the two magnetic ions. Remembering the particle in a box problem and that the energy associated with the length of a one-dimensional box L is proportional to L^{-2}, it is more energetically favorable to form bonds and allow the electron to wander around both atoms as opposed to just one (essentially, extending L and making a "bigger box"). This effect arises because there is a kinetic energy advantage for antiferromagnetism, as can be seen in Fig. 2.10. Most simply, the magnetic atoms can be assumed to have a single unpaired electron. In the simple case having a perfect system, the transition metal ions would have a single unpaired electron in its outermost d orbital and the oxygen would have two p electrons in its outermost shell. Figure 2.10 ((a) being the ground state and (b,c) being excited states) demonstrates how antiferromagnetic coupling lowers the energy of the system by allowing electrons to become delocalized over the whole structure, thus lowering the kinetic energy. Figure 2.10(d) is allowed for the ferromagnetic ground state, but (e,f) both violate the Pauli exclusion principle. In this type of exchange, there is a parameter deemed the hopping integral t, where J can be expressed as

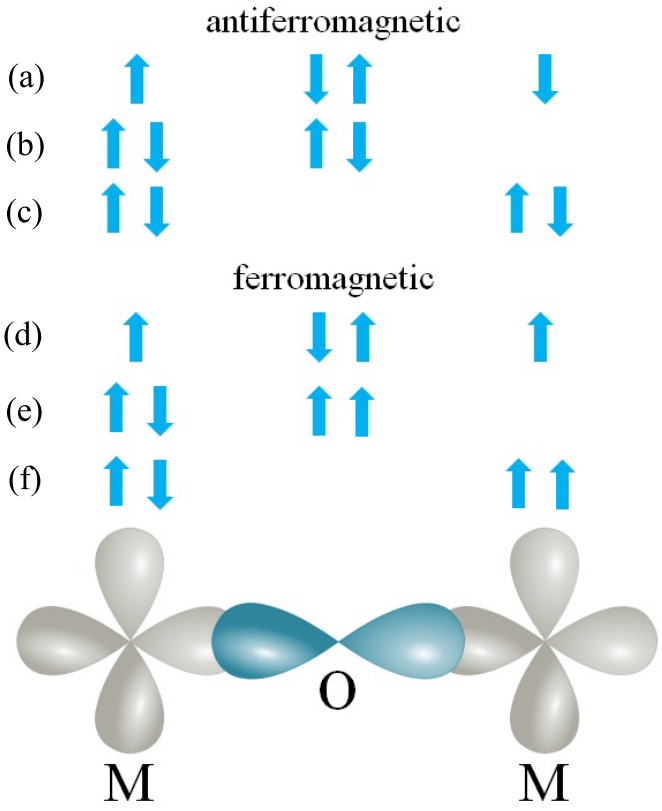


Figure 2.10: Depicts the superexchange in a magnetic oxide. The arrows show how the spins of the four electrons would arrange and be distributed over the transition metal (M) and oxygen (O) atoms. (a-f) Show different arrangements of spins, with (e,f) violating the Pauli exclusion principle.

$$J \sim -\frac{t^2}{U} \tag{2.19}$$

and U is the Coulomb energy. [48]

A couple of very general rules are associated with this hopping parameter t, called the Goodenough-Kanamori rules. These rules give guidelines with a prediction about the type of magnetic order will occur. These rules state that interactions favor antiferromagnetism when an electron transfer is between overlapping orbitals that are half-filled, but they favor ferromagnetism when the electron transfer is from a half-filled to an empty orbital, or from a filled to a half-filled orbital. In general, it predicts that the specific orbital involved in the exchange is important. If the orbitals involved are the same, it will tend to be antiferromagnetic, and if the orbitals involved are different, it will favor ferromagnetism. Also, there is an angle dependence incorporated into these rules. If the angle of the superexchange is more towards 180°, then antiferromagnetism is favored. For an angle of about 90°, then ferromagnetism is predicted. [55]

It is also possible for spin-orbit coupling to play a role in a similar manner to that of the oxygen atom in a superexchange pathway. The excited state is produced by the spin-orbit interaction in one of the magnetic ions. This is known as the anisotropic exchange interaction, or also the Dzyaloshinsky-Moriya (DM) interaction. This interaction can be written into the Hamiltonian by

$$\hat{\mathcal{H}}_{DM} = \mathbf{D} \cdot S_1 \times S_2. \tag{2.20}$$

The vector $\mathbf{D}$ is only present when the crystal field has broken inversion symmetry with respect to the two magnetic ions. This anisotropic element can lead to a canting of spins at a very small angle. In antiferromagnets, this can lead to a small

ferromagnetic component in a direction perpendicular to the spins easy-axis of the antiferromagnet. [48]

Some being mentioned above, there are many different types of long range magnetic orders. Figure 2.11 gives several different relevant examples to this work. A ferromagnet has a spontaneous magnetization even in the absence of an applied field, and all of the magnetic moments lie along a single unique direction, giving a positive exchange constant J for all nearest neighbor interactions. An antiferromagnet gives an exchange constant that is negative, and the nearest neighboring spins align antiparallel to one another. Paramagnetism is when all the spins are unordered and fluctuating randomly. Ferrimagnetic is when there is a small net magnetic moment, as different spin magnitudes do not completely cancel out arranged antiferromagnetically.

Several different types of antiferromagnetism can exist. A noncollinear case is depicted in Fig. 2.11, and more typical cases include G, A, and C type antiferromagnetic ordering. However, the situations can be much more complex. Several examples are presented in Fig. 2.12. Each of these types of antiferromagnetism may have different J terms between adjacent ions, but the total magnetic moment of each orientation will be zero. [48] For example, $BiFeO_3$ is a well-known antiferromagnet with a cycloid spin system, shown in Fig. 2.12(a). [56, 57] The periodicity of this spin cycloid is approximately 620 Å. Figure 2.12(b) shows a different noncollinear

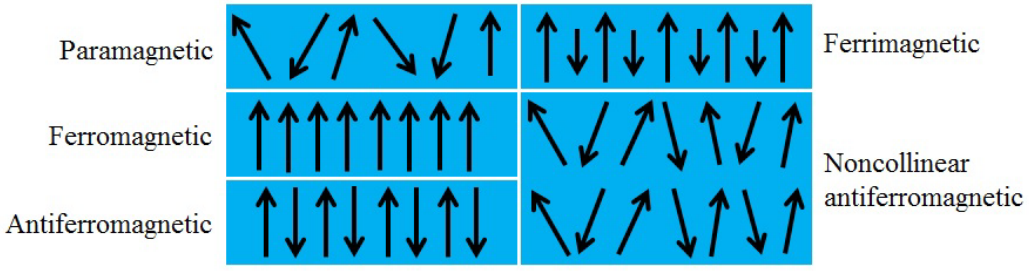


Figure 2.11: Lists and depicts many different magnetic states.

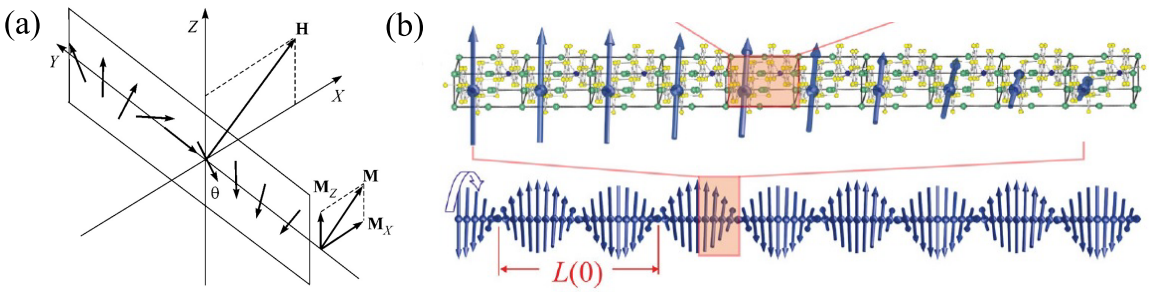


Figure 2.12: (a) Spin spiral diagram of $BiFeO_3$. [56] (b) Spin structure of $Cr_{1/3}NbS_2$. The spin magnetic moments of localized electrons rotate in the *ab*-plane along the helical *c*-axis.

spin system in $Cr_{1/3}NbS_2$. Here, the spins form what is called a chiral helimagnetic structure, with the *c*-axis being the helix and the electron spins rotating in the *ab*-plane. [58] This type of antiferromagnetic structure is possible because of DM interactions.

Many materials will have a magnetic phase transition at a specific temperature. For a simple ferromagnetic case, the Weiss model of ferromagnetism can be applied:

$$\frac{M}{M_S} = B_J(y) \tag{2.21}$$

$$y = \frac{g_J \mu_B J(B + \lambda M)}{k_B T} \tag{2.22}$$

where λM is the molecular field strength. The temperature at which a transition occurs can be obtained by finding the gradients of the line $M = k_B T y / g_J \mu_B J \lambda M_S$ and the curve $M = M_S B_J(y)$ are equal at the origin. For small y, the Curie temperature T_C can be defined by

$$T_C = \frac{g_J \mu_B (J+1) \lambda M_S}{3k_B} = \frac{n \lambda \mu_{eff}^2}{3k_B}. \tag{2.23}$$

A phase transition is essentially a consequence of broken symmetry. A simple analysis of an order parameter such as magnetization can determine the behavior of a material

at a phase transition. Finding a critical exponent can give hints to the behavior of the phase transition. Applying the equations below, the critical exponent can be found.

$$\chi \propto (T - T_C)^{-\gamma}, T > T_C \tag{2.24}$$

$$M \propto (T_C - T)^{\beta}, T < T_C \tag{2.25}$$

$$M \propto H^{1/\delta}, T = T_C. \tag{2.26}$$

A table of critical exponent values and their typical behaviors are described in Table 2.2. [48]

In order to describe and deem a material as having a certain type of magnetism, the Curie Weiss law can be used. Taking the magnetic susceptibility χ, the Curie Weiss law can be fit to the measurable data range with the relation

$$\chi \propto \frac{1}{T - \theta} \tag{2.27}$$

and the temperature dependence of χ can be plotted as $1/\chi$. The x-intercept of this graph and fit can determine what type of magnetism the material possesses, as shown

Table 2.2: Critical exponents for various models of magnetic phase transitions

Model	**Mean-field**	**Ising**	**Ising**	**Heisenberg**
D	any	1	1	3
d	any	2	3	3
β	$\frac{1}{2}$	$\frac{1}{8}$	0.326	0.367
γ	1	$\frac{7}{4}$	1.2378(6)	1.388(3)
δ	3	15	4.78	4.78

in Fig. 2.13. For a positive θ value, the system is ferromagnetic. Furthermore, for a value of zero or a negative value the system is paramagnetic or antiferromagnetic, respectfully. [48]

Phase transitions can be probed with temperature, but it is much more interesting when an external magnetic field is applied to a magnetic sample. In terms of a paramagnet, the spins on each individual ion just begin to align with the direction of the applied magnetic field. However, when applying an external field to an antiferromagnet, the situation becomes quite complex. The direction of the external field determines the behavior of the spins. If a magnetic field is applied perpendicular to the principle axis of the magnetic spins, the spins will just cant until they fully align with the direction of the applied field, as shown in Fig. 2.14(a). If the external field is applied parallel to the easy axis, the situation is quite different. Figure 2.14(b) describes this situation, with M_+ and M_- being the up and down spins, respectively. At small applied fields, the magnetic moments do not rotate but stay in line. At some critical field, the spins will suddenly snap into a different configuration, shown in Fig. 2.14(c). This sudden rearrangement is called a spin-flop transition. This transition stems from the energy difference between the spins aligned parallel to the magnetic

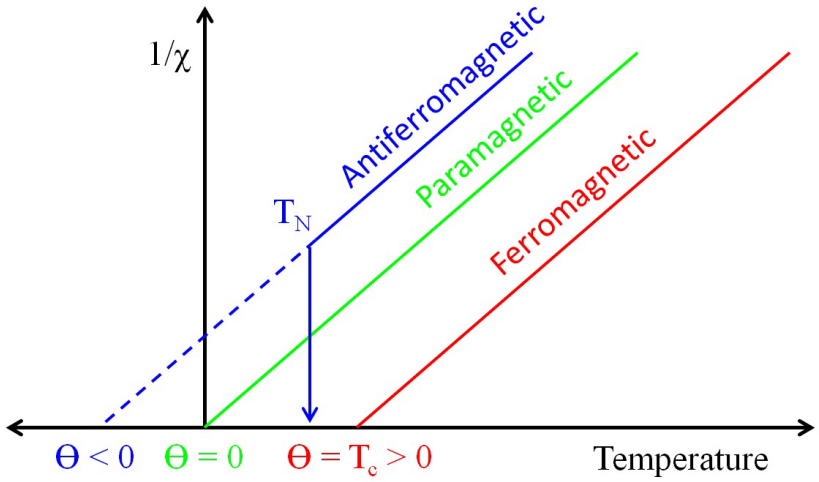


Figure 2.13: A plot of $1/\chi$ vs. T

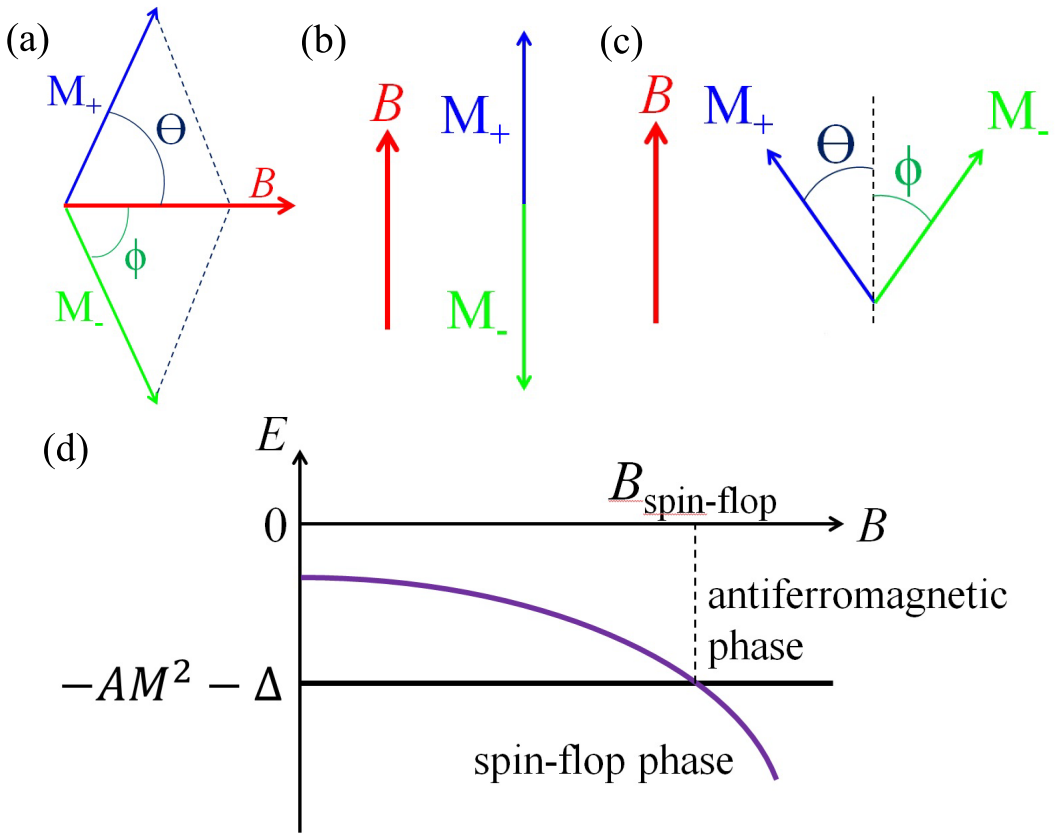


Figure 2.14: (a) Depicts how an external magnetic field applied perpendicular to the easy spin axis affects the magnetic spins in an antiferromagnet. (b,c) Depicts how external magnetic field parallel to the easy spin axis affects the antiferromagnetic spins. (d) Energy diagram of energy of the magnetic state vs. external magnetic field, showing different phases.

field (lower in energy) compared to those aligned antiparallel to the magnetic field (higher in energy). This effect can be described with a simple energy calculation. Assuming that the total energy is due to the sum of the Zeeman energies of the individual sublattices and also an exchange coupling term, it leads to this equation:

$$E = -MBcos(\theta) - MBcos(\phi) + AM^2cos(\theta + \phi), \tag{2.28}$$

where A is a constant associated with exchange coupling. The magnetic anisotropy can be modeled with

$$-\frac{1}{2}\Delta(cos^2\theta + cos^2\phi), \tag{2.29}$$

where Δ is a constant. This accounts for the fact that the magnetic spins prefer to lie along a certain crystallographic axis so that θ and ϕ are either exactly 0 or π. In the case of small magnetic fields, we can assume θ=0 and ϕ=π so that the energy $E = -AM^2 - \Delta$. When the spins flop, they flop perpendicular of the applied field and original easy axis. Therefore, the angles are equal ($\theta = \phi$). The energy equation then reads

$$E = -2MBcos(\theta) + AM^2cos(2\theta) - \Delta cos^2(\theta). \tag{2.30}$$

Finding a minimum energy with $\partial E/\partial\theta = 0$, $\theta = cos^{-1}(B/2AM)$, ignoring the anisotropy term. Substituting this back into the energy equation, a graph like Fig. 2.14(d) can be plotted, showing that at a certain external magnetic field (called the critical field $B_{spin-flop}$), the spin-flop phase is more energetically favored over the antiferromagnetic phase. Above this field, the behavior then acts as the prior perpendicular case, and the magnetic spins will just cant to align towards the direction of the magnetic field. [48] It should be noted that most of spin-flop transitions are

normally first order in nature.

2.1.4.1 Spectroscopy in high magnetic fields

Spectroscopy can be a powerful tool in uncovering mechanisms and unveiling which types of excitations are sensitive to magnetic rearrangements. Several examples of optical and infrared excitations that are sensitive to magnetic field are shown in Fig. 2.15. First, $Ni_3V_3O_8$ is a multiferroic material with a frustrated crystal structure. Figure 2.15(a) shows the absorption in the visible region of $Ni_3V_3O_8$ at 300 K, 1.6 K at 0 T, and 1.6 K at 37 T. Here, the optical band gap is changing with respect to temperature and magnetic field. Figure 2.15(b) tracks the band gap as a function of magnetic field at different temperatures. Since the magneto-optical excitations are in the visible energy region, there is actually a color difference of the sample at different temperatures and magnetic fields, as shown in the inset of Fig. 2.15(c), along with absorption difference spectra ($\alpha(B) - \alpha(0T)$) throughout the entire visible region. [59]

Along with optics, infrared excitations can be sensitive to applied magnetic fields. Figure 2.15(d-f) gives an overview of how multiferroic $[(CH_3)_2NH_2]Mn(HCOO)_3$ shows magneto-infrared activity. Figure 2.15(d) shows the absorption of the formate bending mode at 0 and 35 T, along with absorption difference spectra ($\alpha(B) - \alpha(0T)$) at 35 T, while (b) shows how the changes grow with increasing magnetic field. $[(CH_3)_2NH_2]Mn(HCOO)_3$ has a saturation magnetic field at 15.3 T, and Fig. 2.15(f) shows how the integrated absorption differences track with the magnetization squared. This work reveals that the formate bending mode is the mode that is not only sensitive to magnetic fields but also contributes to the mechanism of reaching the fully polarized magnetic state. [17]

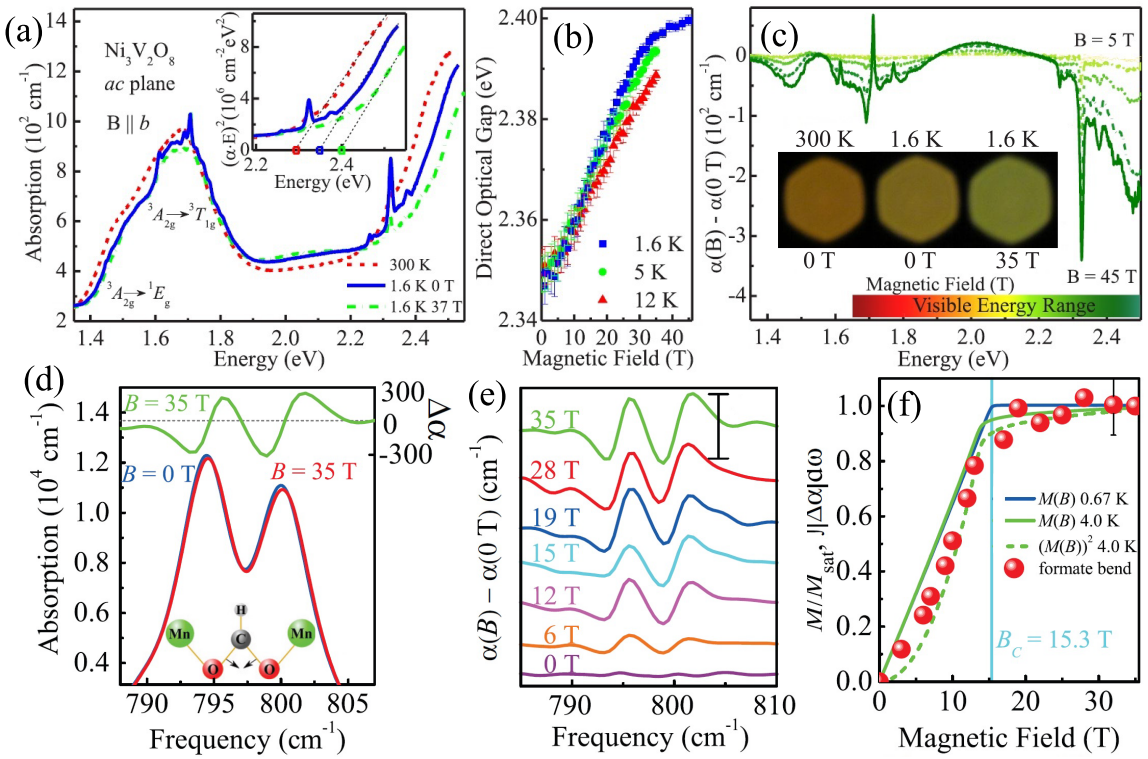


Figure 2.15: (a-c) Magneto-optical data on $Ni_3V_2O_8$. (a) Absorption coefficient, $\alpha(E)$, in the visible range at selected fields and temperatures. The inset shows a direct optical gap analysis. (b) Optical gap analysis as a function of magnetic field at selected temperatures. (c) Absorption difference spectra $\alpha(B) - \alpha(0T)$ at selected fields in the visible region. The inset shows photograph images of $Ni_3V_3O_8$ at different temperatures and magnetic fields. [59] (d-f) Magneto-infrared data on $[(CH_3)_2NH_2]Mn(HCOO)_3$. (d) Infrared response of the absolute absorption spectrum of the formate bending mode at 0 and 35 T at 4.2 K along with the 35 T absorption difference spectrum. (e) Waterfall plot of the formate bending mode at incremental fields, showing that the magneto-infrared response grows as a function of magnetic field. (f) Normalized magnetization, square of magnetization, and integrated absorption difference as a function of applied field. [17]

2.2 Multifunctional and multiferroic materials

2.2.1 Multifunctional materials and charge-spin-lattice coupling

Multifunctional materials display a rich interplay between charge, spin, and lattice interactions that leads to a high level of tunability of their physical properties, as shown in Fig. 2.16. These properties often have competing phases which can be mapped out by a phase diagram. Many materials have extremely rich phase diagrams, and by applying external stimuli such as chemical doping, pressure, magnetic field, or temperature, these materials undergo various magnetic and structural transitions. These materials are attractive as magnetic storage, superconductivity, and energy harvesting and storage. [60]

2.2.2 Multiferroic materials

Materials can have a wide range of properties. One specific type of property, known as a ferroic, is a material that adopts a spontaneous and switchable property alignment. For example, in ferromagnets, the alignment of electron spins can be switched by a magnetic field. In a ferroelectric, the electric dipole-moment alignment can be switched by an electric field. Lastly, in ferroelastics, strain alignment can be switched by an applied stress. Individually, these properties are of great interest both scientifically and for their technological applications. [60–64]

However, in the 19th century, electricity and magnetism were combined into a common discipline, culminating in Maxwell's equations. [62] This combination of electric and magnetic components extends to materials containing primary ferroic orders. The combination of two or more ferroic orders in a single phase is called a multiferroic. These joined properties can be very useful in technological applications.

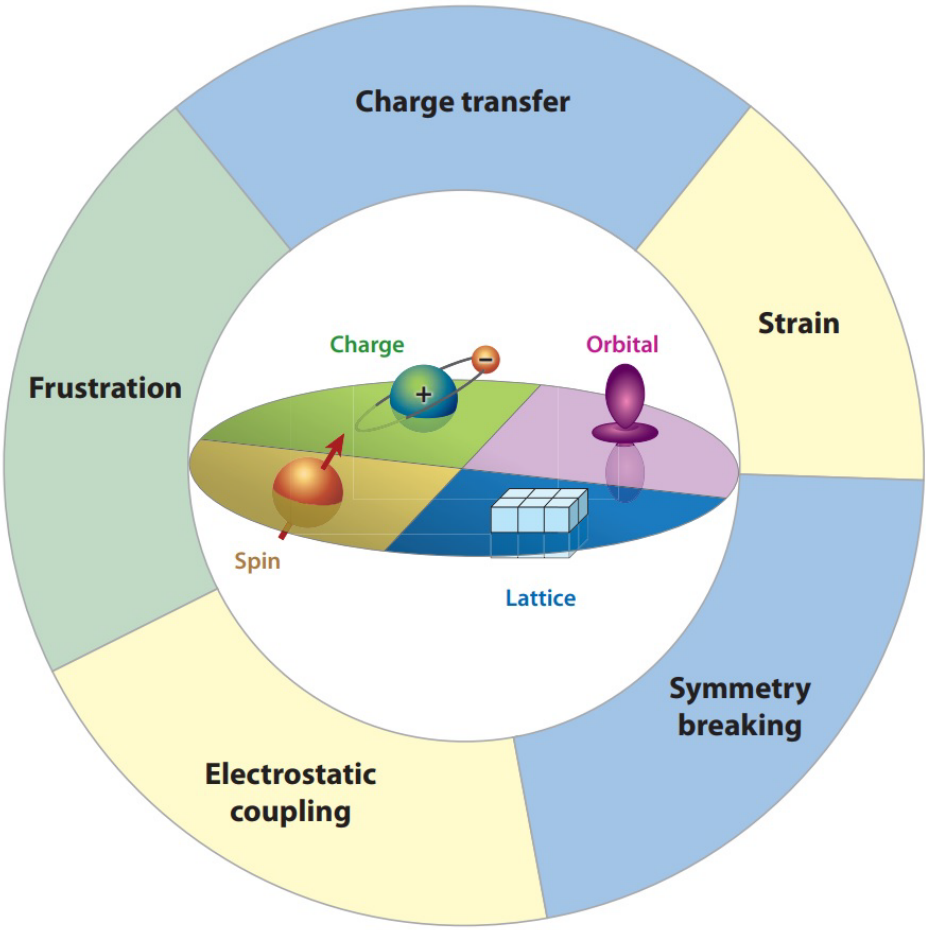


Figure 2.16: Diagram of the correlations and interplay between multiple degrees of freedom, including charge, magnetic spins, orbital, and lattice degrees of freedom. [3]

For example, electrical polarization in ferroelectrics and magnetization in ferromagnets are exploited in data storage, with opposite orientations of the polarization or magnetization representing "1" or "0" data bits. [61] The most well studied ferroic orders include ferroelectricity, ferromagnetism, and ferroelasticity [Fig. 2.17]. [61]

A specific type of ferroicity requires that some symmetry must be broken. For example, magnetic materials must break time reversal symmetry. With an orbiting electron, a magnetic moment is created (from the circular movement of charge, in a simple sense). If time reversal symmetry is applied, the electron will orbit in the opposite direction, hence changing the direction of the magnetic moment. Therefore, for a ferromagnetic material, time reversal symmetry must be broken. Ferroelectrics must break spatial inversion symmetry. In order to have a multiferroic material, two or more of these symmetry conditions must be broken. Figure 2.18 and Table 2.3 give a full picture of the symmetries that a multiferroic must break. [63]

Perhaps the most studied of all multiferroic materials are ones that combine ferroelectricity and ferromagnetism in a single phase. More loosely, ferromagnetism includes any type of magnetism. Scientists have often wondered why there are so few of these materials that exist. The reason is that the existence of both ferroelectricity and ferromagnetism is, in itself, a contraindication (typically, ferroelectricity and

Table 2.3: Spatial-inversion and time-reversal symmetry in ferroics

Characteristic symmetry	Spatial-inversion symmetry?	Time-reversal symmetry?
Ferroelastic	Yes	Yes
Ferroelectric	No	Yes
Ferromagnetic	Yes	No
Multiferroic	No	No

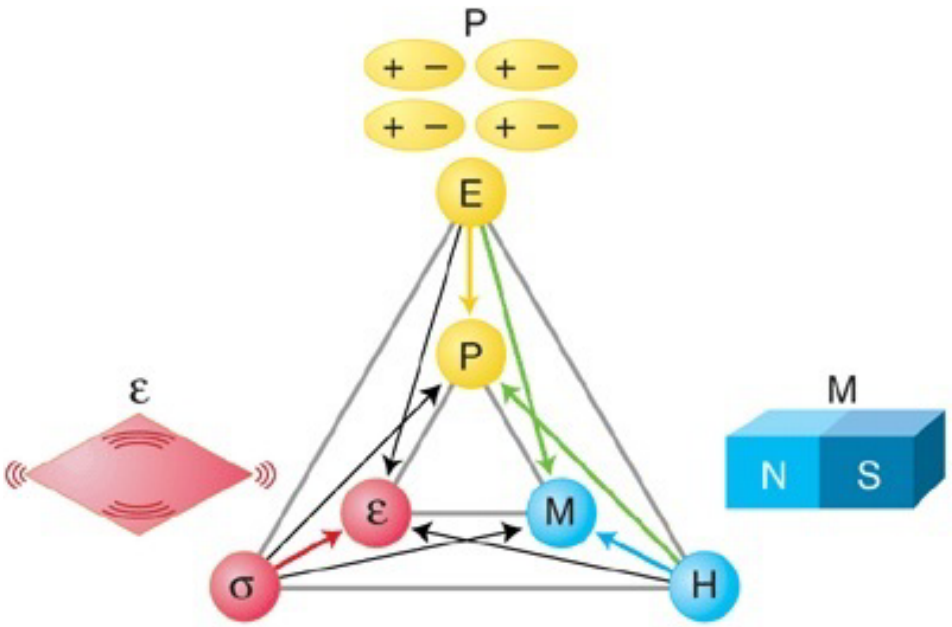


Figure 2.17: The electric field E, magnetic field H, and stress σ control the electric polarization P, magnetization M, and strain ϵ, respectively. In a ferroic material, P, M, or σ are spontaneously formed to produce ferromagnetism, ferroelectricity, or ferroelasticity, respectively. In a multiferroic, the coexistence of at least two ferroic forms of ordering leads to additional interactions. In a magnetoelectric multiferroic, a magnetic field may control P or an electric field may control M (green arrows). [60]

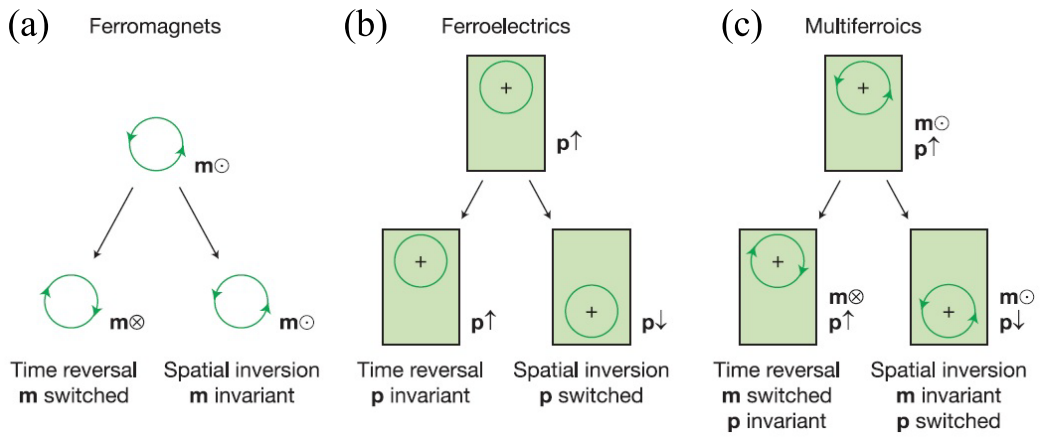


Figure 2.18: (a) Ferromagnets - The local magnetic moment **m** may be represented classically by a charge that dynamically traces an orbit, as indicated by the arrowheads. A spatial inversion produces no change, but time reversal switches the orbit and thus **m**. (b) Ferroelectrics - The local dipole moment **p** may be represented by a positive point charge that lies asymmetrically within a crystallographic unit cell that has no net charge. There is no net time dependence, but spatial inversion reverses **p**. (c) Multiferroics that are both ferromagnetic and ferroelectric possess neither symmetry. [63]

magnetism are mutually exclusive). [65–67] There are several different reasons for why this is the case. First, ferroelectrics are typically robust insulators (to sustain an electric polarization), while magnetic materials are usually the opposite, being conducting metals. Second, in conventional ferroelectric materials, the polarization arises when nonmagnetic cations shift away from the center of their surrounding anions. This uneven displacement, or noncentrosymmetry, between positive and negative charges is what gives rise to an electric dipole moment. Magnetic cations, however, tend to sit exactly at the center of the surrounding anions, in centrosymmetric positions, such that no dipole moment forms. This can be understood by observing the requirements of the d orbitals. Competition between energy-lowering covalent bond formation (larger for d^0 cations with their empty d shells) and energy-raising electronic Coulomb repulsion (larger for cations with d electrons) describes the behavioral difference between magnetic and nonmagnetic cations. This balance favors off-centering of d^0 ions. In contrast, magnetism occurs in materials with un-

paired localized electrons, such as those in a partially filled d orbital of a transition metal. These physical phenomena have exceptions, but they also describe why it is quite rare to have a simultaneously ferroelectric and magnetic material. [65–67] Therefore, often times, multiferroicity is achieved in different ways, as will be explained below.

Multiferroic materials are categorized as type-I and type-II. [62] Type-I multiferroics are systems where the ferroelectric polarization and magnetism stem from different sources, the most famous example being $BiFeO_3$. [68, 69] These are commonly seen in ABO_3 perovskites, where the A-site cation (typically a d^0 cation) bonds and can move off center, breaking inversion symmetry and inducing a ferroelectric response. In the B-site cation (typically a transition metal with unpaired d electrons), the magnetism is found. This is categorized as a proper ferroelectric, as no magnetic transition is inducing ferroelectricity. The ferroelectric transition temperature is often much higher than the magnetic transition. Since the ferroic orders stem from different ions, the coupling between them is very weak. Type-II multiferroics, however, typically have much larger couplings between their ferroic orders. This stems from something known as an improper ferroelectric, as the magnetic transition in the material induces a ferroelectric response. [62, 64] The prototypical case is $TbMnO_3$, [70] and Ni_3TeO_6 also falls under this category. [28]

An extremely interesting scenario is when a material couples their ferroelectric and magnetic responses. The cross coupling of these ferroic orders is deemed magnetoelectric coupling. Magnetoelectric coupling is defined as the influence of a magnetic (electric) field on the polarization (magnetization) of a material. [63, 70–72] This is depicted by the green arrows in Fig. 2.17. Though simultaneous electric and magnetic dipoles can exist in a single material, it does not guarantee strong coupling between them, as the microscopic mechanisms of ferroelectricity and magnetism are

quite different and do not strongly interfere with each other. Strong magnetoelectric coupling in materials can play a significant role in technological advancements.

2.2.3 Magnetoelectric coupling

Conventionally, it is known that an electric field can alter electric polarization and a magnetic field can alter magnetization. However, often times, within the realm of multiferroics, there are materials that have magnetoelectric coupling. This is when an applied electric (magnetic) field changes the magnetism (electric polarization) of a material. [63, 70–72] This cross coupling can be very useful in the development of many different technological advancements. Figure 2.19 shows a diagram of different requirements for magnetoelectric coupling.

From a mathematical perspective, the coupling between electric field and magnetic field can be linear. Looking at the Landau's equation of free energy, (Eqn. 2.31), there is a slew of different terms.

$$F(E,H) = F_0 - P_i^S E_i - M_i^S H_i - \frac{1}{2}\epsilon_0 \chi_{ij}^e E_i E_j - \frac{1}{2}\mu_0 \chi_{ij}^m H_i H_j - \alpha_{ij} E_i H_j - \frac{1}{2}\beta_{ijk} E_i H_j H_k ... \tag{2.31}$$

The first term is the free energy, and the next two are the static polarization and magnetizations. The fifth term is the magnetoelectric coupling term, with constant α. Taking the derivative with respect to either electric field or magnetic field leads to the following two equations (Eqns. 2.32 and 2.33):

$$P_i = -\frac{\partial F(E,H)}{\partial E_i} = P_i^S + \epsilon_0 \chi_{ij}^e E_j + \alpha_{ij} H_j + \frac{\beta_{ijk}}{2} H_j H_k + ... \tag{2.32}$$

$$M_i = -\frac{\partial F(E,H)}{\partial H_i} = M_i^S + \mu_0 \chi_{ij}^m H_j + \alpha_{ij} E_i + \beta_{ijk} E_i H_j + ... \tag{2.33}$$

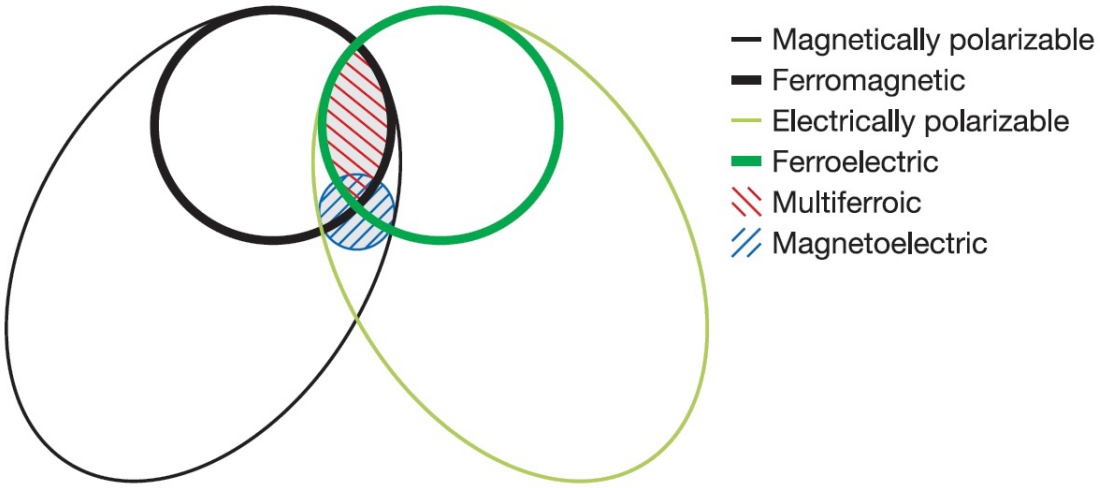


Figure 2.19: Ferromagnets (ferroelectrics) form a subset of magnetically (electrically) polarizable materials such as paramagnets and antiferromagnets (paraelectrics and antiferroelectrics). The intersection (red hatching) represents materials that are multiferroic. Magnetoelectric coupling (blue hatching) is an independent phenomenon that can, but need not, arise in any of the materials taht are both magnetically and electrically polarizable. In practive, it is likely to arise in all such materials, either directly or via strain. [63]

From this, it shows that the polarization can be affected by magnetic field and the magnetization can be affected by electric field. The constant α can then be shown as followed:

$$\alpha_{ij} \approx (\frac{\partial P_i}{\partial H_j})_{E_i=H_i=0} \approx (\frac{\partial M_i}{\partial E_j})_{E_i=H_i=0} \tag{2.34}$$

Several examples of this coupling through experimentation can be seen in Fig. 2.20 for a Y-type hexaferrite (a) and in $Fe_2Mo_3O_8$ (b). [5, 73] For the Y-type hexaferrite, the magnetic state is being controlled and tuned by the application of an electric voltage. The reverse situation is happening with $Fe_2Mo_3O_8$, where the electric polarization is being tuned by the application of a magnetic field, which changes the magnetic state and, through coupling, inherently changes the polarization.

2.2.4 Nonreciprocal Directional Dichroism

Although magnetoelectric coupling can alter different states of magnetism (polarization) by applying an external electric (magnetic) field, it is not only a static effect. In fact, magnetoelectric coupling can persist throughout the entire electromagnetic spectrum. The requirement is that an excitation must contain both an electric and magnetic component to be considered a magnetoelectric excitation. [30] Different regions of the electromagnetic spectrum can give rise to different type of magnetoelectric excitations. For example, in the low energy infrared region, electromagnons (defined as a spin wave excitation probed by an oscillating electric field) can exist. In the optical region, *d*-to-*d* excitations are typically seen as purely electronic excitations, but with large spin-orbit coupling in a system, they can have a magnetic component to them as well. A list of candidate materials having the correct symmetry for a magnetoelectric excitation is shown in Fig. 2.21(a). [30, 31, 74, 75]

When the motion of an object in one direction is different from that in the

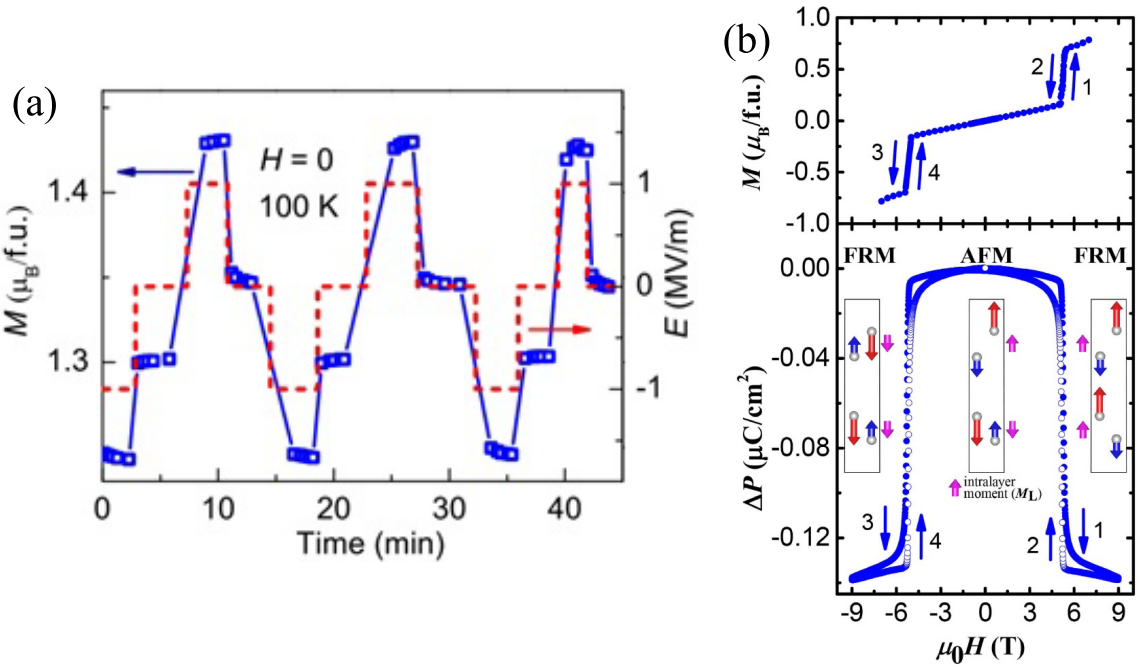


Figure 2.20: (a) Four magnetization levels controlled by applying electric field in a repeated sequence of -1 MV/m $\rightarrow$ 0 $\rightarrow$ 1 MV/m $\rightarrow$ 0 in a Y-type hexaferrite. [73] (b) Magnetic field dependence of magnetization $M(H)$ and polarization $P(H)$ at T = 55 K in $Fe_2Mo_3O_8$. Numbers and arrows indicate the measurement sequence. [5]

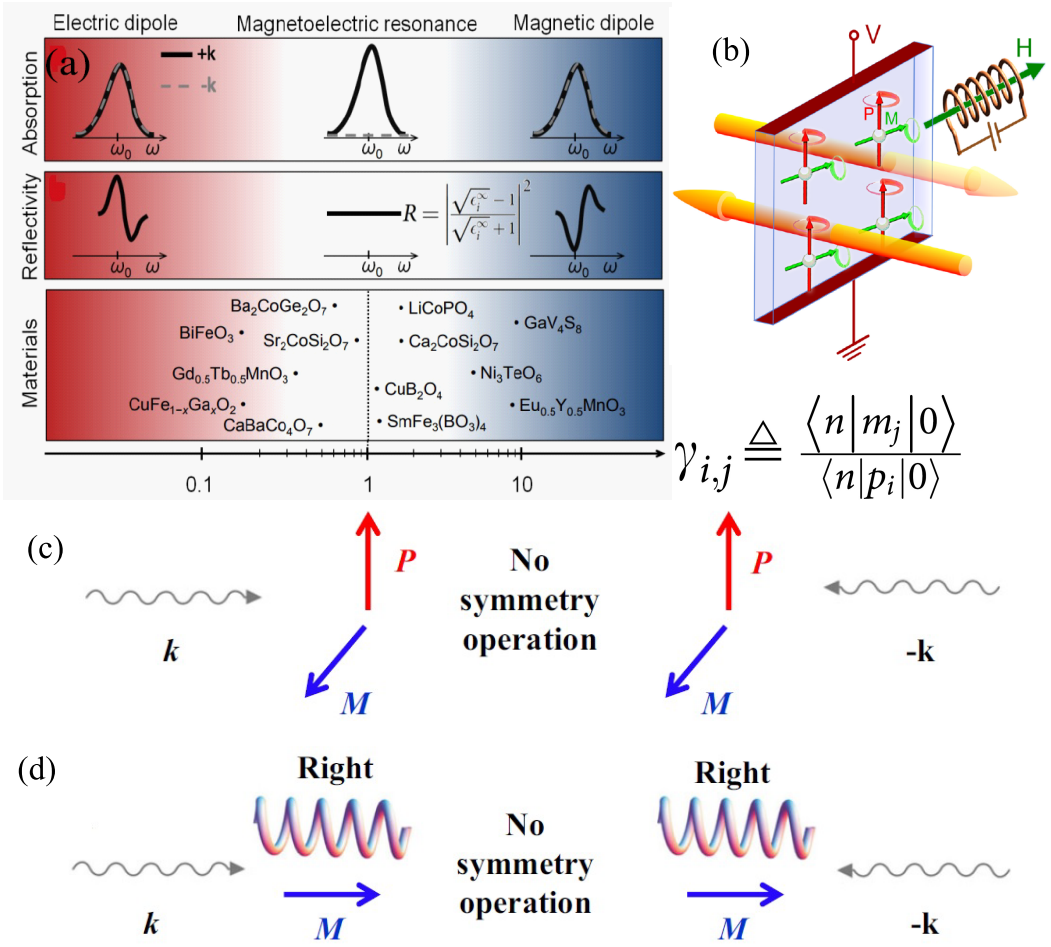


Figure 2.21: (a) List of materials exhibiting this nondirectional dichroism effect. [30] (b) Visualization of how opposite light propagations can give different responses. [32] (c) An object moving along the ferro-toroidal vector direction (**P**x**M** direction) is non-reciprocal, since two relevant reciprocal situations cannot be linked by symmetry operations. [31] (d) An object moving along the chiral axis is non-reciprocal if the chiral system is ferromagnetic with magnetization (**M**) along the chiral axis or when a magnetic field is applied along the chiral axis, since two relevant reciprocal situations cannot be related by any one or combination of symmetry opterations. [31]

opposite direction, it is known as a nonreciprocal effect. This is another result of magnetoelectric coupling. The basic idea of this effect in spectroscopy is that the direction of light propagation through a material can give different responses based on the symmetry of the sample. For example, light propagating in the $+k$ direction can be highly transmitting through a sample, whereas light traveling in the -k direction through a material can be very absorbing. This is depicted in Fig. 2.21(b). In order for a nonreciprocal effect to take place, five different symmetries must be broken for the +/-k directional anisotropy. The five symmetries that must be broken are translational, rotational, mirror reflection, space inversion, and time reversal. [31]

In magnetoelectric multiferroics, the coupling between the electric and magnetic states leads to the dynamical or optical magnetoelectric effect described by the response function $\chi^{me}(\omega)$ and $\chi^{em}(\omega)$. Consequently, oscillating magnetization and polarization (M^{ω} and P^{ω}) are induced by the electric and magnetic components of light(E^{ω} and H^{ω}), respectively. The conventional terms of dielectric permittivity ($\hat{\epsilon}$) and magnetic permeability ($\hat{\mu}$) contribute, but the tensors for magnetization and polarization become

$$M^{\omega} = [\hat{\mu}(\omega) - 1]\mathbf{H}^{\omega} + \sqrt{\epsilon_0/\mu_0}\hat{\chi}^{me}(\omega)\mathbf{E}^{\omega} \tag{2.35}$$

$$P^{\omega} = \epsilon_0[\hat{\epsilon}(\omega) - 1]\mathbf{E}^{\omega} + \sqrt{\epsilon_0/\mu_0}\hat{\chi}^{em}(\omega)\mathbf{H}^{\omega}. \tag{2.36}$$

By solving the Maxwell equations with these generalized forms, the refractive index for a given polarization is

$$N_{ij}^{\pm} \approx \sqrt{\epsilon_{ii}(\omega)\mu_{jj}(\omega)} \pm \frac{1}{2}[\chi_{ji}^{me}(\omega) + \chi_{ij}^{em}(\omega)]. \tag{2.37}$$

The $\pm$ signs correspond to wavevectors in the $\pm k$ directions. [30]

The optical magnetoelectric effect is generated by transitions where both the electric and magnetic dipoles have moments. These moments induced by an absorbed photon with energy $\hbar\omega$ are finite:

$$\chi_{ji}^{me}(\omega) = \frac{2}{V\hbar}\sqrt{\frac{\mu_0}{\epsilon_0}}\sum_n [\frac{\omega_{n0}\Re< 0|m_j|n >< n|p_i|0 >}{\omega_{n0}^2 - \omega^2 - 2i\omega\delta_n} + \frac{i\omega\Im< 0|m_j|n >< n|p_i|0 >}{\omega_{n0}^2 - \omega^2 - 2i\omega\delta_n}] \approx \chi_{ji}^{'}(\omega) + \chi_{ji}^{''}(\omega). \tag{2.38}$$

If both the electric and magnetic dipole matrix elements are nonvanishing, then an excitation can be determined to be magnetoelectric and a nonreciprocal effect can occur. When this effect is sufficiently strong, a material can either be fully absorbing or fully transparent. The magnetoelectric ratio can be defined as

$$\gamma_{i,j} \equiv \frac{< n|m_j|0 >}{< n|p_i|0 >} \tag{2.39}$$

When the magnetoelectric ratio is one, the material can be fully one way transparent - a diode. [30]

For spectroscopy, there are a few different orientations in which a sample can show nonreciprocal effects. The first is when the static polarization and magnetization of a material creates a toroidal moment, and the light propagation k is parallel or antiparallel to the toroidal moment. This is shown in Fig. 2.21(c) and is known as toroidal dichorism. Second, if the material contains a chiral axis, the combination of the chiral axis plus a magnetic component along the same direction as that chiral axis can give a nonreciprocal effect, as shown in Fig. 2.21(d). This symmetry is known as magnetochiral dichroism. A chart of known space groups having low enough symmetry to show nonreciprocal effects has been tabulated. [75] Nonreciprocal directional

dichroism ($\Delta\alpha_{DD}$) is defined as

$$\Delta\alpha_{DD} = \alpha_{+k} - \alpha_{-k}. \tag{2.40}$$

Often times, this is not the easiest or most convenient way to measure a sample. Since this effect is a magentoelectric one involving the magnetic moment in a material (as shown in the two examples in Fig. 2.21(c,d)), the switching of an external applied magnetic field can also give the same response, as

$$\Delta\alpha_{DD} = \alpha_{H_{up}} - \alpha_{H_{down}}. \tag{2.41}$$

Several different materials have been known to show a nonreciprocal effect. Most often, the effects are seen in the far infrared and terahertz regions, as magnetoelectric excitations tend to arise there. $BiFeO_3$ is the pioneer of the multiferroic community. Figure 2.22(a) shows how, with the correct orientation of light propagation and magnetic field direction, this effect can be observed. [33] Several different examples in the terahertz region include $CaBaCo_4O_7$, $FeZnMo_3O_8$, and $Ba_2CoGe_2O_7$ are presented in Fig. 2.22(b,c,d), respectively. [34, 35, 37] Few examples are seen in higher energy regions. The material must have significant spin-orbit coupling in order to introduce a magnetic dipole component into the typically purely electronic component. Two examples of the nonreciprocal effect in *d*-to-*d* energy regions are $GaFeO_3$ and CuB_2O_4, shown in Fig. 2.23(a,b), respectively. [76, 77] These materials have strong spin-orbit coupling, which intrinsically mixes the magnetic and electric dipole matrix elements. Therefore, these excitations are magnetoelectric. With such low crystallographic and magnetic symmetry, these excitations show nonreciprocal directional dichroism.

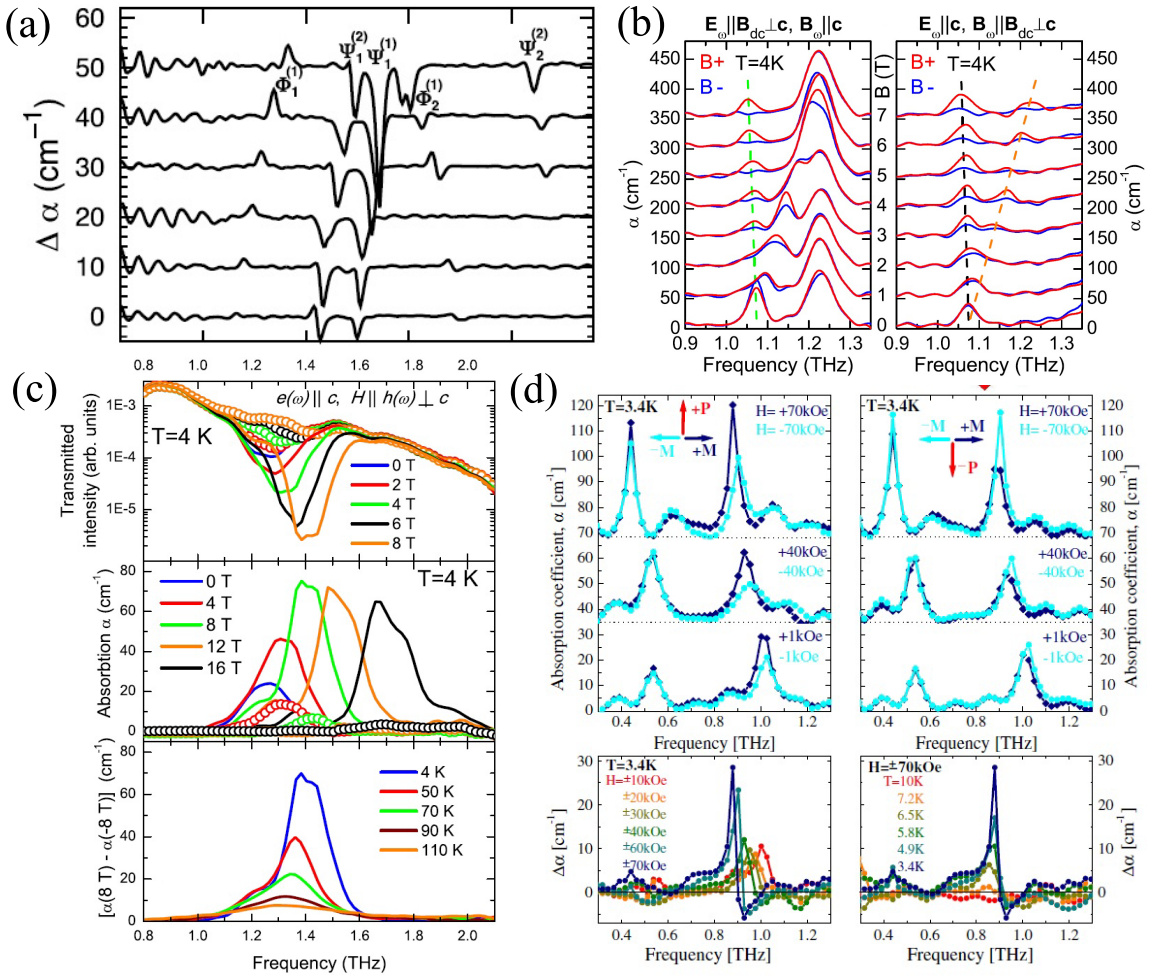


Figure 2.22: Nonreciprocal effect of different materials in the terahertz infrared region. The materials shown are $BiFeO_3$ (a) [33], $CaBaCo_4O_7$ (b) [34], $FeZnMo_3O_8$ (c) [35], and $Ba_2CoGe_2O_7$ (d) [37]

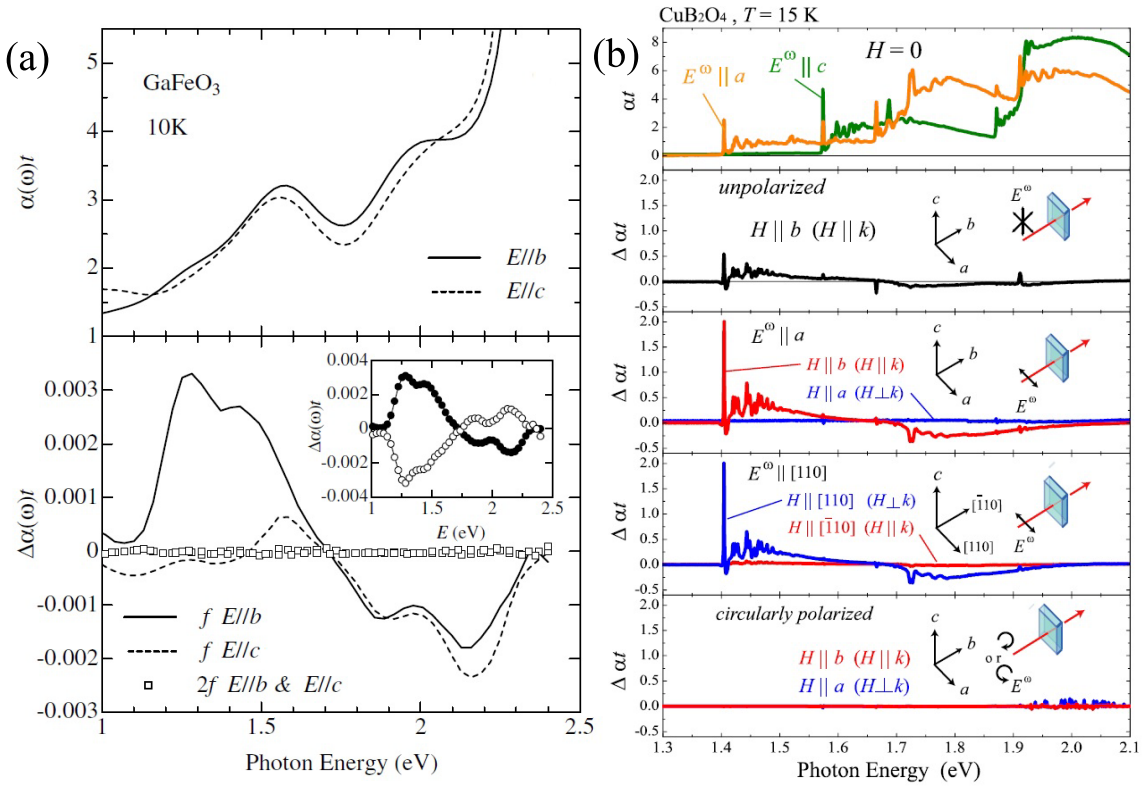


Figure 2.23: Nonreciprocal effect of different materials in the optical region. The materials shown are $GaFeO_3$ (a) [76] and CuB_2O_4 (b) [77]

2.2.5 Magnetoelastic coupling

Another interesting property that can arise from multiferroics is magnetoelastic coupling. Both experimentally and theoretically, this coupling is intensely studied due to its potential application for magneto-optical storage, transducers, oscillators, and sensors. [78–80] Magnetoelastic coupling is a complex idea that arises due to the interaction between magnetic centers and interatomic distances. Consequently, the magnetic and elastic degrees of freedom are coupled. For instance, a sample's shape and dimensions can be affected by its magnetic state, and/or magnetic properties can be sensitive to mechanical stress. [79] One of the most well known effects from this coupling is magnetostriction. Magnetostriction is a deformation of the sample that reduces the total energy (sum of the magnetic and elastic energy). In a magnetic material, the main energies that vary with the state of strain are elastic, magnetostatic, anisotropy, and isotropic exchange energy. The anisotropy energy may include anisotropic exchange, dipole-dipole interaction, and anisotropy due to the crystal-field effects. [80, 81]

Strain dependence of three magnetic energies gives rise to magnetostriction $\delta l/l$:

$$\frac{\delta l}{l} = \frac{[l(H) - l(0T)]}{l(0T)} = \lambda_f + \lambda_{anisotropic} + \lambda_{isotropic} \tag{2.42}$$

where l is the length of the sample, and λ_f, $\lambda_{anisotropic}$, and $\lambda_{isotropic}$ are the form effect (result of the strain dependence of the magnetostatic energy and arises purely from the shape of the sample), anisotropic and isotropic parts of the (forced) magnetostriction, respectively. [81]

Though magnetostriction is a very informative measurement about magnetostructural correlations in magnetic materials, it is limited in the information it can provide. It is a bulk technique that can only give information about lattice parameters as a whole. However, infrared spectroscopy can be very revealing in terms of magnetoelas-

tic phenomena. Infrared focuses on local structure, offering a unique opportunity to study how and which atomic displacements are affected by magnetic rearrangements within a system.

Spectroscopy is a highly sensitive technique for investigation of coupling phenomena between multiple degrees of freedom. The spin-Peierls transition in $CuGeO_3$ is one of the most famous examples of coupling magnetic moments to lattice phonons. [82,83] For a displacement x from the equilibrium position, the total potential energy of the crystal in the harmonic approximation can be written as:

$$U = \frac{1}{2}k_0x^2 + \sum_{ij} J_{ij}(x)\langle \mathbf{S}_i \cdot \mathbf{S}_j \rangle. \tag{2.43}$$

The second term provides the magnetic contribution to the potential energy and arises due to the dependence of the exchange integral J on structural parameters and its modulation by lattice vibrations. From Eqn. 2.43 the second derivative with respect to x gives an expression for the force constant, k:

$$\frac{d^2U}{dx^2} = k = k_0 + \sum_{ij} \frac{d^2J_{ij}}{dx^2}\langle \mathbf{S}_i \cdot \mathbf{S}_j \rangle. \tag{2.44}$$

The phonon frequency ω is now written as:

$$\omega^2 = \omega_0^2 + \frac{4J^n}{m}\langle \mathbf{S}_i \cdot \mathbf{S}_j \rangle, \tag{2.45}$$

where m is the ion mass and $J^n = d^2J_{ij}/dx^2$. This equation (2.45) can be expanded to give:

$$\omega \approx \omega_0 + \lambda\langle \mathbf{S}_i \cdot \mathbf{S}_j \rangle. \tag{2.46}$$

Here, ω_0 is the frequency in the absence of spin-phonon coupling and λ is the coupling

constant. [84–87] These equations have been employed in several different examples, including $CrSiTe_3$, $CuGeO_3$, among many others. [16, 82, 83, 88–90]

An example of how phonons are affected by magnetic spins is presented in Fig. 2.24. Here, the compound $Mn[N(CN)_2]_2$ has many different infrared phonon modes. Applying an external magnetic field, many of the phonon modes are sensitive. With increasing magnetic field, the more the absorption changes as a function of field. The trend of Mn displacement along with several different modes grow steadily with magnetic field, tracking very well with the magnetization squared. [91] However, the effects of spin-orbit coupling and its effect on spin-lattice interactions is highly underexplored.

2.3 Materials of interest

2.3.1 Ni_3TeO_6

Multiferroic materials have been largely investigated for many various potential applications in technology. [60–64] One such example is Ni_3TeO_6, attractive from many different aspects including its rich phase diagram, magnetic-field driven polarization changes, and incommensurate spin structure. [28] In this material, the crystal structure is a rhombohedral lattice with polar space group $R3$. Each nickel is surrounded by six oxygen ions, typically seen as an octahedral environment; however, here, the distortion is so large that the six ions form more of a trigonal bipyramidal structure. The three nickel centers are inequivalent and align along the c-axis, with a tellurium ion separating each nickel chain. The chain can be simply written as Ni1, Ni2, Ni3, Te. The crystal structure is depicted in Fig. 2.25(a). Each Ni has a 2+ oxidation state with S=1. The nonmagnetic Te creates a hole in the magnetic sublattice. Several different interactions compete within the magnetic sublattice. However, from

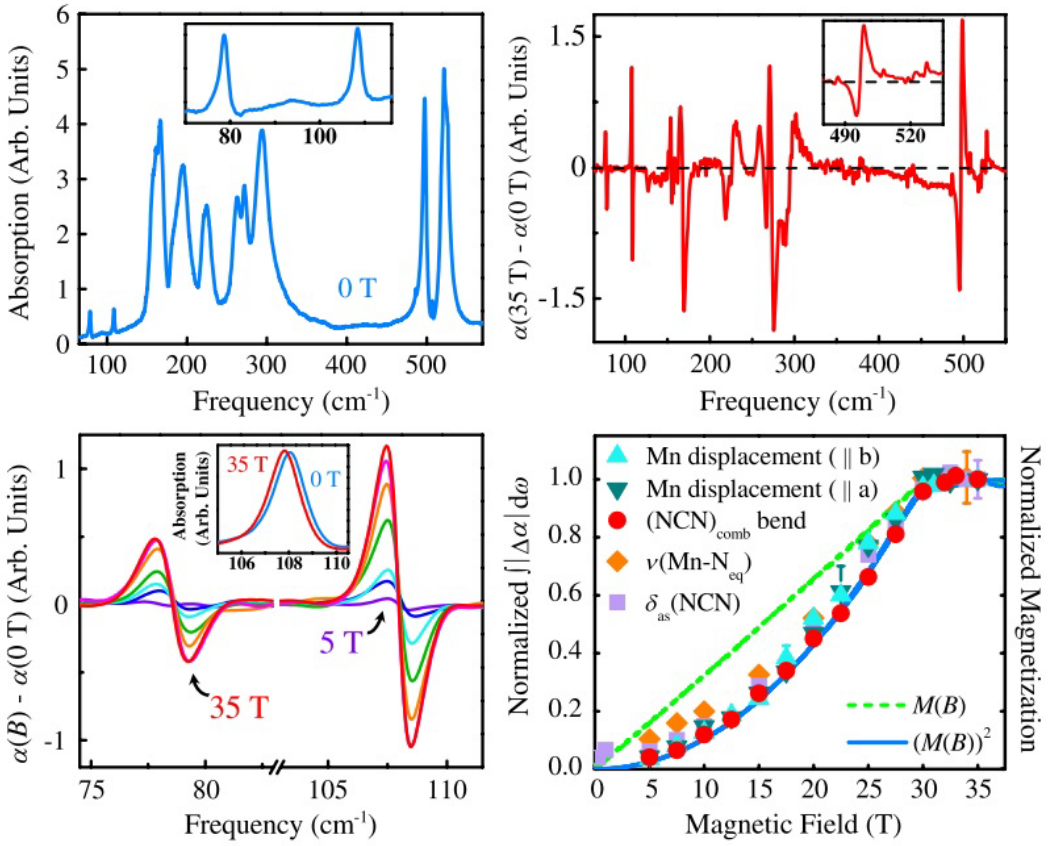


Figure 2.24: Far infared absorption and magneto-infrared results on $Mn[N(CN)_2]_2$. [16]

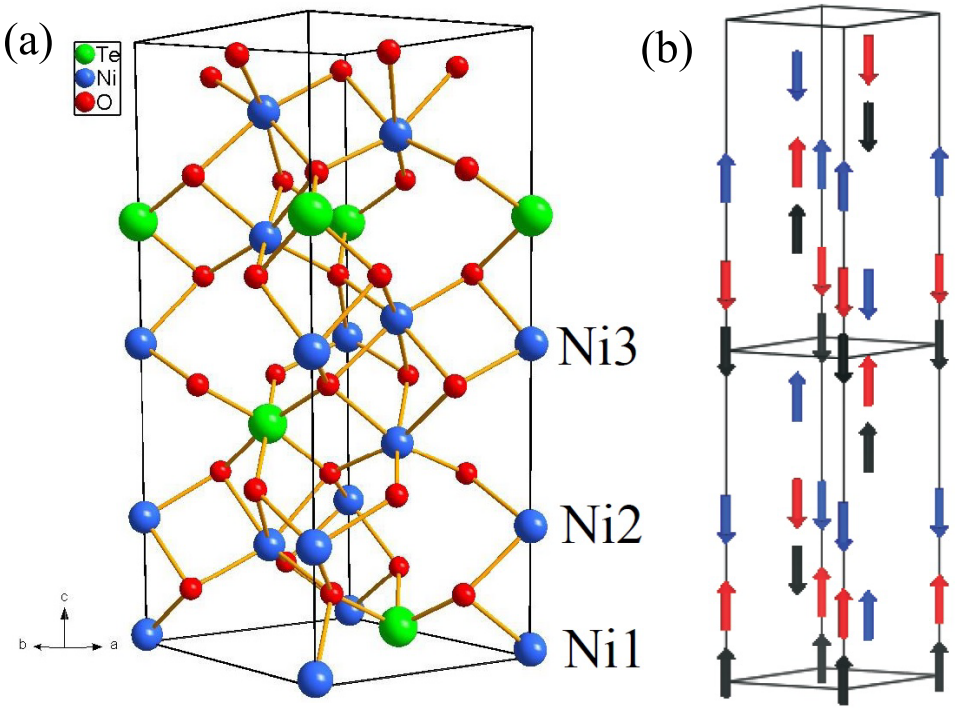


Figure 2.25: (a) Crystal structure of Ni_3TeO_6. (b) Magnetic structure of Ni_3TeO_6 from neutron powder diffraction. Arrows denote magnetic moments in particular nickel sites: Ni1-black, Ni2-red, Ni3-blue. [92]

neutron powder diffraction experiments, the magnetic ground state is determined to be a collinear antiferromagnet, with the Ni1-Ni2-Ni3 chain having the spin sequence <↑↑↓>. The magnetic unit cell is doubled compared to the structural unit cell, as there is no net magnetic moment when the unit cell is doubled. The spin alignment can be seen in Fig. 2.25(b). [92]

With the space group $R3$, Ni_3TeO_6 is polar at ambient conditions. However, the polarization suddenly changes as a function of temperature when magnetic order sets in [Fig. 2.26(a,b)]. The pyroelectric current in (a) clearly shows a sharp peak at T_N. The static polarization at 2 K is 3,280 $\mu C/m^2$, as shown in Fig. 2.26(b). [28]

Ni_3TeO_6 sports an exotic H-T phase diagram. With an 8.5 T applied field, a second peak arises in J, evidence of two different phases. Here, the polarization also changes when an applied field of 9 T is reached, by ∼290 $\mu C/m^2$. Ni_3TeO_6 also sports one of the largest magnetoelectric coupling coefficients known to date at 1,300 ps/m. Figure 2.26(c) represents the isothermal magnetization $M(H)$ along the c-axis for both increasing and decreasing temperatures, while Fig. 2.26(d) shows the magnetic-field dependence of ϵ across the spin-flop transition. These observations indicate that the magnetic-induced transition is a spin-flop transition. Here, the magnetic spins aligned along the c-axis will flop ≈90°. Spin-flop transitions are typically accompanied by hysteresis; however, no hysteresis is observed in Ni_3TeO_6.

The magnetoelectric coupling in Ni_3TeO_6 can be understood through an exchange striction argument. The exchange striction between Ni-Ni centers makes the bond length dependent on the scalar product of spins. Since these Ni ions are in inequivalent environments with different rigidities, and their charges may be slightly different, they induce different dipole moments, which results in a change of polarization $\Delta P_z = \alpha \overrightarrow{S}_1 \cdot \overrightarrow{S}_2$, with the $\overrightarrow{S}$ terms being the magnetization of the antiferromagnetic Ni sublattices. These dipole moments, and henceforth the polarization, will change as

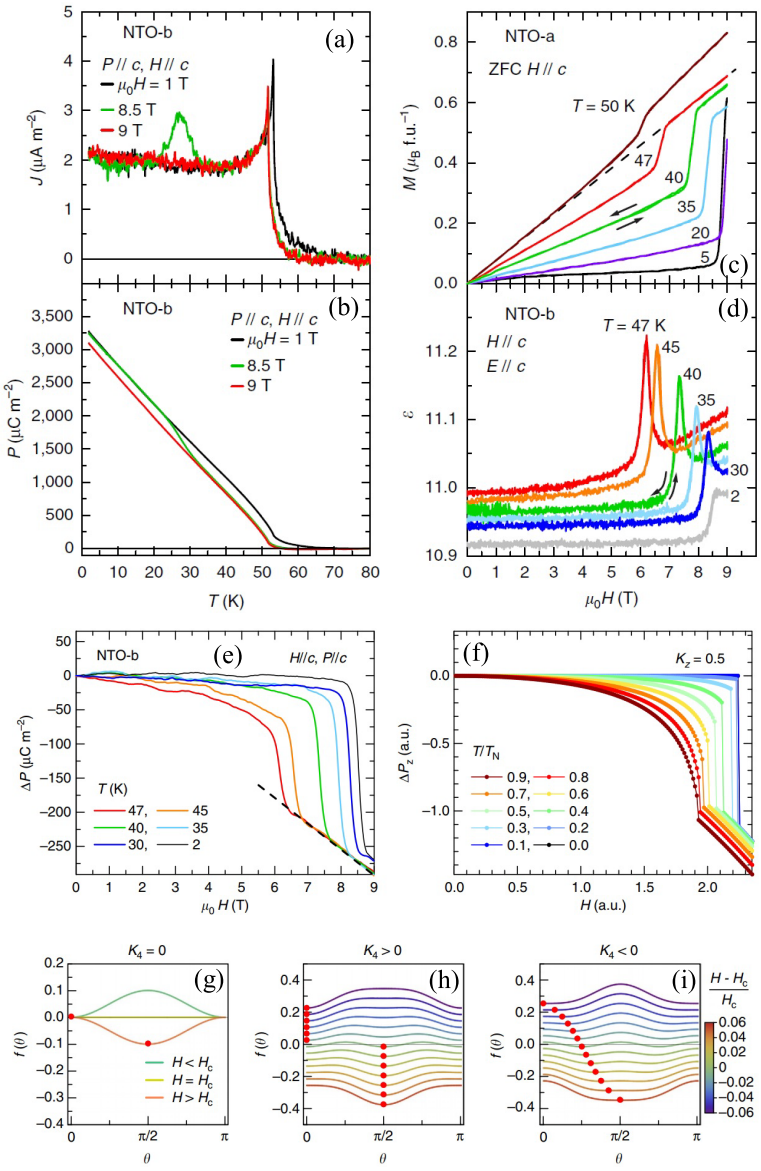


Figure 2.26: (a,b) Temperature dependence of pyroelectric current $J(T)$, and electric polarization $P(T)$ of Ni_3TeO_6 at 1, 8.5, and 9 T, respectively. (c,d) Magnetic field dependence of magnetization $M(H)$ and dielectric constant $\epsilon(H)$ of Ni_3TeO_6 at various temperatures for both increasing and decreasing magnetic fields. A black dashed line in (c) depicts linear fit to $M(H)$ curve for $H > H_c$ and at T=47 K. (e,f) Experimental results and theoretical calculations for the magnetic field dependence of the electric polarization $\Delta P(H)$ at various temperatures, respectively. A black dashed line in (e) indicates linear fit to $\Delta P(H)$ curve for $H > H_c$ and at T=47 K. (g-i) The dependence of $f(\theta)$ of the free-energy density on the direction of the antiferromagnetic order parameter for different values of fourth-order anisotropy constant K_4 in various magnetic fields. Free-energy minima are indicated by red dots. [28]

the spins reorient in the applied magnetic field. Plotting the results as polarization, it is clear that the calculations in Fig. 2.26(f) clearly represent the experimental results in Fig. 2.26(e). [28]

To further investigate the lack of hysteresis in the vicinity of the spin-flop transition, the uniform part of the Landau free-energy density was modeled:

$$f = (L^2 + \tau)^2 - \frac{K_z}{2}L_z^2 - \frac{K_4}{4}L_z^4 + \frac{\beta}{2}(\overrightarrow{\mathbf{L}} \cdot \overrightarrow{\mathbf{H}})^2 + \frac{\gamma}{2}L^2H^2, \tag{2.47}$$

with τ=$\alpha(T - T_c)$, K_z describes the easy hexagonal c-axis anisotropy, K_4 describes the quartic anisotropy, and the terms with H describe the most general coupling to the external magnetic field. The two anisotropy terms result from spin-orbit coupling $\hat{H}_{\mathrm{SO}}$=$\lambda\,\overrightarrow{\mathbf{l}} \cdot \overrightarrow{\mathbf{s}}$. Plotting the free energy as a function of the direction of θ (antiferromagnetic order parameter) give results on the character of the transition. For K_4=0 the barrier is absent and the switching occurs instantaneously in the bulk. For K_4 >0 there is a finite barrier and the transition should be of the first order with a hysteresis. If K_4 <0 the minimum of the free energy shifts continuously from θ=0 to θ=$\pi/2$ as the magnetic field increases. This case is consistent with experimental observation. This reveals that the underlying mechanism at the spin-flop transition is second order in character. [28]

Typically, after a spin-flop transition, the magnetic spins will begin to align with increasing magnetic field until the spins are full saturated. However, in Ni_3TeO_6, the story is very different. Figure 2.27(a) shows the magnetization as a function of magnetic field. The 9 T spin flop is observed, but there is another magnetic transition at 52 T. This transition is associated with a metamagnetic transition in the material. Since polarization is linked to the magnetic order, there is another large change in polarization at 52 T (Fig. 2.27(b)). However, this change in polarization is $\approx$10$\times$ larger than the change at 9 T. Along with the polarization, magnetostriction

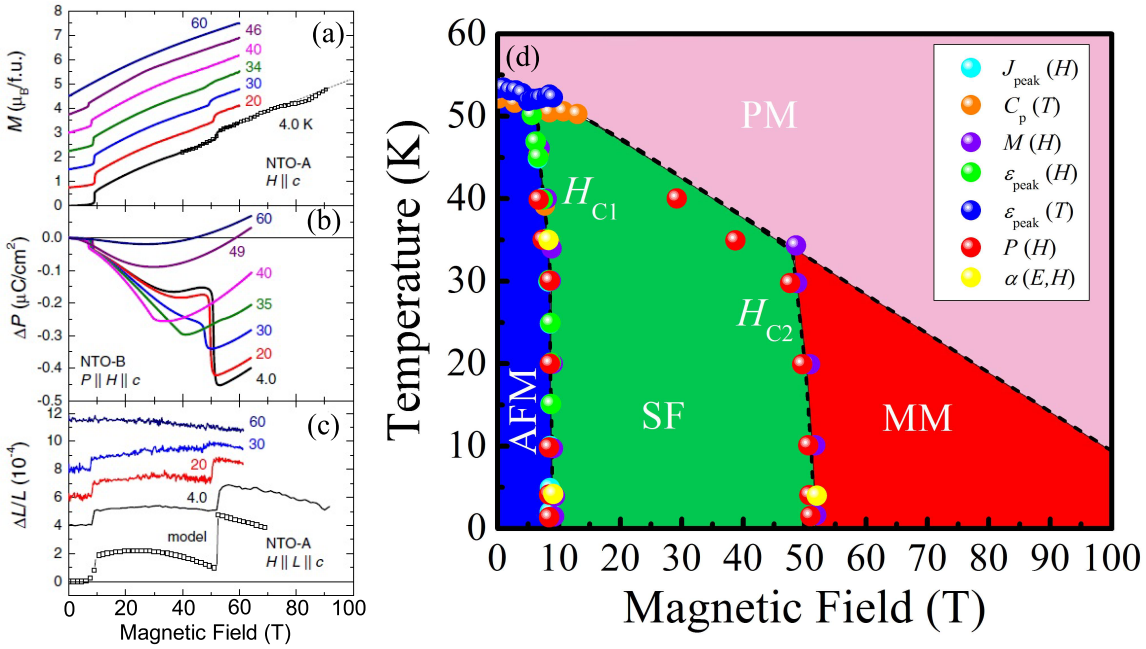


Figure 2.27: (a,b) Magnetization and change of electric polarization (ΔP) of Ni_3TeO_6 for magnetic fields applied along the c-direction. (c) c-axis magnetostriction as a function of magnetic field applied along the c-axis. Solid lines are experimental data taken under isothermal conditions and open squares are from model calculations. [29] (d) Phase diagram of Ni_3TeO_6 from an assortment of measurements including dielectric constant, magnetoelectric current, polarization, magnetization, specific heat measurements, and optics. [28, 29, 93]

measurements (Fig. 2.27(c)) show that the lattice is also linked to the spin structure, implying magnetoelastic coupling. A magnetic field-temperature phase diagram is given in Fig. 2.27(d) to summarize all of the magnetic transition temperatures and phases. [28, 29]

Of the 32 crystallographic symmetry groups, 21 are non-centrosymmetric. Out of these 21 groups, 11 are chiral, 10 are polar, and five groups are simultaneously chiral and polar. Ni_3TeO_6 falls under one of these five. Figure 2.28 gives an overview of the chirality in Ni_3TeO_6. To clarify the chirality, red and blue triangles are depicted in Fig. 2.28(a). Both the blue and red triangles are associated with three unequal bond lengths. The shortest bonds are highlighted in bold for tracking purposes along the *c*-axis. This tracking reveals a 120° rotation of neighboring "the-same-color" triangles and hence a chirality. The three red triangles rotate counterclockwise while the blue triangles rotate clockwise. These two helices have opposite chirality; however, the opposite rotations are not canceled due to the degree of chirality of each helix. The chiral value for the blue helix is twice as large than that of the red helix. Therefore, Ni_3TeO_6 forms a ferri-chiral state [Fig. 2.28(b)]. [27]

Since chiral materials rotate the polarization of light, simple transmission optical microscope images can be used to identify chiral domains. Using a polarizer and an analyzer, different chiral domains can be seen in Ni_3TeO_6, as shown in Fig. 2.28(d-j). The optical images differ either by changing the orientation of the polarizer to analyzer angle, by flipping of the sample, or just by 60° rotation of the sample in plane. [27]

Ni_3TeO_6 covers a wide range of interesting effects, from large magnetoelectric coupling, a second-order spin-flop transition, magnetostriction effects (stemming from magnetoelastic coupling), and chirality. Along with broken symmetry and large spin-orbit coupling, these characteristics yields an excellent opportunity to study

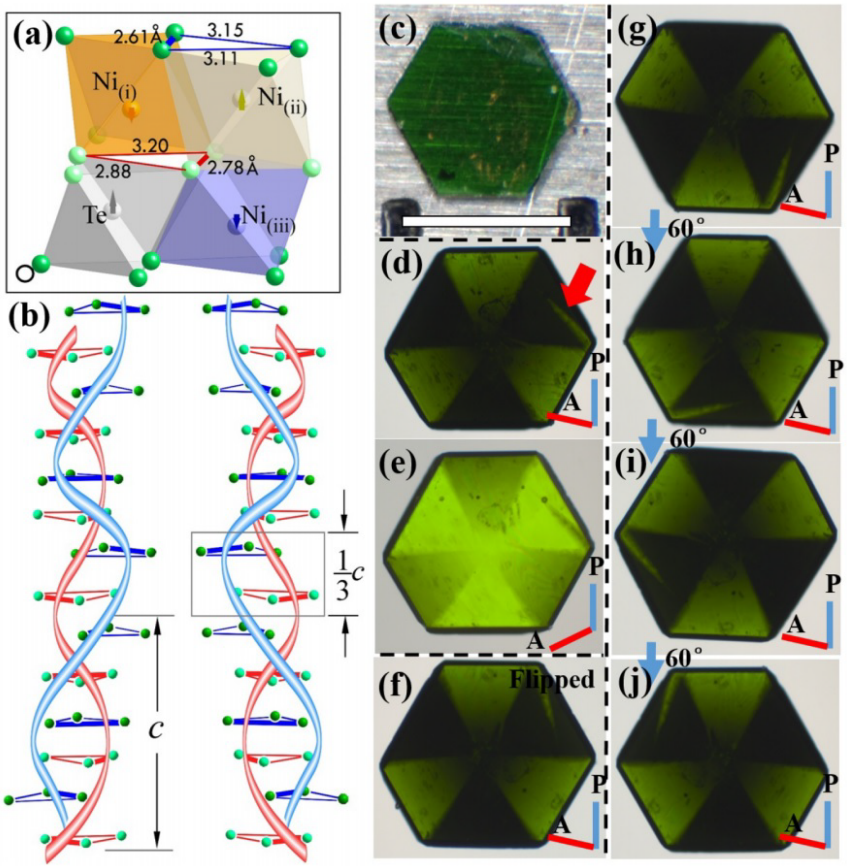


Figure 2.28: (a) displays the basic building block of Ni_3TeO_6, which corresponds to one third of one unit cell. The red triangle is associated with unequal bond lengths: 2.78, 2.88, and 3.20 Å, which can be considered as a part of the first $Ni_{(iii)}O_6$-TeO_6 honeycomb layer. Then, the neighboring $Ni_{(i)}O_6$-$Ni_{(ii)}O_6$ layer is associated with the blue triangle with unequal bond lengths: 2.61, 3.11, and 3.15 Å. We denoted the shortest bonds in red and blue triangles as bold lines. (b) shows two different ferri-chiral states: left panel with net left-handed chirality and right panel with net right-handed chirality. Red and Blue helixes, shown by following the rotation of the bold red and blue bonds, respectively, rotate in an opposite fashion, and a net chirality exists due to the asymmetry of red and blue triangles (helices). (c) is an optical microscope image of a 100 μm-thick single crystal of Ni_3TeO_6: the scale bar equals to 1 mm. The chiral domains of a Ni_3TeO_6 crystal are visible in transmission polarized optical microscope images shown in (d-j). Blue and red bars represent the angles of a polarizer and an analyzer, respectively. (d,e) show the contrast inversion of the chiral domains with rotating the analyzer from θ=90°-φ to 90°+φ. (f), compared with (d) shows no contrast change with flipping the crystal with a fixed polarizer/analyzer angle. (g-j) demonstrate no contrast change with in-plane rotation of the crystal with a fixed polarizer/analyzer angle (a red arrow labels one landmark which is an embedded different chiral domain, with which the crystal orientation can be identified). [27]

the frequency dependence of all of these unique phenomena, from high-field optics, high-field infrared, and nonreciprocal directional dichroism.

2.3.2 $EuTiO_3$ and Nb-substitution

Electric field control of magnetism is the overall driver for research on multiferroic materials. Measurements of prototypical $BiFeO_3$ demonstrate the effect, [94, 95] although it is limited by relatively weak coupling between electric polarization and magnetization as well as a modest magnetic moment. Several approaches have been proposed to address these issues including A- and B-site chemical substitution, strain, the trilinear coupling mechanism that relies upon non-cancelling distortions within a unit cell, and the proximity effect. [96–102] A number of important systems have been discovered using these strategies. One example is $EuTiO_3$ - a well-known magnetic analog of the perovskite $SrTiO_3$ [Fig. 2.30(a)]. [103]

In its ground state, $EuTiO_3$ is a quantum paraelectric antiferromagnet. The subtle $Pm\bar{3}m \leftrightarrow I4/mcm$ structural transition in pure and substituted compounds is marked by a dramatic step-wise softening of the elastic moduli [42] - an effect that has been attributed to both displacive and order-disorder effects. [42, 104–106] The significant drop in the dielectric constant across T_N combined with its strong magnetic field dependence is evidence for substantial magnetoelectric coupling. [107] This interaction arises from coupling between G-type spin ordering and a soft polar phonon in dynamic equilibrium with antiferrodistortive oxygen octahedral rotations. [108] Under strain, $EuTiO_3$ thin films are multiferroic - ferroelectric and ferromagnetic at the same time - with enormous property coefficients. [89, 103, 109] More specifically, strain moves the Ti ion off-center, decreasing the third nearest neighbor antiferromagnetic interactions while maintaining the first- and second-near-neighbor ferromagnetic interactions. [89, 103, 109] This observation highlights the importance of

spin-phonon coupling and implies that $EuTiO_3$ may be close to a ferroelectric quantum critical point. [42] The dream is to switch the strain-induced multiferroicity on and off with electric field. [89, 109] Pressure and magnetic field effects are also of interest. [106, 110] Chemical substitution provides another strategy for controlling properties. The $Eu(Ti_{1-x}Nb_x)O_3$ system is a supurb platform for testing predictions for B-site substitution and local strain as a route to multiferroicity. [102, 103]

Figure 2.29 provides information on the parent and Nb-substituted samples of $EuTiO_3$. As substitution increases, the temperature at which the structural transition takes place (indicated by the sudden drop in the shear modulus in Fig. 2.29(a)) also increases. The temperature - substitution phase diagram is plotted in Fig. 2.29(b). The parent compound is antiferromagnetic in its ground state, but as substitution increases, the ground state switches to ferromagnetic. This occurs around a substitution concentration of $\sim$10%. Along with a change in magnetic ground state, the structural transition broadens and increases with increasing substitution. [42,111] The crystal structure is cubic [Fig. 2.30(a)].

As summarized in Fig. 2.30(c), Nb substitution shifts the structural transition in $EuTiO_3$ to higher temperatures, drives an insulator $\rightarrow$ metal transition [Fig. 2.30(b)], and destabilizes the antiferromagnetic ground state of the parent compound in favor of long range ferromagnetic ordering. [42] These physical property changes are thought to arise from the way in which Nb substitution weakens the octahedral tilt amplitude and modifies Ti-O bond covalency. [42] Moreover, Nb is present as a 4+ ion, so in addition to introducing disorder, it acts as an electron donor, explaining why heavy substitution results in a metallic response [Fig. 2.30(b)].

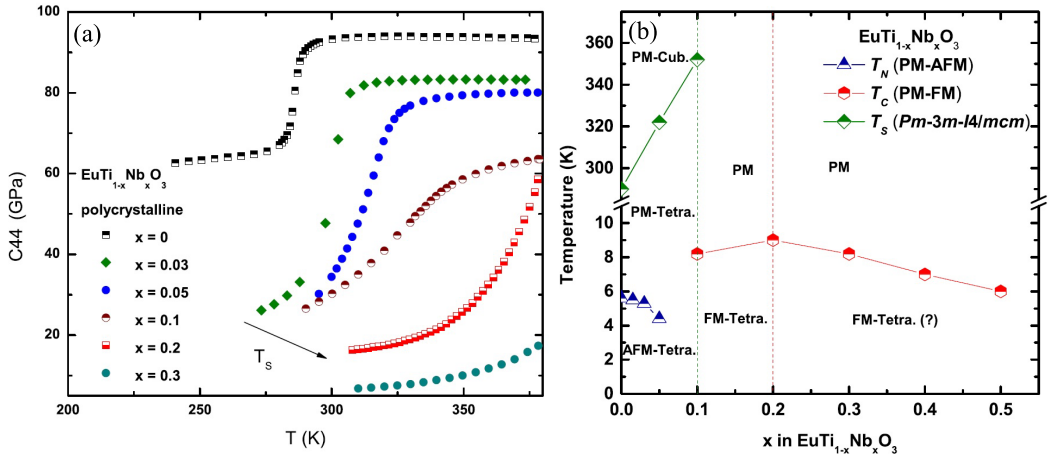


Figure 2.29: (a) Temperature dependence of the shear modulus C_{44} for selected values of substitution concentration of $Eu(Ti_{1-x}Nb_x)O_3$. Data is shifted for clarity. [42] (c) The temperature vs substitution phase diagram indicating structural and magnetic phase transitions in $Eu(Ti_{1-x}Nb_x)O_3$. [42]

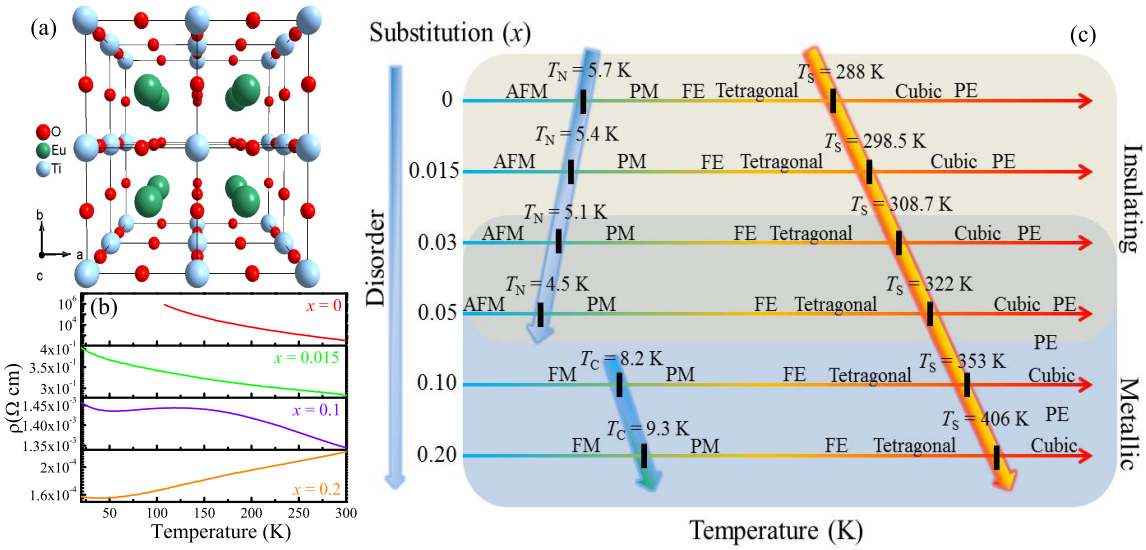


Figure 2.30: (a) Crystal structure of $EuTiO_3$ at room temperature with space group $Pm\bar{3}m$. (b) Summary of the *dc* resistivity for several different substitution concentrations. [42] (c) Schematic view of the properties of $EuTiO_3$ as a function of temperature and Nb substitution. [42]

Chapter 3

Experimental and theoretical techniques

3.1 Optical theory

Optical properties describe and quantify the interaction between electromagnetic radiation and matter. Since electromagnetic radiation has an electric field vector and a magnetic field vector, the interaction with matter is directly related to the electronic and magnetic character of a solid. Therefore, interpretation of optical properties is fundamental to understand the spin and charge dynamics from a microscopic viewpoint. Optical properties can be obtained from a transmittance $T(\omega)$ or reflectance $R(\omega)$ measurement. Further analysis, such as using Beer's Law or a Kramers-Kronig analysis, can then yield optical constants such as absorption $\alpha(\omega)$, optical conductivity $\sigma_1(\omega)$, among others.

3.1.1 Maxwell's equations

From experimentation, the most available and common optical property is from frequency-dependent transmittance or reflectance. However, the dielectric function is most directly relatable to understanding the electronic structure of a solid. In order to relate the experimental techniques to the electronic properties of solids, an understanding of Maxwell's equations is necessary. Therefore, we must retain equations to write Maxwell's equations in terms of macroscopic quantities and still retain the form of the microscopic equations. By averaging the microscopic details, the following exact macroscopic equations are obtained (SI units) [112]:

$$\nabla \cdot \mathbf{D} = \rho^{ext} \tag{3.1}$$

$$\nabla \cdot \mathbf{B} = 0 \tag{3.2}$$

$$\nabla \times \mathbf{E} = -\frac{\partial \mathbf{B}}{\partial t} \tag{3.3}$$

$$\nabla \times \mathbf{H} = \frac{\partial \mathbf{D}}{\partial t} + \mathbf{J}^{cond} + \mathbf{J}^{ext}, \tag{3.4}$$

where $\mathbf{E}$ and $\mathbf{H}$ are the electric and magnetic fields, $\mathbf{D}$ and $\mathbf{B}$ are the displacement field and magnetic induction, J^{cond} is current density arising from the motion of conduction electrons, and J^{ext} and ρ^{ext} are current and charge density induced by external force.

As for the properties of the medium, it is clear that the polarization and free current density are related to the electric field strength. Furthermore, the magnetization is related to the magnetic induction and hence to the magnetic field strength. To further simplify the properties, looking at only isotropic media, several linear approximations can be assumed:

$$\mathbf{P} = \chi_e \mathbf{E} \tag{3.5}$$

$$\mathbf{M} = \chi_m \mathbf{H} \tag{3.6}$$

$$\mathbf{D} = \epsilon \mathbf{E} \tag{3.7}$$

$$\mathbf{B} = \mu \mathbf{H} \tag{3.8}$$

$$\mathbf{J}^{cond} = \sigma \mathbf{E}, \tag{3.9}$$

where $\mathbf{P}$ is polarization, $\mathbf{M}$ is magnetization, χ_e is the electric susceptibility, χ_m is the magnetic susceptibility, ϵ is the dielectric function, μ is the magnetic permeability, and σ is the conductivity. The properties of the medium can now be included in the set of macroscopic Maxwell's equations. However, the equations are no longer exact for anisotropic media.

Considering light interactions with a medium, the equations can be simplified. For isotropic media, no external forces exist ($\rho^{ext} = 0$) and there is no spatial variation in ϵ. By solving these equations, a wave equation for a plane wave propagating in an energy-absorbing medium can be obtained:

$$\nabla^2 \mathbf{E} = \frac{\epsilon}{c^2} \frac{\partial^2 \mathbf{E}}{\partial t^2} \tag{3.10}$$

Since experiments on the optical properties of solids are usually conducted with monochromatic light, the propagation of light of a single plane wave within an isotropic medium must be considered. The wave vector must be complex, so:

$$\mathbf{E} = \mathbf{E_0} e^{[i(\mathbf{k}\cdot\mathbf{r} - \omega t)]} \tag{3.11}$$

where $\mathbf{k}$ is the wave vector and ω is the frequency. Substituting equation 3.11 into

equation 3.10 yields

$$k^2 = \frac{\omega^2}{c^2}\epsilon(\omega). \tag{3.12}$$

Expressing k by the complex index of refraction $\tilde{N} = \sqrt{\epsilon(\omega)}$ gives:

$$k = \frac{\tilde{N}\omega}{c}. \tag{3.13}$$

The complex index of refraction $\tilde{N}(\omega)$ is defined by the following expression:

$$\tilde{N}(\omega) = n + i\kappa \tag{3.14}$$

and the complex dielectric function:

$$\epsilon(\omega) = \epsilon_1 + i\epsilon_2 \tag{3.15}$$

with n and κ being the refractive index and the extinction coefficient, respectively. Other important relationships are $\epsilon_1 = n^2 - \kappa^2$ and $\epsilon_2 = 2n\kappa$.

Many different relations can come about from these equations; however, here, the focus will be on finding the absorption coefficient α. Because experiments are done on solids, the electromagnetic wave will be dampened when hitting the solid. Therefore, a new wave equation must be used. Using these new terms, rewriting equation 3.11 yields:

$$E(x,t) = E_0 e^{i[(\tilde{N}\omega/c)x - \omega t]} = E_0 e^{-(2\pi\kappa/\lambda_\omega)x} e^{i(kx-\omega t)} \tag{3.16}$$

The expression $2\pi\kappa/\lambda_\omega$ describes the attenuation of the field and λ_ω is the light wavelength in vacuum. The first exponential factor describes the attenuation of wave amplitude with distance. Since intensity can be seen as proportional to the

square of the electric field, using Beer's law gives

$$I(x) = EE^* = I_0 e^{-\alpha x}, \tag{3.17}$$

and a relationship between κ and α is found as

$$\alpha = \frac{2\omega\kappa}{c} = \frac{4\pi\kappa}{\lambda_\omega}. \tag{3.18}$$

Similarly, α can be related to the imaginary part of the dielectric function as:

$$\alpha = \frac{\omega\epsilon_2}{cn} \tag{3.19}$$

For a medium with finite conductivity, the important expression for the dielectric function becomes

$$\epsilon(\omega) = 1 + \frac{i\sigma(\omega)}{\omega\epsilon_0}, \tag{3.20}$$

and for the absorption:

$$\alpha = \frac{\sigma_1}{n\epsilon_0 c}. \tag{3.21}$$

It is important to point out that $\sigma(\omega)$ has both complex and imaginary components as well ($\sigma = \sigma_1 + i\sigma_2$). It follows that a material with low resistivity (high conductivity) has high absorption. Table 3.1 lists the relationships between the various response functions of $\epsilon(\omega)$, $\sigma(\omega)$, and $\tilde{N}(\omega)$. [112, 113]

In most materials, these response functions and optical constants do not depend on the symmetry of the experiment. However, some materials that have very low symmetry can have different responses due to the experimental details. For example, light propagation along the $+k$ and $-k$ directions can give different values for the

Table 3.1: Relationships between the various response function $\epsilon(\omega)$, $\sigma(\omega)$, and $N(\omega)$

Dielectric constant $\epsilon(\omega)$	Conductivity $\sigma(\omega)$	Refractive index $N(\omega)$
$\epsilon = \epsilon_1 + i\epsilon_2$	$\epsilon_1 = 1 - \frac{4\pi\sigma_2}{\omega}$	$\epsilon_1 = n^2 - k^2$
$\sigma_1 = \frac{\omega\epsilon_2}{4\pi}$	$\epsilon_2 = \frac{4\pi\sigma_1}{\omega}$	$\epsilon_2 = 2nk$
$\sigma_2 = (1-\epsilon_1)\frac{\omega}{4\pi}$	$\sigma = \sigma_1 + i\sigma_2$	$\sigma_1 = \frac{nk\omega}{2\pi}$
$n = (\frac{1}{2}((\epsilon_1^2+\epsilon_2^2)^{1/2}+\epsilon_1))^{1/2}$	$n = (\frac{1}{2}(((1-\frac{4\pi\sigma_2}{\omega})^2 + (\frac{4\pi\sigma_1}{\omega})^2)^{1/2} + (1-\frac{4\pi\sigma_2}{\omega})))^{1/2}$	$\sigma_2 = (1-n^2+k^2)\frac{\omega}{4\pi}$
$k = (\frac{1}{2}((\epsilon_1^2+\epsilon_2^2)^{1/2}-\epsilon_1))^{1/2}$	$n = (\frac{1}{2}(((1-\frac{4\pi\sigma_2}{\omega})^2 + (\frac{4\pi\sigma_1}{\omega})^2)^{1/2} - (1-\frac{4\pi\sigma_2}{\omega})))^{1/2}$	$N = n + ik$

refractive index. [30] This can be seen from the equations listed below:

$$N_{ij}^{\pm} \approx \sqrt{\epsilon_{ii}(\omega)\mu_{jj}(\omega)} \pm \frac{1}{2}[\chi_{ji}^{me}(\omega) + \chi_{ij}^{em}(\omega)] \tag{3.22}$$

where

$$\begin{aligned}\chi_{ji}^{me}(\omega) = \frac{2}{V\hbar}\sqrt{\frac{\mu_0}{\epsilon_0}}\sum_n [\frac{\omega_{n0}\Re < 0|m_j|n >< n|p_i|0 >}{\omega_{n0}^2 - \omega^2 - 2i\omega\delta_n} \\ + \frac{i\omega\Im < 0|m_j|n >< n|p_i|0 >}{\omega_{n0}^2 - \omega^2 - 2i\omega\delta_n}] \approx \chi_{ji}^{'}(\omega) + \chi_{ji}^{''}(\omega)\end{aligned} \tag{3.23}$$

For magnetoelectric media, it is evident that the refractive index is not only dependent on electric-dipole transitions, but also on the magnetic-dipole component. From the $\pm$ in Eq. 3.22, we can see that the refractive index, as well as all other optical constants, can differ from opposite light propagation directions. [30]

3.1.2 Beer's law

Many spectroscopic experiments are done as transmittance measurements. In order to convert transmittance spectra as a function of frequency to an absorption coefficient, Beer's law must be used. For a sample thickness $d < \delta = \frac{c}{\omega k}$, the penetration depth, the absorption coefficient can be directly determined from transmittance.

If the optical density allows for transmittance experiments, then the Beer-Lambert law can be used:

$$I = I_0 e^{-\alpha d} \tag{3.24}$$

with I and I_0 being the intensities of the transmitted and incident beams, respectively, d being the thickness, and α the absorption coefficient. Spectroscopists commonly use these two equations:

$$T = \frac{I}{I_0} \tag{3.25}$$

$$A = -ln\frac{I}{I_0} = \alpha d. \tag{3.26}$$

Rearranging and combining equations 3.25 and 3.26 yields

$$\alpha = -\frac{1}{d} ln(T\omega), \tag{3.27}$$

giving the absorption coefficient α directly from sample thickness d and from transmittance as a function of frequency ($T(\omega)$). [114]

Beer's law is only viable if there is transmittance of the material with minimal or negligible reflectance. However, the reflectance is not always small enough to be ignored. Therefore, a correction to calculated transmittance to include minimal reflectance is given as

$$T = \frac{(1-R)^2 e^{-ad}}{1 - R^2 e^{-2ad}} \tag{3.28}$$

where R is the reflectance at the sample surface. [115, 116]

3.1.3 Kramers-Kronig analysis and sum rules

Sometimes, samples and the materials of interest do not always transmit light. Therefore, reflectance measurements are used. Measuring the reflectivity at normal incidence and the use of dispersion relations can determine optical properties. The reflectivity for normal incidence is given by r and the power reflectance is given by:

$$R(\omega) = rr^* = \frac{(n-1)^2 + \kappa^2}{(n+1)^2 + \kappa^2}. \tag{3.29}$$

The power reflectance $R(\omega)$ and phase-dispersion shift $\phi(\omega)$ are related by Kramers-Kronig transformation [112]:

$$\phi(\omega) = \frac{\omega}{\pi} \int_0^\infty \frac{lnR(\omega) - lnR(\omega')}{\omega'^2 - \omega^2} d\omega'. \tag{3.30}$$

Since reflectivity is shown as

$$r = \sqrt{R} e^{i\phi}, \tag{3.31}$$

and combining equations 3.29, 3.30, and 3.31, n and k can be determined by $R(\omega)$ and $\phi(\omega)$ as

$$n(\omega) = \frac{1 - R(\omega)}{1 + R(\omega) - 2\sqrt{R(\omega)} cos\phi(\omega)} \tag{3.32}$$

$$\kappa(\omega) = \frac{2\sqrt{R(\omega)} sin\phi(\omega)}{1 + R(\omega) - 2\sqrt{R(\omega)} cos\phi(\omega)}. \tag{3.33}$$

From earlier identities and relationships, the real part of dielectric function and the real part of optical conductivity can be determined:

$$\epsilon_1 = n^2 - k^2 \tag{3.34}$$

$$\sigma_1 = \frac{\omega\epsilon_2}{4\pi} = \frac{\omega nk}{2\pi}. \tag{3.35}$$

All of these optical constants are frequency dependent. In Eq. 3.30, the integration is from zero to ∞. Since our optical measurements usually cover the frequency range from far-infrared to ultraviolet, proper extrapolations should be used for the low and high frequencies of the spectrum. In practice, the phase shift relation can be broken into three different equations:

$$\phi(\omega) = \frac{\omega}{\pi}\int_0^{\omega_1} \frac{lnR(\omega) - lnR(\omega')}{\omega'^2 - \omega^2} d\omega' \tag{3.36}$$

$$\phi(\omega) = \frac{\omega}{\pi}\int_{\omega_1}^{\omega_2} \frac{lnR(\omega) - lnR(\omega')}{\omega'^2 - \omega^2} d\omega' \tag{3.37}$$

$$\phi(\omega) = \frac{\omega}{\pi}\int_{\omega_2}^{\infty} \frac{lnR(\omega) - lnR(\omega')}{\omega'^2 - \omega^2} d\omega' \tag{3.38}$$

For Eqn. 3.36, several possibilities are presented, depending on the behavior of the material at hand. Most commonly, a Hagen-Rubens relation, ($R(\omega) = 1 - (2\omega/\pi\sigma_0)^{1/2}$), is used for a metallic materials, and a constant extrapolation is used for insulators/semiconductors in the low frequency range. If the DC conductivity is known, that can also be input. The second equation (3.37) is the portion where the experimental data is, from ω_1 to ω_2. In the high frequency range (Eqn. 3.38), the optical response is controlled by two parameters. First, the program prompts to input the frequency at which free electron behavior sets in (typically 1E6). Second,

the equation is modeled as $R \sim \omega^{-x}$, where x varies from 0-4 and can be determined by comparing the absorption and calculated optical conductivity.

Together with physical arguments about the behavior of the response in certain limits, the Kramers-Kronig relation can also be used to derive sum rules. That is

$$\int_0^\infty \omega' Im(-1/\epsilon(\omega'))d\omega' = 1/2\pi\omega_p^2, \tag{3.39}$$

where ω_p is the plasma frequency. A partial sum rule [112] is also useful in quantifying the change of absorption spectra

$$f \equiv \frac{2c}{N_e \pi \omega_p^2} \int_{\omega_1}^{\omega_2} n\alpha(\omega, B)\, \mathrm{d}\omega. \tag{3.40}$$

Here, f is the oscillator strength, N_e is the number of electrons per magnetic ion site, n is the refractive index, ω_p is the plasma frequency $\equiv\sqrt{\frac{e^2\rho}{m\epsilon_0}}$, e and m are the charge and mass of an electron, ϵ_0 is the vacuum dielectric constant, ρ is the density of magnetic ion sites, c is the speed of light, and ω_1 and ω_2 are the frequency limits of integration.

3.1.4 Drude and Lorentz models

The dielectric function can be modeled by three parts:

$$\epsilon = \epsilon_{free} + \epsilon_{bound} + \epsilon_\infty, \tag{3.41}$$

where ϵ_{bound} is contributed from bound carriers and ϵ_{free} is the contribution from free electrons. The model to describe the contribution of bound electrons is modeled with a Lorentz oscillator, and the model to describe the contribution of free carriers is the Drude model. They are related, and the first to consider is the Lorentz model.

The Lorentz model supposes that the bound electrons to the nucleus act sim-

ilar to a harmonic oscillator, or a mass-spring system. The electrons react to an electromagnetic field via vibrating. The bound electron's equation of motion can be described

$$m\frac{d^2r}{dt^2} + m\Gamma\frac{dr}{dt} + m\omega_0^2 r = -eE_{loc} \tag{3.42}$$

where the m is the electron mass, e is the electron charge, ω_0 is Hooke's law frequency, Γ is the damping constant, and E_{loc} is the local electric field acting on the electron. The first term is the acceleration force, the second term refers to the viscous force, and the third term is Hooke's force. The solution to this equation yields

$$r(\omega) = \frac{1}{m}\frac{-eE_{loc}}{(\omega_0^2 - \omega^2) + i\Gamma\omega}. \tag{3.43}$$

From this, the induced dipole moment μ is related to r through this equation:

$$\mu(\omega) = \frac{e^2 E_{loc}}{m[(\omega_0^2 - \omega^2) + i\Gamma\omega]} \tag{3.44}$$

Since $\mu(\omega) = \alpha(\omega)E(\omega)$, the polarization per unit volume is given by

$$P(\omega) = N\alpha(\omega)E(\omega) = \epsilon_0\chi(\omega)E(\omega). \tag{3.45}$$

The susceptibility $\chi(\omega)$, from the prior equation, is then

$$\chi(\omega) = (\frac{Ne^2}{\epsilon_0 m})\frac{1}{\omega_0^2 - \omega^2 + i\Gamma\omega} \tag{3.46}$$

where $(4\pi Ne^2/m$ is the plasma frequency squared (ω_p^2). The dielectric function can then be written as

$$\epsilon(\omega) = 1 + \frac{\omega_p^2}{\omega_0^2 - \omega^2 + i\Gamma\omega}. \tag{3.47}$$

where ω_p equals

$$\omega_p == \sqrt{\frac{Ne^2}{\epsilon_0 m}} \tag{3.48}$$

From this dielectric function, many optical parameters can be calculated, such as absorption ($\alpha(\omega)$), optical conductivity ($\sigma(\omega)$), refractive index ($n(\omega)$), and so on.

The Drude model of electrons usually describe a metallic system. It is a free electron model without bound electrons to the nucleus. In this case, there is no Hooke's law oscillator term ($\omega_0 = 0$), so the dielectric constant becomes

$$\epsilon(\omega) = 1 - \frac{\omega_p^2}{\omega^2 - i\Gamma\omega}. \tag{3.49}$$

It is often times more useful and meaningful to describe the dielectric function in terms of τ, which is a mean collision rate (mean free time between collisions of electrons)

$$\tau = \frac{1}{\Gamma}. \tag{3.50}$$

For this work, several instances call for the use of both the Drude and Lorentz models. Using these fitting parameters, different information can be extracted. For example, the Drude model can give the number of free carriers in a system. Using these fits, trends can be observed, such as how excitations change with variable temperature, applied magnetic field, and chemical substitution. With these trends, we are able to analyze how the material and specific excitations can be sensitive to different phase transitions.

3.1.5 Computational methods

In the scope of this research, two main theoretical/computational methods were used: density functional theory (DFT) and dynamical mean-field theory (DMFT). Density functional theory is a first principles quantum mechanical method that models electronic structure. It is greatly used in the fields of physics, chemistry, and materials science to understand the electronic structure of many-body systems. The method allows the prediction and calculation of a material's behavior on the basis of quantum mechanics and uses approximation of independent electrons. [117–119] Dynamical mean-field theory is another method used to determine the electronic structure of strongly correlated materials. Here, the approximation of independent electrons breaks down. Dynamical mean-field theory is a non-perturbative treatment of local interactions between electrons. [120] In this work, a combination of density functional theory and dynamical mean field theory was used to compute the electronic structure of Ni_3TeO_6.

3.2 Spectroscopic instrumentation

Spectroscopy is the study of how matter interacts with electromagnetic radiation. Traditionally, spectroscopy was deemed how matter interacts with light, but it has now been extended to electromagnetic radiation which is dependent on the wavelength. The technique used is typically classified by the wavelength regime of the spectrum that is observed, ranging from microwaves, terahertz, infrared, near infrared, visible, and ultraviolet radiation. Therefore, spectroscopy can be used as a microscopic probe of the vibrational and electronic properties of a material. In this work, the probing light of interest falls in the infrared through the ultraviolet region. Several different spectrometers were used in the analysis of each of the different re-

gions. Each of these spectrometers overlap in their energy regions as to allow for merging and obtaining a full spectra, sweeping from 20-55,000 cm−1. The following sections will lay out the spectrometers used, from lowest frequency to highest frequency. All three instruments are pictured in Fig. 3.1.

3.2.1 Fourier transform spectroscopy

In this work, two types of instruments (which will be discussed in more detail later) were used for the majority of the infrared investigations. Each of these spectrometers contains several essential componenets: source, interferometer, sample, and detector. Both of these instruments are Fourier-transform infrared (FTIR) spectrometers. The key to any FTIR spectrometer is the interferometer. A general understanding of Fourier-transform spectroscopy can be understood from the basic principles of a Michelson interferometer, a schematic shown in Fig. 3.2.

The main purpose of the interferometer is to introduce a path difference between two beams of light and to produce an interference pattern. The incident beam of radiation from the external source is split into two parts by a beamsplitter. Half of

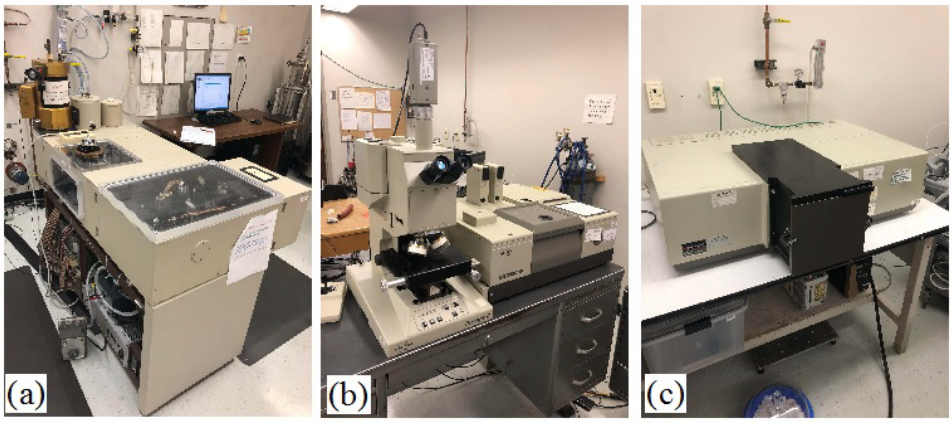


Figure 3.1: The instruments used in the lab: (a) Bruker IFS 113v FTIR spectrometer (b) Bruker Equinox 55 FTIR Spectrometer with Bruker IR Scope II (c) Perkin Elmer λ-900 Grating Spectrometer

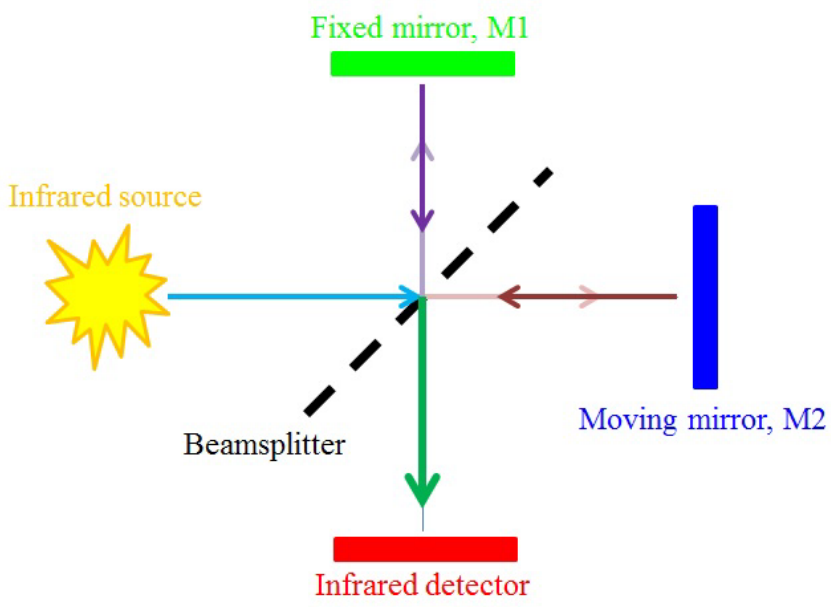


Figure 3.2: Schematic view of a Michelson interferometer

the radiation is transmitted by the beamsplitter and continues to the movable mirror M2. The other half is reflected onto the fixed mirror M1. Both beams return to the beamsplitter where they recombine. Some of the recombined light returns to the source, but the recombined light of interest proceeds to the detector (or through the sample and then to the detector). The movable mirror M2 is in place so that the recombined beams give constructive/destructive interference from the path length difference between to two mirrors M1 and M2. The intensity of the recombined beams $I(x)$ is the interferogram function, and a plot of $I(x)$ as a function of the moving mirror (M2) displacement x is known as an interferogram. [121] If M2 travels at a constant velocity, the relation between the interferogram function $I(x)$ and the source intensity $B(\omega)$ is given by

$$I(x) = \frac{1}{2}\int_0^\infty B(\omega) cos 2\pi\omega dx, \tag{3.51}$$

where ω is the frequency in wavenumbers. $I(x)$ is the cosine Fourier transform of

$B(\omega)$ and contains complete information about the spectrum. [121] This gives the single beam infrared spectrum. The typical transmittance or reflectance spectrum is the ratio spectrum of sample to reference.

3.2.2 Bruker IFS 113v Fourier transform infrared spectrometer

The majority of the far-infrared (21-700 cm^{-1}) and middle infrared (450-5000 cm^{-1}) reflectance and transmittance spectra in this work were obtained by using Bruker IFS 113v Fourier Transform Infrared (FTIR) spectrometer. The spectrometer is divided into four chambers – source, interferometer, sample, and detector. This system operates under vacuum to reduce atmospheric noise. The Si or B-doped Si bolometer, which is cooled with liquid helium, provides extra sensitivity. A schematic view of the beam path and optics are provided in Fig. 3.3.

In order to capture different energy regions most efficiently, the instrument uses a series of sources, detectors, and beamsplitters for optimal resolution and signal. A list of these different parts are listed in Table 3.2.

Table 3.2: Bruker IFS 113v operating parameters

Range (cm^{-1})	Source	Beam splitter	Opt. Filter	Polarizer	Detector
10-50	Hg arc	Mylar 50 μ	Black PE	1	Si bolometer, DTGS
30-120	Hg arc	Mylar 23μ	Black PE	1	Si bolometer, DTGS
50-240	Hg arc	Mylar 12μ	Black PE	1	Si bolometer, DTGS
100-600	Hg arc	Mylar 3.5μ	Black PE	1	Si bolometer, DTGS
450-4000	Globar	KBr	open	2	B-doped Si bolometer, DTGS

PE = polyethylene. Polarizer 1 = wire grid on oriented PE, Polarizer 2 = wire grid on AgBr

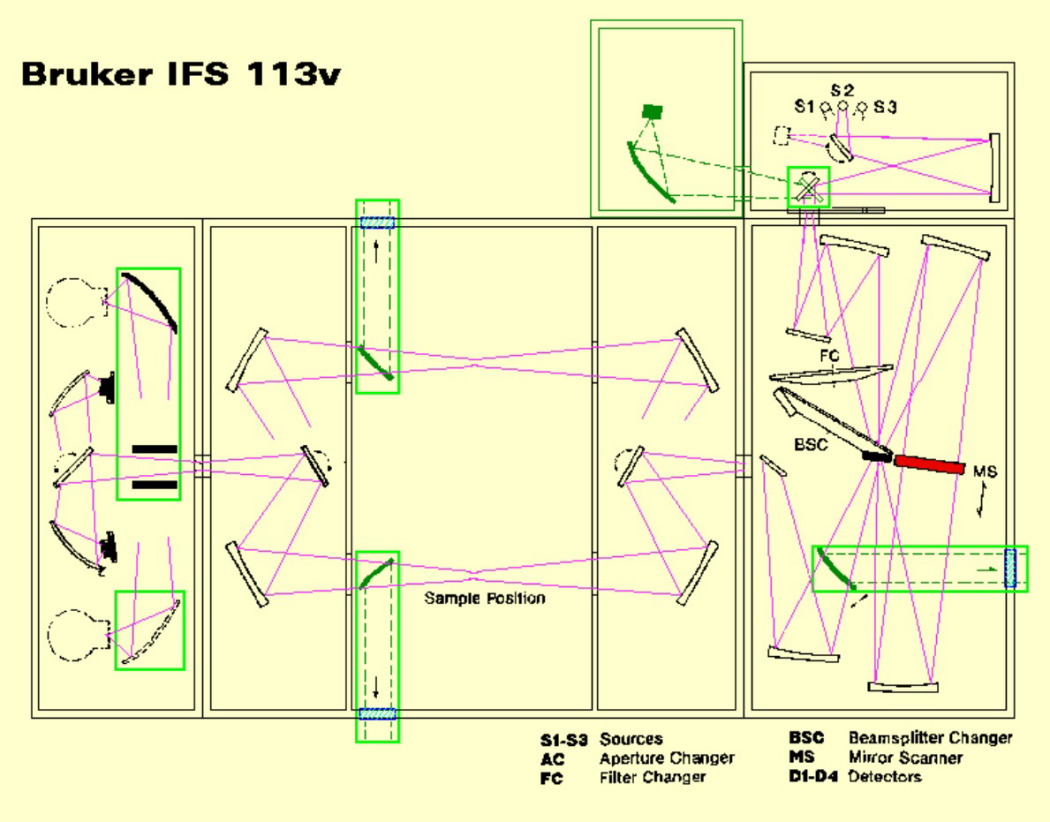


Figure 3.3: Schematic view of the Bruker IFS 113v FTIR spectrometer.

3.2.3 Bruker Equinox 55 FTIR spectrometer with Bruker IR Scope II

This instrument is a combination of a spectrometer with a microscope attachment. The Bruker IR Scope II is designed for accurate measurement of micro samples, or small areas on larger samples. The Bruker Equinox 55 FTIR spectrometer covers the middle infrared through visible region (600-17,000 cm^{-1}). This spectrometer utilizes various combinations of sources, beamsplitters, and detectors to select the region of interest as well, laid out in Table 3.3.

The optical beam path of the spectrometer can be seen in Fig. 3.4.

3.2.4 Perkin Elmer λ-900 grating spectrometer

Another type of spectrometer besides a Fourier-transform spectrometer is one which uses gratings to separate the light. In order to get a specific energy/wavelength of light, a grating is used. An ideal grating is made up of a set of grooves with spacing d. The diffraction grating of a spectrometer determines the wavelength range and partially determines the optical resolution that the spectrometer can achieve. The relationship between the grating spacing and the angles of the incident and diffracted beams of light is known as the grating equation, given by

$$dsin\theta = m\lambda \tag{3.52}$$

Table 3.3: Operating parameters of Bruker IRscope II

Range (cm^{-1})	Source	Beamsplitter	Detector
600-7500	Globar	KBr	MCT
4000-12000 with near-infrared polarizer	Tungsten	Quartz	InSb
9000 -17000 with visible polarizer	Tungsten	Quartz	Si diode

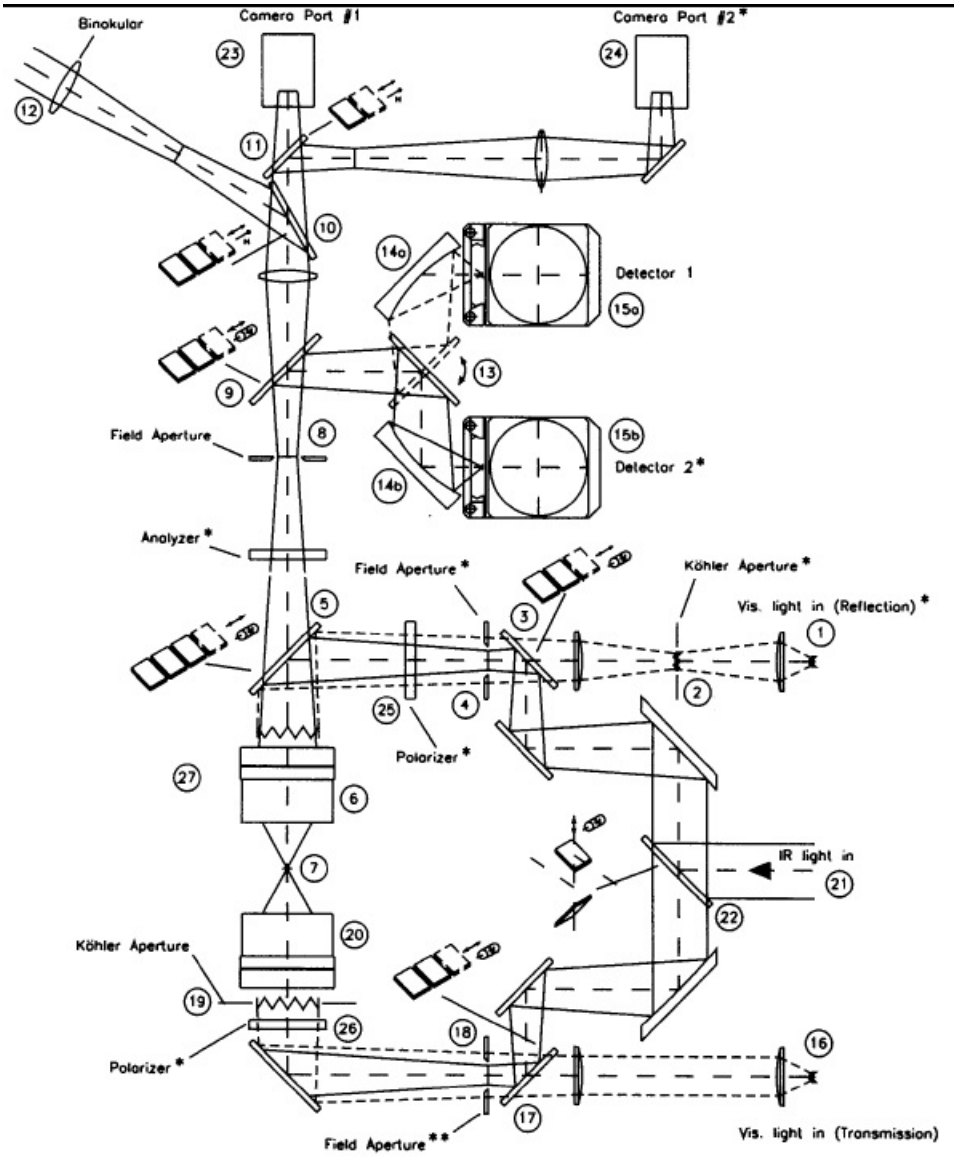


Figure 3.4: Optical path diagram of Bruker IRscope II.
1,16-visible light source; 2,19- visible light aperture; 3,22- motorized switch mirror; 4,18- optional iris or knife edge aperture; 5,9,10,17- beamsplitter changer; 6- Objective lens; 7- Sample; 8- Iris or knife edge aperture which defines the area of sample analyzed; 12- binocular eyepiece; 13- two position detector selection mirror; 14- mirror routing to detector; 15- detector; 20- condenser; 21- IR beam (from spectrometer); 23,24-camera port; 25,26,27- polarizer.

where m is an integer and the order of diffraction, d is the groove spacing, λ is the diffracted wavelength, and θ is the output angle as measured from the surface normal of the grating. [113]

The visible through ultraviolet region can be measured with a Perkin Elmer λ-900 grating spectrometer. This instrument features an all-reflecting, double-grating, double-beam optical system. Source, grating, filter, and detector all change automatically when different energy windows are measured. This spectrometer is operated under nitrogen purging. This instrument also uses a series of sources, polarizers, gratings, and detectors in order to achieve the optical data needed. The optical beam path can be seen in Fig. 3.5 and the different optics with respect to each frequency range can be seen in Table 3.4.

3.3 Spectroscopy under extreme conditions

In order to probe different phase transitions, we apply different external stimuli with our spectroscopic techniques to observe the optical response under these extreme conditions. Two examples relevant to this dissertation are variable temperature and an applied high magnetic field.

Table 3.4: λ-900 operating parameters

Range (cm^{-1})	Source	Grating	Polarizer	Detector
3100-14250	Halogen Lamp	1200 lines/mm	Glan-Thompson prism	PbS
11240-31330	Halogen Lamp	1200 lines/mm	Glan-Thompson prism	Photomultiplier
31330-52000	Deuterium Lamp	2400 lines/mm	Glan-Taylor prism	Photomultiplier

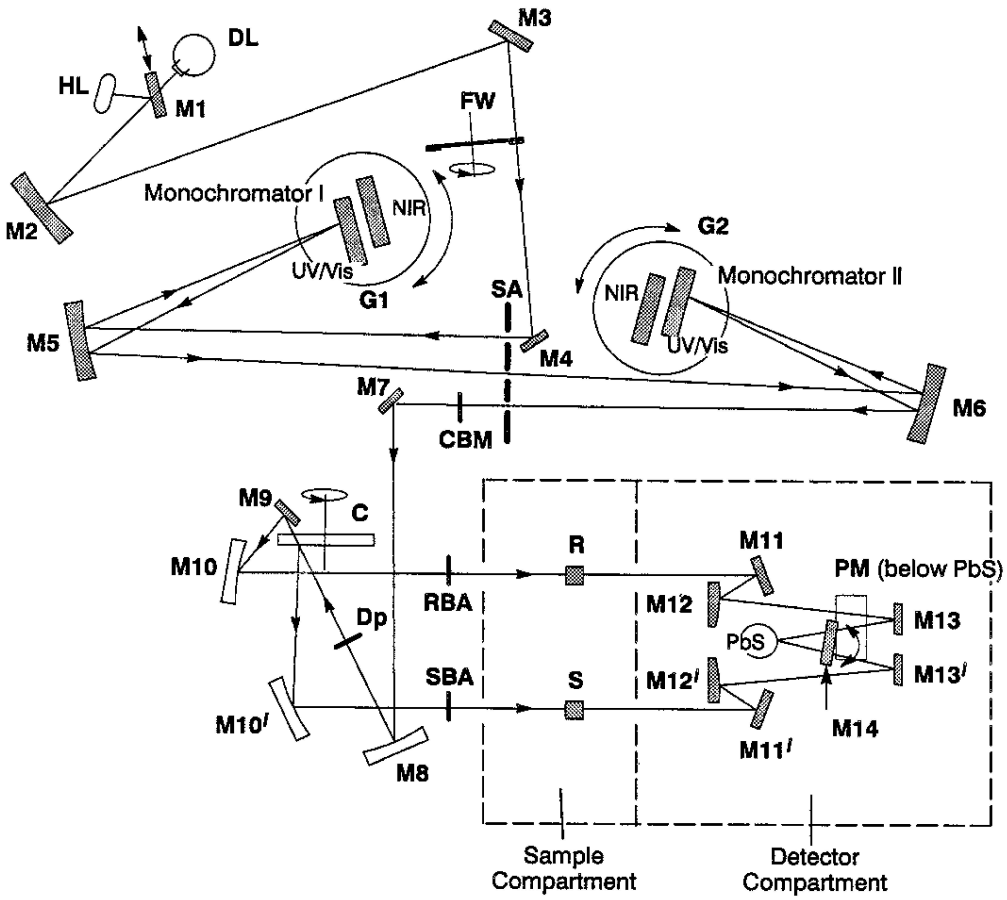


Figure 3.5: Optical layout of Perkin-Elmer λ-900

3.3.1 Variable temperature spectroscopy

The low-temperature measurements were carried out with an open-flow cryostat. The low-temperature experiments with the Bruker IFS 113v and Perkin-Elmer λ-900 are performed in combination with an APD LT-3-110 Heli-Tran cryostat system with dual temperature sensors and a Lakeshore Model 330 temperature controller. Measurements with the Bruker Equinox 55 are made with Oxford Instruments Microstat^{He}. Figure 3.6 shows the complete setup of the system for variable temperature measurements.

In order for helium flow to begin, there must be elevated pressure in the helium dewar. The helium flows through a high efficiency transfer line to the cryostat and a heat exchanger adjacent to the sample interface. The system must precool before helium flow will begin, which often takes 20-25 minutes. The lowest stable temperature is $\sim$5 K. After cooling the sample, the liquid helium evaporates and the gas is distributed in two ways: through the helium exhaust port on the side of the cryostat and back through the transfer line with exit at the shield outlet port. The additional shield/return flow helps to keep the transfer line cold. The base of the cryostat is also equipped with a heater to prevent ice buildup and vacuum seal freezing. Cooling rates can be regulated in several different ways: (i) changing and maintaining pressure in the supply dewar, (ii) adjusting the flowmeter (attached to the helium exhaust port and the shield gas outlet), and (iii) adjusting the knob that controls the position of the needle valve at the end of the transfer line. Samples are mounted with GE varnish, rubber cement, and silver paste. Crycon grease is placed between the cold stage of the cryostat and the sample holder to improve thermal contact. The sample is then mounted on the heat exchanger/sample holder, under vacuum, and optical access is achieved through appropriate windows (depending on the frequency/energy/wavelength of light that is being worked with). Two different

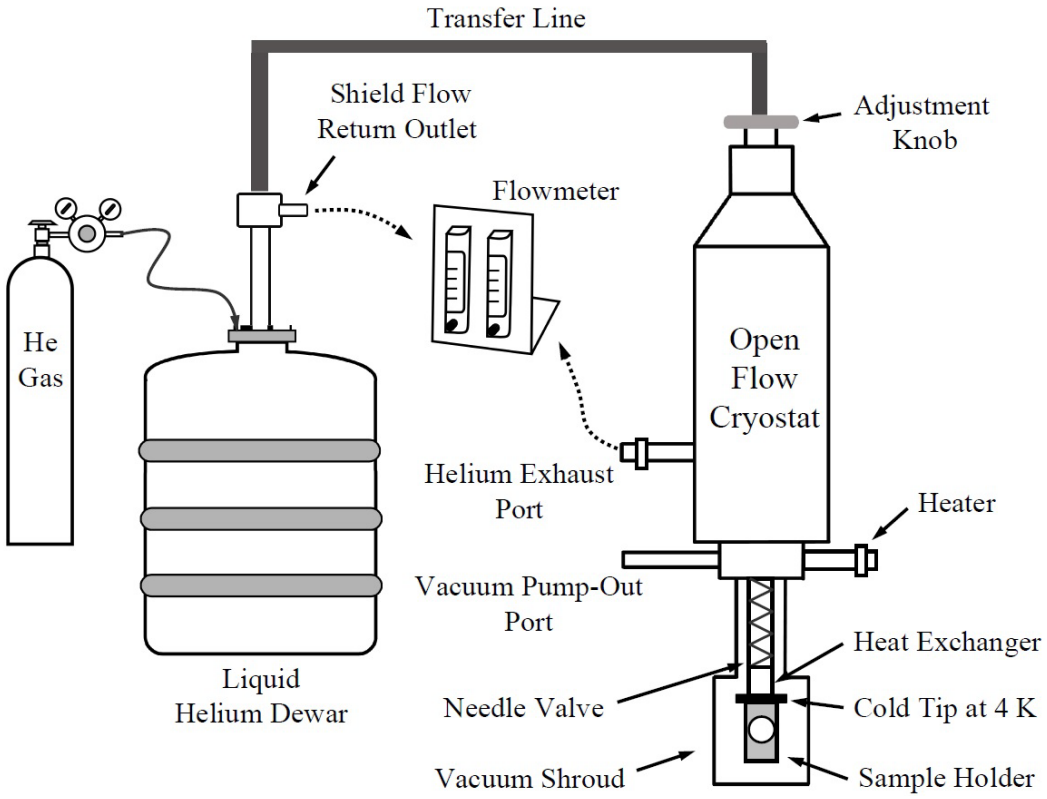


Figure 3.6: Set-up of LT-3-110 Heli-Tran liquid transfer line and cryostat.

thermal sensors are available. One is embedded in the tip of the cold stage and the other is mounted onto the sample holder. This gives a good estimation of the real temperature of the sample.

3.3.2 Applied high magnetic field spectroscopy

The National High Magnetic Field Laboratory (NHMFL) offers a great opportunity to do spectroscopic studies under an applied magnetic field. Different types of magnets are built and used at the NHMFL, including superconducting, resistive, hybrid, and pulsed magnets, as shown in Fig. 3.7. These magnets and the facilities at the NHMFL allow the possibility of measuring and investigating the spectroscopic response in very high magnetic fields. This dissertation will use two different types of magnets from Fig. 3.7 (resistive and pulsed). For more information, visit the NHMFL website at *http://www.nhmfl.gov*.

In all of these type of experiments, it is important to notice several different things. First, the sample here is mounted on an optical probe inside a vacuum jacket. The vacuum jacket is then slightly filled with He exchange gas in order to achieve base temperature. The jacket and probe with the sample are then immersed in a

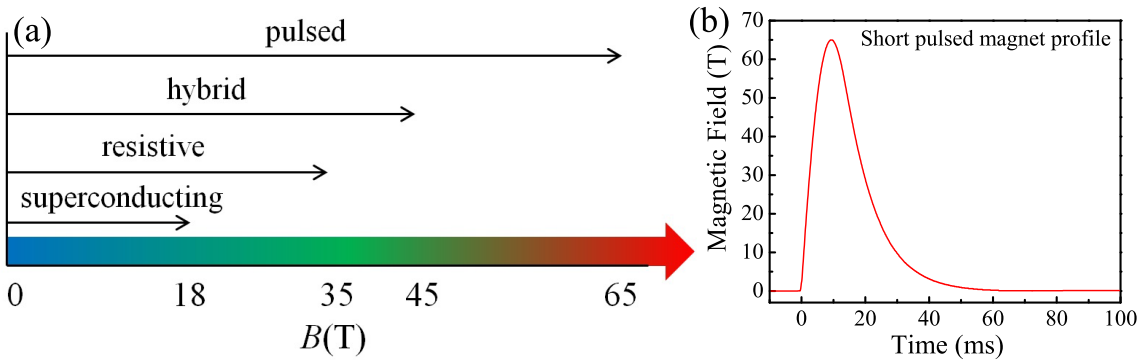


Figure 3.7: (a) A schematic energy scale of various magnets (superconducting, resistive, hybrid, and pulsed magnets) at NHMFL. (b) Magnetic field profile of the short pulsed magnet at NHMFL-LANL.

helium bath for the 4 K measurements. In optical measurements, the temperature can be varied up to around 100 K. In infrared measurements, the experiments must be done at 4 K as the detector (bolometer) must be used at the lowest temperatures. Another important issue is that the sample placement, probe, and vacuum jacket must be measured to be placed directly in the center of the magnetic field.

For magneto-optical experiments, both a steady-field resistive magnet and a pulsed-field magnet were used. The resistive magnet is at the magnet lab in Tallahassee, FL. while the pulsed field experiments were done in Los Alamos, NM. Figure 3.8(a) shows the schematic of the optical set-up for transmittance measurements in the 35 T resistive magnet at the National High Magnetic Field Lab in Tallahassee, FL. For the measurement in the near-infrared, visible, and ultraviolet range, a MacPherson 0.75m single grating monochrometer/spectrometer with a charge coupled device (CCD) or InGaAs detector is used to cover the energy range from 300-1600 nm (0.77-4.13 eV). The light beam is transferred in and out of the probe by red (370-2000 nm) or blue (300-700 nm) optical fibers. Depending on the desired wavelength range and resolution, a series of gratings (150 g/mm, 300 g/mm, 600 g/mm, 1200 g/mm, and 1800 g/mm) can be used. 150 g/mm grating gives the highest light intensity and the broadest coverage but the lowest resolution.

The setup at the National High Magnetic Field Laboratory in Los Alamos, NM is very similar to the setup in Tallahassee. Magneto-optical spectroscopy was performed in the Faraday geometry at cryogenic temperatures (4.0 K) in a capacitor-driven 65 T pulsed magnet at the National High Magnetic Field Laboratory in Los Alamos, New Mexico. Our focus was on the 0.75 - 2.6 eV range with 2.4 meV resolution. Broadband light from a tungsten lamp was coupled to optical fibers and focused onto the sample for transmittance experiments. A collection fiber brought the light from the top of the probe to the grating spectrometer, where both charge-coupled device

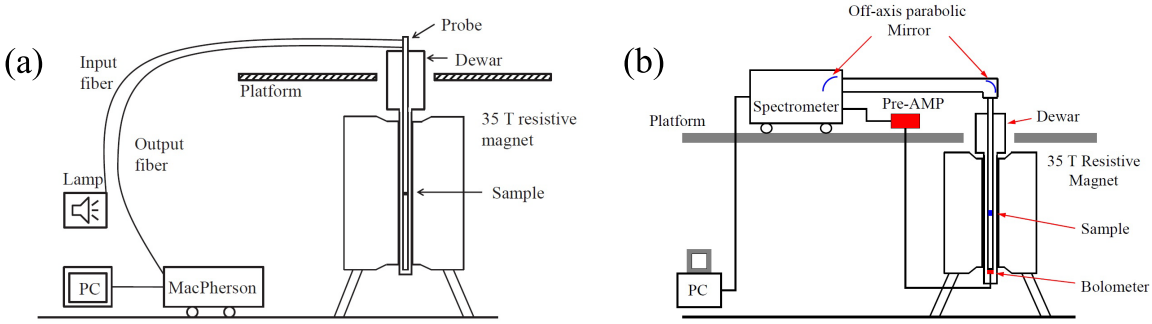


Figure 3.8: (a) Schematic of the magneto-optical set-up at the NHMFL. (b) Schematic of the magneto-infrared set-up at the NHMFL

and InGaAs detectors were employed as appropriate.

Figure 3.8(b) shows a schematic representation of the magneto-infrared set-up for the 35 T resistive magnet. The emitted radiation from the IR spectrometer is directed out of the instrument towards the light pipe by an off-axis parabolic mirror. A second mirror in the light pipe, located just above the probe, further diverts the beam by 90° and sends it onto the sample located in the center of the magnet. After light passes through the sample, it is collected by a bolometer inside the probe and transformed into an electrical signal. The signal is further amplified, electronically filtered, and sent back to the spectrometer to be processed by a computer.

3.4 Materials of interest: sample preparation, measurements, and complementary calculations

3.4.1 Ni_3TeO_6

High quality single crystals and polycrystals were grown using a chemical vapour transport method at 700°C for 4 days, followed by furnace cooling. [28] The crystals show only a few distinct features in regards to orienting them. The *ab*-plane intrinsically grows exposing an equilateral triangle on either side of the crystal. Once that

face is determined, the sample can be mounted according to which direction we want to measure. Since the material is highly absorbing in some regions, the sample has to be polished down by hand to approximately 28 μm. The crystal polishing process is shown in Fig. 3.9.

In order to measure Ni_3TeO_6 for a nonreciprocal response, the sample had to be polished thin enough for light transmittance, the same as for optical measurements. However, here, an additional test had to be done. As discussed earlier, nonreciprocal effects can manifest within a chiral and magnetic material. Ni_3TeO_6 is magnetic below 53 K, but it is also chiral. Each sample is different with how the chirality exists. Chiral domains can be present in the sample. For a nonreciprocal response, the sample must have a net chirality. After polishing the sample, transmittance tests on an optical microscope using a polarizer and analyzer proved that the polished sample was prominently single domain, as can be seen in Fig. 3.10.

Optical measurements were performed as a function of temperature in the *ab*-plane and along the *c*-direction using a series of spectrometers (0.4-3.0 eV; 4.2-300 K). Absorption was calculated as $\alpha(E) = -(1/d)\ln T(E)$, where $T(E)$ is the transmittance and d is the sample thickness. Magneto-optical measurements were carried out at the National High Magnetic Field Laboratory in Tallahassee, Florida

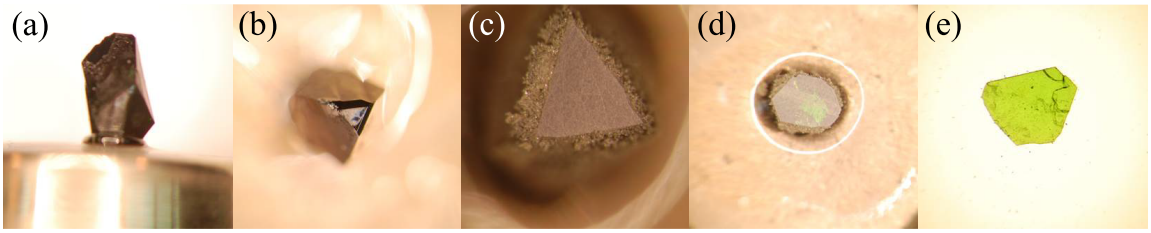


Figure 3.9: The image displays the polishing process of the crystal. (a) Displays the mounted crystal on the polishing puck. (b) Displays the *ab*-plane equilateral triangle exposed and ready to be polished and thinned. (c,d) Shows the same crystal at different times during the polishing process. (e) Shows the resulting crystal thinned and polished down to 28 μm.

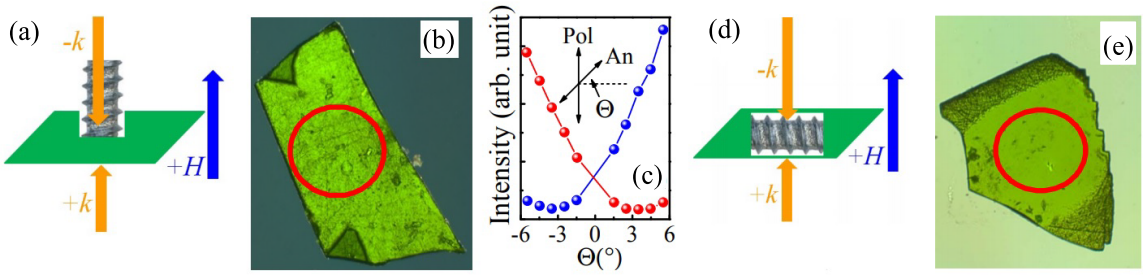


Figure 3.10: (a,d) Depicts how the measurements were performed with respect to the chiral axis in Ni_3TeO_6. (b,e) Shows crossed polarizer images of the crystals, where lighter and darker green regions indicate different chiral domains. The red circles in these images indicate the area of measurement. (c) Intensity signal of the light throughput of the crystal in (b) under crossed polarizer and analyzer images.

(4.2 K, 0 - 35 T) using a resistive magnet and in Los Alamos, New Mexico (4 K, 0 - 65 T) using a pulsed field magnet. Spectra were taken in four different measurement configurations in the Faraday configuration: ($+H$, up k), ($-H$, up k), ($+H$, down k), and ($-H$, down k). Each run was carried out sequentially and consistently, starting with one k direction (and pulsing to obtained both $\pm H$) and then switching to the other k direction (again measuring both H directions). To switch k, we swapped the optical fibers from the source to the detector and vice versa. We can also The first-principles calculations were performed using the Elk full-potential code using linearized augmented plane-wave basis [122], LDA+U in the fully localized limit [123] with Slater parameters $F^{(0)} = 8.0$ eV, $F^{(2)} = 8.18$ eV, $F^{(4)} = 5.11$ eV [124], and the Perdew-Wang/Ceperley-Alder exchange-correlation functional [125]. The 20-atom rhombohedral magnetic unit cell with the $\uparrow\uparrow\downarrow\downarrow\downarrow\uparrow$ magnetic ordering was used in the calculations, and a $4\times4\times4$ k-point grid was employed for reciprocal-space sampling.

For the infrared spectrum, reflectance measurements were performed using a series of spectrometers in the ab-plane and along the c-axis between 5 and 300 K. A Kramers-Kronig analysis was used to obtain the optical constants. Magneto-infrared experiments employed a polycrystalline sample in either a polyethylene or KBr matrix and a resistive magnet at the National High Magnetic Field Lab-

oratory (100-3000 cm^{-1}; 4.2 K; 0-35 T). The absorption $\alpha(\omega)$ was calculated as $\alpha(\omega) = -\frac{1}{hd} ln(T(\omega))$, where $T(\omega)$ is the measured transmittance, h is the loading, and d is the effective thickness. Absorption differences were also calculated in order to highlight small field-induced changes. Here, $\Delta\alpha = \alpha(\omega, H) - \alpha(\omega, H = 0)$. Standard peak fitting techniques were employed as appropriate. Phonon frequencies were computed using frozen-phonon method as implemented in phonopy and VASP software packages. [126–131] Calculations used generalized gradient approximation within projector-augmented wave formalism [132], plane wave cutoff of 500 eV, 4×4×4 Γ-centered k-point grid, up-up-down spin ordering in a 1×1×1 rhombohedral unit cell. Using a 1×1×2 unit cell where spin exchanges are not frustrated is computationally more expensive, and magnetic field-induced phonon frequency shifts are much smaller than the frequencies themselves, so that a 1×1×1 rhombohedral unit cell seems appropriate for phonon assignment purposes.

3.4.2 $EuTiO_3$ and Nb-substituted analogs

Polycrystalline samples of $EuTi_{1-x}Nb_xO_3$ were grown via a standard solid state reaction method. [111] Stoichiometric mixtures of high-purity (at least 99.99%) starting materials were mixed and ground in an agate mortar and pressed into pellets. The pressed pellets were sintered in a MTI tube furnace with flowing 90:10 Ar:H_2 atmosphere at around 1300-1400°C with intermediate grindings.

High quality single crystals of $EuTi_{1-x}Nb_xO_3$ (x=0, 0.015, 0.03, 0.05, 0.1, and 0.2) were grown by the floating zone technique in an infrared-heated image furnace equipped with two 1500 W lamps and double ellipsoidal mirrors. The pulling speed was 10 mm/h with feed and seed rods rotating in opposite directions at 25 rpm. [42] Crystal quality was confirmed by clear, round spots in the Laue back-scattering pattern. Single crystals were cut into rectangular parallelpipeds with all faces perpen-

dicular to the a-axis. Resonant ultrasound spectroscopic techniques were employed to determine the complete elastic tensor of a small single crystal. [133]

Room and low temperature x-ray diffraction was performed with a laboratory Huber imaging plate Guinier camera 670 with Ge monochromatized $CuK_{\alpha 1}$ radiation, confirming all single crystals to be single phase. Magnetization experiments were performed using a Quantum Design magnetic property measurement system in the temperature interval 2 - 300 K. Electrical resistivity measurements were performed on dense cold-pressed samples by means of a four-probe method in a PPMS between 3 - 300 K. [42, 111]

For our spectroscopic measurements, we measured the ab-plane reflectance of this series of materials over a wide energy range (2 meV - 6 eV) using a series of different spectrometers. The resolution was between 2 and 8 cm^{-1}, depending on the range. The optical constants were obtained from a Kramers-Kronig analysis of the measured reflectance. [112] An open flow cryostat was used to control temperature, and traditional peak fitting techniques were employed as appropriate.

Chapter 4

Magnetoelectric coupling through the magnetic transitions in Ni_3TeO_6

We combined high field optical spectroscopy and first principles calculations to analyze the electronic structure of Ni_3TeO_6 across the 53 K, 9 T, and 52 T magnetic transitions, all of which are accompanied by large changes in electric polarization. The color properties are sensitive to magnetic order due to field-induced changes in the crystal field environment, with those around Ni1 and Ni2 most affected. These findings advance the understanding of magnetoelectric coupling in materials in which magnetic $3d$ centers coexist with non-magnetic heavy chalcogenide cations.

4.1 Electronic structure of Ni_3TeO_6

Figure 4.1 displays the absorption of Ni_3TeO_6 in the *ab*-plane and *c*-direction at 300 and 4.2 K. We clearly observe two broad bands below 2 eV. Focusing first on the *ab*-plane data, we find color band excitations near 1.0, 1.55, and 1.72 eV. Each appears

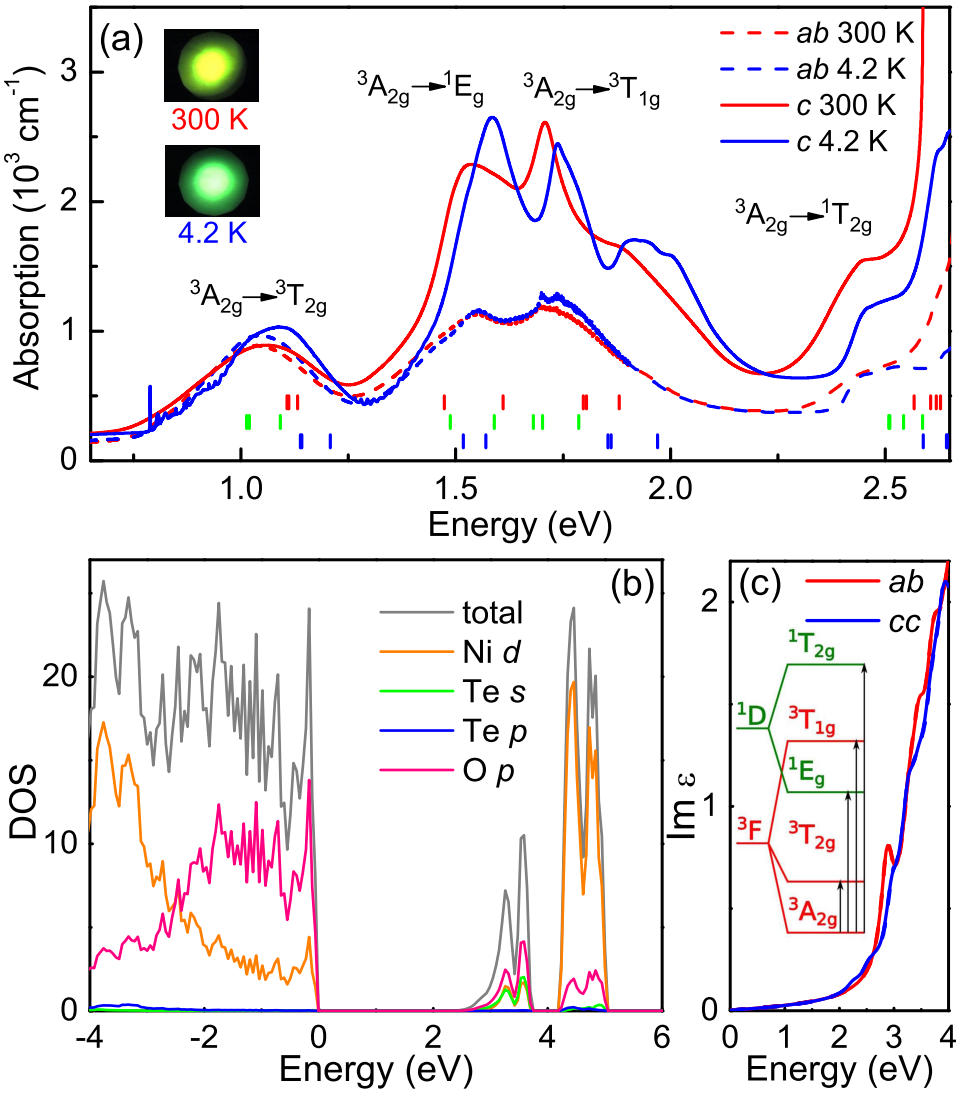


Figure 4.1: (Color online) (a) Absorption coefficient of Ni_3TeO_6, $\alpha(E)$, in the *ab*-plane and the *c*-direction at 300 and 4.2 K. Vertical lines near the bottom mark the computed *d*-to-*d* excitations for the d^8 Ni ions, with red, green, and blue indicating excitations on Ni1, Ni2, and Ni3 sites, respectively. The insets show photographs of the crystal along *c*. (b) Ion-projected density of states per magnetic unit cell obtained from DFT and (c) components of linear optical dielectric response tensor calculated within the random phase approximation in the $q \rightarrow 0$ limit with no microscopic contributions (solid lines: with spin-orbit coupling included; dashed: without). The splitting of free Ni ion d^8 multiplets in the presence of an octahedral crystal field and the crystal field excitations between these levels is shown in the inset.

with significant oscillator strength due to non-centrosymmetric local environments around each of the Ni sites. Combined with the absorption minimum near 2.25 eV and small shoulder at 2.5 eV, these features are responsible for the striking green color of the crystal. The absorption rises sharply above 2.6 eV, suggesting the start of strong interband transitions.

A Tanabe-Sugano diagram provides a useful framework with which to reveal the nature of on-site d-to-d excitations in transition metal-containing materials. The diagram for a d^8 electron configuration (for Ni^{2+}) is shown in Fig. 4.2(a). The strength of the crystal field is, of course, given by Dq/B. The red vertical line indicates a best fit of the crystal field strength for Ni_3TeO_6. Taking a closer look, the lowest energy excitations (at that value of Dq/B) are expected to be $^3A_2 \rightarrow {}^3T_2$, $^3A_2 \rightarrow {}^1E$, and $^3A_2 \rightarrow {}^3T_1$. Here, $^3A_2$ is the ground state. Figure 4.2(b) shows a close-up view of the same diagram, rotated by 90° for comparison with the measured absorption spectrum of Ni_3TeO_6. Each excitation in the absorption matches with predicted excitations from the Tanabe-Sugano diagram. This indicates that the peaks seen the absorption spectrum of Ni_3TeO_6 should be assigned as on-site d-to-d excitations. This very general framework for Ni^{2+}-containing materials is extended by our more detailed calculations (described below) which account for the subtly different environments of Ni1, Ni2, and Ni3.

To further test whether the lower-energy peaks might arise from interband transitions, we calculated the Kohn-Sham band structure at the LDA+U level for Ni_3TeO_6 in the zero-temperature antiferromagnetic configuration. The results are shown in Fig. 4.1, and where comparable, they are in excellent agreement with Ref. 134. The gap, clearly visible in the density of states plot in Fig. 4.1(c), is determined to be 2.2 eV, which rules out any interband transitions below 2 eV. To drive this point home, the components of LDA+U optical dielectric response tensor calculated

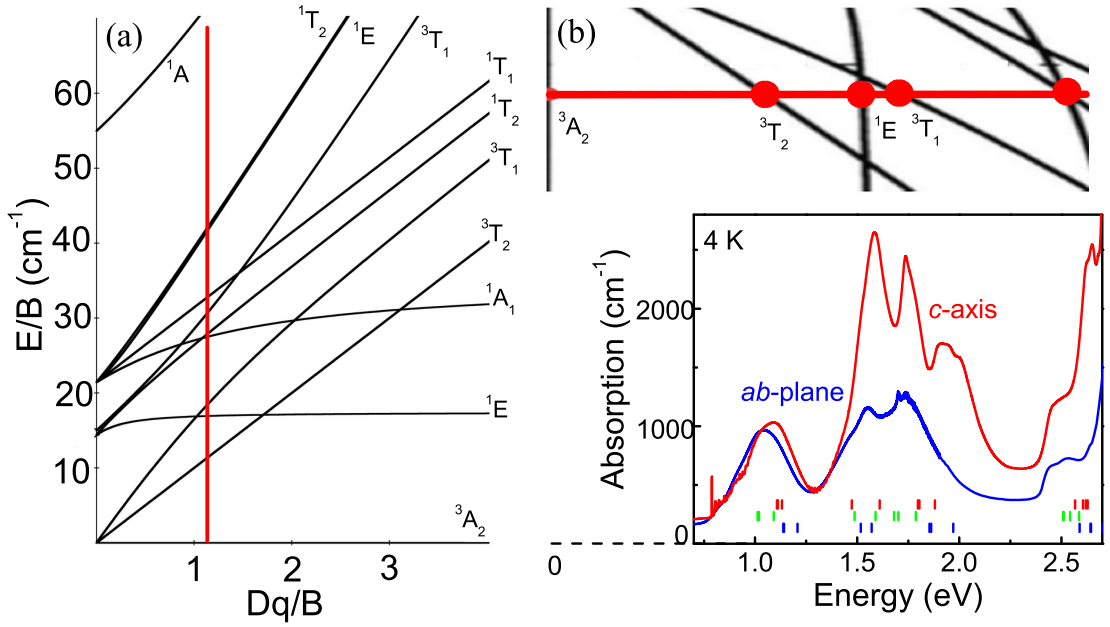


Figure 4.2: (a) Tanabe-Sugano diagram for a Ni^{2+} center in the d^8 configuration. The crystal field strength of Ni_3TeO_6 is shown in red. (b) Here, the Tanabe-Sugano diagram is turned on its side and paired with the absorption spectrum along the *ab*-plane and *c*-axis. The calculated Ni *d*-to-*d* excitations for each of the three distinct Ni centers are displayed as red, green, and blue hash marks. Expectations from the Tanabe-Sugano diagram and the theoretically predicted excitations align very well with our experimental observations.

within the random phase approximation in the $q \to 0$ limit are plotted in Fig. 4.1(d). The interband transitions naturally account for the sharply rising absorption near 2.6 eV (Fig. 4.1(a)). They are dominated by excitations from hybridized O p and majority Ni e_g states at the top of the valence band to Te s and minority Ni e_g conduction bands. We therefore assign the features below 2 eV to on-site Ni d-to-d excitations, an assignment that is strengthened by the resemblance to $Ni_3V_2O_8$, [59] where similar d-to-d transitions occur and where the charge-transfer gap of 2.4 eV is only slightly smaller than ours. We shall give further theoretical support for this assignment shortly.

As noted above, we have assigned the color-band excitations below 2.5 eV to on-site d-to-d transitions, which are not expected to appear in a single-particle framework such as DFT+U. To confirm this assignment, we turn to a crystal field model. The Coulomb interactions for a spherically symmetric d^8 ion give rise to the ground state ${}^3F$. These are correlated states that generally cannot be represented as a single Slater determinant. In particular, the state with the largest orbital moment, 2^+2^-, where both holes in the d shell have $m_l = 2$ and opposite spins (indicated by superscripts "+" and "−"), is a single Slater determinant. Instead, the state obtained by applying the angular momentum lowering operator L^-, and thus belonging to the same multiplet, is made up of the microstates 2^+1^- and 2^-1^+, and so is not a single-determinant state. [135, 136] The next multiplet is ${}^1D$, followed by ${}^3P$, ${}^1G$, and ${}^1S$ states. In the (approximately) octahedral crystal field of the oxygen cage surrounding the Ni ions, the lowest multiplet splits as ${}^3F \to \Gamma_2 = {}^3A_{2g}$ ($E = -12Dq$), $\Gamma_5 = {}^3T_{2g}$ ($E = -2Dq$), and $\Gamma_4 = {}^3T_{1g}$ ($E = 6Dq$), where $10Dq$ corresponds to the splitting of a single d-level that would be produced by the same octahedral crystal field. The next lowest multiplet splits as ${}^1D \to \Gamma_3 = {}^1E_g$ ($E = 5F_2 + 45F_4 - \frac{24}{7}Dq$) and ${}^1T_{2g}$ ($E = 5F_2 + 45F_4 + \frac{16}{7}Dq$). These splittings are shown schematically in Fig. 4.1(b),

where the vertical black arrows indicate the optical excitations of interest.

In order to estimate the d-to-d transition energies, we performed exact diagonalization of an atomic Hamiltonian in the d^8 sector for each of the three inequivalent Ni sites. The Hamiltonian included the Hund's exchange energy, $J_H = 0.9$ eV, and the orbital energies in the crystal field, approximated by the energies of Wannier functions obtained from the DFT calculations for each of the three Ni ions. The vertical marks in Fig. 4.1(a) show that these predicted excitation energies coincide well with the peaks observed in our experiment. The excitations near 1.0, 1.55, 1.72, and above 2.5 eV are therefore associated with transitions to the Γ_5, Γ_3, Γ_4, and Γ_5 multiplets, respectively. This confirms the interpretation of the absorption bands below 2 eV as resulting from d-to-d transitions. The assignment also clarifies that the shoulder near 2.5 eV is related to on-site excitations and not yet the beginning of the interband transitions. This framework and the position of the spectral peaks allow us to estimate that Dq and the Racah parameter B are both (coincidentally) equal to 0.11 eV, consistent with expectations for a Ni^{2+} complex. [137]

The density of states and RPA susceptibility were calculated using the Elk code and LDA+U approximation with $U = 4$ eV on Ni d orbitals [Fig. 4.3]. In order to estimate the d-to-d transition energies we have used the Wien2K-DMFT code by Kristjan Haule to calculate the Wannier functions within the energy window spanning only the $3d$ Ni orbitals. The dynamic crystal field produced by oxygens in DMFT is then replaced by the static crystal field, encoded in the Wannier orbital energies. The on-site Hamiltonians (using $J_H = 0.9$ eV) in the basis of these Wannier functions were diagonalized independently for the three Ni sites and the distances between the ground and excited states were used to approximate the d-to-d transition energies. These energies are marked by red, green, and blue vertical bands in Fig. 4.1(a). The calculated excitations for Ni1, Ni2, and Ni3 group into band clusters

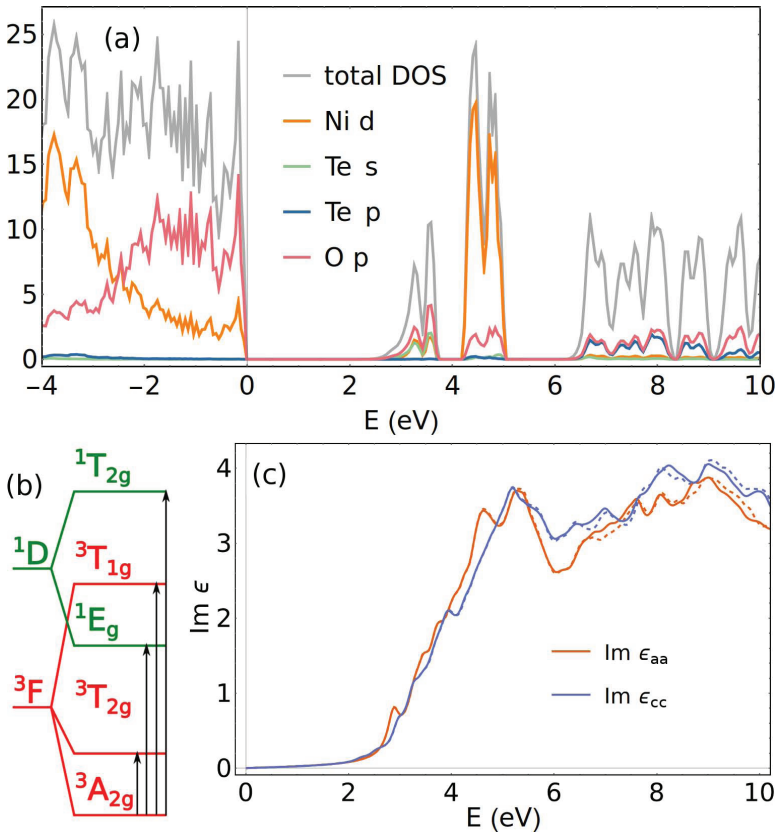


Figure 4.3: (Color online) Results of DFT calculations on Ni_3TeO_6: (a) ion-projected density of states per magnetic unit cell, (b) splitting of free Ni ion d^8 multiplets in the presence of an octahedral crystal field and the crystal field excitations between these levels, and (c) components of linear optical dielectric response tensor calculated within the random phase approximation in the $q \to 0$ limit with no microscopic contributions (solid lines: with spin-orbit coupling included; dashed: without).

that are located in the general vicinity of the d-to-d transitions identified from the much simpler Tanabe-Sugano model discussed above.

Returning to the experimental data and focusing now on comparing the c-axis response of Ni_3TeO_6 with the in-plane spectra (Fig. 4.1(a)), we immediately notice that while the intensities of the 1.2 eV peaks are similar, there is a large anisotropy between 1.5 and 2.2 eV, with the absorption being much stronger along c ($\approx$2500 cm^{-1}) than in the ab plane ($\approx$1300 cm^{-1}). Temperature effects are also more interesting in this direction, with the 4.2 K data showing (i) an overall hardening of the excitations, (ii) an intensity increase near 1.9 eV, and (iii) fine structure on the leading edge of the 1.1 eV band that may correspond to phonon side bands [18]. Examination of the 1.9 eV excitation reveals that the peak shape is a strong function of temperature. The additional orange light absorption at 4.2 K causes Ni_3TeO_6 to appear more green to the naked eye (inset, Fig. 4.1(a)).

Along with the field induced changes across the spin flop transition, we also tested whether the electronic properties of Ni_3TeO_6 were sensitive to the 53 K magnetic ordering transition. Figure 4.4 shows absorption difference spectra as a function of temperature at fixed field. No distinctive changes are observed across the Neél transition. In other words, the temperature dependence in this range is very systematic. [93]

4.2 Magneto-optics on Ni_3TeO_6 through the spin-flop transition

We now turn to the optical response in applied field. Figures 4.5(a) and (b) summarize the magneto-optical properties of Ni_3TeO_6 in the ab-plane ($B \parallel c$) and in the c-direction ($B \perp c$) at 4.2 K. The data are displayed as a set of absorption difference

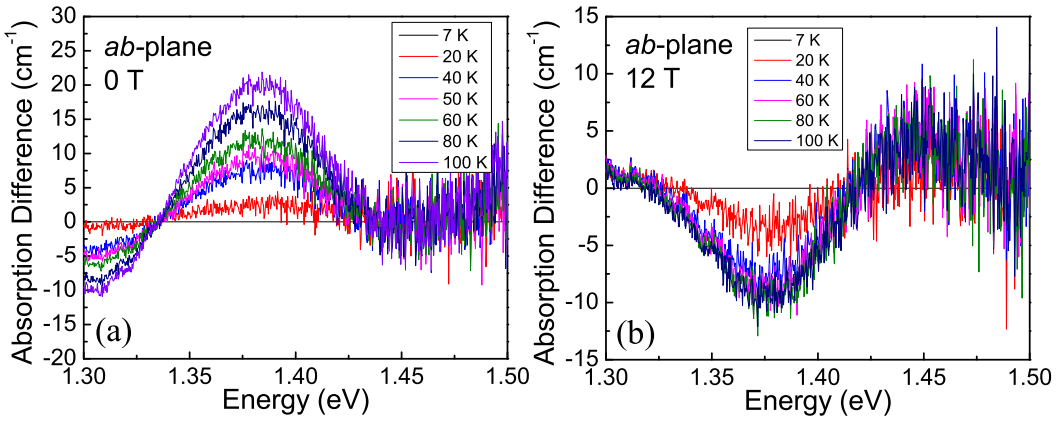


Figure 4.4: Variable temperature absorption difference, $\Delta\alpha$ = [$\alpha(E, T)$ - $\alpha(E, T =$ 7 K)], at (a) 0 T and (b) 12 T.

spectra, $\Delta\alpha(E, B) = \alpha(E, B) - \alpha(E, B = 0)$, for selected fields ranging from 4 to 35 T. The zero-field linear absorption $\alpha(E)$ is also shown at the bottom of panel (a) for reference. In general, the contrast increases with field, although the peak near 1.4 eV (related to changes in $^3\mathrm{A}_{2g} \rightarrow {}^1\mathrm{E}_g$ excitations) is an exception.

Figure 4.5(b) brings together the full field absorption difference spectra, $\Delta\alpha(E, B) =$ $\alpha(E, B = 35$ T) - $\alpha(E, B = 0$ T), with the theoretical locations of the three different sets of d-to-d transitions indicated at the bottom as in Fig. 4.1. Comparison of these spectra with the predicted crystal-field excitations verifies that the observed features are due to field-induced changes in the Ni d-to-d excitations.

Inspection of Fig. 4.5(c) reveals that the ab-plane absorption difference spectra ($B \parallel c$) display a sharp discontinuity across the 9 T spin flop transition. This discontinuity is not seen in the c-axis data of Fig. 4.5(d), which is not surprising since these were taken with $B \perp c$ where the spin-flop transition does not occur. Figure 4.5(e) quantifies these trends by plotting the absorption difference, integrated over an energy window near 1.4 eV, as a function of magnetic field. The ab-plane response to the magnetic field ($B \parallel c$) displays a sharp jump across the 9 T transition,

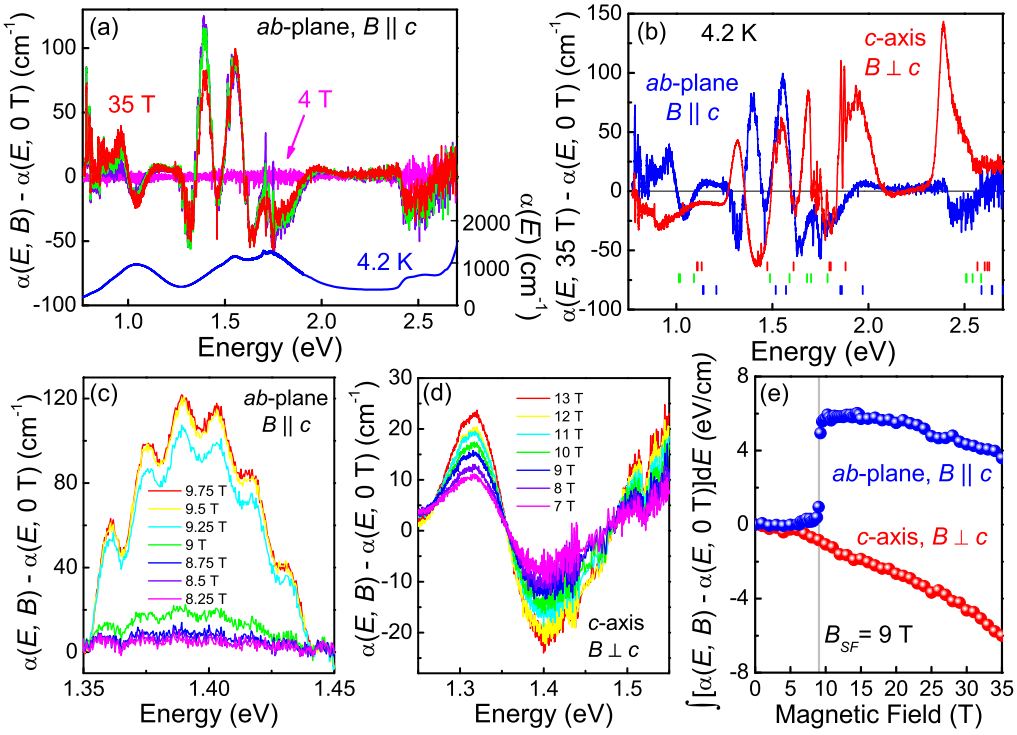


Figure 4.5: (Color online) Absorption difference spectra, $\Delta\alpha$ = [$\alpha(E,\ B)$ - $\alpha(E,\ B = 0$ T)], of Ni_3TeO_6 in the (a) *ab*-plane for $B \parallel c$ at selected fields up to 35 T: (pink 4 T, purple 10 T, green 20 T, red 35 T). The 4.2 K absolute absorption spectrum is included for comparison (on the bottom, in blue). (b) Full field (35 T) absorption difference spectra taken in the *ab*-plane and along the *c*-direction. Red, green, and blue vertical lines indicate the predicted *d*-to-*d* excitations. (c,d) Absorption difference spectra in the *ab*-plane ($B \parallel c$) and *c*-direction ($B \perp c$) at selected fields around the spin-flop transition. (e) Integrated absorption difference of the data in panels (c) and (d).

along with precursor effects (both below and above the spin-flop transition) and no hysteresis (not shown). This indicates that the electronic properties are sensitive to changes in the microscopic spin pattern - a direct consequence of spin-charge coupling and analogous to the dielectric response. [28] By contrast, in the absence of a spin-flop transition, the c-axis response ($B \perp c$) shows only a gradual decrease in the integrated $\Delta\alpha$ with no distinguishing characteristics.

Another interesting aspect of the magneto-optical response is that $\Delta\alpha$ has not saturated by 35 T, suggesting that higher fields are likely to uncover new magnetic phases. Recent magnetization and magneto-infrared experiments do in fact reveal the possibility of an unexplored transition between 30 and 35 T as well as metamagnetic transitions at 52 and 70 T for $B \parallel c$ [18, 29].

The full field absorption compared to the 0 T absorption is shown in Fig. 4.6(a,b) for the ab-plane and c-direction, respectively. A close-up view of the color bands of Ni_3TeO_6 (Figs. 4.7,4.8) along with an analysis of the local structure [92, 138] unveils the role of each of the three distinct Ni ions. The Ni3 centers, for instance, have a relatively irregular environment and strong crystal field associated with their face-shared proximity to the unusual Te^{6+} cations As expected, this distorted environment correlates with the appearance of d-to-d transitions (blue vertical lines) on the high-energy side of each cluster of predicted excitations. This is precisely the range with little or no magneto-optical response. By contrast, the Ni2 ions have the least distorted environment and weakest crystal field, and their predicted on-site excitations (green lines) are at lower energies compared to those of the other two Ni centers. Since absorption difference structures always appear on the leading edge of each band - both in the ab-plane and along c - we can conclude that Ni2 ions are involved. The same is true for the Ni1-related features, which are predicted to be in the middle. We therefore surmise that electronic structure changes through

the spin flop transition derive from field-induced modifications to the crystal field environment of Ni1 and Ni2 (and associated adaptations in hybridization). Recent calculations support the dominant contribution of Ni1$\cdots$Ni2 interactions to the magnetic properties [134] and magnetically-induced electric polarization [29].

Figure 4.6 shows the absorption spectra of Ni_3TeO_6 in the ab-plane and along c at 0 and 35 T. The full field data was back-calculated by adding the absorption difference curve at 35 T (calculated as $\Delta\alpha = \alpha(E, B = 35\ T) - \alpha(E, B = 0\ T)$) to the spectrum taken at 0 T. As in the main text, the absorption difference spectrum is plotted for comparison. Because the three Ni ions have different local environments (and therefore different crystal field splittings), each set of Ni d-to-d excitation energies is distinct. Since the Ni3 environment is most distorted from a perfect octahedral environment, it has the largest crystal field splitting, and the predicted excitations emanating from these sites have the overall highest energies. By contrast, the Ni2 centers have the least distortion, the smallest crystal field splitting, and the overall lowest energies within each cluster of excitations. This is equivalent to moving left and right along the Dq/B axis of Fig. 4.6(a).

It's easy to see from Fig. 4.6 that the optical properties of Ni_3TeO_6 change with applied field. A closer view is, however, required to link these modifications with distortions and the associated crystal field splittings around each of the Ni centers. For comparison, each cluster of excitations (both predicted and measured) is shown separately in Figs. 4.7 and 4.8. While some energy windows are more revealing than others, several general trends emerge.

For instance, in the majority of cases, the leading edge of the band (and sometimes other energy windows near the center) are affected by magnetic field. This suggests that the local environment around Ni2 (and probably Ni1 as well) becomes more distorted, although probably still remaining within the same point group. By

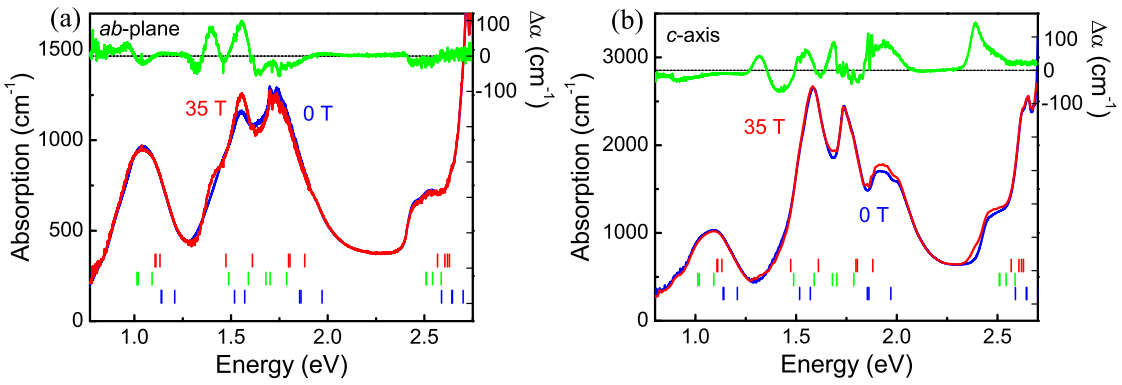


Figure 4.6: (a) Absolute absorption spectrum of Ni_3TeO_6 at 0 and 35 T in the *ab*-plane along with the full field absorption difference at 4.2 K. (b) Absorption spectrum at 0 and 35 T in the *c*-direction along with the absorption difference given by $\Delta\alpha = \alpha(E, B = 35\ T) - \alpha(E, B = 0\ T)$ at 4.2 K. The vertical tick marks at the bottom of each graph indicate the predicted *d*-to-*d* excitation energies of each of the Ni centers (Ni1 in red, Ni2 in green, Ni3 in blue).

contrast, the trailing edge of each of the bands has very limited or no field dependence. Since we know (based upon the predicted sequence of excitations) that the *d*-to-*d* excitations emanating from the Ni3 centers always govern the shape of the band tail, we surmise that the local structure around the Ni3 centers is not very sensitive to magnetic field. This is probably because the Ni3 site is already strongly distorted, allowing this metal center and the ligands around it to remain rigid under applied field. These findings are in excellent agreement with the predictions of Wu *et al.* on the importance of superexchange within the Ni1···Ni2 pair to the magnetic properties. [134]

The fundamental electronic excitations of Ni_3TeO_6 display a number of different trends across the 9 T spin flop transition. These are best seen in the absorption difference, $\Delta\alpha(E, B) = \alpha(E, B) - \alpha(E, B = 0)$, which eliminates spectral commonalities. In a complex spectrum, it is challenging to fully disentangle energy, linewidth, and oscillator strength trends. $Ni3TeO_6$ is even worse than usual because there are three different Ni centers. This means that the band centered at 1.0 eV has 9 different

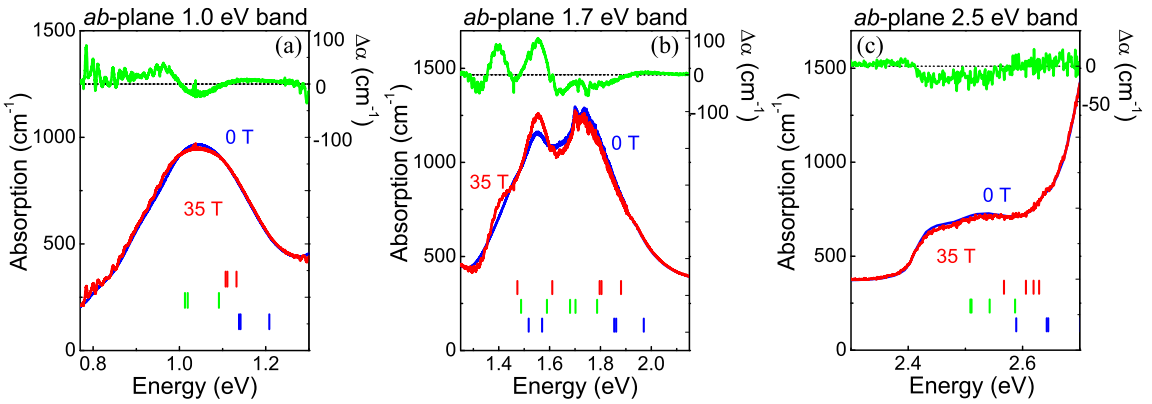


Figure 4.7: Close-up views of the Ni d-to-d excitations in the vicinity of the (a) 1.0, (b) 1.7, and (c) 2.5 eV bands in the ab-plane. The set of vertical tick marks show the calculated excitations for each type of Ni center (Ni1 in red, Ni2 in green, Ni3 in blue). As discussed here and in the main text, the relative position of these excitations reveals the relative size of the crystal field splitting.

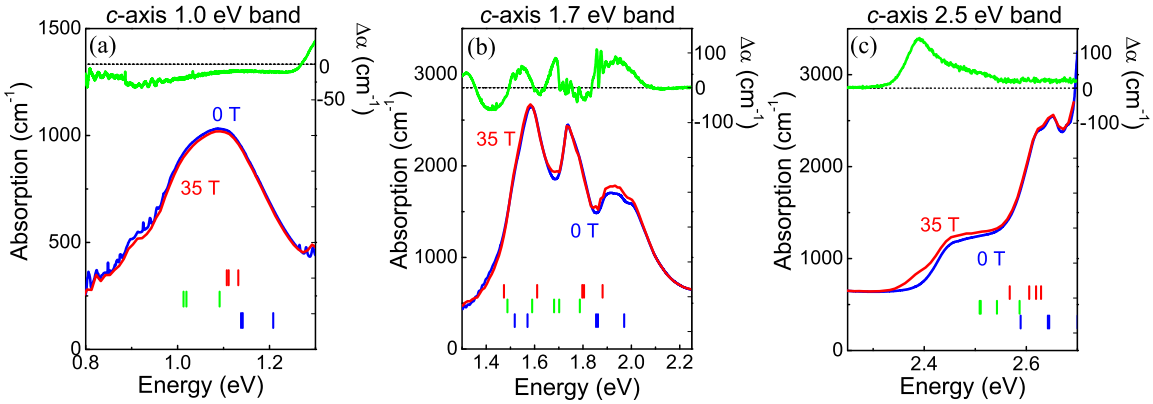


Figure 4.8: Close-up views of the Ni d-to-d excitations in the vicinity of the (a) 1.0, (b) 1.7, and (c) 2.5 eV bands in the c-direction. The set of vertical tick marks at the bottom of each panel indicate the calculated excitations for each type of Ni center (Ni1 in red, Ni2 in green, Ni3 in blue). [139]

oscillators! And the bands centered near 1.7 eV have a total of 15 underlying d-to-d excitations - each with their own oscillator parameters! So while we examined the lineshapes carefully to see whether specific energy, linewidth, and oscillator strength trends could be unraveled, there are no unambiguous trends. We therefore elected to employ an integral of the absolute value of the absorption difference $\int(\Delta\alpha)\mathrm{d}E$ over an appropriate energy window to track what is actually a combination of energy, linewidth, and oscillator strength changes for 9 or 15 individual oscillators. Examples of these trends, which are responsive to the static structural environment, are shown in Fig. 4.9. Sharp changes are observed across the spin flop transition, irrespective of the energy window in which the magneto-optical properties are analyzed. That said, oscillator strength changes can increase or decrease and even (in the case of the response centered around 1.4 eV) give an indication of the higher field transitions to come. These interesting differences may contain clues to the complex interplay of competing interactions in this material. [93]

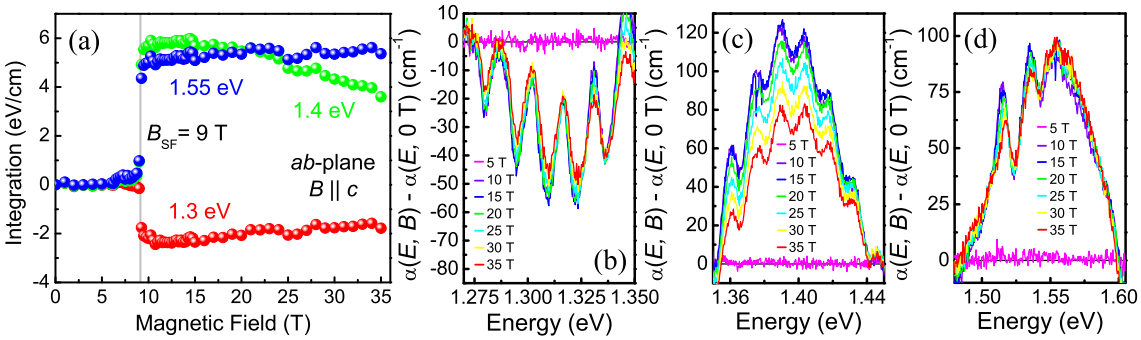


Figure 4.9: (a) Integrated absorption difference vs. magnetic field in several different energy windows in the *ab*-plane. The red points correspond to analysis of the spectral data in panel (b), the green points with (c), and the blue with data in (d). The 9 T spin-flop transition is indicated by a vertical gray line.

4.3 Driving through the metamagnetic transition in Ni_3TeO_6

A common misconception in $3d$ transition metal oxides is that the effect of atomic spin-orbit coupling on the electronic and magnetic properties is marginal, especially for Ni_3TeO_6 in its orbitally inert Ni^{2+} high-spin ($S = 1$) d^8 configuration. In the excitation channels, however, spin-orbit coupling may induce significant change in optical transitions involving $t_{2g}^5 e_g^3$ excited configurations with an open t_{2g} shell. Figure 4.10(a, b) displays the theoretically-predicted absorption spectrum of Ni_3TeO_6 both with and without spin-orbit coupling. We projected the contribution of the three different Ni centers explicitly. All of these features are Ni on-site d-to-d excitations, [93] the specific assignments of which are given above panel (a). A comparison of these predictions with the experimental spectrum in Fig. 4.10(c) reveals that the simulations including spin-orbit coupling indeed provide the superior match. This is particularly evident in the relative height of the color bands as well as the presence of the shoulder near 2.5 eV.

Figure 4.10(f) displays the magneto-optical response of Ni_3TeO_6 in the AFM, SF, and MM phases. These curves are presented as absorption differences, $\Delta\alpha = \alpha(E, H) - \alpha(E, H = 0)$, in order to highlight subtle field-induced spectral changes. The clearest indication of the phase and the largest changes are near 1.4 eV. Comparing theoretical simulation results with and without spin-orbit coupling [Fig. 4.10(d,e)], [140] we find that the overall field-induced features are better captured by including spin-orbit coupling - especially (i) the largest difference in the SF phase and (ii) the triplet-singlet transition near 2.5 eV that is only captured when spin-orbit coupling is included. In other words, the presence of atomic spin-orbit coupling from Ni d (and possibly Te p through hybridization) amplifies the effect of the magnetic field.

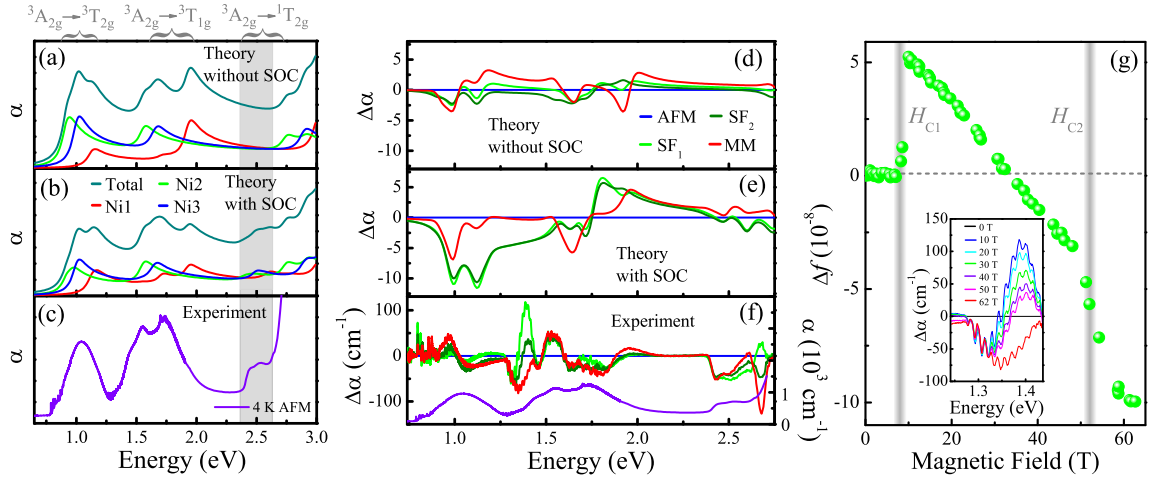


Figure 4.10: Summary of the optical and magneto-optical properties of Ni_3TeO_6 in the antiferromagnetic, spin flop, and metamagnetic phases. (a, b, c) Optical absorption spectrum obtained from first principles calculations with and without spin orbit coupling as compared with the experimental absorption spectrum (α) at 4.2 K. The three different Ni centers are projected out (Ni1 in red, Ni2 green, Ni3 blue, and the total in teal). The gray band highlights a region where spin-orbit coupling is needed to capture features in the experimental data. (d, e, f) Field-induced absorption difference of Ni_3TeO_6 from first principles calculations and experiment. Here, the absorption difference is defined as $\Delta\alpha = \alpha(H) - \alpha(H = 0\ \mathrm{T})$. The absolute absorption spectrum is reproduced at the bottom of the experimental panel. (g) Oscillator strength change in the 1.3 - 1.4 eV energy region as a function of applied field. The 9 T spin-flop and 52 T metamagnetic transition are indicated. The inset shows a close-up view of the absorption difference data in the relevant energy window.

We also extracted the field-induced change in oscillator strength, Δf, over the 1.3 - 1.4 eV energy window [Fig. 4.10(g)]. As mentioned above, $\Delta\alpha$ in this range is substantial [inset, Fig. 4.10(g)]. Δf displays a sharp jump at 9 T indicating that the absorption difference is sensitive to the spins flop. Δf also drops across the 52 T transition to the MM phase, although not as sharply. There is certainly some smearing due to the statistics of data taking in a pulsed magnetic field [Fig. 5.1(c)], but this may also be due to the fact that (i) only half of the Ni spins are affected at the 52 T transition and (ii) only small components of magnetic moments perpendicular to the *c*-axis are flipped, which should not induce significant differences in terms of local atomic configuration. [29] In any case, the magneto-optical response of Ni_3TeO_6 is sensitive to the entire series of spin reorientations that are currently accessible in pulsed field.

Chapter 5

Nonreciprocal directional dichroism in Ni_3TeO_6

Strong spin-orbit coupling and broken symmetries give rise to many novel properties in materials. One of the more peculiar is nonreciprocal directional dichroism or "one-way transparency." [30, 141] A nonreciprocal effect occurs when the motion of an object in one direction is different from that in the opposite direction. [31] Superconductivity in chiral WS_2 nanotubes, [142] spin wave nonreciprocity in antiferromagnetic $Ba_3NbFe_3Si_2O_{14}$, [143] and propagation of excitations along skyrmion strings in chiral Cu_2OSeO_3 [144] are proof-of-principle examples. Spectroscopically, the effect occurs in the vicinity of a magnetoelectric excitation and arises from how absorption depends on the light propagation direction. [30, 31, 75] Thus a given sample may be highly transmitting when measured with light propagating in the $+k$ direction but strongly absorbing for light in the -k direction.

In order for a nonreciprocal effect to take place in a material, five different symmetries (translational, rotational, mirror reflection, space inversion, and time reversal) must be broken. [75] As one might anticipate, this is relatively rare. There are also several different measurement configurations that can be used to take advantage of

various types of symmetry breaking. [31] Toroidal dichroism is a relatively well studied case. [34, 37, 145] It occurs when electric polarization, magnetic moment, and light propagation are orthogonal to one another. In other words, $k \parallel T = P \times M$. A second, less common mechanism takes place in a chiral material with a magnetic moment. [36, 77, 146, 147] Here, light can be directed along the chiral axis and the external field direction. This nonreciprocal effect is called magnetochiral dichroism. We also point out that while it is often anticipated that linearly or circularly polarized light must be used to induce a nonreciprocal response, even unpolarized light can reveal the effect. [35]

Because nonreciprocal directional dichroism depends upon both the electric and magnetic dipole matrix elements, [30] magnetoelectric multiferroics - with their ultralow crystallographic and magnetic symmetries - are promising platforms with which to search for these effects. Most materials identified so far have been studied in the terahertz region due to the similarity with the magnetic energy scale in order to reveal nonreciprocity in the vicinity of the electromagnon. Examples include $BiFeO_3$, [32,33] $CaBaCo_4O_7$, [34] $FeZnMo_3O_8$, [35] and $Ba_2CoGe_2O_7$. [36,37] There are also examples of broad band nonreciprocal directional dichroism at higher energies - for instance in $GaFeO_3$ [76] and CuB_2O_4. [77, 146, 148] In many of the aforementioned cases, the authors reversed the direction of the external magnetic field rather than the light propagation direction. This technique has clear experimental advantages and is valid for materials with a switchable magnetic moment.

Ni_3TeO_6 is a superb system with which to test these ideas. The material is multiferroic with one of the largest magnetoelectric coupling constants to date. [28, 29] The crystal structure is corundum-like with an $R3$ space group. [92] Each Ni and Te ion is surrounded by six oxygen centers - all of which are inequivalent. [92] In addition to a Ni1, Ni2, Ni3, Te alignment along c, the $R3$ space group supports a

c-directed chiral axis. [27] The magnetic field - temperature (H - T) phase diagram in Fig. 5.1(a) summarizes the important energy scales. [28, 29] Below $T_{\mathrm{N}} = 53$ K, the Ni spins align to form a collinear antiferromanget (AFM). Polarization grows substantially below T_{N}. Under magnetic field ($H \parallel c$), there is a 9 T spin flop (SF) and a 52 T transition to the metamagnetic (MM) phase. Polarization can be controlled across both of these magnetically-driven transitions. [28, 29] Importantly, a pulsed magnetic field is required to access the MM phase [Fig. 5.1(c)]. The optical absorption of Ni_3TeO_6 is summarized in Fig. 5.1(b). These features are assigned as Ni d-to-d on-site excitations, and the anisotropy is a consequence of the crystal structure. [93] In a material like Ni_3TeO_6, the direction of the chiral axis and the pitch of the rotation [27] impacts the magneto-optical response. Figure 5.1(d) and (e) illustrate the two orientations of interest here. In (d), the chiral axis is out of the ab-plane, whereas in (e), the chiral axis is in-plane. These crystal settings enable spectroscopic measurements in the magnetochiral and transverse magnetochiral orientations, respectively [Fig. 5.1(f, i)]. Both are in the Faraday geometry as shown in the schematics, but the direction of applied field and light propagation are different with respect to the chiral axis. While the magnetochiral orientation has been previously demonstrated, [31,36,77] the transverse magnetochiral orientation is completely unexplored - although it clearly breaks the requisite symmetries. With these ideas in mind, we polished two different single crystals [Fig. 5.1(g, j)]. Evidence for single domain character [27] - at least in the measurement area - is given in Fig. 5.1(g, h, j) and in additional information.

As discussed in detail above, Ni_3TeO_6 is a well-known magnetoelectric material with a number of different magnetic phases accessible under external stimuli [Fig. 5.1(a)]. The Ni^{2+} d-to-d on-site excitations can be considered to be magnetoelectric as well, not only because the excitations are sensitive to the microscopic spin

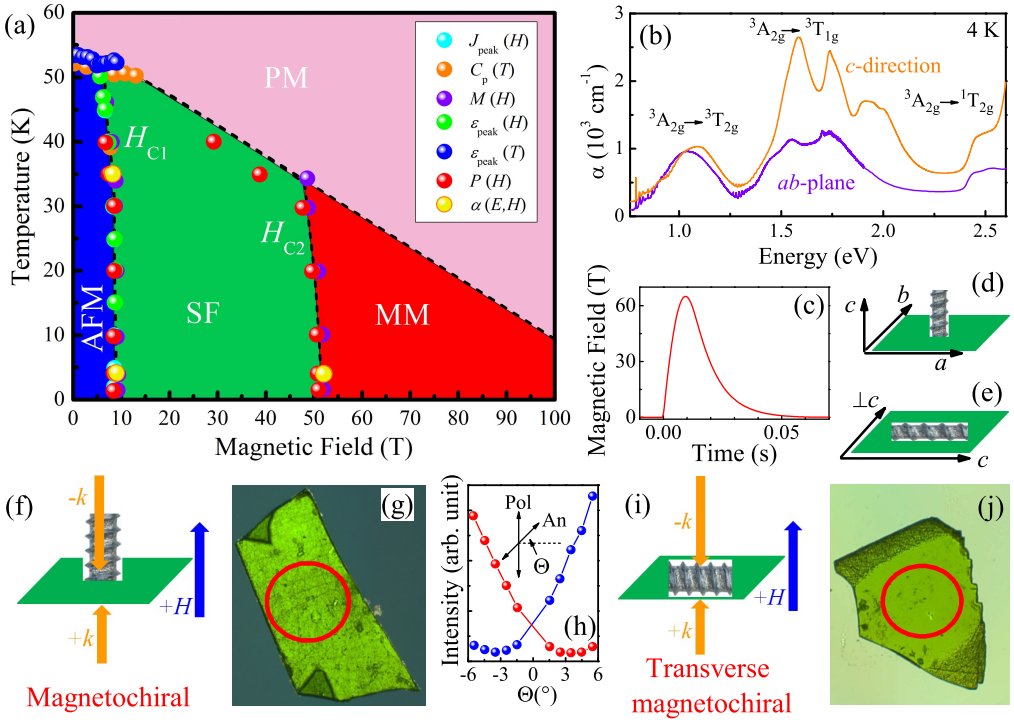


Figure 5.1: Phase diagram, optical properties, and measurement geometries of Ni_3TeO_6. (a) Comprehensive phase diagram. [28, 29, 93] (b) Optical absorption of Ni_3TeO_6. (c) Field vs. time profile from the short pulse magnet. (d,e) Our two samples expose the chiral c-axis differently. In (d), the chiral axis is out of the plane of the polished crystal. In (e), the chiral axis is in-plane. (f) Schematic representation of magnetochiral dichroism. It requires a chiral axis in the material as well as light ($\pm k$) and field $\pm H$ aligned along that same chiral direction in the Faraday geometry. The nonreciprocal effect will depend upon light propagation and field direction. (g) Image of the ab-plane sample under crossed polarizer and analyzer in transmittance. The red circle indicates the location of our measurement. (h) Optical rotation measurement using crossed polarizer and analyzer. The angle Θ corresponds to the angle between the analyzer and normal from the polarizer. The red data points correspond to the lighter green portion of the crystal, and the blue data points correspond to the darker green triangles in the corners. (i) The nonreciprocal effect can also take place in the transverse magnetochiral orientation. Here, we maintain the Faraday geometry (with $\pm k$ and $\pm H$) but the chiral (c) axis is in the plane of the polished crystal. (j) Image of the polished crystal in which the c-axis is exposed under crossed polarizer and analyzer.

arrangement in the AFM, SF, and MM phases, [93] but also due to spin-orbit coupling which becomes significant in the excited states (as observed in the absorption spectra). It turns out that the presence of spin-orbit coupling is crucial to the d-to-d dynamic magnetoelectric channel as well. The linear magnetoelectric matrix element can be written as

$$\chi^{\mathrm{me}}_{\alpha\beta} \sim \langle 0|P_\alpha|n\rangle\langle n|M_\beta|0\rangle,$$

where $|0\rangle$ ($|n\rangle$) is the ground (excited) d^8 atomic multiplet states, and P_α and M_β are electric and magnetic dipole operators respectively ($\alpha, \beta = x, y, z$). Here, $\mathbf{M} \propto \mathbf{L}+2\mathbf{S}$ (where the electron g-factor is considered to be 2). For the d-to-d channel to be active in the magnetoelectric tensor, especially in the excitations from $^3\mathrm{A}_{2\mathrm{g}}$ to $^3\mathrm{T}_{2\mathrm{g}}$ and $^3\mathrm{T}_{1\mathrm{g}}$ states between 1 and 2 eV [Fig. 4.10(a)], the $\langle n|\mathbf{L}|0\rangle$ channel which can induce $t_{2g} \rightarrow e_g$ orbital excitations (while $\langle n|\mathbf{S}|0\rangle$ does not) should be nonzero. Such a condition can be achieved only when we have nonvanishing atomic spin-orbit coupling. As a result, spin-orbit coupling becomes a crucial ingredient in dynamical magnetoelectric responses from the d-to-d excitations. [74]

Figure 5.2 summarizes nonreciprocal directional dichroism in Ni_3TeO_6. Focusing first on the magnetochiral orientation [Fig. 5.2(a-f)], we find a large nonreciprocal response in the vicinity of the on-site d-to-d excitations. Changing the direction of magnetic field H with while keeping k constant yields absorption difference curves ($\Delta\alpha$) that are distinct in several respects [Fig. 5.2(b)]. To find the nonreciprocal response, we subtract the two $\Delta\alpha$ curves: $\Delta\alpha_{NDD} = \Delta\alpha_{+H} - \Delta\alpha_{-H}$ [Fig. 5.2(c)]. This difference corresponds to the absorption of light in one field direction versus that in the other field direction. To further test the nonreciprocal effect, we held H constant while varying the light propagation direction k [Fig. 5.2(d-f)]. The absorption difference spectra and $\Delta\alpha_{NDD}$ are virtually identical to the data obtained

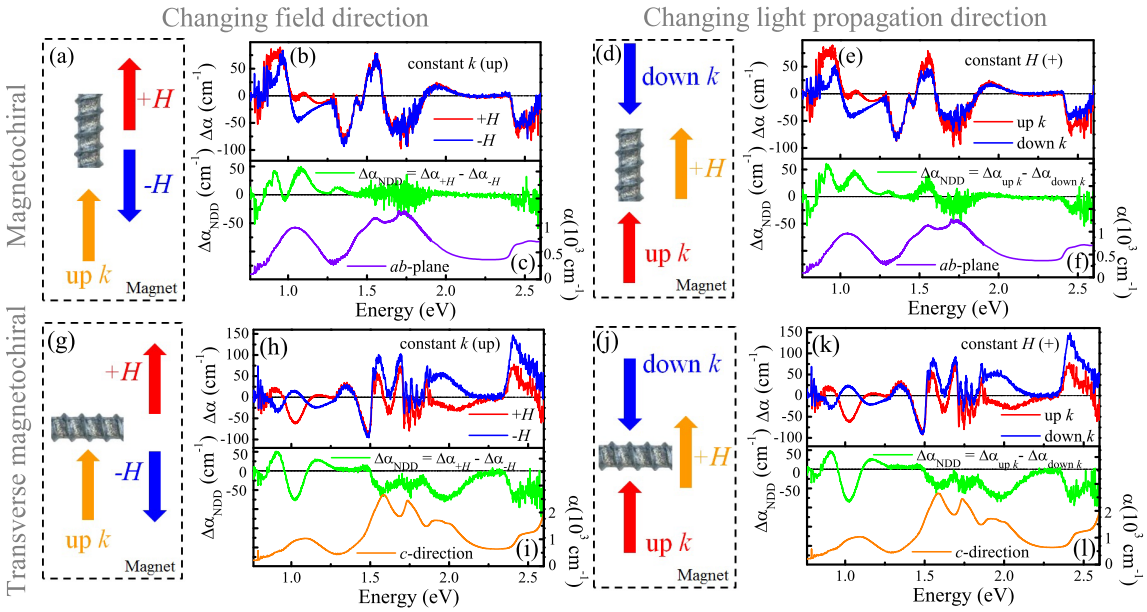


Figure 5.2: Directional dichroism for different measurement symmetries. (a, d) Schematic view of H and k relative to the chiral axis of Ni_3TeO_6 in the magnetochiral orientation. (b) Magneto-optical response as measured by the absorption difference at full field, $\Delta\alpha = \alpha(H = \pm 62\text{ T}) - \alpha(H = 0\text{ T})$. Data in the $+H$ direction are different than those in the $-H$ direction. (c) Nonreciprocal directional dichroism of Ni_3TeO_6 in the metamagnetic phase in the magnetochiral orientation, obtained by reversing the field direction with fixed k. Thus, $\Delta\alpha_{NDD} = \alpha(H_{up} = 62\text{ T}) - \alpha(H_{down} = 62\text{ T})$ which is the same as $\Delta\alpha(H_{up} = 62\text{ T}) - \Delta\alpha(H_{down} = 62\text{ T})$. For reference in (c, f), we include the linear absorption spectrum, α. (e, f) Similar $\Delta\alpha$ and $\Delta\alpha_{NDD}$ spectra are obtained by reversing the light propagation direction under constant field. Here, $\Delta\alpha$ is $\alpha(H = +62\text{ T}) - \alpha(H = 0\text{ T})$ for $\pm k$, and $\Delta\alpha_{NDD}$ is $\alpha(k_{up}) - \alpha(k_{down})$ which is the same as $\Delta\alpha(k_{up}) - \Delta\alpha(k_{down})$ with $H_{up} = 62$ T. (g, j) Schematic view of H and k relative to the chiral axis of Ni_3TeO_6 in the transverse magnetochiral orientation. (h, i) Magneto-optical and nonreciprocal directional dichroism of Ni_3TeO_6 at 62 T in the transverse magnetochiral orientation obtained by reversing the field direction under constant k. For reference in (i, l) we include the linear absorption spectrum. (k, l) Similar $\Delta\alpha$ and $\Delta\alpha_{NDD}$ spectra are obtained by varying the light propagation direction under constant field.

by switching the direction of the applied field under constant k. Thus, in addition to revealing broad band nonrecriprocal directional dichroism at much higher energies than usual in Ni_3TeO_6, the effect is also very large. All of this work was done with unpolarized light. Magnetochiral dichroism in the optical region has also been realized in CuB_2O_4 - both with and without polarized light [77]. In this copper oxide, magnetochiral dichroism arises from the mixing of the electronic- and magnetic-dipole transitions due to spin-orbit coupling which activate in turn the intra-atomic d-to-d Cu^{2+} transitions. [77] This is similar to the Ni^{2+} on-site excitations presented here in Ni_3TeO_6. [93]

We also reached beyond the magnetochiral orientation to explore nonreciprocal directional dichroism in other settings. Our objectives are to (i) seek out strange new types of light-matter interactions in chiral materials and (ii) to compare their character with the more established variants. Figure 5.1(e,i,j) summarizes the sample requirements (exposing the chiral c-axis in the plane of the polished single domain crystal) and Faraday measurement geometry for uncovering the nonreciprocal directional dichroism in the transverse magnetochiral orientation. The lower portion of Fig. 5.2 summarizes our spectroscopic results. As before, we switch both allowed parameters. We changed the applied field direction while keeping the light propagation fixed [Fig. 5.2(g-i)], and we varied k under constant H [Fig. 5.2(j-l)]. Clearly, nonreciprocal directional dichroism in the transverse magnetochiral orientation differs greatly from that in the magnetochiral orientation. Not only is it overall broader, encompassing two active spectral regimes across the near infrared and visible that are more than 0.5 eV wide, but it is also large - on the order of ± 50 cm^{-1}. More importantly, the measurement configuration is unique - and even unexpected - within the current framework of magnetochiral dichroism. [31] Again, these results were achieved with unpolarized light.

Figure 5.3(a,b) presents $\Delta\alpha_{NDD}$ taken under varying H and k conditions for the magnetochiral and transverse magnetochiral measurement symmetries, respectively. As anticipated for a monochiral system with a switchable moment, the overall shape of $\Delta\alpha_{NDD}$ in Ni_3TeO_6 does not depend upon whether the magnetic field or light propagation direction is switched. The response in the magneto- and transverse magnetochiral orientations is, however, quite different. In particular, $\Delta\alpha_{NDD}$ in the transverse magnetochiral orientation includes a large contribution from the c-direction and, as a result, has an extra functional region (highlighted by the green band) that does not have a counterpart in the more traditional magnetochical response. To provide additional insight into the variation of the nonreciprocal effect across the spin flop and metamagnetic transitions, we calculated the change in oscillator strength Δf_{NDD} [149] and plotted the result as a function of applied field. For the magnetochiral orientation [Fig. 5.3(d)], Δf_{NDD} is initially zero. This is because there is no overall magnetic moment because spins are collinear along c. [29] A small moment develops at 9 T when the spins flop into the ab-plane. Above 9 T, the spins cant with increasing field, inducing large changes in $\Delta\alpha_{NDD}$. The nonreciprocal response in the transverse magnetochiral orientation is different [Fig. 5.3(e)]. Here, Δf_{NDD} increases gradually as the spins cant toward the field and the overall magnetic moment increases. As a reminder, the easy axis is along c and in-plane in this geometry (and perpendicular to the magnetic field). There are no hysteresis effects within our sensitivity.

From the symmetry standpoint, the nonreciprocal effect arises from the reversal of H or k. Further, when both H and k are switched, $\Delta\alpha_{NDD}$ should be obviated. We can test this supposition in Ni_3TeO_6 since we performed both sets of experiments. Figure 5.3(f-i) summarizes the effect of switching both field and the direction of light propagation for the two measurement orientations of interest. For the magnetochiral

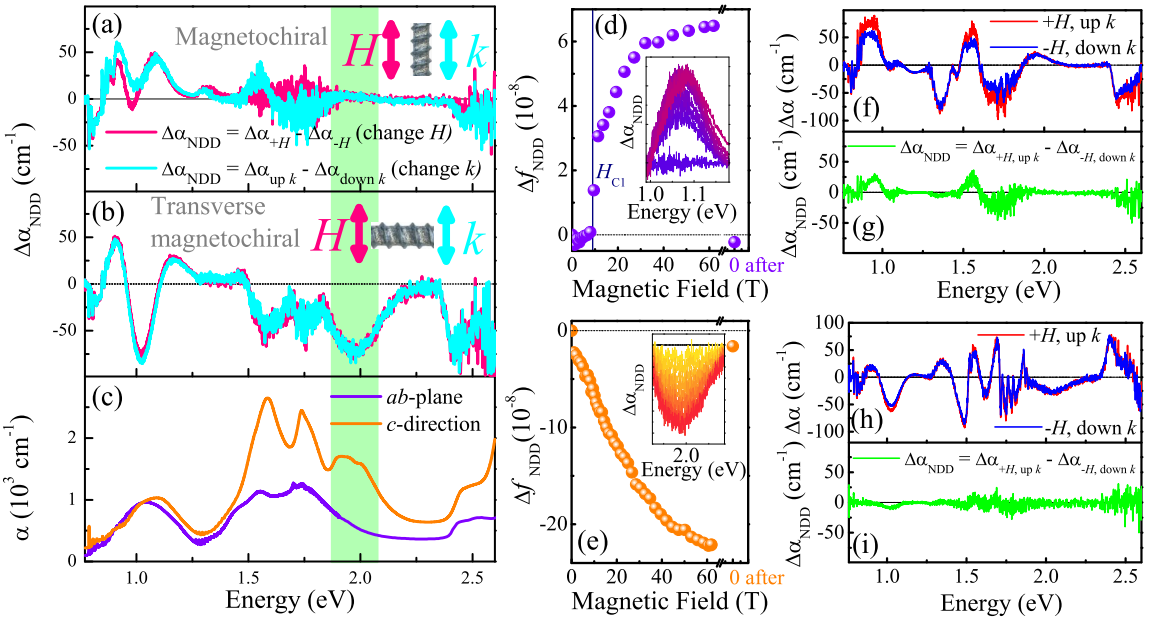


Figure 5.3: Reciprocal non-reciprocal optical effect. (a) $\Delta\alpha_{NDD}$ under different field and light propagation directions in the magnetochiral orientation for Ni_3TeO_6. (b) $\Delta\alpha_{NDD}$ under different field and light propagation directions in the transverse magnetochiral orientation. (c) Linear absorption spectrum at 4.2 K for reference. (d,e) Changes in the nonreciprocal response of Ni_3TeO_6, as measured by the change in oscillator strength Δf, as a of function magnetic field for the magnetochiral and transverse magnetochiral orientations, respectively. Zero field data, both before and after the field pulse, is shown. Insets display close-up views of $\Delta\alpha_{NDD}$ spectra as a function of magnetic field. (f-i) Comparison of $\Delta\alpha$ and $\Delta\alpha_{NDD}$ spectra when both H and k are switched in the magnetochiral (f,g) and transverse magnetochiral (h,i) orientations.

orientation [Fig. 5.3(f, g)], we calculated $\Delta\alpha_{NDD} = \Delta\alpha_{+H,\mathrm{up}k} - \Delta\alpha_{-H,\mathrm{down}k}$. There is, unexpectedly, a small residual response, although it is greatly diminished compared to the $\Delta\alpha_{NDD}$ obtained by switching just one parameter. One might wonder whether this contrast might be attributed to additional symmetry breaking due the polarization along c or the effect of the chiral axis on switching k, but polarization does not do this [150] and chirality is invariant under rotation because a screw always retains its directionality. Turning to the transverse magnetochiral orientation [Fig. 5.3(h, i)], switching both H and k simultaneously reveals almost no residual nonreciprocal response.

5.1 Additional information

5.1.1 Evidence for a single chiral domain in our polished crystals

Since Ni_3TeO_6 can show chiral domains throughout a polished sample [27], it is important to confirm that our sample contains a single chiral domain. The different chiral domains can be revealed using a transmission optical microscope with a polarizer and an analyzer. When the polarizer and analyzer are at slightly different angles, the light throughput through the sample will reveal lighter and darker green regions indicating different chiral domains. Figure 5.1(g) in the main text shows the microscope image of the crossed polarizer measurement of the *ab*-plane crystal, where we see two different chiral domains, indicated by the large light green portion and the dark green triangles at two different corners of the crystal. For our measurements, we expose light on the center of the crystal, indicated by the red circle in the figure. Hence, we can confirm that we measured a single chiral domain. Figure 5.1(h) shows an optical rotation measurement using crossed polarizer and analyzer

(schematic within the panel). The angle Θ corresponds to the angle between the analyzer and normal from the polarizer. With the red data points corresponding to the lighter green portion of the crystal, we can deem a majority of the crystal to contain right-handed chirality, as it has a positive value of Θ. Therefore, we can deem the small darker green trianlges to have left-handed chirality with a negative Θ (as shown by the blue data points). Figure 5.1(j) is a photographic image of a polished single crystal that exposes the *c*-axis. If the sample was not polished to reveal a perfect *c*-axis in-plane, then color differentiation would emerge when using the polarizer/analyzer test. However, we see very little to no color difference when tested. Again, the red circle indicates the portion of the crystal that was exposed to light during our measurements.

5.1.2 Nonreciprocal effects in raw data

Figure 5.4 gives an overview of some of the raw power spectra data to show the nonreciprocal effect. Focusing first on the magnetochiral orientation data, it is clear that the 0 T spectra before the magnet pulse are exactly the same, as indicated by the pink and light blue curves. Moving on to the middle plot, the 0 T power spectrum before the pulse is kept on the plot for reference (black dotted curve). Here, even in the raw data it is obvious that the $+H$ and -H spectra at full field are different, between 1.25 and 1.4 eV. The third plot for the magnetochiral orientation is used to eliminate any doubt of hysteresis effects. Plotted here are the 0 T spectra after the magnet pulse has ramped back down. Again, the 0 T before curve is still plotted. It is very obvious that the 0 T after-pulse curves again match exactly to the 0 T before-pulse curves. Therefore, no hysteresis effects are in play here.

Turning our attention to the transverse magnetochiral orientation in Fig. 5.4, we can see the same progression of data. First, the 0 T before-pulse data is plotted,

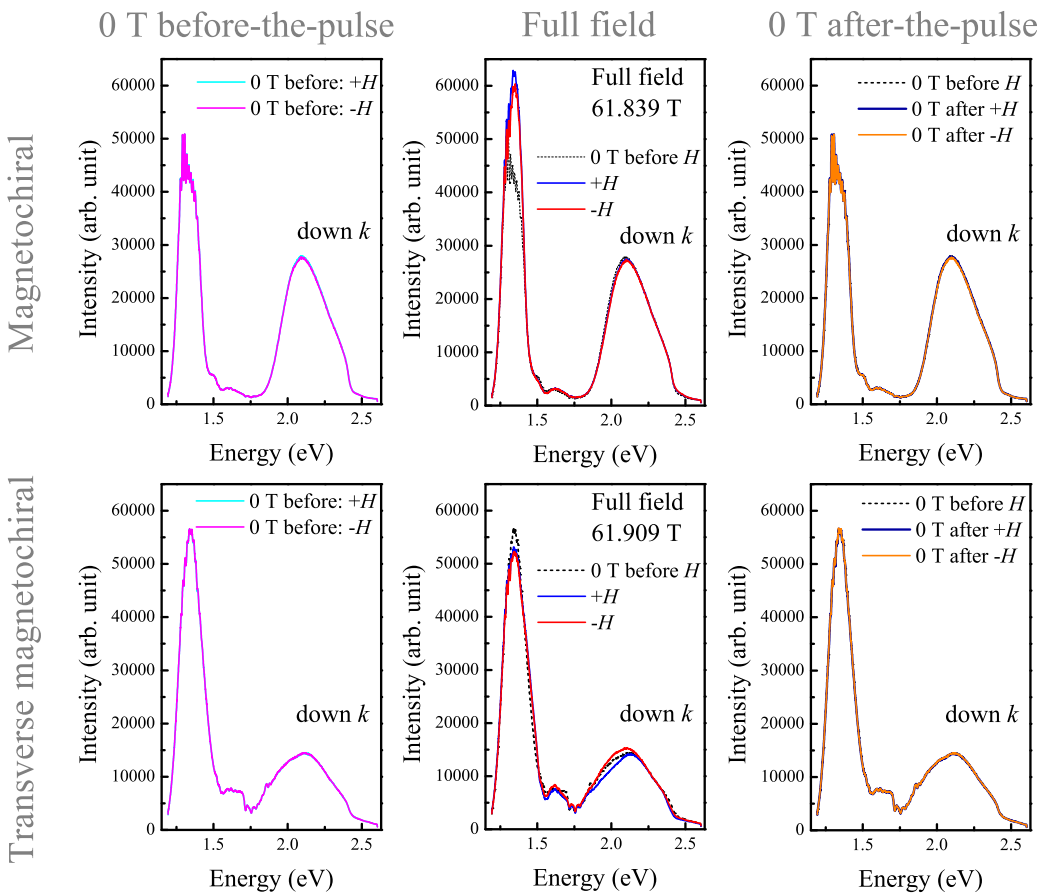


Figure 5.4: Raw power spectra data of Ni_3TeO_6 in both the magnetochiral and transverse magnetochiral orientations. The first plot in each is the 0 T power spectra before the magnet pulse. The second plot is the full field power spectra for the respective orientations. The final plot is the 0 T power spectra after the magnet pulse compared to 0 T spectra before the magnet pulse. This eliminates hysteretic concerns.

again in pink and light blue. The second plot is the full field response for the $+H$ and -H pulses. At 2.0 eV, it is very obvious that the curves deviate from the 0 T before-pulse. Also, they seem to even have an opposite effect. The $+H$ curve lowers in transmittance while the -H curve increases in transmittance slightly. Finally, the last plot shows the 0 T spectra after the magnet pulse. Again, it is clear that no hysteresis effects are in play. It is important to note that the data here are the raw, power spectra straight from the spectrometer. Furthermore, it is important to note that the changes here are so large that they can be seen even in the raw power spectra data without any data treatment.

5.1.3 Comparing all of the different orientations by absorption differences

In order to calculate nonreciprocal effects, we first take an absorption difference of the high field spectra for each different orientation. Again, the four different orientations we can measure are ($+H$, up k), (-H, up k), ($+H$, down k), and (-H, down k). In order to obtain an absorption difference, we take the full field power spectra and divide by the zero field power spectra for the same experiment. Importantly, the reference spectra is eliminated from the final result. Absorption is typically obtained as

$$\alpha_B = -\frac{1}{d} ln(\frac{T_H}{T_r}), \text{and} \tag{5.1}$$

$$\alpha_0 = -\frac{1}{d} ln(\frac{T_0}{T_r}), \tag{5.2}$$

where d is the sample thickness, T_B is transmittance at full field, T_r is the transmittance of the reference, and T_0 is the transmittance at zero field. For our $\Delta\alpha$ spectra,

we subtract the two absorption equations.

$$\Delta\alpha = \alpha_H - \alpha_0 = [-\frac{1}{d} ln(\frac{T_H}{T_r})] - [-\frac{1}{d} ln(\frac{T_0}{T_r})] \tag{5.3}$$

$$= [-\frac{1}{d}(ln(T_H) - ln(T_r))] - [-\frac{1}{d}(ln(T_0) - ln(T_r))] \tag{5.4}$$

$$= -\frac{1}{d}[ln(T_H) - ln(T_0)] \tag{5.5}$$

$$= -\frac{1}{d} ln(\frac{T_H}{T_0}) \tag{5.6}$$

Thus, we can see that the absorption difference eliminates the reference.

The different H and k orientations affect the absorption difference curves. Figure 5.5 gives an overview of all six different comparisons that can be made from the four different measurement orientations in Ni_3TeO_6. From these comparisons, we can definitively see (as we also could in the raw data) that several of these orientations give quite different responses in their absorption difference spectra. Focusing first on the left-most panel for the magnetochiral orientation, we can see many differences. However, there are some spectra that are very similar, such as in (c) and (d). Upon closer observation, we can see that they are the two comparisons in which both H and k are being changed. From a symmetry perspective, changing both parameters should give very little to no nonreciprocal effects. Therefore, it is convincing that when we change both parameters, even though they are not exact, they are very similar.

Moving to the transverse magnetochiral orientation in Fig. 5.5(h-m), we clearly see many differences between the $\Delta\alpha$ spectra. In fact, in some regions, the responses are exactly opposite. However, in panels (j) and (k), the curves are basically overlapping. Here, again, we are comparing the curves when both parameters are changed. Moving forward, we can take each of these six comparisons for both the magnetochi-

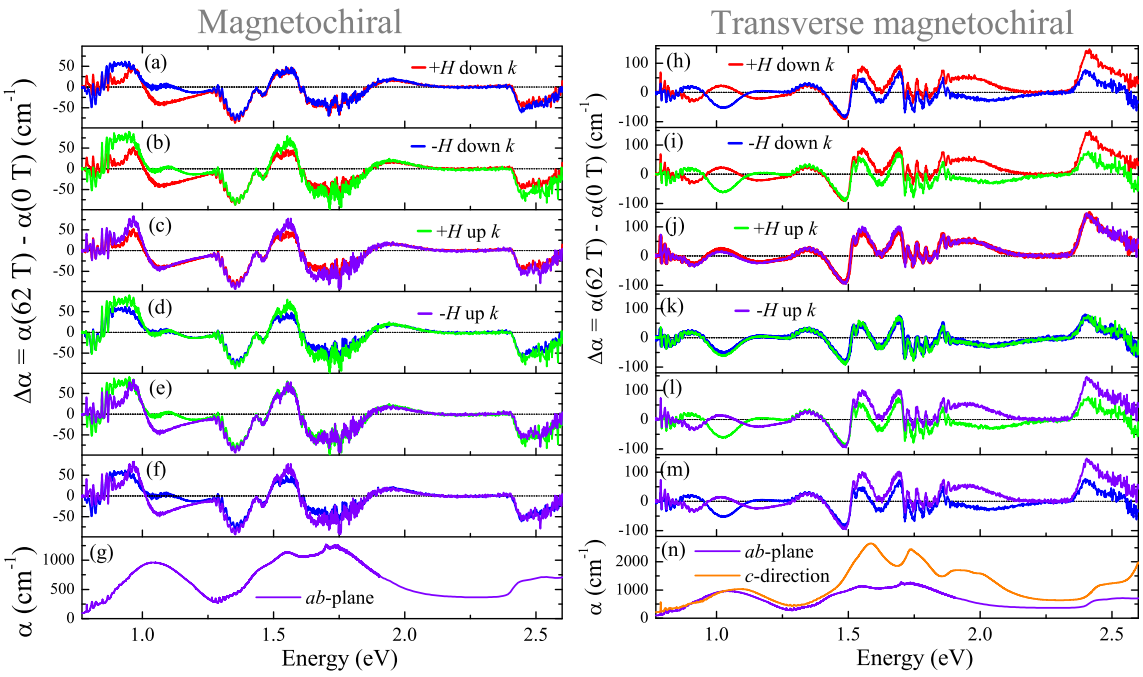


Figure 5.5: Absorption difference spectra for each comparison are plotted, with the (+H, up k) in green, (-H, up k) in violet, (+H, down k) in red, and (-H, down k) in blue. The left most panel (a-f) is the magnetochiral orientation while the right most panel (h-m) is the transverse magnetochiral orientation. The bottom-most curve is the linear absorption of the *ab*-plane for the magnetochiral orientation on the left in (g) and both *ab*-plane and *c*-direction absorption for the right transverse magnetochiral orientation in (n).

ral and transverse magnetochiral orientations and subtract the $\Delta\alpha$ curves to get the nonreciprocal directional dichroism response $\Delta\alpha_{NDD}$.

5.1.4 Comparing the nonreciprocal response for each experimental orientation

The nonreciprocal response is defined as $\Delta\alpha_{NDD} = \alpha_{+H} - \alpha_{-H}$, where the terms $+H$ and -H can be switched to $+k$ and -k.

$$\Delta\alpha_{NDD} = \Delta\alpha_{+H} - \Delta\alpha_{-H} \tag{5.7}$$

$$= (\alpha_{+H} - \alpha_{+H_0}) - (\alpha_{-H} - \alpha_{-H_0}) \tag{5.8}$$

From here, it is obvious that if the 0 T spectra are the same for each measurement (α_{+H_0} and α_{-H_0}), then finding $\Delta\alpha_{NDD}$ by using absorption differences yields the same result. Also, because of the ratio we take using the absorption difference method shown above, even if the 0 T spectra are not exact, we can still find $\Delta\alpha_{NDD}$ accurately.

Six different comparisons can be made from the four different measurement orientations. Figure 5.6 summarizes the $\Delta\alpha_{NDD}$ spectra for each comparison. Focusing first on the magnetochiral orientation, we can see that most every $\Delta\alpha_{NDD}$ curve shows a response. However, two curves show a significantly lower response than the others. These two curves are the navy and green ones, in which both parameters H and k were changed. Again, there should be no nonreciprocal response in play here.

Turning our attention to the transverse magnetochiral orientation, we can see the same type of response as in the magnetochiral orientation. The major difference here is that the two curves (navy and green) that change both parameters are almost

completely zero and show no nonreciprocal response.

5.1.5 Observation of fine structure

Many of these nonreciprocal changes are prominent in the fine structure in the leading edge of the d-to-d excitations. Figure 5.7 summarizes how the fine structure along the leading edges of these on-site excitations are nonreciprocal. All six comparisons can be observed; however, for simplicity, we only plot the data in which H is reversed while keeping k constant. Looking at the $\Delta\alpha_{NDD}$ spectra for each of the magnetochiral and transverse magnetochiral orientations, it is very clear that these effects line up perfectly with the fine structure in each of the Ni_3TeO_6 samples.

There are two possibilities as for the origin of the fine structure on the leading edge of these on-site excitations. First, they could be related to the onset of magentic order and be magnon sidebands. [151, 152] The second possibility is that they are a series of phonon sidebands. [153, 154] To assign these features, a variable temperature analysis is revealing. Figure 5.8(a) and (b) give the absorption as a function of temperature at a very close-up view of this fine structure for the ab-plane and c-direction, respectively. The data is very zoomed-in so that small hints of fine structure with respect to temperature can be visibly seen. Here, it is obvious that at base temperature, the features are at their sharpest and most clear. With increasing temperature, these features start to broaden, lose intensity, and disappear. With a Néel temperature of $\approx$53 K, it is evident that this fine structure sustains even when above the magnetic ordering temperature. For example, in both plots, the 60 K absorption data still shows subtle but definite hints of the fine structure. With this information, we can conclude that these features are probably not magnetic in origin (magnon sidebands), revealing that these are a progression of phonon sidebands.

As another test, we can observe how the fine structure lines up with the progres-

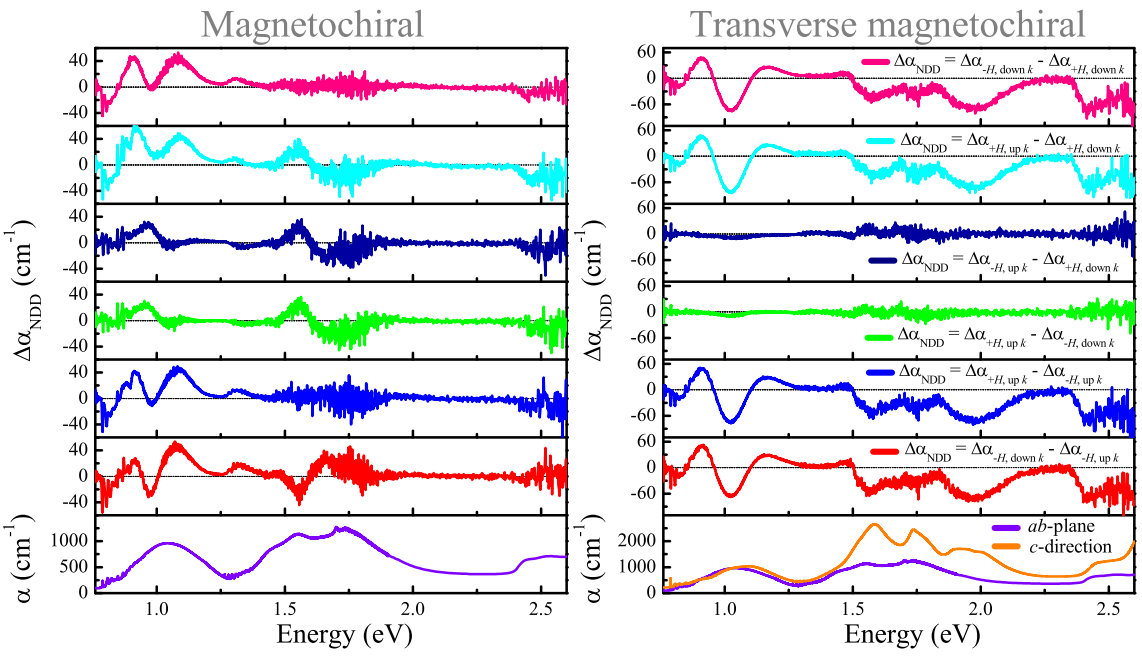


Figure 5.6: Comparison of all six different subtractions for both the magnetochiral and transverse magnetochiral orientations.

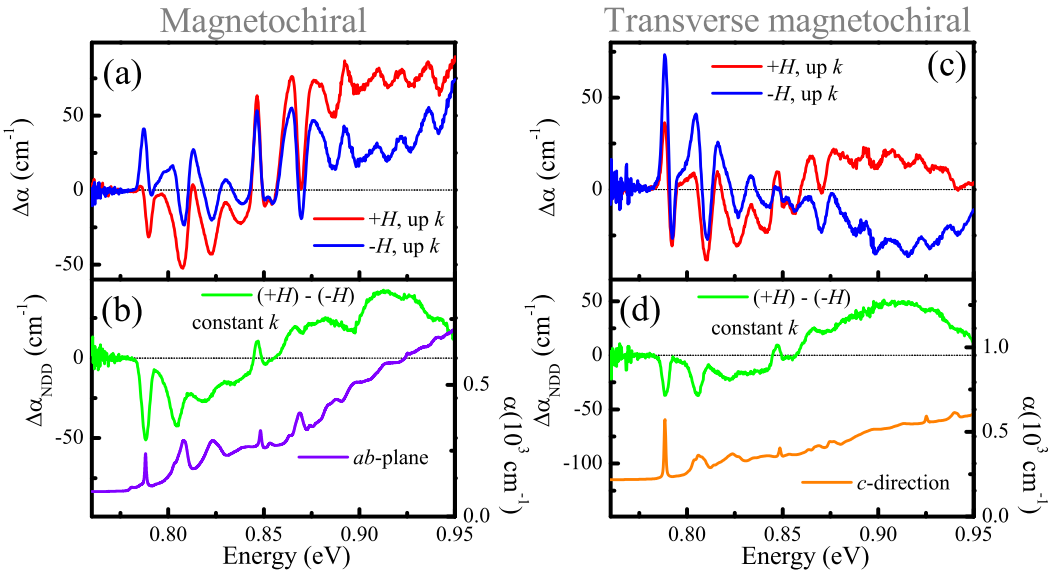


Figure 5.7: Close-up view of the $\Delta\alpha$ spectra for the $+H$, up k (red) and $-H$, up k (blue) for the magnetochiral (a) and transverse magnetochiral (c) orientations. The nonreciprocal effects are plotted in green underneath in (b) magnetochiral and (d) transverse magnetochiral orientations. The *ab*-plane and *c*-axis absorption spectra are underneath for reference.

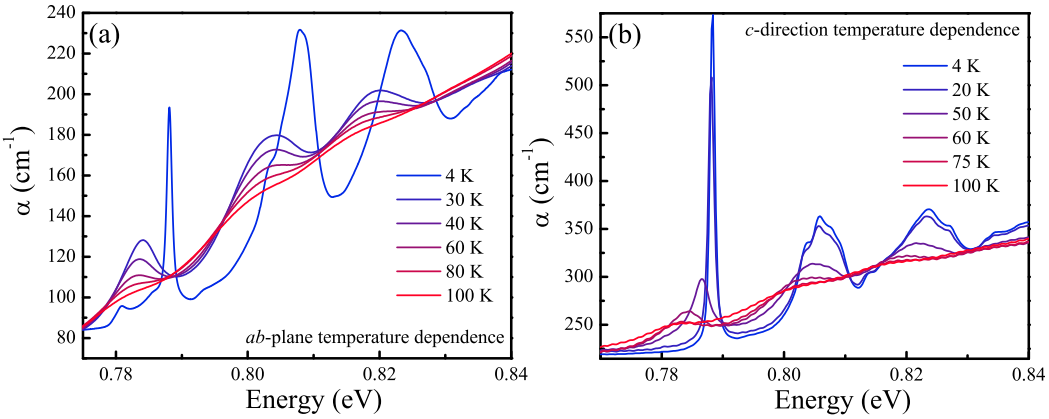


Figure 5.8: Close-up view of the absorption data data as a function of temperature around the vicinity of the fine structure in both the *ab*-plane (a) and *c*-direction (b).

sion of phonons measured in the infrared spectra. Figure 5.9 shows how both the *ab*-plane and *c*-direction fine structure data line up with the abundance of *ab*-plane and *c*-directed phonons. The phonon data has been shifted in order to match the energy of the fine structure.

5.1.6 Size of the broadband nonreciprocal directional dichroism effect

To quantify the size of this nonreciprocal effect, we normalize the data and plot the result as a percentage. Figure 5.10 demonstrates this for both the magnetochiral and transverse magnetochiral orientations. For the magnetochiral orientation, we compare the nonreciprocal response to the *ab*-plane absorption data, as we are measuring that face of the sample response. Upon observation, we can see that changes in the magnetochiral orientation reach as high as 35% in certain ranges. Since most other materials showing nonreciprocal directional dichroism with a magnetochiral orientation are measured in the terahertz region, it is not surprising that the size of their effect can reach nearly 100% since the absorption strength is typically much

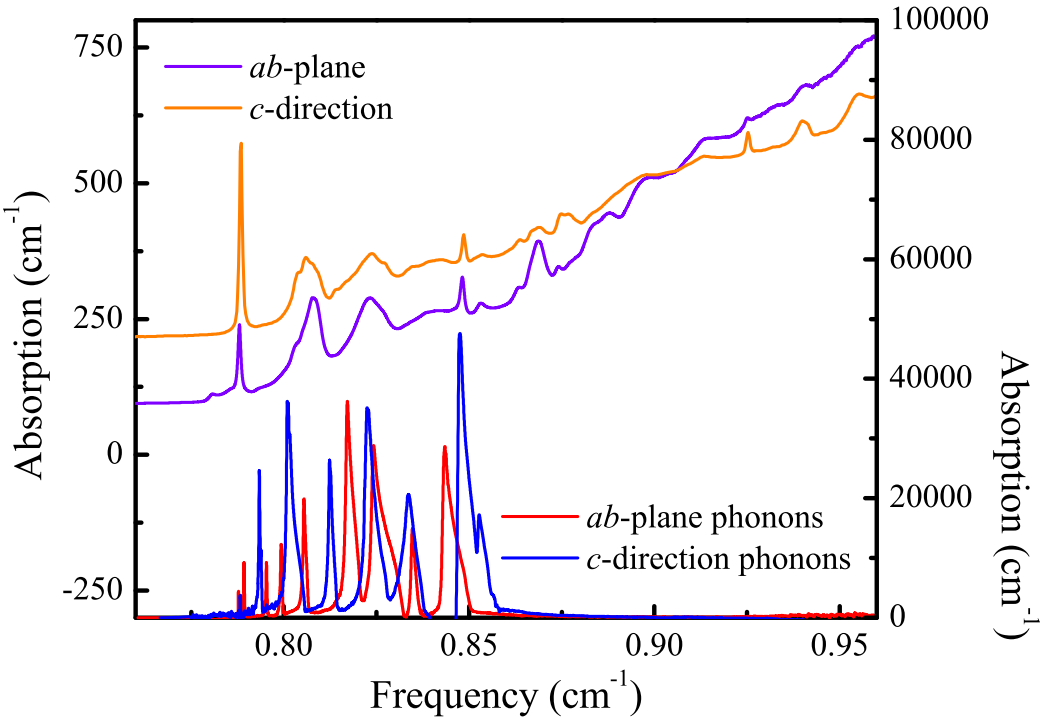


Figure 5.9: Close-up view of the absorption data around the vicinity of the fine structure in both the *ab*-plane and *c*-direction. Here, the phonon spectra of the *ab*-plane and *c*-direction is plotted underneath for reference.

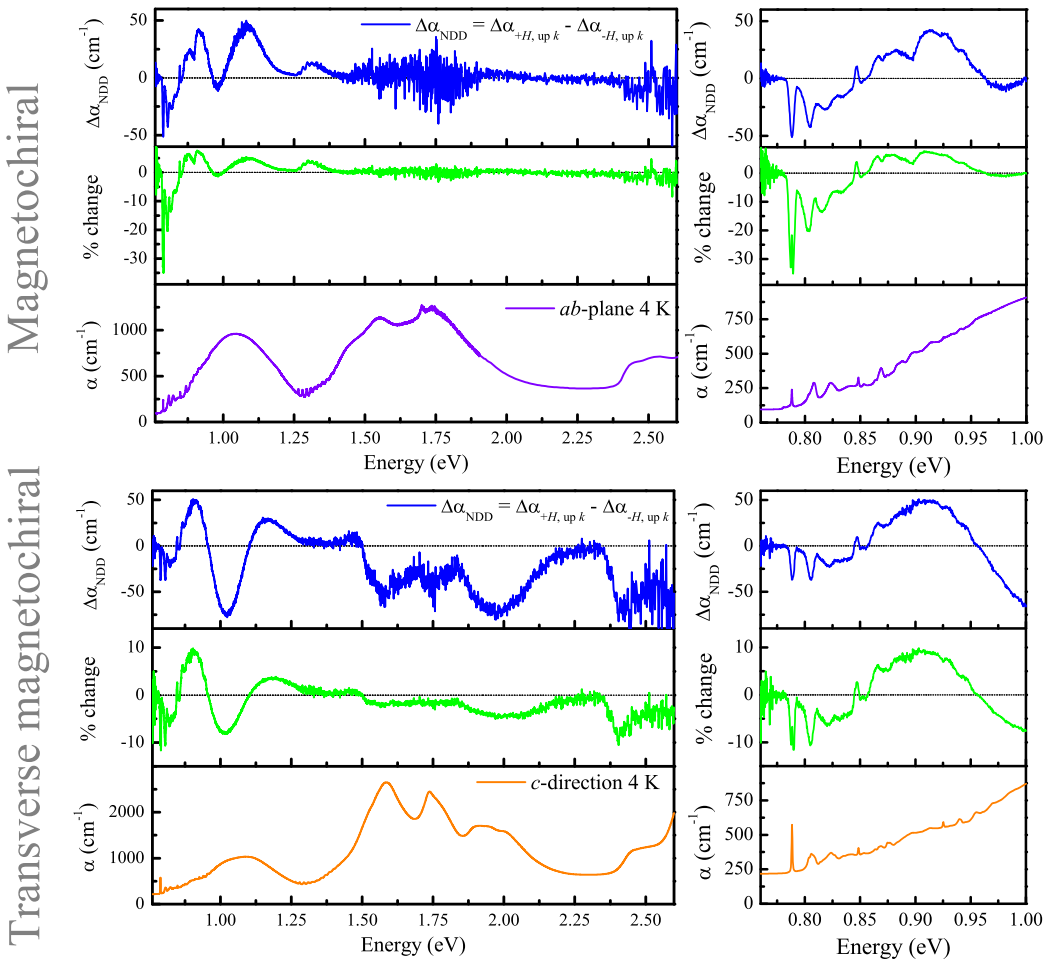


Figure 5.10: Nonreciprocal effects for both the magnetochiral (top) and transverse magnetochiral (bottom) orientations. The middle plot in green represents the percent change of the entire observed nonreciprocal response. The rightmost two panels are zoomed in on the fine structure of Ni_3TeO_6.

lower there. [36] However, for the very few cases of magnetochiral dichroism in the optical region, the changes they present are on the order of 10-25% and can be up to 100%. [77, 146]

For the transverse magnetochiral orientation, the calculation is less clear. Here, we are measuring both a component of the c-direction as well as the $\perp c$ response. For ease of calculation, we only find the percent change using the c-direction absorption data. From this, we can see that these changes in the transverse magnetochiral orientation are as large as 11% in certain regions. The lesser strength of the effect can be attributed to the overall larger absorption coefficient of the c-direction compared with the ab-plane.

Chapter 6

Tracking the continuous spin-flop transition in Ni_3TeO_6 by infrared spectroscopy

Easy axis antiferromagnets usually exhibit a first order spin-flop transition when the magnetic field is applied along the easy axis. Recently, a colossal magnetoelectric effect was discovered in Ni_3TeO_6, suggesting a continuous spin-flop transition across a narrow phase in this material. [28] Additional evidence is, however, desirable to verify this mechanism. Large magnetostriction effects also prove that the lattice is sensitive to different magnetic orientations. [29] Here we measure the infrared vibrational properties of Ni_3TeO_6 in high magnetic fields and demonstrate that the phonon anomalies are consistent with a second-order mechanism.

6.1 Vibrational spectra of Ni_3TeO_6

Figure 6.1 displays the polarized infrared absorption of Ni_3TeO_6 at 300 K. A symmetry analysis predicts 9 E symmetry optical phonons in the ab-plane and 9 optical

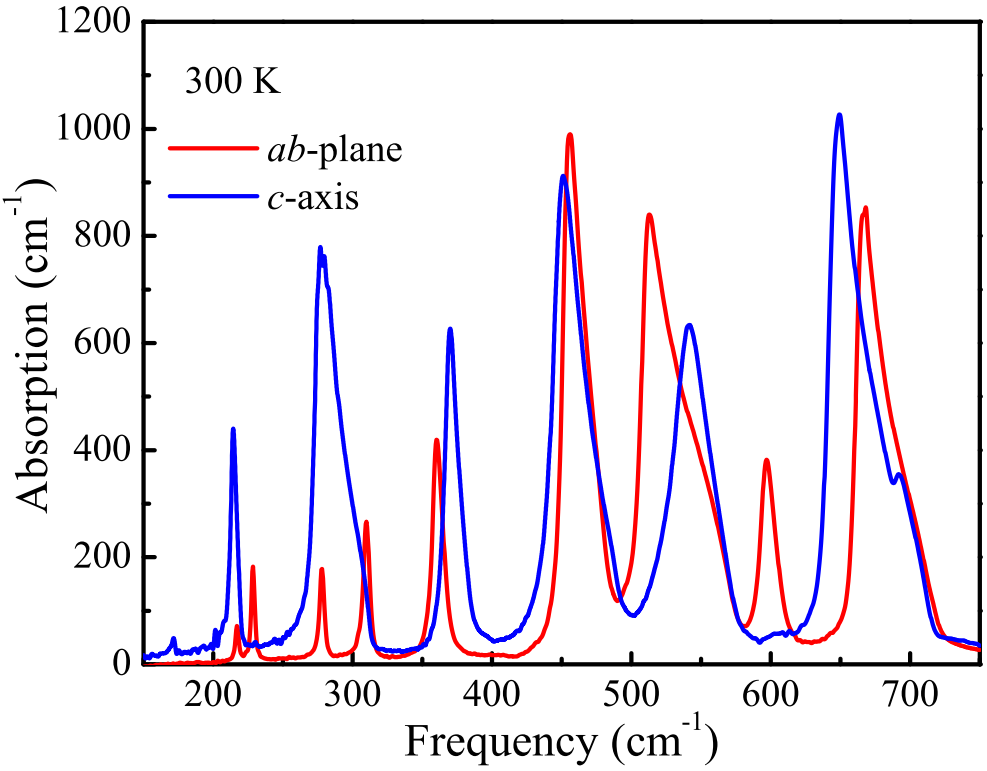


Figure 6.1: (a) Polarized infrared absorption spectrum of Ni_3TeO_6 at 300 K for both the *ab*-plane and *c*-direction phonons.

modes of A symmetry polarized along c ($\Gamma_o = 9E + 9A$). In the polar $R3$ structure, [92, 155] the optical modes are both infrared and Raman active. [156] All are present in the infrared response of Ni_3TeO_6 save one, and that mode is observed clearly in the Raman spectrum. The vibrational features are assigned according to our lattice dynamics calculations. A comparison of the theoretically predicted and experimentally observed mode frequencies is shown in Table 6.1 along with a description of the displacement patterns. For instance, the phonon at 310 cm^{-1} corresponds to Ni1 displacing opposite to Te in the *ab*-plane in a symmetric stretch with Ni2 and Ni3 remaining at rest. By contrast, the 597 and 666 cm^{-1} modes are octahedral stretching modes, differentiated by the cluster of oxygens that move with respect to the nickel centers (in- vs. out-of-phase oxygen shifts between consecutive planes). Recently, additional work with lower-energy excitations, Raman spectra, and high pressure effects have been observed in Ni_3TeO_6. [157, 158]

The optical absorption measurements on Ni_3TeO_6 provide microscopic information on the elementary excitations of the lattice. Frequency shifts of these excitations are sensitive probes of structural dynamics, and spin-phonon coupling communicates information on magnetic phase transitions to the structural degrees of freedom. Therefore by tracking the phonon frequencies across the Néel and spin-flop transitions, we can shed light on the mechanism of spin-lattice coupling. [18]

Table 6.1: Phonon frequencies obtained from DFT calculations ($U = 8$ eV), experimental mode frequencies, mode symmetries, spin-lattice coupling constants (the λ's in the text), and displacement patterns. The mode description in the final column encodes shifts of the three Ni ions and the Te center in the sequence Ni1-Ni2-Ni3-Te. u/d = shifts up/down along the c axis; l/r = motion to the left/right in the ab-plane; "-" indicates almost no displacement; octahedral distortions (compression/extension along certain axis/in plane) and rotations are also indicated.

Theoretical Frequencies (cm^{-1})	Experimental Frequencies (cm^{-1})	Mode Symmetries	Coupling Constants (cm^{-1})	Mode Displacement Patterns
167	171	A	–	uudd
205	214	A	–	udud
209	217	E	–	lrrl
217	228	E	–	lrlr
264	278	A	–	-ddu
265	278	E	–	llrr, oct rot around a(b)
297	310	E	0.4	l–r, oct rot
343	360	E	–	oct compression ab
353	370	A	–	udud oct compr c
399	–	A	–	oct twist
425	456	E	–	oct compr ab+twist
426	451	A	–	d-dd+oct twist
488	513	E	–	oct twist ab
512	541	A	–	oct contr c+rot c
562	597	E	0.3	oct contr a(b)
601	649	A	–	oct axial stretching
622	666	E	3.7	oct contr a+b(a-b)
653	692	A	–	oct asymmetric stretching

6.2 Spin-lattice coupling across the Néel transition

The frequency vs. temperature plots in Fig. 6.2(b-f) summarize the elastic properties of Ni_3TeO_6 across the 53 K paramagnetic (PM) $\rightarrow$ antiferromagnetic-I (AFM-I) transition. Three *ab*-plane modes at 310, 597, and 666 cm^{-1} are sensitive to the Néel transition, an indication that lattice behavior is coupled to the magnetic structure. From the displacement patterns in Fig. 6.3, we see that all these modes involve ionic shifts within the *ab*-plane along with octahedral stretching or bending. Softening of the 666 cm^{-1} stretching mode below T_N is perhaps the clearest change, with a frequency shift of $\approx$ 3.7 cm^{-1}. If this were a simple binary spin system, then using $\delta\omega = \lambda\langle S_1 \cdot S_2 \rangle$ and assuming a limiting low-temperature value of the spin-spin correlation function of $S^2 = 1$ would lead to a spin-lattice coupling constant of the 666 cm^{-1} mode of approximately 3.7 cm^{-1}. [84,159,160] The coupling constants of the 310 and 597 cm^{-1} modes, 0.4 and 0.3 cm^{-1}, respectively, are estimated in a similar manner (Table 6.1). These spin-lattice coupling constants compare well with those in ferromagnetic $CrSiTe_3$ but are smaller than what is observed in $SrMnO_3$. [88,161] By contrast, spin-lattice coupling in α-$RuCl_3$ manifests primarily as a line width effect. [162] A mean-field analysis of relative slopes of the frequency vs. temperature data near T_N, including an explicit treatment of the multiple sublattices, reveals similar results as discussed below.

The other vibrational modes in Ni_3TeO_6 are insensitive to the magnetic ordering transition, with the peak position vs. temperature data following a sigmoidal Boltzmann curve that captures anharmonicity effects and the temperature dependence of short-range magnetic interactions. [88] Two examples of this behavior are shown in Fig. 6.2(b, c). Clearly the *c*-directed 171 and 214 cm^{-1} shearing displacements do

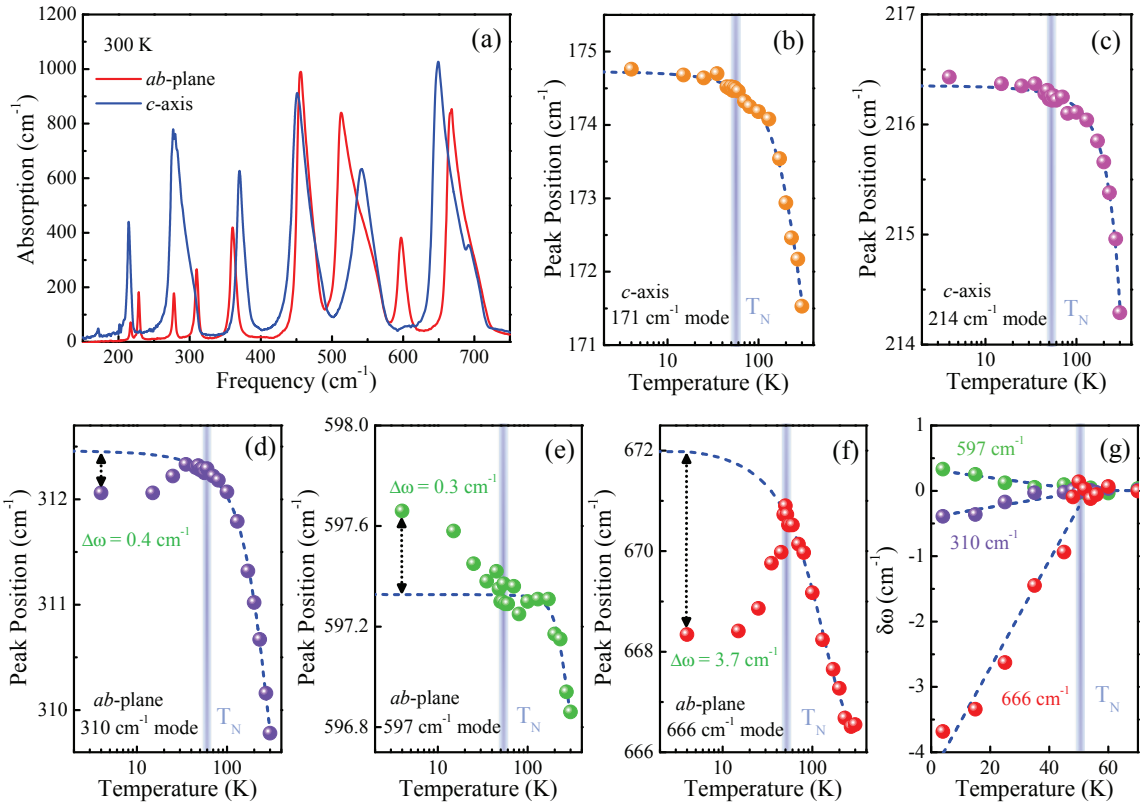


Figure 6.2: (a) Polarized infrared absorption spectrum of Ni_3TeO_6 at 300 K. (b-f) Peak position vs. temperature for several characteristic phonons. A Boltzmann sigmoid fit was used to model traditional anharmonic effects, and the difference between the low temperature limit of this model (which gives the unperturbed frequency) and the phonon position at base temperature was used to extract the frequency shifts ($\delta\omega$'s). The Néel temperature is indicated by a vertical line at 53 K. (g) Spin-lattice coupling-induced frequency shifts, $\delta\omega$'s, for the three *ab*-plane phonon modes from panels (d-f), now plotted on a linear temperature scale, together with linear fits.

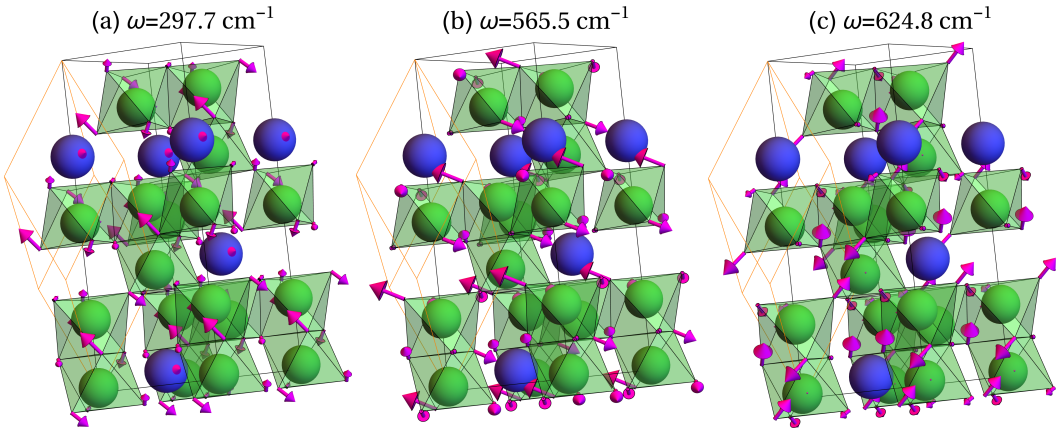


Figure 6.3: Displacement patterns for the three characteristic phonons that display large spin-lattice coupling across the Néel transition. Ni and Te ions are shown in green and blue respectively; oxygens (not drawn) are at octahedral vertices. Ionic displacements are are indicated by pink arrows whose length is proportional to the displacement. The rhombohedral unit cell, indicated by the orange lines, contains one Ni_3TeO_6 formula unit.

not display spin-lattice coupling. The rigidity of these (and other) c-directed modes is somewhat unexpected since the macroscopic polarization develops in this direction. The local lattice distortions in the ab-plane induced by the magnetic ordering, and the manner in which the displacements modify the super-exchange interactions between the magnetic centers and break inversion symmetry, clearly play a much more important role.

A generic Hamiltonian for a phonon mode with a coordinate q, mass m and frequency w is given by

$$H = \frac{p^2}{2m} + \frac{m\omega^2 q^2}{2} + \sum_{ij} \left(q\alpha_{ij} + \frac{q^2}{2}\gamma_{ij} \right) \vec{S}_i \cdot \vec{S}_j + \frac{\beta q^4}{4}, \tag{6.1}$$

where the first two terms are the kinetic and potential energy in the paramagnetic state, the term with α_{ij} describes the force on q due to Heisenberg exchange striction, and the term with γ_{ij} – the spin-dependent part of the mode stiffness. [163] As a result of magnetic ordering, the mode frequency will shift due to two reasons: (i) the

stiffness will change due to the γ_{ij} term and the force described by the α_{ij} term will shift the equilibrium position to q_0, and (ii) the anharmonic effects (term with β) will further shift the frequency. One can obtain the frequency shift by substituting $q = q_0 + \delta q$, and completing the full square in δq we obtain for the phonon frequency shift to the linear order in small α_{ij} and γ_{ij}:

$$\delta\omega = \frac{1}{2m}\left(\Gamma + \frac{3\beta A}{2m\omega^2}\right), \tag{6.2}$$

where we denote

$$A = \sum_{ij} \alpha_{ij}\vec{S}_i \cdot \vec{S}_j \tag{6.3}$$

$$\Gamma = \sum_{ij} \gamma_{ij}\vec{S}_i \cdot \vec{S}_j. \tag{6.4}$$

Above the Néel temperature $\vec{S} = 0$, while below the ordered magnetic moments grow with some critical exponent $S \sim (T_c - T)^{\nu}$. That leads to $A \sim \Gamma \sim (T_c - T)^{2\nu}$.

Since the frequency shift away from normal temperature trends due to anharmonicity and short-range magnetic interactions is related to the square of the order parameter, plots of $\delta\omega$ vs. temperature provide insight into the nature of the ordering transition. The 666 cm^{-1} NiO_6 stretching mode is most revealing in this regard. To test the predictions outlined above, we fit the experimental frequency shift $\delta\omega$ as $\alpha(T_c - T)^{2\nu}$. The results for all three of the *ab*-plane phonons that engage in spin-lattice coupling through T_N are shown in Fig. 6.2(g). We immediately observe the linear $\delta\omega$ vs. temperature relationships and exponents of 2ν that are very close to 1.0. This is consistent with expectations for a continuous second order transition. The coupling is strongest for the 666 cm^{-1} mode with $\alpha = 8 \times 10^{-2}$ cm^{-1}/K. The 310 and 597 cm^{-1} modes have α's of 8×10^{-3} and 6×10^{-3} cm^{-1}/K, respectively. [164]

When one multiplies by an appropriate temperature scale such as T_N, these α's are in good agreement with the aforementioned λ's.

As we can see from the size of the coupling constants, the 666 cm^{-1} mode dominates spin-lattice coupling through the 53 K Neél transition. This mode compresses the octahedra in the *ab* plane with out-of-phase motion between consecutive planes. [165] The latter is essentially an antiphase accordion-like pattern that modulates super-exchange between Ni1 and Ni2 in the *c* direction. This aspect of the inter-plane motion reinforces the development of the remarkable low temperature polarization.

A Kramers-Kronig analysis of the measured reflectance also provides the frequency dependent dielectric response of Ni_3TeO_6, which we can extrapolate to zero frequency for comparison with the permittivities reported in Ref. 28. Just above T_N, we find $\epsilon_1(0) = 7.6$ in the *ab*-plane, typical of a magnetic oxide, whereas $\epsilon_1(0)$ is 6.5 at 4.2 K. The difference is 1.1. The noise level is much larger in the *c*-direction. Here, we find that ϵ_1 is approximately 17.2 near T_N and about 16 at 4.2 K, giving $\Delta\epsilon_1 = 1.2$ within our sensitivity. These values of ϵ_1 are in reasonable agreement with the size and temperature dependence of the dielectric constant reported previously, [28] suggesting that there will be limited dispersion between the THz and MHz regimes. [18]

6.3 Spin-lattice coupling through the field-driven spin flop transition

We can more deeply examine the role of Heisenberg exchange striction in generating spin-lattice interactions by investigating the magnetic field-driven AFM I $\rightarrow$ AFM II spin-flop transition. Analogous to the temperature-driven PM $\rightarrow$ AFM I transition

that was modeled as $A \sim \Gamma \sim (T_c - T)^{2\nu}$ in Fig. 6.2(g), the magnetization is predicted to grow from zero as $(H - H_c)^{\mu}$ at a second-order spin-flop transition. Therefore A and Γ acquire analogous contributions, growing as $(H - H_c)^{2\mu}$. This according to Eq. 6.2 leads to $\delta\omega \sim (H - H_c)^{2\mu}$, and a cusp in $\delta\omega(H)$ should be observed. In the case of a first-order phase transition, magnetization should emerge in a jump-like fashion, and therefore a sudden jump is expected in $\delta\omega$. Furthermore, the jump must be hysteretic. This scenario describes a traditional spin-flop transition such as that found in hematite. [166–168] A second-order transition will be different in that field-induced frequency shifts and line width modifications should be continuous. We test these ideas against the behavior of several representative phonons below.

Figure 6.4(a) displays the magneto-infrared response of Ni_3TeO_6, $\Delta\alpha$ = [$\alpha(H$ = 20 T) - $\alpha(H$ = 0 T)], along with the linear absorption for comparison. Several phonons are sensitive to changes in the microscopic spin pattern across the 9 T transition. The absorption difference spectrum reveals a number of small, sharp structures below 280 cm^{-1} along with larger derivative-like features that correspond to modifications of the 310, 597, and 666 cm^{-1} modes. While the latter correspond to changes in the familiar E symmetry vibrational modes (polarized in the ab-plane), the structures below 280 cm^{-1} arise from both ab-plane and c-polarized structures with E and A symmetries, respectively (Table 6.1). No spectral hysteresis is observed, consistent with expectations for a non-hysteretic transition.

Figure 6.4(b) shows a close-up view of the field-induced absorption difference in the vicinity of the 310 cm^{-1} mode. A clear derivative-like structure develops above 9 T in the $\Delta\alpha$ spectrum. Driving through the spin-flop transition modifies both frequency and linewidth - different from the trends across the 53 K Néel transition. The field-induced frequency shift and change in line width extracted from an analysis of the 310 cm^{-1} feature are shown in Fig. 6.4(c, d). We find that $\delta\omega$ is rigid in the

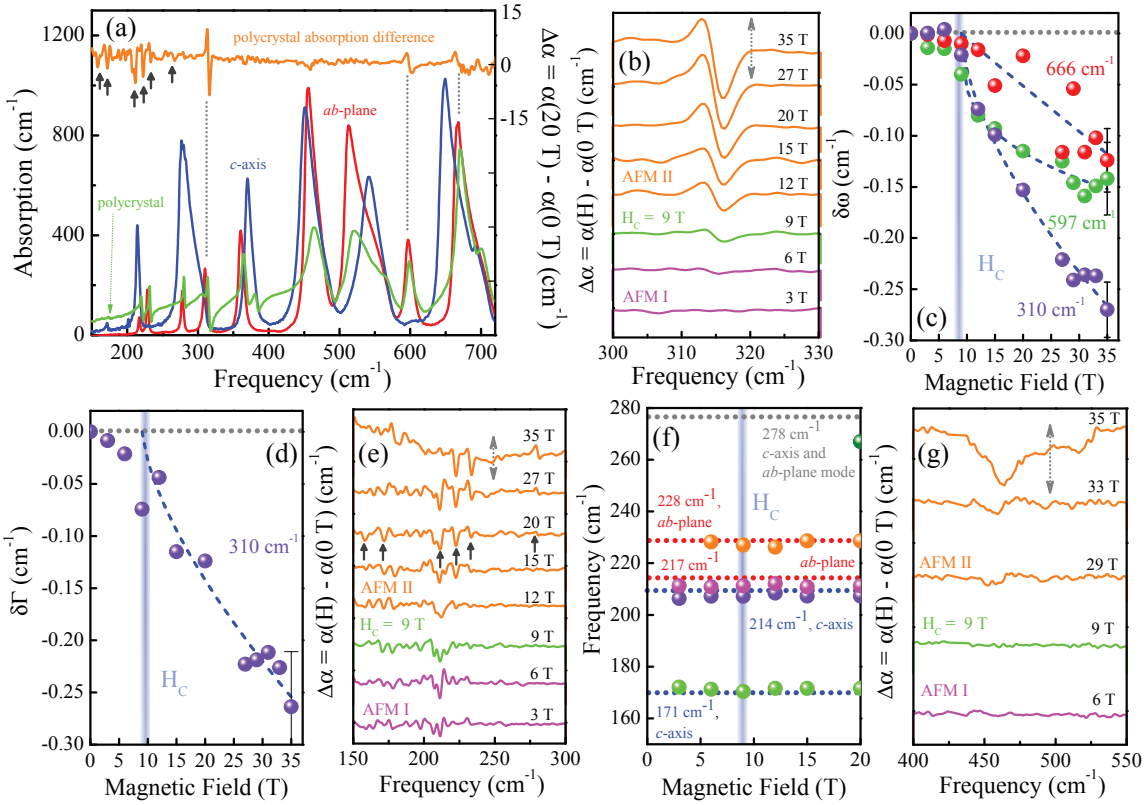


Figure 6.4: (a) Polarized infrared absorption spectrum, the polycrystal response, and the absorption difference spectrum at 20 T. The latter highlights the changes in the local lattice distortions between the AFM I and AFM II phases and is defined as $\Delta\alpha = \alpha(\omega, H) - \alpha(\omega, H = 0)$. (b, c, d) Close-up view of the field-induced absorption difference spectrum in the vicinity of the 310 cm^{-1} mode through the 9 T spin flop transition along with the field-induced frequency shift and line width changes. The curves in (b) are offset by 80 cm^{-1} for clarity, and the dotted arrow is a 20 cm^{-1} scale bar. The vertical line in (c, d) indicates the 9 T critical field. (e, f) Close-up view of the field-induced absorption difference spectra in the vicinity of the most collective vibrational modes along with a contour plot revealing the subtle frequency shifts through the spin flop transition. The curves in (e) are offset by 80 cm^{-1}, and a 20 cm^{-1} scale bar is included. (g) Waterfall plot in the vicinity of the 451 and 456 cm^{-1} modes providing evidence for an unexplored transition between 30 and 35 T. Each curve in the waterfall plot is offset by 85 cm^{-1}, and the scale bar is 20 cm^{-1}. All data was taken at 4.2 K.

AFM I phase whereas it softens with increasing field in AFM II. The latter trend is fit as $\delta\omega \sim (H - H_c)^{2\mu}$. Although the number of points in the vicinity of H_c is not enough to precisely determine the critical exponent, there is no characteristic first-order jump. The 597 and 666 cm^{-1} modes display similar behavior, although the error bars are larger. Likewise, the linewidth is relatively constant in the AFM I phase whereas it narrows with increasing field in AFM II. A fit to $\delta\Gamma \sim (H - H_c)^{2\mu}$ again yields a reasonable match (within error bars), in line with expectations for a continuous phase transition.

The absorption difference spectrum in Fig. 6.4(a) also reveals a great deal of low frequency fine structure. These features are indicated by arrows. The majority correspond to changes in the 171, 214, 217, 228, and 278 cm^{-1} fundamentals, although the 158 cm^{-1} structure, for example, is new. Figure 6.4(e) shows a close-up view of how these features change with magnetic field, and Fig. 6.4(f) diagrams the development of the magneto-infrared contrast in a more graphical way, pointing out the extent to which applied field modifies a particular feature. The zero-field phonon frequencies are indicated with horizontal dotted lines for comparison. All of these modes involve displacements of the Ni and Te centers that alter the magnetic exchange pathway between the Ni centers. Remembering that polarization is along c, these shifts of the magnetic centers along with the movement of Te ions and oxygen octahedra contribute to altering the magnetic exchange pathway and furthermore the polarization. The intermediate phase, across which the antiferromagnetic order parameter rotates continuously by 90 degrees, is narrow, and present measurements do not resolve it.

The magneto-infrared spectra also reveal the possibility of an additional, as yet unexplored, transition at higher fields. Figure 6.4(g) displays the strongest evidence for this crossover, although the absorption difference curves in Fig. 6.4(e) show

additional fine structure developing in this regime as well. These changes correlate well with a slope change in the high field magnetization, [29] which presumably corresponds to an important rotation or canting of the spin. Alternately, the high field transition may be related to elongation of the unit cell. In this scenario, zone folding will activate zone boundary modes - in addition to narrowing the 451 and 456 cm^{-1} features. Spin-lattice interactions between 30 and 35 T are probably just a prelude to more dramatic property changes at 52 T. [29] At this time, magneto-infrared experiments are limited to a max field of 45 T. A pulsed field magnet can reach higher magnetic fields, but because of the nature of infrared experiments, a steady field magnet is necessary at this time. [18]

Chapter 7

$EuTiO_3$ and Nb-substituted

Our spectroscopic work reveals the development of metallicity and its nature as a function of substitution in the $Eu(Ti_{1-x}Nb_x)O_3$ series of materials. Figure 7.1 summarizes the temperature and substitution effects including the development of structural and magnetic phase transitions. [42, 111] $EuTiO_3$ undergoes a structural transition from the high temperature cubic phase to the low temperature tetragonal phase ($Pm\bar{3}m \leftrightarrow I4/mcm$). From here, it is clear that as a function of substitution concentration, this structural transition starts below room temperature and increases to higher temperatures.

Our initial measurements proved difficult due to the increase in temperature of the structural distortion. With our lower substituted samples being in the cubic phase and our higher substitution levels in the tetragonal phase, it was difficult to identify the true room temperature spectra for each analog. Furthermore, the onset of metallicity at room temperature as well as the increase in disorder with each substitution level added to the challenge. Typically, variable temperature spectra are renormalized to the room temperature spectra, further complicating the situation.

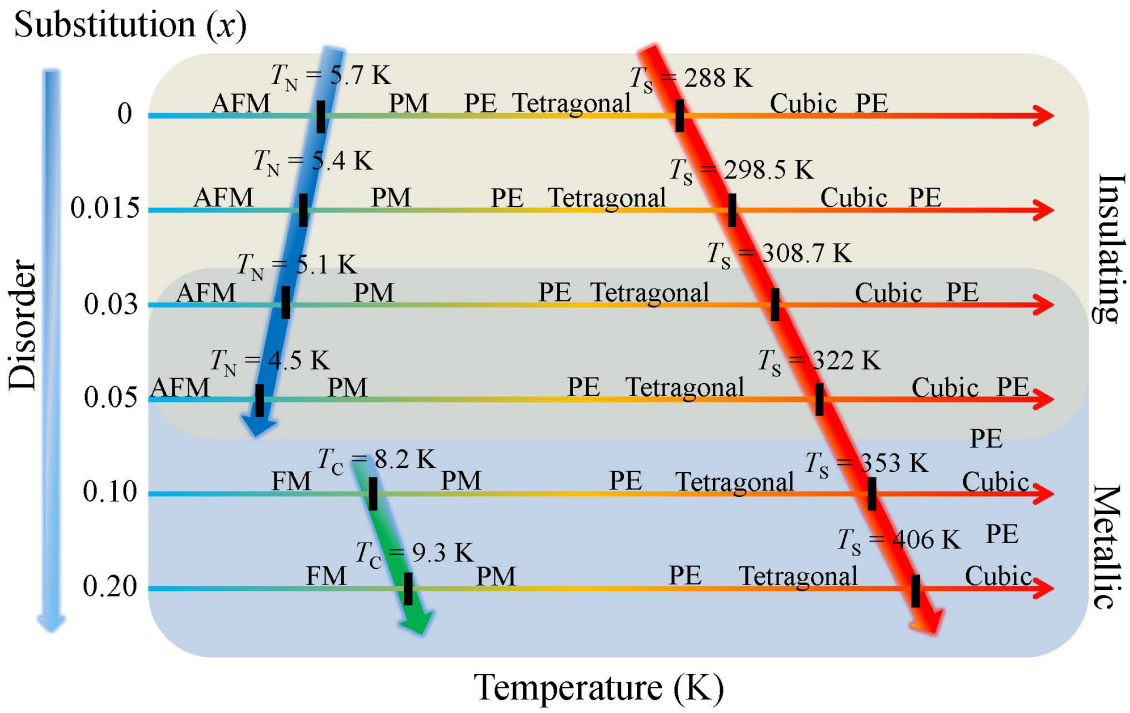


Figure 7.1: Summary of temperature and substitution effects in $Eu(Ti_{1-x}Nb_x)O_3$. The cubic to tetragonal phase transition increases in temperature as substitution increases. A crossover between an AFM and FM state occurs between $x = 0.05$ and 0.10. PE = paraelectric, PM = paramagnetic, AFM = antiferromagnetic, FM = ferromagnetic. [42, 111]

7.0.1 Variable temperature studies on $EuTiO_3$

Figure 7.2 summarizes the infrared response of $EuTiO_3$. The spectrum is that of a semiconductor with clear phonons and a flat electronic background at 300 K. Group theory predicts three infrared-active T_{1u} modes - one of which is the Slater mode. [169] We assign the feature near 530 cm^{-1} as the Ti-O stretching mode and that near 160 cm^{-1} as the Ti-O-Ti bend. The mode centered at 98 cm^{-1} involves primarily Eu motion. As a reminder, all of our work was performed on single crystals - not sintered pellets, different from prior infrared spectroscopy of $EuTiO_3$. [170, 171] As a result, we can analyze the 288 K cubic $\rightarrow$ tetragonal transition in detail. Focusing first on the 530 cm^{-1} Ti-O stretching mode, we find a small red shift in the peak position suggesting that hybridization is slightly better in the low temperature tetraganol phase of pristine $EuTiO_3$ [Fig. 7.2(b)]. We also extract phonon lifetimes (τ_{ph}'s) from fits to the Ti-O stretching mode as $\hbar/\gamma$. [172] We find that $\tau_{ph} = 0.89$ ps at room temperature. Typical values for GaAs, ZnSe, and GaP are between 2 and 10 ps, so $EuTiO_3$ is significantly shorter than these traditional semiconductors. In fact, τ_{ph} of $EuTiO_3$ at room temperature is similar to what is observed in MoS_2 nanoparticles (1.4 ps). [172] Moreover, phonon lifetimes are 22% longer in the low temperature tetragaonal phase compared with those in the high temperature (cubic) phase [Table 7.1]. We analyzed symmetry breaking across the 288 K structural distortion in $EuTiO_3$ as well. One signature of the tetraganol phase is development of a new mode near 430 cm^{-1}. This feature grows systematically with decreasing temperature - although an integrated area vs. temperature plot does not have the usual second order behavior of an order parameter. Turning our attention to the Ti-O-Ti bending mode near 160 cm^{-1}, we find that this feature develops strong doublet character with decreasing temperature in the tetraganol phase [Fig. 7.2(c)]. The splitting is extraordinarily wide - nearly 50 cm^{-1} [Fig. 7.2(d)]. A partial sum

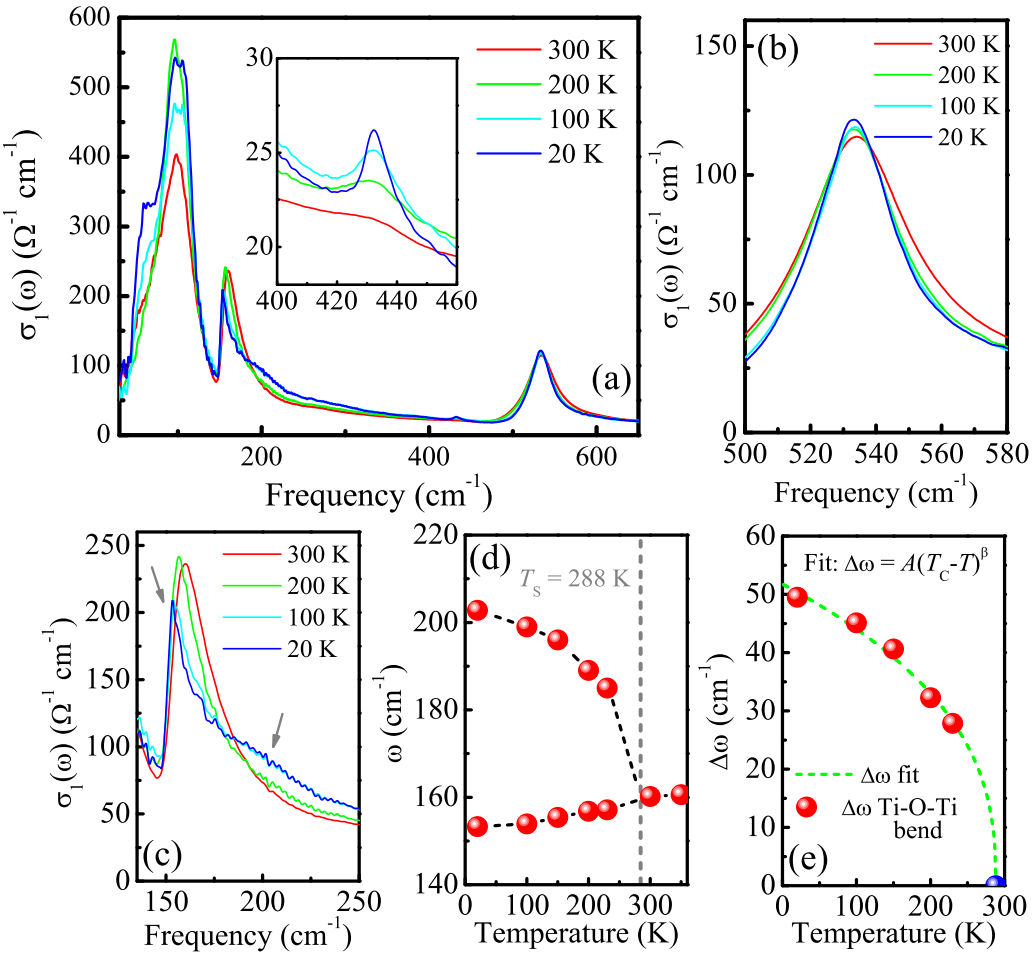


Figure 7.2: (a) Optical conductivity of $EuTiO_3$ at several different temperatures. (b,c) Close-up view of the Ti-O stretching and Ti-O-Ti bending modes, respectively. (d) Frequency vs. temperature plot of the Ti-O-Ti bending mode showing doublet splitting in the low temperature phase. The structural phase transition at 288 K is indicated, and the dotted lines guide the eye. (e) Splitting of the Ti-O-Ti bending mode vs. temperature along with a power law fit. We find $\beta = 0.39$.

Table 7.1: Phonon lifetime τ_{ph} of the Ti-O stretching mode in $EuTiO_3$ at several characteristic temperatures.

Temperature (K)	τ_{ph} (ps)
300	0.118
230	0.129
200	0.134
150	0.141
100	0.148
20	0.159

rule analysis reveals that oscillator strength is conserved over the relevant frequency window. This type of peak splitting has been shown to be proportional to the square of the order parameter in other materials likeNPrQn$(TCNQ)_2$. [173] To test this idea, we plotted the frequency difference as a function of temperature [Fig. 7.2(e)]. These data can fit to a typical power law response as $\Delta\omega = A(T_S - T)^{\beta}$, where β is the critical exponent. We find an exponent of 0.39, indicative of second order character to the structural phase transition. The Eu-containing vibrational mode near 98 cm^{-1} also displays strong splitting in the low temperature phase although the peak shape is fairly complicated - precluding a detailed analysis.

7.0.2 Development of metallicity at room temperature

Figure 7.3 gives an overview of the room temperature spectra of the $Eu(Ti_{1-x}Nb_x)O_3$ series of materials. From a group theory investigation, three infrared-active phonons are allowed in the parent compound with space group $Pm\bar{3}m$. The symmetries of these allowed modes are all T_{1u}. Evident in the optical conductivity data, we clearly observe all three of these allowed phonons. Between the parent and the $Eu(Ti_{0.985}Nb_{0.05})O_3$, the intensity of the lowest frequency phonon slightly increases.

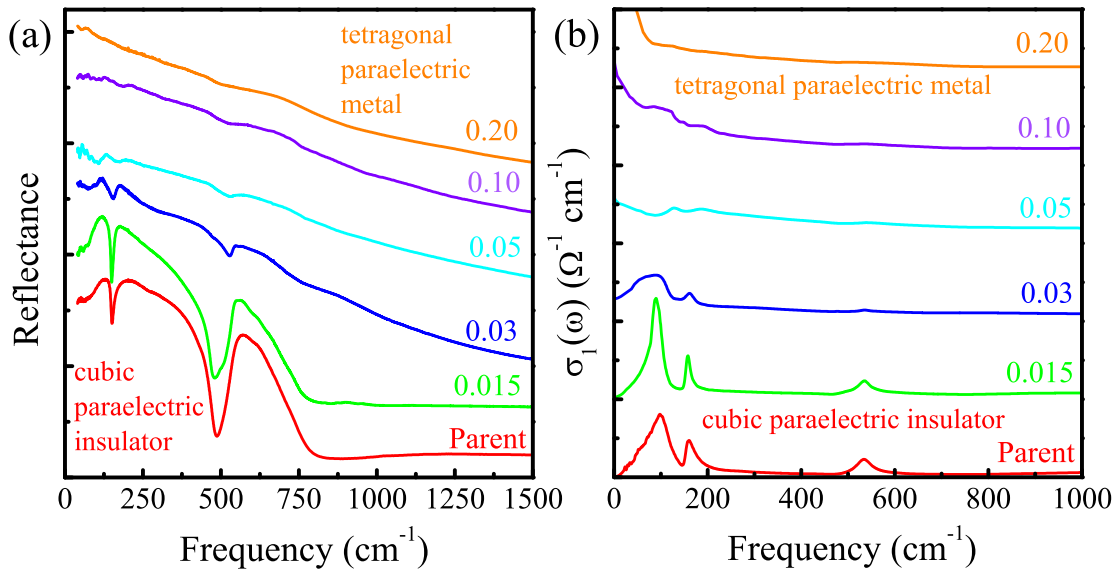


Figure 7.3: (a) Reflectance of the $Eu(Ti_{1-x}Nb_x)O_3$ series of materials at room temperature. (b) Optical conductivity of $Eu(Ti_{1-x}Nb_x)O_3$ at 300 K obtained from a Kramers-Kronig analysis of the reflectance. The spectra are offset for clarity.

Beyond the $x = 0.015$ sample and especially apparent in the $x = 0.03$ compound, there is a broadening effect of that same lowest frequency phonon, persisting throughout the rest of the series. This broadening can be related to the fact that with increasing Nb substitution, more disorder is brought into the system. However, with even higher substitution levels, the onset of metallicity begins to dominate the infrared response. We use the Drude model (below) to explain the onset of metallicity at room temperature.

In this work, we fit optical conductivity data $\sigma_1(\omega)$ at room temperature with the Drude model, where $\sigma_1(\omega) = \frac{\sigma_{DC}}{1+\tau^2\omega^2}$. From this, we extract both *dc* conductivity σ_{DC} and relaxation time τ. These parameters are summarized in Table 7.2, with prior *dc* conductivities included for comparison. [42, 111] From here, it is evident that σ_{DC} from our fit increases as a function of substitution. The fit values are somewhat different than those from literature, but the general trend is similar, with the largest increase coming between the $x = 0.1$ and 0.2 samples. Also, τ increases as a function

Table 7.2: Parameters extracted from Drude fits for $Eu(Ti_{1-x}Nb_x)O_3$ at 300 K

Substitution concentration (x)	σ_{DC} (Ω^{-1}cm^{-1}) (from literature) [42, 111]	σ_{DC}(Ω^{-1}cm^{-1}) (from fit)	τ (s) (from fit)
0	0.00285	–	–
0.015	3.5	–	–
0.03	–	102.1	8.25×10^{-14}
0.05	–	217.6	7.59×10^{-14}
0.1	743.1	309.7	1.35×10^{-13}
0.2	4420.8	1009.3	8.25×10^{-13}

of substitution concentration, with further evidence seen in the reflectance spectra. The slope of the $x = 0.2$ sample becomes sharper compared to the lesser substituted samples. Looking at the trend of τ, it is clear that the relaxation time increases with increasing Nb substitution. This can be understood as the mean free time between collisions becomes longer, which is straightforward evidence of an onset of metallicity.

Figure 7.4(a) gives an overview of the optical conductivity of each material out to higher frequencies, where the story becomes quite interesting. It is evident from the lower frequency range [Fig. 7.3] that both the $x = 0$ and 0.015 samples have no Drude response. Therefore, the inset of Fig. 7.4 is more revealing. The inset omits the $x = 0$ and 0.015 samples for ease of observation, and it is clear that the $x = 0.03$ - 0.2 samples all have Drude-like character. Actually, with increasing Nb substitution, the existence of a second Drude model may appear. Moreover, as Nb substitution increases, there may be a localized feature appearing in the optical conductivity at around 5,000 cm^{-1}, with hints being observable in the $x = 0.1$ and 0.2 samples.

To test these ideas, we take the highest substituted sample ($x = 0.2$) and fit the optical conductivity data to two different Drude models as well as a Lorentzian oscillator for the localized Nb feature. The fit is presented in Fig. 7.4(b). The lower frequency Drude is relatively sharp in width (as described earlier), so at these

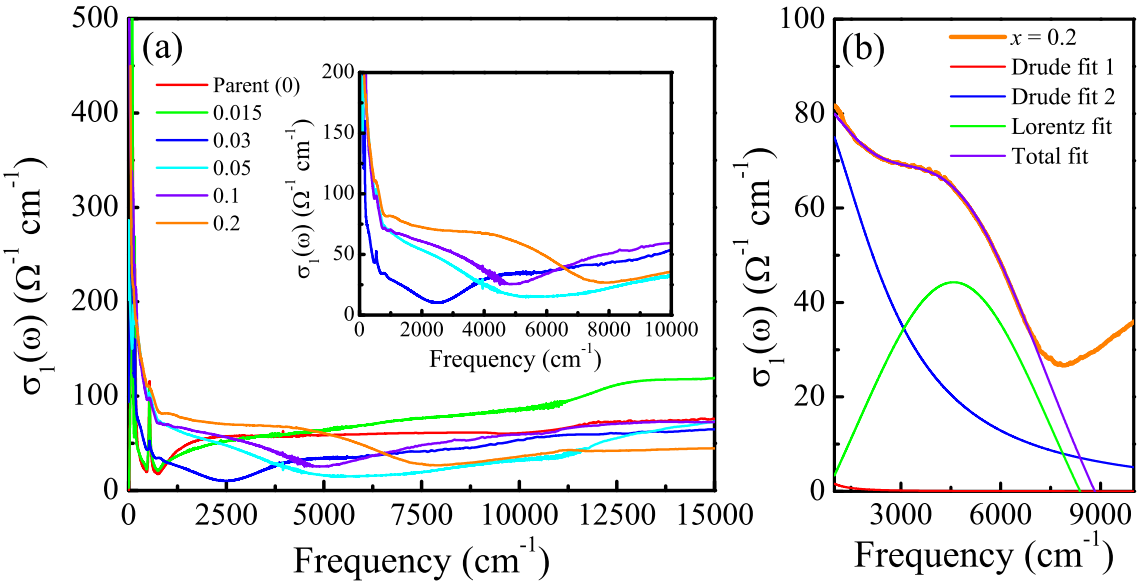


Figure 7.4: (a) Optical conductivity of the $Eu(Ti_{1-x}Nb_x)O_3$ series of materials viewing a larger frequency range. The inset shows only the $x = 0.03$, 0.05, 0.1, and 0.2 data for simplicity. (b) Fits to the $Eu(Ti_{0.8}Nb_{0.2})O_3$ data using two Drude models as well as a Lorentz model.

frequencies, the first Drude model does not contribute much to the overall strength of the optical conductivity. However, a second Drude model is used to fit the overall strength of the conductivity at these frequency ranges. Furthermore, a Lorentz model is used to fit the leftover oscillator strength in our data. Added together, it is very clear that the addition of all three of these fits provide a very accurate description of our optical conductivity data [Fig. 7.4(b)]. The presence of a localized Nb feature appears and grows as a function of Nb substitution. Above 9,000 cm^{-1}, the electronic properties begin to dominate the rest of the spectrum.

7.0.3 Comparing the cubic and tetragonal phases

The problem with only looking at room temperature spectra is that the structural transition crosses room temperature between the $x = 0.015$ to 0.05 samples. Therefore, in order to compare the onset of metallicity in both the tetragonal and cubic phases of these materials, variable temperature reflectance had to be performed. Figure 7.5 gives an overview of the reflectance of $Eu(Ti_{1-x}Nb_x)O_3$ in both the cubic and tetragonal phases. Looking at the parent compound in the high temperature cubic phase, we see that the reflectance spectra is very comparable to the room temperature spectra. This is because even at room temperature, $EuTiO_3$ is in the cubic phase. The problem begins to arise when looking at the $x = 0.015$, 0.03, and 0.05 samples. Here, the reflectance data is still very similar to the room temperature data, as only subtle changes are observed. The main differences would appear in the $x = 0.1$ and 0.2 samples, as here the samples are in their cubic phase and at room temperature they are in their tetragonal phase. However, since the Drude response is so strong, it is difficult to see many or even subtle differences in the spectra.

Moving our focus to the tetragonal phase of each system, the parent compound shows additional splitting at base temperature around 400 cm^{-1}. Again, as previ-

ously seen, this splitting systematically vanishes with increasing temperature. The additional splitting is slightly present in the $x = 0.015$ sample, but again the changes are very subtle compared to the room temperature spectra. As Nb substitution increases, we enter a phase where even at room temperature, the samples are in their tetragonal phase, so even less change is observed here. Overall, the temperature dependence of each of these systems is very minor. The major differences in this set of systems comes when comparing different degrees of Nb substitution.

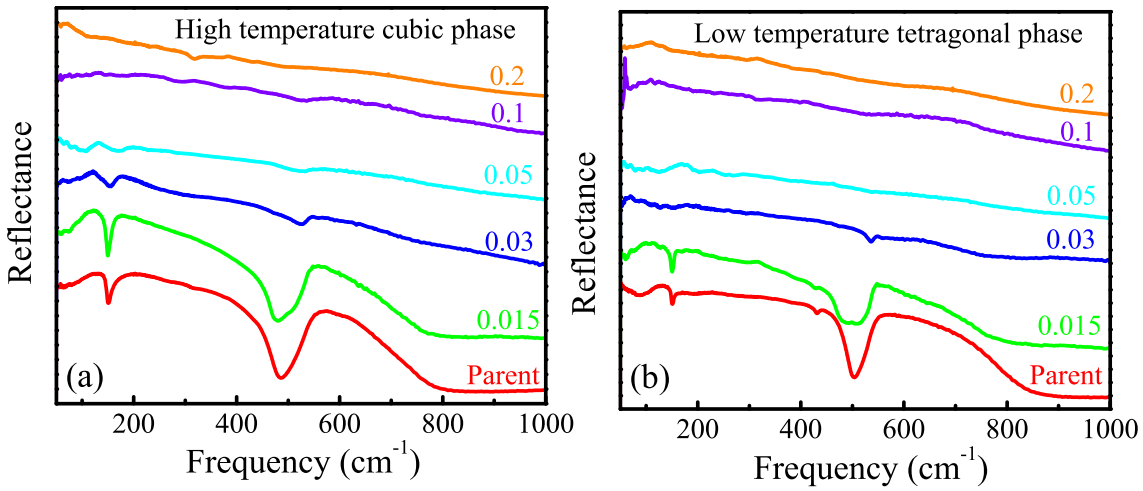


Figure 7.5: (a) Reflectance of the $Eu(Ti_{1-x}Nb_x)O_3$ series of materials well below the structural transition in the tetragonal phase (a) and well above the transition into the cubic phase (b). The spectra are offset for clarity.

Chapter 8

Summary and outlook

In this dissertation, I present the spectroscopic investigation of two different novel materials, revealing how large spin-orbit coupling and broken symmetry leads to interesting and exotic properties. While probing the phase transitions in these materials with variable temperature, applied high magnetic fields, and chemical substitution, I reveal the microscopic mechanism underlying these quantum phase transitions. These findings are important for understanding and developing novel multifunctional materials with intrinsically large coupling of orbital, lattice, spin, and charge degrees of freedom.

The first problem focuses on the magnetoelectric coupling through the spin-flop and metamagnetic transitions in Ni_3TeO_6. We bring together optical spectroscopy and first principles calculations to reveal how and why the electronic properties of Ni_3TeO_6 can be controlled by magnetic field, and we trace the color property tunability to field-induced changes in crystal field environments of the associated Ni d-to-d excitations. The decomposition of on-site excitations according to their precise local environment offers a very useful perspective on electronic excitations in magnetic materials. Here, the comparison exposes dominant Ni1$\cdots$Ni2 interactions. In addition to providing a superb platform for the exploration of coupled charge

and spin degrees of freedom, these findings reveal that the remarkable polarization properties and magnetoelectric coupling in Ni_3TeO_6 extend to much higher energies than previously supposed [28, 29]. This is interesting and important because similar energy transfer processes may exist in other materials - particularly those in which transition metal centers and heavy chalcogenide cations coexist.

The second area of investigation is one which is highly under explored. We report that the magnetically-induced changes in the d-to-d transitions in Ni_3TeO_6 include a large contribution from the magnetic matrix elements, stemming from non-vanishing atomic spin-orbit coupling. These excitations are therefore magnetoelectric. Based upon a symmetry analysis, we extended our work to search for the rare effect of nonreciprocal directional dichroism. Using unpolarized light, we observe nonreciprocal directional dichroism in two different measurement orientations and at much higher energies than typically seen. A few cases have observed a magnetochiral orientation, in which the chiral axis, light propagation k, and applied magnetic field H are all parallel to one another. We reveal this type of mechanism in Ni_3TeO_6 both with varying H and k. From a strictly symmetry perspective, we understood that all necessary symmetries are broken in a brand new transverse magnetochiral orientation, having the chiral axis of the material perpendicular to both H and k. We confirm the validity of our symmetry arguments for this orientation by revealing nonreciprocal effects in Ni_3TeO_6, again with varying both H and k. By understanding a detailed symmetry argument and how spin-orbit coupling can manifest, we provide a platform for an entirely new class of experiments to emerge on different types of magnetoelectric materials.

Our third area of investigation was in the infrared response of Ni_3TeO_6 and the $Eu(Ti_{1-x}Nb_x)O_3$ set of materials, both of which break certain symmetries and include intrinsically large spin-orbit coupling. Summarizing, vibrational property measure-

ments on Ni_3TeO_6 were brought together with complementary first principles lattice dynamics calculations and a mean field analysis to uncover the elastic properties of Ni_3TeO_6 across the Néel and spin flop transitions. Our analysis unexpectedly reveals that the 666 cm^{-1} in-plane octahedral stretching mode is most sensitive to the 53 K magnetic ordering transition, a finding that we discuss in terms of modified superexchange interactions between Ni1 and Ni2 as well as the development of the sizable polarization. At the same time, magneto-infrared spectroscopies demonstrate the gradual evolution of a number of modes across the 9 T spin flop transition, consistent with a continuous second-order mechanism and quite distinct from expectations for a first-order process. These findings reveal another aspect of magnetoelectric coupling and are important for understanding the development of large, controllable responses in Ni_3TeO_6 and other multifunctional materials. Lastly, we explored the onset of metallicity in the Nb-substituted $EuTiO_3$ system. With higher substitution concentrations, we uncover the onset of the Drude response via infrared spectroscopy. Being able to introduce itinerant electrons into a system as needed can lead to the development of materials with desirable properties. Further analysis will describe, from a microscopic viewpoint, how the onset of metallicity differs in both the cubic and tetragonal phases in this series of materials.

Taken together, these comprehensive findings give insight into the interplay between spin, charge, orbital, and lattice degrees of freedom in multifunctional materials. With the application of external magnetic fields, we can identify collective transitions (such as a magnetic spin reorientation) and how they change the material optically. This can lead to the development of next generation color change materials. Also, with correct symmetry stipulations, new materials can be designed to enhance one-way transparency in desirable energy regions. This could be highly advantageous in applications. Furthermore, they motivate fundamental research on

other complex oxides under extreme conditions and away from the static limit.

Bibliography

[1] I. Kanno, S. Fujii, T. Kamada, and R. Takayama. Applied Physics Letters, **70**, 1378 (1997).

[2] T.-g. Lee, H.-j. Lee, S.-w. Kim, D.-h. Kim, S. Ho, H.-w. Kang, C.-y. Kang, and S. Nahm. Journal of the European Ceramic Society, **37**, 3935 (2017).

[3] P. Zubko, S. Gariglio, M. Gabay, P. Ghosez, and J.-m. Triscone. Annual Review Condensed Matter Physics, **2**, 141 (2011).

[4] A. P. Ramirez. Journal of Physics: Condensed Matter, **9**, 8171 (1997).

[5] Y. Wang, G. L. Pascut, B. Gao, T. A. Tyson, K. Haule, V. Kiryukhin, and S.-w. Cheong. Scientific Reports, **5**, 12268 (2015).

[6] T. Kurumaji, S. Ishiwata, and Y. Tokura. Physical Review X, **5**, 031034 (2015).

[7] T. Isono, D. Iguchi, T. Matsubara, Y. Machida, B. Salce, J. Flouquet, H. Ogusu, J.-i. Yamaura, Z. Hiroi, and K. Izawa. Journal of the Physical Society of Japan, **82**, 114708 (2013).

[8] M. H. Hamidian, S. D. Edkins, C. K. Kim, J. C. Davis, A. P. Mackenzie, H. Eisaki, S. Uchida, M. J. Lawler, E. Kim, S. Sachdev, and K. Fujita. Nature Physics, **12**, 150 (2016).

[9] S. Sachdev. Phil. Trans. R. Soc. A, **374**, 20150248 (2016).

[10] M. H. Phan, N. A. Frey, M. Angst, J. D. Groot, B. C. Sales, D. G. Mandrus, and H. Srikanth. Solid State Communications, **150**, 341 (2010).

[11] A. H. Arkenbout, T. T. M. Palstra, T. Siegrist, and T. Kimura. Physical Review B, **74**, 184431 (2006).

[12] F. Ye, S. Chi, J. A. Fernandez-baca, H. Cao, K. Liang, Y. Wang, B. Lorenz, and C. W. Chu. Physical Review B, **86**, 094429 (2012).

[13] H. Szymczak. Journal of Magnetism and Magnetic Materials, **211**, 186 (2000).

[14] D. N. Basov, R. D. Averitt, and D. Hsieh. Nature Materials, **16**, 1077 (2017).

[15] N. W. Ashcroft and N. D. Mermin. *Solid state physics*. Brooks Cole (1976).

[16] T. V. Brinzari, P. Chen, Q. Sun, J. Liu, L. Tung, Y. Wang, J. A. Schlueter, J. Singleton, J. L. Manson, M. Whangbo, A. P. Litvinchuk, and J. L. Musfeldt. Physical Review Letters, **110**, 237202 (2013).

[17] K. D. Hughey, A. J. Clune, M. O. Yokosuk, K. R. O. Neal, S. Fan, N. Abhyankar, H. Xiang, Z. Li, J. Singleton, N. S. Dalal, and J. L. Musfeldt. Physical Review B, **96**, 180305(R) (2017).

[18] M. O. Yokosuk, S. Artyukhin, X. Wang, J. Yang, Z. Li, S.-W. Cheong, D. Vanderbilt, and J. L. Musfeldt. Physical Review B, **92**, 144305 (2015).

[19] P. Chen, X. Xu, C. Koenigsmann, A. C. Santulli, S. S. Wong, and J. L. Musfeldt. Nano Letters, **10**, 4526 (2010).

[20] X. S. Xu, T. V. Brinzari, S. Lee, Y. H. Chu, L. W. Martin, A. Kumar, S. McGill, R. C. Rai, R. Ramesh, V. Gopalan, S. W. Cheong, and J. L. Musfeldt. Physical Review B, **79**, 134425 (2009).

[21] P. Chen, N. Lee, S. McGill, S. Cheong, and J. L. Musfeldt. Physical Review B, **85**, 174413 (2012).

[22] P. G. Russell, D. S. McClure, and J. W. Stout. Physical Review Letters, **16**, 176 (1966).

[23] V. V. Eremenko, Y. G. Litvinenko, and V. I. Myatlik. Journal of Experimental and Theoretical Physics Letters, **12** (1970).

[24] V. V. Eremenko and E. G. Petrov. Advances in Physics, **26**, 31 (1977).

[25] L. D. Landau and E. M. Lifshitz. *Quantum Mechanics: Non-relativistic Theory.* Pergamon Press, second ed. (1981).

[26] K. V. Shanavas, Z. S. Popović, and S. Satpathy. Physical Review B, **90**, 165108 (2014).

[27] X. Wang, F.-T. Huang, J. Yang, Y. S. Oh, and S.-W. Cheong. APL Materials, **3**, 076105 (2015).

[28] Y. S. Oh, S. Artyukhin, J. J. Yang, V. Zapf, J. W. Kim, D. Vanderbilt, and S.-W. Cheong. Nature Communications, **5**, 3201 (2014).

[29] J. W. Kim, S. Artyukhin, E. D. Mun, M. Jaime, N. Harrison, A. Hansen, J. J. Yang, Y. S. Oh, D. Vanderbilt, V. S. Zapf, and S.-W. Cheong. Physical Review Letters, **115**, 137201 (2015).

[30] I. Kézsmárki, D. Szaller, S. Bordács, V. Kocsis, Y. Tokunaga, Y. Taguchi, H. Murawake, Y. Tokura, H. Engelkamp, T. Rõõm, and U. Nagel. Nature Communications, **5**, 3203 (2014).

[31] S.-W. Cheong, D. Talbayev, V. Kiryukhin, and A. Saxena. npj Quantum Materials, **19**, 1 (2018).

[32] I. Kézsmárki, U. Nagel, S. Bordács, R. S. Fishman, J. H. Lee, H. T. Yi, S. Cheong, and T. Rõõm. Physical Review Letters, **115**, 127203 (2015).

[33] J. H. Lee, I. Kézsmáki, and R. S. Fishman. New Journal of Physics, **18**, 043025 (2016).

[34] S. Bordács, V. Kocsis, Y. Tokunaga, U. Nagel, T. Rõõm, Y. Takahashi, Y. Taguchi, and Y. Tokura. Physical Review B, **92**, 214441 (2015).

[35] S. Yu, B. Gao, J. W. Kim, S.-W. Cheong, M. K. L. Man, J. Madéo, K. M. Dani, and D. Talbayev. Physical Review Letters, **120**, 037601 (2018).

[36] S. Bordács, I. Kézsmárki, D. Szaller, L. Demkó, N. Kida, H. Murakawa, Y. Onose, R. Shimano, T. Rõõm, U. Nagel, S. Miyahara, N. Furukawa, and Y. Tokura. Nature Physics, **8**, 734 (2012).

[37] I. Kézsmárki, N. Kida, H. Murakawa, S. Bordács, Y. Onose, and Y. Tokura. Physical Review Letters, **106**, 057403 (2011).

[38] M. M. Qazilbash, M. Brehm, B.-G. Chae, P.-C. Ho, G. O. Andreev, B.-J. Kim, S. J. Yun, A. V. Balatsky, M. B. Maple, F. Keilimann, H.-T. Kim, and D. N. Basov. Science, **318**, 1750 (2007).

[39] A. Sharoni, J. G. Ramírez, and I. K. Schuller. Physical Review Letters, **101**, 026404 (2008).

[40] D. Bessas, K. Z. Rushchanskii, M. Kachlik, S. Disch, O. Gourdon, J. Bednarcik, K. Maca, I. Sergueev, S. Kamba, M. Ležaić, and R. P. Hermann. Physical Review B, **88**, 144308 (2013).

[41] A. Bussmann-Holder, J. Köhler, R. K. Kremer, and J. M. Law. Physical Review B, **83**, 212102 (2011).

[42] L. Li, J. R. Morris, M. R. Koehler, Z. Dun, H. Zhou, J. Yan, D. Mandrus, and V. Keppens. Physical Review B, **92**, 024109 (2015).

[43] J. Tauc. Materials Research Bulletin, **3**, 37 (1968).

[44] S. Kimiagar and F. Abrinaei. Nanophotonics (2017).

[45] M. Meinert and G. Reiss. Journal of Physics: Condensed Matter, **26**, 115503 (2014).

[46] N. Ghobadi. International Nano Letters, **3**, 2 (2013).

[47] T. Zhu, W. L. Ong, L. Zhu, and G. W. Ho. Nature Publishing Group, **5**, 10601 (2015).

[48] S. Blundell. *Magnetism in Condensed Matter*. Oxford University Press Inc., New York (2001).

[49] F. A. Cotton. *Chemical Applications of Group Theory*. A Wiley-Interscience Publication, third ed. (1990).

[50] D. A. McQuarrie. *Quantum Chemistry*. University Science Books, second ed. (2008).

[51] B. J. Kim, H. Jin, S. J. Moon, J. Kim, B. Park, C. S. Leem, J. Yu, T. W. Noh, C. Kim, S. Oh, J. Park, V. Durairaj, G. Cao, and E. Rotenberg. Physical Review Letters, **101**, 076402 (2008).

[52] K. Rossnagel and N. V. Smith. Physical Review B, **73**, 073106 (2006).

[53] H. J. Xiang and M.-H. Whangbo. Physical Review B, **75**, 052407 (2007).

[54] D. J. Singh, P. Blaha, K. Schwarz, and J. O. Sofo. Physical Review B, **65**, 155109 (2002).

[55] J. B. Goodenough. *Magnetism and the Chemical Bond*. Interscience Publishers, New York - London (1963).

[56] A. M. Kadomtseva, A. K. Zvezdin, A. P. Pyatakov, Y. F. Popov, A. P. Pyatakov, and G. P. Vorob'ev. Journal of Experimental and Theoretical Physics Letters, **79**, 571 (2004).

[57] B. Ruette, S. Zvyagin, A. P. Pyatakov, A. Bush, J. F. Li, V. I. Belotelov, A. K. Zvezdin, and D. Viehland. Physical Review B, **69**, 064114 (2004).

[58] Y. Togawa, T. Koyama, K. Takayanagi, S. Mori, Y. Kousaka, J. Akimitsu, S. Nishihara, K. Inoue, A. S. Ovchinnikov, and J. Kishine. Physical Review Letters, **108**, 107202 (2012).

[59] P. Chen, B. S. Holinsworth, K. R. O'Neal, T. V. Brinzari, D. Mazumdar, Y. Q. Wang, S. McGill, R. J. Cava, B. Lorenz, and J. L. Musfeldt. Physical Review B, **89**, 165120 (2014).

[60] N. A. Spaldin and M. Fiebig. Science, **309**, 391 (2005).

[61] N. A. Spaldin, S.-W. Cheong, and R. Ramesh. Physics Today, **October**, 38 (2010).

[62] D. Khomskii. Physics, **2**, 20 (2009).

[63] W. Eerenstein, N. D. Mathur, and J. F. Scott. Nature, **442**, 759 (2006).

[64] S.-W. Cheong and M. Mostovoy. Nature Materials, **6**, 13 (2007).

[65] J. M. Rondinelli, A. S. Eidelson, and N. A. Spaldin. Physical Review B, **79**, 205119 (2009).

[66] I. B. Bersuker. Journal of Physics: Conference Series, **428**, 012028 (2013).

[67] N. A. Hill. Journal of Physical Chemistry B, **104**, 6694 (2000).

[68] F. Kubel and H. Shmid. Acta Crystallographica, **B46**, 698 (1990).

[69] J. Wang, J. B. Neaton, H. Zheng, V. Nagarajan, S. B. Ogale, B. Liu, D. Viehland, V. Vaithyanathan, D. G. Schlom, U. V. Waghmare, N. A. Spaldin, K. M. Rabe, M. Wuttig, and R. Ramesh. Science, **299**, 1719 (2003).

[70] T. Kimura, T. Goto, H. Shintani, K. Ishizaka, T. Arima, and Y. Tokura. Nature, **426**, 55 (2003).

[71] H. Schmid. International Journal of Magnetism, **4**, 337 (1973).

[72] E. Ascher, H. Rieder, H. Schmid, and H. Stössel. Journal of Applied Physics, **37**, 1404 (1966).

[73] S. Shen, Y. Chai, and Y. Sun. Scientific Reports, **5**, 8254 (2015).

[74] V. N. Muthukumar, R. Valent, and C. Gros. Physical Review B, **54**, 433 (1996).

[75] D. Szaller, S. Bordács, and I. Kézsmárki. Physical Review B, **87**, 014421 (2013).

[76] J. H. Jung, M. Matsubara, T. Arima, J. P. He, Y. Kaneko, and Y. Tokura. Physical Review Letters, **93**, 037403 (2004).

[77] M. Saito, K. Ishikawa, K. Taniguchi, and T. Arima. Physical Review Letters, **101**, 117402 (2008).

[78] A. G. Olabi and A. Grunwald. Materials and Design, **29**, 469 (2008).

[79] A. V. Andreev and N. V. Mushnikov. *Concise encyclopedia of magnetic and superconducting materials*. Elsevier, Amsterdam, 2nd ed. (2005).

[80] E. W. Lee. Reports on Progress in Physics, **18**, 184 (1955).

[81] L. Gunther. Physical Review B, **14**, 3007 (1976).

[82] J. W. Bray, L. V. Interrante, I. S. Jacobs, and J. Bonner. *Extended Linear Chain Compounds*. Plenum, New York, 3rd ed. (1983).

[83] M. Hase, I. Terasaki, and K. Uchinokura. Physical Review Letters, **70**, 3651 (1993).

[84] A. B. Sushkov, O. Tchernyshyov, W. R. Ii, S. W. Cheong, and H. D. Drew. Physical Review Letters, **94**, 137202 (2005).

[85] J. Lockwood and M. G. Cottam. Journal of Applied Physics, **64**, 5867 (1988).

[86] X. K. Chen, J. C. Irwin, and J. P. Franck. Physical Review B, **52**, 130 (1995).

[87] J. S. Lee, T. W. Noh, J. S. Bae, I.-s. Yang, T. Takeda, and R. Kanno. Physical Review B, **69**, 214428 (2004).

[88] L. D. Casto, A. J. Clune, M. O. Yokosuk, J. L. Musfeldt, T. J. Williams, H. L. Zhuang, M. Lin, K. Xiao, B. C. Sales, J. Yan, and D. Mandrus. APL Materials, **3**, 041515 (2015).

[89] J. H. Lee, L. Fang, E. Vlahos, X. Ke, Y. W. Jung, L. F. Kourkoutis, J.-W. Kim, P. J. Ryan, T. Heeg, M. Roeckerath, V. Goian, M. Bernhagen, J. W. Freeland, R. Uecker, P. C. Hammel, K. M. Rabe, S. Kamba, D. A. Muller, C. J. Fennie, P. Schiffer, V. Gopalan, E. Johnston-Halperin, and D. G. Schlom. Nature Letters, **466**, 954 (2010).

[90] T. V. Brinzari, J. T. Haraldsen, P. Chen, Q. Sun, Y. Kim, L. Tung, A. P. Litvinchuk, J. A. Schlueter, D. Smirnov, J. L. Manson, J. Singleton, and J. L. Musfeldt. Physical Review Letters, **111**, 047202 (2013).

[91] E. Granado, A. García, J. A. Sanjuro, C. Rettori, I. Torriani, F. Prado, R. D. Sánchez, A. Caneiro, and S. B. Oseroff. Physical Review B, **60**, 11879 (1999).

[92] I. Živković, K. Prša, O. Zaharko, and H. Berger. Journal of Physics: Condensed Matter, **22**, 056002 (2010).

[93] M. O. Yokosuk, S. Artyukhin, K. R. O. Neal, D. Mazumdar, P. Chen, J. Yang, Y. S. Oh, S. A. McGill, K. Haule, S.-W. Cheong, D. Vanderbilt, and J. L. Musfeldt. Physical Review Letters, **117**, 147402 (2016).

[94] Y.-H. Chu, L. W. Martin, M. B. Holcomb, M. Gajek, S.-J. Han, Q. He, N. Balke, C.-H. Yang, D. Lee, W. E. I. Hu, Q. Zhan, P.-L. Yang, A. Fraile-Rodriguez, A. Scholl, S. X. Wang, and R. Ramesh. Nature Materials, **7**, 478 (2008).

[95] R. de Sousa, M. Allen, and M. Cazayous. Physical Review Letters, **110**, 267202 (2013).

[96] J. H. Lee and K. M. Rabe. Physical Review Letters, **104**, 207204 (2010).

[97] C. Becher, L. Maurel, U. Aschauer, M. Lilienblum, C. Magén, D. Meier, E. Langenberg, M. Trassin, J. Blasco, I. P. Krug, P. A. Algarabel, N. A. Spaldin, J. A. Pardo, and M. Fiebig. Nature Nanotechnology, **10**, 661 (2015).

[98] N. A. Benedek and C. J. Fennie. Physical Review Letters, **106**, 107204 (2011).

[99] N. A. Benedek, J. M. Rondinelli, H. Djani, P. Ghosez, and P. Lightfoot. Dalton Transactions, **44**, 10543 (2015).

[100] Y. S. Oh, X. Luo, F.-T. Huang, Y. Wang, and S.-W. Cheong. Nature Materials, **14**, 407 (2015).

[101] J. A. Mundy, C. M. Brooks, M. E. Holtz, J. A. Moyer, H. Das, A. F. Rébola, J. T. Heron, J. D. Clarkson, S. M. Disseler, Z. Liu, A. Farhan, R. Held, R. Hovden, E. Padgett, Q. Mao, H. Paik, R. Misra, L. F. Kourkoutis, E. Arenholz,

A. Scholl, J. A. Borchers, W. D. Ratcliff, R. Ramesh, C. J. Fennie, P. Schiffer, D. A. Muller, and D. G. Schlom. Nature, **537**, 523 (2016).

[102] K. Xu, X.-Z. Lu, and H. Xiang. npj Quantum Materials, **2**, 1 (2017).

[103] C. J. Fennie and K. M. Rabe. Physical Review Letters, **97**, 267602 (2006).

[104] D. S. Ellis, H. Uchiyama, S. Tsutsui, K. Sugimoto, K. Kato, D. Ishikawa, and A. Q. R. Baron. Physical Review B, **86**, 220301(R) (2012).

[105] L. J. Spalek, S. S. Saxena, C. Panagopoulos, T. Katsufuji, J. A. Schiemer, and M. A. Carpenter. Physical Review B, **90**, 054119 (2014).

[106] J. Schiemer, L. J. Spalek, S. S. Saxena, C. Panagopoulos, T. Katsufuji, and M. A. Carpenter. Euro Physics Letters, **109**, 57004 (2015).

[107] T. Katsufuji and H. Takagi. Physical Review B, **64**, 054415 (2001).

[108] J.-W. Kim, P. Thompson, S. Brown, P. S. Normile, J. A. Schlueter, A. Shkabko, A. Weidenkaff, and P. J. Ryan. Physical Review Letters, **110**, 027201 (2013).

[109] P. J. Ryan, J.-W. Kim, T. Birol, P. Thompson, J.-H. Lee, X. Ke, P. S. Normile, E. Karapetrova, P. Schiffer, S. D. Brown, C. J. Fennie, and D. G. Schlom. Nature Communications, **4**, 1334 (2013).

[110] P. Parisiades, E. Liarokapis, J. Köhler, A. Bussmann-Holder, and M. Mezouar. Physical Review B, **92**, 064102 (2015).

[111] L. Li, H. Zhou, J. Yan, D. Mandrus, V. Keppens, L. Li, H. Zhou, J. Yan, and D. Mandrus. APL Materials, **2**, 110701 (2014).

[112] F. Wooten. *Optical Properties of Solids* (1972).

[113] H. Kuzmany. *Solid-State Spectroscopy.* Springer, Berlin, second ed. (2009).

[114] J. R. Ferraro, K. Nakamoto, and C. W. Brown. *Introductory Raman Spectroscopy*. Academic Press, San Diego, second ed. (2003).

[115] K. D. Mielenz. Journal of Research of the National Bureau of Standards, **76A**, 455 (1972).

[116] K. D. Mielenz and R. Mavrodineanu. Journal of Research of the National Bureau of Standards, **77A**, 699 (1973).

[117] R. M. Dreizler and E. K. U. Gross. *Density Functional Theory*. Springer (1990).

[118] R. G. Parr and Y. Weitao. *Density-functional Theory of Atoms and Molecules*. Oxford University Press Inc. (1994).

[119] P. Fulde. *Electron Correlations in Molecules and Solids*. Springer (1995).

[120] A. Georges and G. Kotliar. Physical Review B, **45**, 6479 (1992).

[121] P. R. Griffiths and J. A. de Haseth. *Fourier transform infrared spectrometry*. Jon Wiley and Sons Inc., Hoboken, 2nd ed. (2007).

[122] K. Dewhurst, S. Sharma, L. Nordström, F. Cricchio, F. Bultmark, O. Grånäs, H. Gross, C. Ambrosch-Draxl, C. Persson, C. Brouder, *et al.* The Elk FP-LAPW Code. 2015. http://elk.sourceforge.net.

[123] F. Bultmark, F. Cricchio, O. Grånäs, and L. Nordström. Physical Review B, **80**, 035121 (2009).

[124] V. I. Anisimov, I. V. Solovyev, M. A. Korotin, M. T. Czyżyk, and G. A. Sawatzky. Physical Review B, **48**, 16929 (1993).

[125] J. P. Perdew and Y. Wang. Physical Review B, **45**, 244 (1992).

[126] A. Togo, F. Oba, and I. Tanaka. Physical Review B, **78**, 134106 (2008).

[127] G. Kresse and J. Hafner. Physical Review B, **47**, 558 (1993).

[128] G. Kresse and J. Hafner. Physical Review B, **49**, 14251 (1994).

[129] G. Kresse and J. Furthmiiller. Computational Materials Science, **6**, 15 (1996).

[130] G. Kresse and J. Furthmu. Physical Review B, **54**, 169 (1996).

[131] P. E. Blöchl. Physical Review B, **50**, 17953 (1994).

[132] PAW_GGA Ni_pv 19Apr2000; PAW_GGA Te 07Sep2001; PAW_GGA O 05Jan2001.

[133] A. Migliori, J. L. Sarrao, W. M. Visscher, T. M. Bell, M. Lei, Z. Fisk, and R. G. Leisure. Phisica B, **183**, 1 (1993).

[134] F. Wu, E. Kan, C. Tian, and M.-h. Whangbo. Inorganic Chemistry, **49**, 7545 (2010).

[135] C. J. Ballhausen. *Introduction to ligand field theory.* McGraw-Hill, New York (1962).

[136] R. Eder. In E. Pavarini, E. Koch, F. Anders, and M. Jarrell (editors), *Correlated Electrons: From Models to Materials*, vol. 2, chap. 8. Forschungszentrum Jülich GmbH, Verlag (2012).

[137] S. L. Reddy, T. Endo, and G. S. Reddy. In M. A. Farrukh (editor), *Advanced Aspects of Spectroscopy*, chap. 1. IntechOpen, Rijeka (2012).

[138] Ni1 is strongly distorted, Ni2 is the most symmetric C_3 site, and Ni3 is the most distorted of all.

[139] Additional resolution is requred to track changes in the exciton and phonon sidebands in applied field.

[140] In the calculated results, the SF phase is separated into SF_1 and SF_2 to see how the spectrum changes from just after the spin-flop transition and directly before the metamagnetic transition.

[141] Y. Tokura and N. Nagaosa. Nature Communications, **9**, 3740 (2018).

[142] F. Qin, W. Shi, T. Ideue, M. Yoshida, A. Zak, R. Tenne, T. Kikitsu, D. Inoue, D. Hashizume, and Y. Iwasa. Nature Communications, **8**, 14465 (2017).

[143] C. Stock, R. D. Johnson, N. Giles-Donovan, M. Songvilay, J. A. Rodriguez-Rivera, N. Lee, P. Radaelli, L. Chapon, A. Bombardi, S. Cochran, C. Niedermayer, A. Schneidewind, Z. Husges, Z. Lu, S. Meng, and S. W. Cheong. under preparation (2019).

[144] V. P. Kravchuk, U. K. Rößler, J. van den Brink, and M. Garst. arXiv:1902.01420v1 (2019).

[145] G. L. J. A. Rikken, C. Strohm, and P. Wyder. Physical Review Letters, **89**, 13 (2002).

[146] M. Saito, K. Taniguchi, and T.-h. Arima. Journal of the Physical Society of Japan, **77**, 013705 (2008).

[147] G. L. J. A. Rikken and E. Raupach. Nature, **390**, 493 (1997).

[148] S. Toyoda, N. Abe, S. Kimura, Y. H. Matsuda, T. Nomura, A. Ikeda, S. Takeyama, and T. Arima. Physical Review B, **115**, 267207 (2015).

[149] For the oscillator strength analysis, $\Delta f_{NDD} = \frac{2c}{N_e \pi \omega_p^2} \int_{E_1}^{E_2} n \Delta \alpha_{NDD}(E) dE$, where N_e is the number of electrons per Ni site, n is the refractive index, ω_p is the plasma frequency $\omega_p \equiv \sqrt{\frac{e^2 \rho}{m \epsilon_0}}$, e and m are the charge and mass of

an electron, ϵ_0 is the vacuum dielectric constant, ρ is the density of Ni sites, c is the speed of light, and E_1 and E_2 are the energy limits of integration.

[150] J. Hlinka. Physical Review Letters, **113**, 165502 (2014).

[151] R. S. Meltzer, M. Lowe, and D. S. McClure. Physical Review, **180**, 561 (1969).

[152] M. O. Ramirez, A. Kumar, S. A. Denev, N. J. Podraza, X. S. Xu, R. C. Rai, Y. H. Chu, J. Seidel, L. W. Martin, S. Yang, E. Saiz, J. F. Ihlefeld, S. Lee, J. Klug, S. W. Cheong, M. J. Bedzyk, O. Auciello, D. G. Schlom, R. Ramesh, J. Orenstein, J. L. Musfeldt, and V. Gopalan. Physical Review B, **79**, 224106 (2009).

[153] R. M. Hochstrasser and P. N. Prasad. The Journal of Chemical Physics, **56**, 2814 (1972).

[154] D. Christiansen, M. Selig, G. Berghäuser, R. Schmidt, I. Niehues, R. Schneider, A. Arora, S. M. de Vasconcellos, R. Bratschitsch, E. Malic, and A. Knorr. Physical Review Letters, **119**, 187402 (2017).

[155] R. Becker and H. Berger. Acta crystallographica, **E62**, i222 (2006).

[156] G. Blasse and W. Hordijk. Journal of Solid State Chemistry, **5**, 395 (1972).

[157] S. Skiadopoulou, F. Borodavka, C. Kadlec, F. Kadlec, M. Retuerto, Z. Deng, M. Greenblatt, and S. Kamba. Physical Review B, **95**, 1844353 (2017).

[158] K. R. O'Neal, A. J. Clune, N. C. Harms, S.-w. Cheong, J. Yang, Z. Liu, T. Birol, and J. L. Musfeldt. Physical Review B, **98**, 184101 (2018).

[159] C. J. Fennie and K. M. Rabe. Physical Review Letters, **96**, 205505 (2006).

[160] T. Rudolf, F. Mayr, J. Hemberger, V. Tsurkan, and A. Loidl. Physical Review B, **76**, 174307 (2007).

[161] S. Kamba, V. Goian, V. Skoromets, J. Hejtmánek, V. Bovtun, M. Kempa, F. Borodavka, P. Vaněk, A. A. Belik, J. H. Lee, O. Pacherová, and K. M. Rabe. Physical Review B, **89**, 064308 (2014).

[162] L. J. Sandilands, Y. Tian, K. W. Plumb, and Y.-J. Kim. Physical Review Letters, **114**, 147201 (2015).

[163] We assume a phonon irrep for which q^3 terms vanish by symmetry.

[164] Examination of the displacement patterns reveals that all three modes either shift the Ni^I center or modify the environment around Ni^I and Ni^{II}. The magnetic interaction between these centers is strong because the octahedra share edges.

[165] This is different from the 597 cm^{-1} mode which also modulates the octahedra and has an in-phase relationship between consecutive layers.

[166] S. Foner and Y. Shapira. Physics Letters A, **29**, 276 (1969).

[167] Y. Shapira. Physical Review, **184**, 589 (1969).

[168] T. Kaneko and S. Abe. Journal of the Physical Society of Japan, **20**, 2001 (1965).

[169] J. H. Lee and K. M. Rabe. Physical Review B, **84**, 104440 (2011).

[170] M. Kachlik, K. Maca, V. Goian, and S. Kamba. Materials Letters, **74**, 16 (2012).

[171] S. Kamba, D. Nuzhnyy, P. Vaněk, M. Savinov, K. Knížek, Z. Shen, E. Šantavá, K. Maca, M. Sadowski, and J. Petzelt. Europhysics Letters, **80**, 27002 (2007).

[172] Q. Sun, D. Mazumdar, L. Yadgarov, R. Rosentsveig, R. Tenne, and J. L. Musfeldt. Nano Letters, **13**, 2803 (2013).

[173] J. L. Musfeldt, K. Kamarás, and D. B. Tanner. Physical Review B Condensed Matter, **45**, 197 (1992).

Vita

Michael O. Yokosuk was born in Nashville, Tennessee. He attended Lee University between 2008 and 2012, where he received two B.S. degrees majoring in Mathematics and Chemistry. Michael joined the research group of Dr. Janice L. Musfeldt in the Spring of 2013 pursuing his Masters degree from the University of Tennessee. In Summer of 2014, he switched from the Masters program to pursue his Ph.D. degree. His research focuses on the spectroscopic investigation of complex oxides and the coupling they present between charge, magnetism, and the lattice. Michael O. Yokosuk received a Doctor of Philosophy Degree in Chemistry from the University of Tennessee in the Spring of 2019.